Summer 9-20-2022

Kinetic Modeling of Ionospheric Outflows Observed by the VISIONS-1 Sounding Rocket

Robert M. Albarran II
Embry-Riddle Aeronautical University, albarrar@my.erau.edu

KINETIC MODELING OF IONOSPHERIC OUTFLOWS OBSERVED BY THE VISIONS-1 SOUNDING ROCKET

BY
ROBERT M. ALBARRAN II

A Dissertation
Submitted to the Department of Physical Sciences
and the Committee on Graduate Studies
In partial fulfillment of the requirements
for the degree of
Doctor of Philosophy in Engineering Physics

09/2022
Embry-Riddle Aeronautical University
Daytona Beach, Florida

KINETIC MODELING OF IONOSPHERIC OUTFLOWS OBSERVED BY THE VISIONS-1 SOUNDING ROCKET

by

Robert M. Albarran II

This dissertation was prepared under the direction of the candidate's Dissertation Committee Chair, Dr. Matthew Zettergren, Ph.D., and has been approved by the Dissertation Committee. It was submitted to the Department of Physical Sciences in partial fulfillment of the requirements of the degree of

Doctor of Philosophy in Engineering Physics

DISSERTATION COMMITTEE:

Matthew Zettergren

Dr. Matthew Zettergren, Ph.D.,
Committee Chair

Dr. Kshitija Deshpande, Ph.D.,
Committee Member

Dr. Katariina Nykyri, Ph.D.,
Committee Member

Dr. Jeffrey Klenzing, Ph.D.,
Committee Member

Dr. Edwin Mierkiewicz, Ph.D.,
Graduate Program Chair,
Ph.D. Engineering Physics

Dr. John Hughes, Ph.D.,
Department Chair, Physical Sciences

Dr. Peter Hoffmann, Ph.D.,
Dean, College of Arts and Sciences

Lon Moeller, J.D.,
Senior VP for Academic Affairs and Provost

Abstract

Plasma escape from the high-latitude ionosphere (ion outflow) serves as a significant source of heavy plasma to magnetospheric plasma sheet and ring current regions. Outflows alter mass density and reconnection rates, hence global responses of the magnetosphere. The VISIONS-1 (VISualizing Ion Outflow via Neutral atom imaging during a Substorm) sounding rocket was launched on Feb. 7, 2013 at 8:21 UTC from Poker Flat, Alaska, into an auroral substorm with the objective of identifying the drivers and dynamics of nightside ion outflow at altitudes where it is initiated, below 1000 km. Energetic ion data from the VISIONS-1 polar cap boundary crossing show evidence of an ion "pressure cooker" effect whereby ions energized via transverse heating in the topside ionosphere travel upward and are impeded by a parallel potential structure at higher altitudes.

A new fully kinetic model is constructed from first principles which traces large numbers of individual O^+ ion macro-particles along curved magnetic field lines, using a guiding-center approximation, in order to facilitate calculation of ion distribution functions and moments. Particle forces in a three-dimensional global Cartesian coordinate system include mirror and parallel electric field forces, a self-consistent ambipolar electric field, and a parameterized source of ion cyclotron resonance (ICR) wave heating, thought to be central to the transverse energization of ions. The model is initiated with a steady-state ion density altitude profile and Maxwellian velocity distribution and multiple particle trajectories are advanced via a direct simulation Monte Carlo (DSMC) scheme. This document outlines the design and implementation of the kinetic outflow model and shows applications of simulated outflows representative of conditions observed during the VISIONS-1 campaign. This project provides quantitative means to interpret VISIONS-1 data and related remote sensing approaches to studying ion outflows and serves to advance our understanding of the drivers and particle dynamics in the auroral ionosphere and to improve data analysis for future sounding rocket and satellite missions.

Acknowledgments

I primarily thank the Dissertation Advisory Committee Chair and project advisor, Dr. Matthew Zettergren, for making this study possible. I am grateful for the Dissertation Advisory Committee, Dr. Nykyri, Dr. Klenzing, and Dr. Deshpande, for their invaluable input and support. I also greatly thank Dr. Doug Rowland, Dr. Robert F. Pfaff, Dr. Micheal Collier, Dr. Jim Clemmons and others involved in the VISIONS-1 mission. I would like to thank my brother, Stephen, for the late night science discussions. Thank you to my wonderful wife, Sadie, for tolerating my unorthodox sleep schedule and being patient with my trials and tribulations. This dissertation is dedicated to my parents, Roberto and Charlene, and my grandmothers, Gerline and Leticia. This project was supported by NASA grants: NNX15AJ08G and NNX16AF06G and NSF grant: AGS-1255181.

We do not rise to the level of our expectations. We fall to the level of our training.

-Archilochus, Greek Soldier, 650 BC

Contents

List of Tables

List of Figures

Chapter 1

INTRODUCTION

1.1 Earth's Magnetosphere

Earth's strong intrinsic magnetic field shields the planet from the solar wind- a supermagnetosonic collisionless plasma radially emitted from the Sun. Solar wind compresses the geomagnetic field on the day-side and generates the bow shock about 12 Earth radii (R_E) from Earth's surface and extends the geomagnetic field into the magnetotail on the night-side. Solar wind is decelerated and heated at the bow shock and deflected around Earth to form a $\sim 3R_E$ layer called the magnetosheath. Earth's magnetic field dominates the region known as the magnetosphere. The magnetopause- the layer between the magnetosheath and the magnetosphere- is marked by the balance between the dynamic solar wind pressure and the magnetic pressure of the magnetosphere. Some of the solar plasma may directly enter the day-side magnetosphere through the polar cusp (cleft) and deposit energy in the upper atmosphere. The magnetospheric system is illustrated in Figure 1.1.

Terrestrial plasma that has escaped the Earth's atmosphere and solar wind particles that convect around the Earth to the night-side populate the plasma sheet. Plasma sheet particles may access the night-side upper atmosphere magnetic field lines. Field lines extend to the day-side cusp to form the auroral oval at low altitudes. Aurora borealis (australis) displays are generated as plasma sheet particles collide with the upper atmosphere in the auroral oval of the northern (southern) hemisphere. A large-scale current flow across the plasma sheet from dawn to dusk separates the magnetic hemispheres known as the neutral current sheet. Currents in the magnetotail connect with those of the magnetopause on the day-side and generate voltage drops greater than 10^5 V with more than 10^{12} W of power [Shunk and Nagy, 2000]. The magnetotail voltage drop maps to the poleward region of the auroral oval known as the polar cap.

Van Allen radiation belts are populated partially by inward motion of particles from the plasma

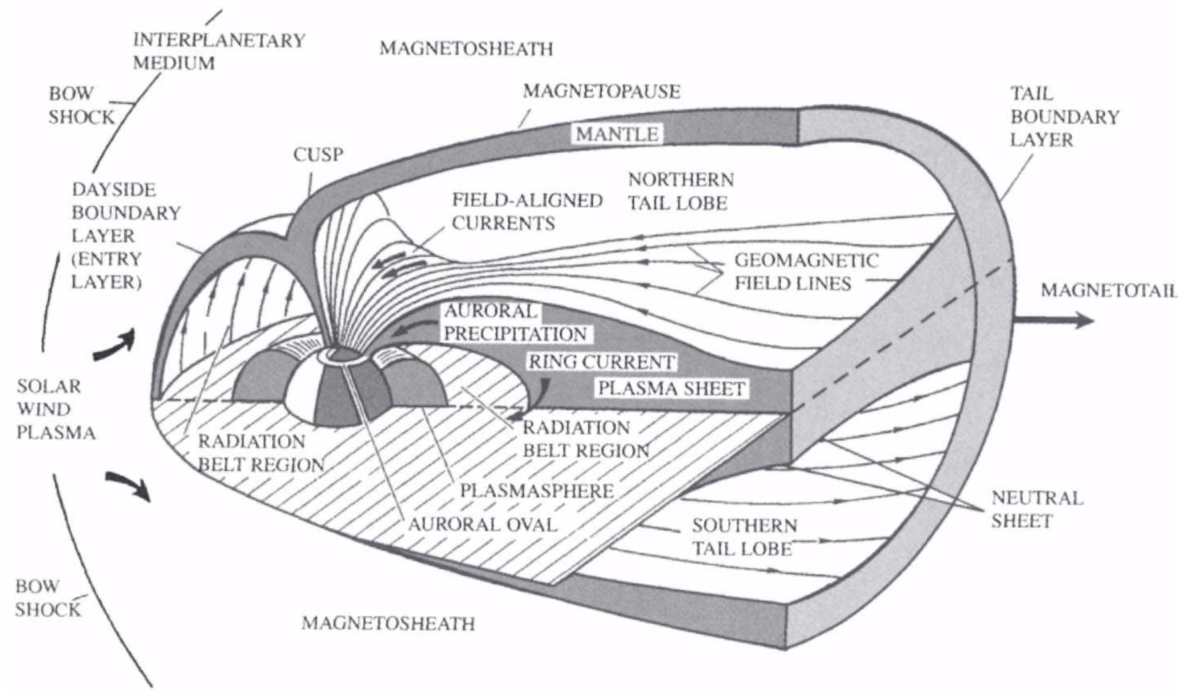

Figure 1.1: The magnetospheric system of the Earth illustrating the magnetospheric regions and boundaries. Courtesy of J. R. Roederer, Geophysical Institute, University of Alaska [Shunk and Nagy, 2000].

sheet. Radiation belt particles gyrate around the magnetic field lines poleward where they reflect and bounce to the opposite hemisphere and thus get trapped on closed geomagnetic field lines. Low-energy (10-300 keV) radiation belt particles drift in the azimuthal direction around the Earth and form the ring current [Shunk and Nagy, 2000]. Within the radiation belts is a torus-shaped region around the Earth extending $\sim$ 4-8 R_E of high-density $\sim 10^8$ m^{-3}, relatively cool $\sim$ 5000 K co-rotating ionospheric plasma. The plasmapause is the boundary between the co-rotating plasmasphere and the plasma subject to magnetospheric electric fields [Shunk and Nagy, 2000].

1.2 Earth's Ionosphere

The terrestrial ionosphere is ultimately produced by particles from the Earth's atmosphere- a spherical envelope of the planet's surface to beyond $\sim$ 1000 km in altitude. Atmospheric layers are illustrated in Figure 1.2. Relative composition of primary neutral gases N_2 and O_2 remains constant below $\sim$ 90 km and the density decreases exponentially with altitude. Below $\sim$ 10 km is the troposphere where most atmospheric weather occurs. From $\sim$ 10-45 km is the stratosphere where the ozone layer resides. Above this is the mesosphere from $\sim$ 45-90 km where most meteors are visible. The thermosphere is the upper atmosphere from $\sim$ 95-500 km where N_2 and O_2 gases are dissociated by solar flux to produce N and O particles which are gravitationally separated such that heavy neutral molecules dominate low altitudes and light neutral atoms dominate high altitudes. The exosphere is characterized by the region at $\sim$ 500 km where neutral densities become so low that it is nearly collisionless and no longer described as a fluid [Shunk and Nagy, 2000].

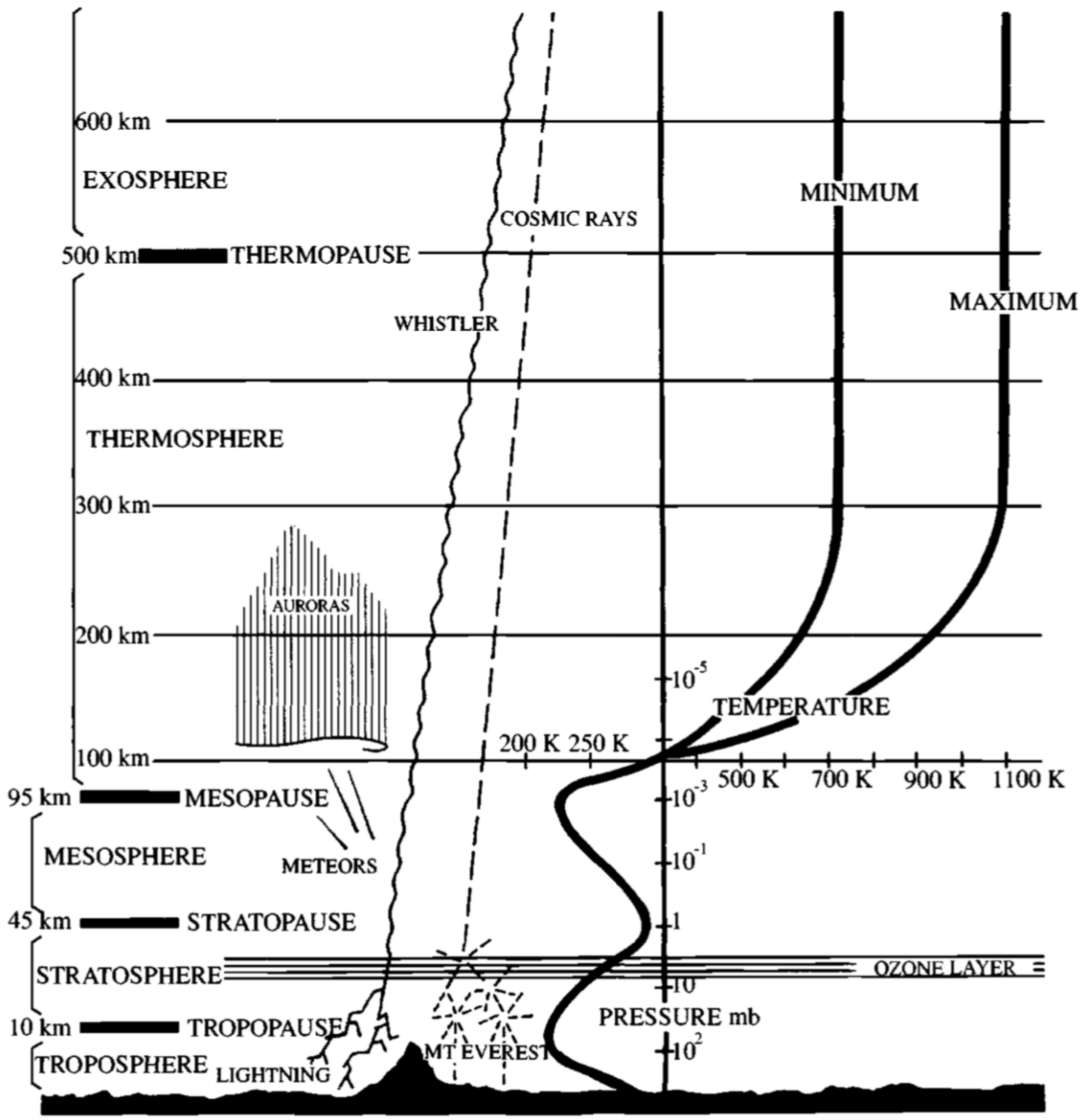

Figure 1.2: The atmospheric system of the Earth illustrating the atmospheric layers and boundaries. The solid black lines correspond to the temperature profiles for solar maximum and minimum [Shunk and Nagy, 2000].

Earth's ionosphere completely envelops the Earth and extends from $\sim$ 60 km to beyond $\sim$ 1000 km in altitude, as illustrated in Figure 1.3. It is produced by the photoionization of neutral molecules of the upper atmosphere primarily by solar EUV and soft X-ray radiation. Ions in the ionosphere interact chemically with neutral particles, recombine with electrons, and diffuse to different altitudes. Electron density gradients in altitude characterize the ionospheric layers along all latitudes. Chemical interactions of molecular ions such as NO^+ and O_2^+ and neutral particles such as N_2, O_2, and O dominate the low-altitude ionosphere in the D and E regions ($\sim$ 60-100 km). The E region from $\sim$ 100-150 km in altitude is weakly ionized with less complex chemical reactions. E region ion densities are $\sim 10^{11}$ m^{-3} and neutral densities are $\sim 10^{17}$ m^{-3} such that it is highly collisional. The F_1 region from $\sim$ 150-250 km in altitude is characterized by ion-neutral interactions and transport processes become more significant and the ionization peak in altitude occurs by the balance of plasma transport and chemical loss mechanisms at the F_2 region where the peak ion density is $\sim 10^{12}$ m^{-3} and the neutral density is $\sim 10^{14}$ m^{-3} [Rishbeth and Garriott, 1969]. The F regions are partially ionized and collisions are significant. The topside ionosphere is above the F region peak and the protonosphere is where H^+ and He^+ ions dominate. Protonospheric plasma is effectively fully ionized and charged particle collisions must be considered along with plasma transport processes [Shunk and Nagy, 2000].

It is thought that the ionosphere represents a significant source of ions in the magnetosphere [Chappell et al., 1987]. Transport of ionospheric plasma to the magnetosphere is characterized by the ionospheric heating, expansion, and upflow of ions, the transverse acceleration of ions along the geomagnetic field lines, and the conversion of perpendicular ion energy to parallel escape energy [Strangeway et al., 2005] [Zheng et al., 2005]. Type 1 ion upflow and ionospheric expansion is due to frictional heating from differential ion-neutral drifts [Wahlund et al., 1992] [Zettergren and Semeter, 2012]. Type 2 ion upflow is caused by field-aligned ambipolar electric fields generated from ionospheric electrons heated by soft particle precipitation [Su et al., 1999]. Ion upflow has primarily been observed in the cusp or midnight auroral zone with ion velocities of $\sim$ 100-750 m $\cdot$ s^{-1} below 1000 km [Ogawa et al., 2003] [Foster and Lester, 1996]. Ion outflow occurs above the upflow altitudes where ions are further energized to escape velocity by the magnetic mirror force, forming ion conic distributions from $\sim$ 10-1000 eV [Yau and Andre, 1997] [André and Yau, 1997], by broadband extremely low-frequency (BBELF) and very low-frequency (VLF) wave energization by ion cyclotron resonance heating [Crew et al., 1990] [Kintner et al., 1996] [André et al., 1998], by lower hybrid plasma waves [Lynch et al., 1996] [Lynch et al., 1999], and/or by auroral acceleration region parallel electric fields, forming $\sim$ 1-10 keV ion beams [McFadden et al., 1998].

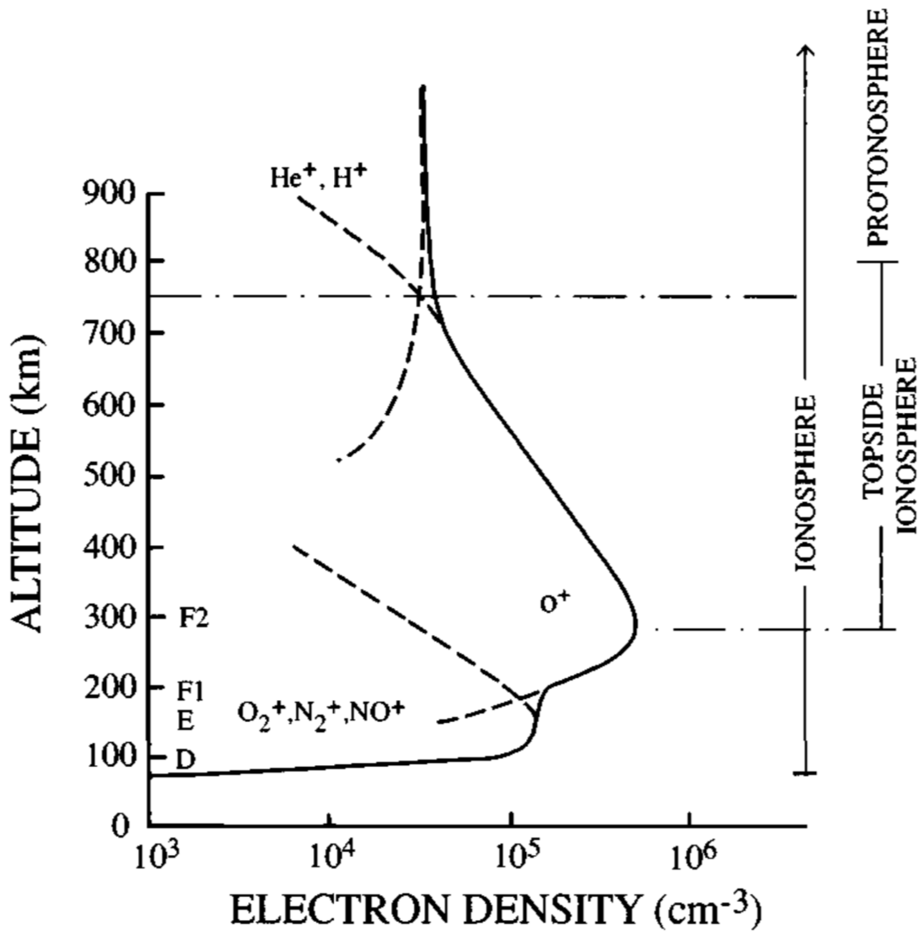

Figure 1.3: The ionospheric system of the Earth illustrating the ionospheric layers and boundaries with ion density profiles for daytime mid-latitudes [Shunk and Nagy, 2000].

1.3 Observations of Ionospheric Outflow

Ionospheric outflow at polar latitudes has been an avid subject of theoretical and experimental study since it was predicted [Dessler and Michel, 1966] [Nishida, 1966]. First evidence of ionospheric plasma populating the magnetosphere was inferred by [Shelley et al., 1972] through observations of precipitating keV O^+ fluxes exceeded H^+ flux values. This was confirmed by > 0.5 keV upflowing H^+ and O^+ ions above 5000 km observed by the polar-orbiting S3-3 satellite [Yau and Andre, 1997] where observations demonstrated ion velocity distribution peaks along the upward magnetic field line direction (ion beams) [Shelley et al., 1976] and distribution peaks at angles to the magnetic field lines (ion conics) [Sharp et al., 1977].

Ion dynamics are characterized by the transition from chemical to diffusion dominance at 500-800 km, from subsonic to supersonic flow at 1000-2000 km, from the collisional to collisionless regime at 1500-2500 km, and from a O^+ to H^+ dominant plasma from 5000-10000 km [Wu et al., 1999]. O^+ and H^+ ions usually have near-Maxwellian distribution functions due to frequent ion-ion collisions below the collisional/collisionless transition region at 1500-2500 km [St-Maurice and Shunk, 1979] [Ho et al., 1997]. Non-Maxwellian distributions develop above the transition region due to macroscopic forces and wave-particle interactions [Ho et al., 1997] [Wilson, 1992]. Characteristic distribution functions at the collisional/collisionless transition region are due to competing processes of collisions, kinetic effects, and macroscopic forces [Wilson, 1995] [Barghouthi et al., 1993] [Barakat et al., 1995]. High-altitude superthermal ion distributions include ion conics, bowls, rings and beams up to tens or hundreds of eV as observed along active auroral field lines [Klumpar et al., 1984] [Hirahara, 1998]. It is indicated by observations that F region and topside ionospheric regions have ion outflows dominantly upward near the cusp and auroral oval and downward in the polar cap regions [Loranc et al., 1991]. Ion outflow flux is much larger in the cusp and auroral oval than in the polar cap [Loranc et al., 1991] [Wu et al., 2000] and increases exponentially with K_p index [Yau and Andre, 1997].

Transport of ions in the high-latitude topside ionosphere polar wind is continuous [Axford, 1968] while the superthermal O^+ ion outflows from auroral regions are intermittent [Moore, 1984]. The polar wind was shown to be a supersonic flow of protons along open geomagnetic field lines in the 1960s [Axford, 1968] [Banks and Holzer, 1968]. Dynamics Explorer (DE-1) satellite measured the outflow rate of the polar wind in the 1980s [Nagai et al., 1984] and O^+ ion outflow was demonstrated the following year [Waite, 1985]. Continuous ion outflows have been observed by the DE-1 satellite and the EISCAT radar [Wu et al., 1992]. DE-1 satellite in the dayside polar cap poleward of the cusp/cleft observed ions heated in the cusp and drifted poleward by magnetospheric convection to form the cleft ion fountain (CIF) [Lockwood et al., 1985a]. Sporadic ion outflows were observed in the topside ionosphere likely driven by magnetospheric energy input [Jones et al., 1988] [Winser et al., 1988] and occured within small scale structures of auroral arcs [McFadden et al., 1990] [Abe et al., 1991]. Statistical studies from data acquired from auroral passes of the Polar satellite in 2000 have investigated ion outflow relations to the Poynting flux, electron density and temperature, and electron energy flux [Zheng et al., 2005]. Wave-particle interactions and anomalous resistivity have been shown by observational data analysis to accelerate ions [Wahlund and Opgenoorth, 1989] [Wahlund et al., 1992] [Li and Temerin, 1993] [Wahlund et al., 1993] [Forme, 1993] [Forme et al., 1993]. Statistical observations from the Freja [Norqvist et al., 1998] and FAST [Lund et al., 2000] satellites demonstrated that a primary source of ion transverse heating is the enhancement of the broadband extremely low-frequency (BBELF) wave turbulence that covers a frequency range from less than 1 Hz to several hundred Hz over the H^+ and O^+ gyrofrequencies from about 1000 km up to a few R_E [Bouhram et al., 2003a]. EISCAT-VHF observations showed 800 $\mathrm{m \cdot s^{-1}}$ O^+ ion outflows associated with electron temperature enhancements up to 7000 K at 1000 km altitudes [Blelly and Alcaydé, 1994]. O^+ ion outflows with upward velocities of 600 $\mathrm{m \cdot s^{-1}}$ at 1000 km altitudes have been observed [Blelly et al., 1996]. Cluster and MMS missions have revealed 10 keV O^+ ions of ionospheric origin at $r \sim$ 5-9 R_E in dayside diamagnetic cavities created by magnetic reconnection both at high [Nykyri et al., 2011] and low latitudes [Nykyri et al., 2019]. Although much research has been done concerning ion outflow and energization mechanisms, the correlations between ion outflow and different energy inputs are less studied [Strangeway et al., 2005].

The last four to five decades of ionospheric ion outflow study has demonstrated that outflow from the Earth's ionosphere to magnetosphere is highly variable in composition, energy, space, and time. Observations have shown that ion outflow is dependent on solar cycle, season, and geomagnetic activity [Yau et al., 1985] [Collin et al., 1998]. The association between the occurrence frequency of dayside ion upwelling and the solar wind dynamic pressure has been demonstrated by observations [Giles, 1993]. Observed ion upflows in the topside ionosphere have been correlated with soft auroral electron precipitation [Seo et al., 1997]. Although it is considered that the solar wind enters the magnetosphere to deposit a significant amount of energetic ions to the plasma sheet [Eastman et al., 1985] [Kivelson and Spence, 1988] [Lennartsson, 2001], the solar wind source alone is not sufficient to supply the plasma sheet and ring current with observed O^+ levels [Shelley et al., 1972]. Ion mass spectrometer data showed evidence for ionospheric plasma outflow into the magnetosphere [Brinton et al., 1971]. Measurements taken in the 1980s from the Dynamics Explorer satellite suggest the plasma in the plasmasphere, plasma trough, plasma sheet, and magnetotail lobes may be sufficiently supplied by the ionosphere [Huddleston et al., 2005]. The enlarged cusp/cleft region in the dayside auroral zone between $\sim$ 9-15 hours magnetic local time (MLT) extending a few degrees in latitude [Bouhram et al., 2003a] has been identified as a major source of ionospheric ions for the magnetosphere [Lockwood et al., 1985b] [Thelin et al., 1990]. It is suggested that all regions of the magnetosphere may be supplied by ionospheric ions except for the inner radiation belt [Huddleston et al., 2005]. Magnetospheric energy may be deposited to the high-latitude ionosphere by precipitating charged particles, field-aligned currents, or Alfvén waves [Zheng et al., 2005].

Downward field-aligned currents generated by quasi-static parallel electric fields in the auroral acceleration region from 800-5000 km in altitude have been observed by radars and sounding rockets [Marklund et al., 1982] [Marklund, 2009], Freja [Marklund et al., 1994] [Marklund et al., 1997] and FAST [Johansson et al., 2004] [Figueiredo et al., 2005] satellite passes, and Cluster multi-point observations between 4-5 R_E [Marklund, 2009] [Johansson et al., 2007] [Johansson et al., 2004]

[Figueiredo et al., 2005] [Marklund et al., 2011]. Upward and downward parallel electric fields in the auroral acceleration region observed by Cluster [Vaivads et al., 2003] [Figueiredo et al., 2005] [Marklund et al., 2001] [Johansson et al., 2004] are either monopolar or bipolar corresponding to S-shaped or U-shaped potential structures, respectively. S-shaped and U-shaped potential structures are associated with strong density gradients at the plasma sheet boundary and weak density gradients inside the plasma sheet, respectively [Marklund et al., 2007] [Johansson et al., 2006]. A combination of downward electric fields and wave heating mechanisms contribute to the generation of ion conic distributions through the "pressure cooker" effect [Gorney et al., 1985] [Barakat and Barghouthi, 1994] [Jasperse, 1998] which is a potential barrier that traps upflowing ions with insufficient energy to overcome the barrier. The "pressure cooker" effect explains observations of conics of a few hundred eV without particle interactions with high-powered waves [Ho et al., 1997]. Typical ion conic temperatures range from 10 eV to at least a few keV depending on the altitude of observation [Bouhram et al., 2003a] [Moore et al., 1999]. Outflowing ions form high-energy conic distributions when observed in the high-altitude heating region and form low-energy field-aligned distributions when observed poleward to the heating region [Horwitz, 1986] [Knudsen et al., 1994] [Dubouloz et al., 1998].

1.4 Models of Ionospheric Outflow

Enhancement of neutral oxygen density ionized by solar EUV flux in the topside ionosphere has been shown by models to result in the association of increased ion outflow [Cannata and Gombosi, 1989]. Upward ion motion in the high-latitude ionosphere may be divided into two broad categories: bulk ion flows and fractional ion flows [Yau and Andre, 1997]. Bulk ion flows, such as polar wind and auroral bulk ion outflows, correspond to ion energies up to a few eV of nearly all ions. Other ion flows, such as transversely accelerated ions (TAIs), upwelling ions, ion conics, and beams, correspond to a fraction of the ion population energized to energies higher than a few eV. H^+ and O^+ ions at the collisional lower ionosphere with average energies of 0.1 eV require an energy increase to reach escape velocity of at least 1 eV to 10 eV, respectively [Zheng et al., 2005]. Several ion energization mechanisms may be at work for this process to occur. Energization mechanisms for heavy ion outflows are either parallel or perpendicular heating mechanisms. Parallel acceleration includes parallel potential drops and parallel electric field enhancements and perpendicular acceleration includes transverse energization at topside ionosphere altitudes by low-frequency waves at higher altitudes where the collision frequency is below the gyro-frequency [Zheng et al., 2005].

It is generally regarded that most transversely heated ion conics are due to cyclotron-resonant interactions with broadband extremely low-frequency (BBELF) waves [Norqvist et al., 1998]. Early polar wind simulations were performed by fluid equations driven by pressure gradients between the ionosphere and magnetosphere. It was subsequently noted that kinetic processes are required for the simulation of O^+ ion outflow [Peterson, 1994] [Khazanov et al., 1997] [Demars et al., 1999].

Several previous models of the high-latitude environment are moment-based fluid treatments [Schunk and Sojka, 1989] [Mitchell and Palmadesso, 1983] which are unable to model in detail high-altitude non-Maxwellian distributions, such as ion conics [Wu et al., 1999]. Other researchers have employed semikinetic models [Wilson, 1992] [Brown et al., 1995] and fully kinetic models [Schriver, 1999] which have encountered difficulties in simulating the collisional regimes below 1000 km [Wu et al., 1999]. There have been several models of ion outflow that couple a fluid moment-based model for the collisional ionosphere to a kinetic distribution function-based model for the transition and collisionless ionosphere [Winske and Omidi, 1996] [Lemaire, 1972] [Barakat and Shunk, 1983] [Schunk and Sojka, 1989] [Lie-Svendsen and Rees, 1996] [Su et al., 1998]. [Wilson, 1992] has employed a collisional semikinetic model to study the topside ionosphere transition region from O^+ to H^+ dominance, subsonic to supersonic H^+ flow, and collisional to collisionless plasma including O^+ and H^+ collisions, H^+ self collisions, magnetic mirror, gravity, and ambipolar field forcing. Semikinetic models have also been employed to simulate the "pressure cooker" effect generated by field-aligned potential drops [Barakat and Barghouthi, 1994] [Brown et al., 1995] and to simulate hot magnetospheric plasmas [Brown et al., 1995]. Semikinetic simulations conducted by [Brown et al., 1995] generated non-Maxwellian ion distribution functions, yet ion-neutral and ion-ion collisions were neglected and a fixed lower boundary at 1500 km was assumed [Wu et al., 2002].

[Wilson, 1994] [Wilson, 1992] [Wilson et al., 1990] developed a collisional semikinetic model with ion-neutral resonant charge-exchange, polarization and Coulomb self collisions with ambipolar, gravity, magnetic mirror, and centripetal force fields at the high-latitude ionospheric F region. A similar time-dependent semikinetic model was employed by [Brown et al., 1991] to investigate the effects of wave-particle interactions on ion conic and ring distributions. A time-dependent coupled fluid-kinetic model, the dynamic fluid-kinetic (DyFK) model, has been developed [Estep, 1998] [Estep et al., 1998] and employed to simulate ion outflow in the auroral region with thermal electron heating and ionization of soft auroral electron precipitation of the F region topside and the transverse heating of ions at higher altitudes [Wu et al., 1999]. The DyFK model is a one-dimensional dynamic flux tube model that combines a truncated version of the field line interhemispheric plasmasphere (FLIP) formalism and generalized semikinetic (GSK) model [Richards and Torr, 1990] [Brown et al., 1995] [Wilson, 1992] [Ho et al., 1997]. GSK is a hybrid guiding center model that simulates the ionosphere from 800 km to 3 R_E where macro-particles are subject to parallel electric fields, the magnetic mirror, and gravitational forces with ion-ion and ion-neutral collisions [Wu et al., 2002]. In the study conducted by [Wu et al., 2002], approximately 5×10^5 O^+ and H^+ macro-particles, each representing several ionospheric ions, are simulated with parallel potential drops, wave-particle interactions, and soft electron precipitation by the DyFK model. The study performed by [Zeng et al., 2006] investigates the roles of Coulomb collisions and kinetic processes in the high-latitude collisional/collisionless transition region with a computational flux tube from 120 km to 3 R_E in altitude by employing the DyFK model.

Several kinetic studies of outflowing ions have been developed in an effort to negotiate limitations of fluid models- such as the resolution of non-Maxwellian distributions at high altitudes- and to make more direct comparisons with spacecraft measurements [Wilson et al., 1990]. These models include one-dimensional, steady-state, kinetic [Lemaire and Scherer, 1973] and semikinetic [Barakat and Shunk, 1983] [Li et al., 1988] models. Two and three-dimensional nonself-consistent codes that trace ionospheric ions of the polar magnetosphere into the magnetotail have been developed [Cladis, 1988] [Horwitz, 1987]. [Wilson et al., 1990] have introduced a kinetic, one-dimensional, time-dependent polar outflow model out to several R_E with a self-consistent ambipolar electric field by computing parallel drifts by the collisionless Boltzmann equation. A small-scale (on the order of a few Debye lengths) particle-in-cell (PIC) code was developed by [Singh and Chan, 1993] to study ion conics, density perturbations, parallel electric fields, ion-ion interactions, and multi-streaming of ions generated by ion heating in the magnetosphere.

Transport of non-thermal H^+ and O^+ flows from the dayside cusp/cleft from 1000-20000 km subject to the mirror force, gravity, ion cyclotron wave heating by BBELF waves, and poleward drift by magnetospheric convection has been modeled by a steady-state, two-dimensional ion trajectory tracing code [Bouhram et al., 2003a]. Guiding center particle motion is traced for poleward drift due to convection and one-dimensional parallel macroscopic forcing such that field curvature is neglected and curvature drifts, gradient drifts, and centrifugal acceleration are not included [Bouhram et al., 2003a]. Since no analytic theory is available in two dimensions, the results of [Bouhram et al., 2003a] have been tested against global conservation laws. In the study by [Bouhram et al., 2003a], the kinetic equation given by [Ichimaru, 1973] for the time-evolution of the ion distribution function is solved by the commonly employed Monte Carlo technique [Retterer et al., 1983] [Retterer et al., 1989].

Models have suggested that parallel ion acceleration is insufficient in depositing observed quantities of heavy ions into the magnetosphere [Arnoldy, 1993]. Although it is believed that perpendicular ion acceleration primarily by wave-particle interactions is a significant mechanism in the generation of low-energy superthermal ion upwelling observed in the cusp/cleft region and low-energy polar wind observed in the polar cap region [Moore et al., 1986] [Ganguli, 1996], it is not sufficient to accelerate ions to kilovolt energies typical in the plasma sheet and ring current [Huddleston et al., 2005]. The total ion outflow flux between 2×10^{25} s^{-1} and 6×10^{26} s^{-1} as simulated by the Generalized Polar Wind (GPW) model was determined to be consistent with observations for the September 27 and October 4 storms of 2002 [Barakat et al., 2015]. Polar wind, cleft ion fountain, and auroral zone guiding center (for low altitudes) and full Lorentz force (beyond 2 R_E altitudes) simulations have been computed by a modified [Sauvaud and Delcourt, 1987] steady-state three-dimensional particle tracing code [Delcourt, 1985] [Delcourt et al., 1988] [Delcourt et al., 1989] [Delcourt et al., 1993] to suggest that the ionosphere is fully capable in supplying the magnetosphere with plasma at observed O^+, H^+, and He^+ densities and energies [Huddleston et al., 2005].

Ion tracing by solving particle equations of motion that include the Lorentz and gravitational forces by a standard fourth-order Runge-Kutta technique has been studied for dispersive Alfvén waves above the auroral oval [Chaston et al., 2004]. This demonstrated that ion acceleration by Alfvén waves from the topside ionosphere occurs by coherent ion motion at low altitudes and stochastic motion that leads to ion energies that exceed 10 keV at higher altitudes where the geomagnetic field weakens and the wave amplitude strengthens [Chaston et al., 2004]. A similar model for Alfvénic plane waves has been formulated by [Thompson and Lysak, 1996] and a kinetic treatment has been formulated by [Chaston et al., 2003]. Major sources of ion energization such as ion cyclotron resonance heating, electric potential drops, and transverse heating by lower hybrid waves have been studied by two-dimensional, steady-state, Monte Carlo, trajectory-based codes [Bouhram et al., 2003a] [Bouhram et al., 2003b]. A GEM (Geospace Environment Modeling) focus group now exists to investigate ionospheric sources of plasma in the magnetosphere and merge outflow and MHD models and compare to observations [Yau and Andre, 1997] [Chappell et al., 2000].

Several studies model ion velocity distribution functions of ionospheric outflows, either by fluid, semikinetic, or kinetic methods [Schunk and Sojka, 1989] [Mitchell and Palmadesso, 1983] [Brown et al., 1995] [Barakat and Barghouthi, 1994] [Brown et al., 1995] [Bouhram et al., 2003a] [Bouhram et al., 2003b]. High-altitude fluid models [Schunk and Sojka, 1989] [Mitchell and Palmadesso, 1983] are unable to generate non-Maxwellian ion distribution functions, such as elevated ion conic, bowl, and toroidal distributions. This dissertation introduces a fully kinetic code based on first principles with the capacity of simulating O^+ ion outflows along altitude ranges of a given L-shell in magnetic dipole coordinates. Altitude ranges of pressure cooker structures depend on plasma scale heights and computational resources available. The aim of this model is to simulate the conditions of ion outflow present during a recent sounding rocket flight and provide a theoretical tool to synthesize and interpret energetic ion observational data sets. As the wave heating and parallel drop parameter space varies in space and time, numerous case studies are needed for kinetic studies to synthesize observational data from spacecraft and sounding rockets. Various wave heating and pressure cooker environments parameterized to VISIONS-1 flight conditions are modeled and differential energy fluxes consistent with observed levels are generated. The primary science question is considered: What are the energy inputs and conditions leading to energized outflowing ion distributions seen from VISIONS-1? More generally, what kinetic processes lead to outflow from auroral zones and/or cusp?

Chapter 2

MODEL METHODOLOGY

The motivation is to construct a kinetic model of ionospheric outflow that (1) can connect easily to other low-altitude models, (2) is flexible enough to handle curved field lines (like many fluid models), and (3) has the ability to investigate highly non-Maxwellian distribution functions corresponding to differential ion energy fluxes observed by the VISIONS-1 sounding rocket. Kinetic processes are required for the simulation of O^+ ion outflow [Peterson, 1994] [Khazanov et al., 1997] [Demars et al., 1999]. High-latitude fluid models [Schunk and Sojka, 1989] [Mitchell and Palmadesso, 1983] are unable to model non-Maxwellian ion distribution functions, such as ion conic, bowl, and toroidal distributions. Such distributions are generated by two-dimensional kinetic models [Bouhram et al., 2003a] [Bouhram et al., 2003b] and semikinetic models [Brown et al., 1995]. Collisional transition ionosphere below 1000 km is included in the computational domain which is a feature not present in many kinetic and semikinetic codes [Wilson, 1992] [Brown et al., 1995] [Schriver, 1999] [Winske and Omidi, 1996] [Lemaire, 1972] [Barakat and Shunk, 1983] [Schunk and Sojka, 1989] [Lie-Svendsen and Rees, 1996] [Su et al., 1998]. Alternative to semikinetic simulations of parallel potential drops by [Barakat and Barghouthi, 1994] [Brown et al., 1995], this dissertation introduces a kinetic model with capability to simulate pressure cooker effects by direct simulation Monte Carlo (DSMC). In this study, non-Maxwellian ion distribution functions are generated in three-dimensional velocity space in particle gyro-frames from fully kinetic formalism. Transverse motion is resolved in two perpendicular components and translational (parallel) motion is described by three-dimensional global Cartesian unit basis to accommodate flux-tube curvature by dipole approximations.

The model introduced in this Chapter computes ion trajectories subject to self-consistent ambipolar electric fields, gravitational and magnetic mirror forcing, parallel potential drops, and ion cyclotron resonance heating in a fully kinetic framework. [Wilson, 1994] [Wilson, 1992] [Wilson et al., 1990] formulated semikinetic models for these energy inputs and [Bouhram et al., 2003a] [Bouhram et al., 2003b] simulated these effects in a two-dimensional trajectory-based code. As opposed to one-dimensional kinetic [Lemaire and Scherer, 1973] and semikinetic models [Barakat and Shunk, 1983] [Li et al., 1988], such as DyFK [Estep, 1998] [Estep et al., 1998], the following model computes wave-heated ionospheric outflows in a dipole magnetic field approximation. Nonself-consistent ambipolar electric fields in two or three dimensions exist in kinetic codes [Cladis, 1988] [Horwitz, 1987]. Self-consistent ambipolar electric fields in one-dimensional kinetic codes have been studied [Wilson et al., 1990]. The following code applies a field-aligned self-consistent ambipolar electric field onto three global Cartesian components for iterative advancement of particle velocities and positions integrated from field-aligned accelerations along curved magnetic field lines. All units in this study are SI units.

2.1 Model Phase-Space

2.1.1 Eulerian Configuration-Space

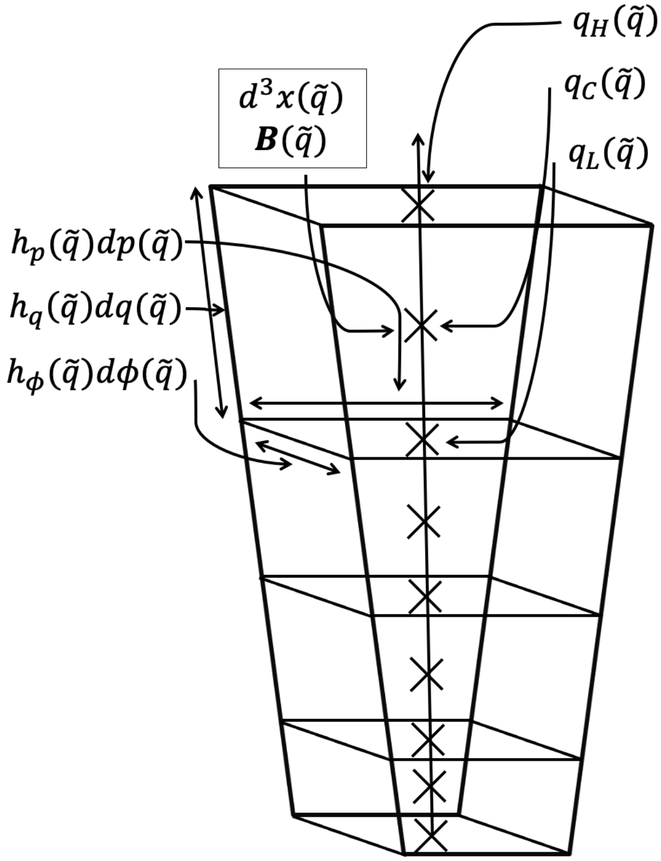

Figure 2.1: Diverging magnetic flux-tube configuration-space where $d^3x(\tilde{q})$ is the grid cell volume element, $B(\tilde{q})$ is the (centered) grid cell magnetic field-strength, $h_p(\tilde{q})dp(\tilde{q})$ is the grid cell dimension along $\hat{\mathbf{e}}_\mathbf{p}$, $h_q(\tilde{q})dq(\tilde{q})$ is the grid cell dimension along $\hat{\mathbf{e}}_\mathbf{q}$, $h_\phi(\tilde{q})d\phi(\tilde{q})$ is the grid cell dimension along $\hat{\mathbf{e}}_\mathbf{\phi}$, $q_H(\tilde{q})$ is the upper (high-altitude) q cell limit, $q_C(\tilde{q})$ is the center q cell coordinate, and $q_L(\tilde{q})$ is the lower (low-altitude) q cell limit.

Field-aligned Eulerian configuration-space grids on given L-shells curved in global Cartesian coordinates are generated in dipole approximations of Appendix .1. Spherical, (r, θ), to dipole, (p, q), coordinate transformations are overviewed in Appendix .10. Spherical coordinates corresponding to (p, q) coordinates are computed by magnetic dipole quartic polynomial root-finding methods detailed in Appendix .5. Dipole unit basis, metric and scale factors, and coordinate transformations are discussed in Appendices .2, .3, and .10, respectively. Plasmas are modeled within magnetic flux-tubes specified by altitude range and co-latitude. To eliminate equatorial discontinuities high-altitude q values are selected to match signs of low-altitude q values such that the grid is on a per-hemisphere-basis, that is, $q \in \begin{bmatrix}-1 & 0\end{bmatrix}$ for the southern magnetic hemisphere or $q \in \begin{bmatrix}0 & 1\end{bmatrix}$ for the northern magnetic hemisphere. Configuration-space grid cells are indexed $\tilde{q} \in \begin{bmatrix}1 & N_q\end{bmatrix}$, $\tilde{q} \in \mathbb{Z}^+$. The r component is measured from the center of the Earth. Each q grid cell has a lower limit, $q_L(\tilde{q})$, center value, $q_C(\tilde{q})$, and upper limit, $q_H(\tilde{q})$. Configuration-space grid cells have volume elements

$$d^3x(\tilde{q}) = h_p h_q h_\phi \, dp \, dq \, d\phi, \tag{2.1}$$

where $h_i(\tilde{q})\, di(\tilde{q})$ are the i^{th} component dimensions $\forall i = p, q, \phi$ according to Figure 2.1. Metric factors in magnetic dipole coordinates are derived in Appendix .3.

2.1.2 Lagrangian Macro-Particle Position Initialization

Initial O^+ ion densities are computed from thermospheric profiles in hydrostatic equilibria with altitude dependent gravitational acceleration. Each flux-tube has macro-particle normalization constant, μ. Configuration-space grid cells are initially populated with ions in steady-state with scale heights consistent with initial temperatures and reference density, n_0, at reference altitude corresponding to spatial grid cell of index $\tilde{q}_0$ [Shunk and Nagy, 2000]. The procedure outlined in Appendix .6 yields

$$n_C(\tilde{q}) = n_0 \exp\left[\frac{m\bar{g}}{k_B\left(T_\parallel + T_e\right)}\right], \quad \bar{g}(\tilde{q}) = \left[I_g(\tilde{q}) - I_g(\tilde{q}_0)\right], \tag{2.2}$$

where $\ell_C = 1 + 3\cos^2(\theta_C)$ and, by Equation 61,

$$I_g(\tilde{q}) = \frac{2GM_\oplus \cos(\theta_C)}{r_C^2\sqrt{\ell_C}} h_q \, dq.$$

$n_C(\tilde{q})$ is the number density of ions per flux-tube cell in [m^{-3}], m is the ion mass, $T_\parallel$ and T_e are the parallel ion temperature and electron temperature, respectively, G is the universal gravitational constant, $M_\oplus$ is the Earth's mass, and k_B is Boltzmann's constant. It is assumed that ions are initialized at isotropic temperatures such that $T_i = T_\parallel = T_\perp$. Ion densities are normalized by the product of macro-particle normalization constant, μ, with spatial cell volume, d^3x. The initial number of ion macro-particles in a given q grid cell is

$$\left|n_C\right|(\tilde{q}) = n_C\left(\frac{d^3x}{\mu}\right). \tag{2.3}$$

A desired altitude range is selected from a beginning and ending grid cell, N_{qICA} and N_{qICB}, such that $N_{qICA} \leq \tilde{q} \leq N_{qICB}$. Number of grid cells initially populated with ions is thus $N_{qIC} = N_{qICB} - N_{qICA} + 1$ each with N_s' ions:

$$N_s'(\tilde{q}) = \left|n_C\right| \left(N_{qICA} + \tilde{q} - 1\right). \tag{2.4}$$

Total number of simulated ion macro-particles initialized across the flux-tube is the summation of $N_s'(\tilde{q})$:

$$N_s = \sum_{\tilde{q}=1}^{N_{qIC}} N_s'(\tilde{q}). \tag{2.5}$$

Each grid cell contains N_s' macro-particles of index $\tilde{j}$ located at q coordinates, $q_0(\tilde{j})$, exponentially distributed within grid cell boundaries:

$$q_0(\tilde{j}) = q_L(N_{qICA} + \tilde{q} - 1) + \left[q_H(N_{qICA} + \tilde{q} - 1) - q_L(N_{qICA} + \tilde{q} - 1)\right] \gamma_{q0}, \tag{2.6}$$

where $\gamma_{q0}(\tilde{j}) \in E\begin{pmatrix}0 & 1\end{pmatrix}$ are random numbers generated from exponential distributions. Initial p coordinates, $p_0(\tilde{j})$, correspond to selected L-shells p_C, where $p_C = p_C(\tilde{q})\ \forall \tilde{q}$:

$$p_0(\tilde{j}) = p_C. \tag{2.7}$$

To avoid artificial discontinuities of density in altitude supercomputer clusters with R processors simulate a total of N_s macro-particles with each processor modeling N_s/R macro-particles. Root processors compute first N_s/R macro-particles at the lower altitude boundary and subsequent processors simulate increments of N_s/R macro-particles up in altitude according to computed densities of spatial grid cells of Equation 2.4. Remaining particles by the division of N_s by R are allocated to root processors. Altitude ranges spanned by N_s depend on plasma scale heights simulated and computational resources available. Azimuthal symmetry of the magnetosphere is assumed in the absence of solar wind forcing such that ϕ_0 is arbitrary. Given initial dipole position coordinates $(p_0,\ q_0,\ \phi_0)$ for each macro-particle the magnetic dipole quartic polynomial root-finder outlined in Appendix .5 computes associated spherical $(r_0,\ \theta_0,\ \phi_0)$ and Cartesian $(x_0,\ y_0,\ z_0)$ coordinates for a total of N_s ion macro-particles of index $\tilde{j} \in \begin{bmatrix}1 & N_s\end{bmatrix}$. Particle positions are updated by the kinetic solver detailed in Appendix .7.

2.1.3 Eulerian Velocity-Space

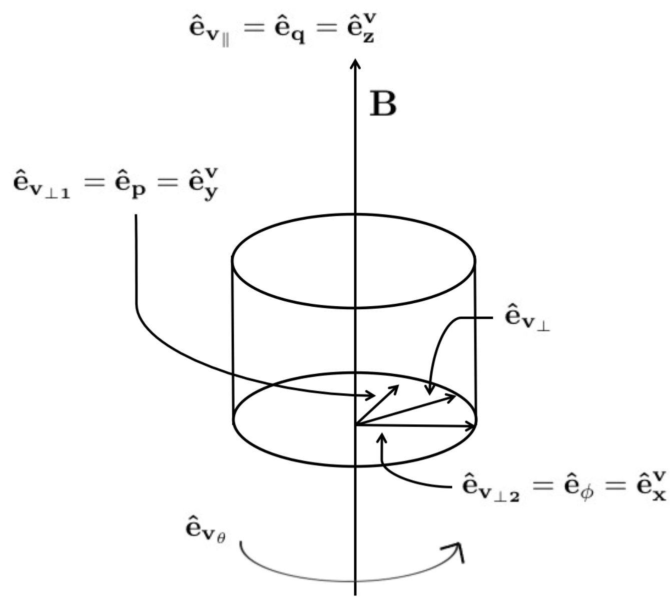

Figure 2.2: Lagrangian velocity-space in gyro-centered magnetic dipole coordinates ($\hat{\mathbf{e}}_{\mathbf{v}_{\perp 1}}, \hat{\mathbf{e}}_{\mathbf{v}_{\perp 2}}, \hat{\mathbf{e}}_{\mathbf{v}_\parallel}$).

Lagrangian ion macro-particle velocities are computed in local gyro-frame Cartesian velocity coordinates ($\hat{\mathbf{e}}^{\mathbf{v}}_{\mathbf{x}}$, $\hat{\mathbf{e}}^{\mathbf{v}}_{\mathbf{y}}$, $\hat{\mathbf{e}}^{\mathbf{v}}_{\mathbf{z}}$) where $\hat{\mathbf{e}}_{\mathbf{v}_\parallel} = \hat{\mathbf{e}}_{\mathbf{q}} = \hat{\mathbf{e}}^{\mathbf{v}}_{\mathbf{z}}$ is the parallel direction (to the magnetic field $\mathbf{B}$). Radial directions $\hat{\mathbf{e}}_{\mathbf{v}_\perp}$ have magnitudes equal to quadrature sums of velocity components along $\hat{\mathbf{e}}_{\mathbf{v}_{\perp 1}} = \hat{\mathbf{e}}_{\mathbf{p}} = \hat{\mathbf{e}}^{\mathbf{v}}_{\mathbf{y}}$ and $\hat{\mathbf{e}}_{\mathbf{v}_{\perp 2}} = \hat{\mathbf{e}}_{\phi} = \hat{\mathbf{e}}^{\mathbf{v}}_{\mathbf{x}}$ as seen in Figure 2.2. Lagrangian velocity vector, $\mathbf{v}$, in dipole coordinates takes the form $\mathbf{v}(v_{\perp 1},\ v_{\perp 2},\ v_\parallel) = v_{\perp 1}\hat{\mathbf{e}}_{\mathbf{v}_{\perp 1}} + v_{\perp 2}\hat{\mathbf{e}}_{\mathbf{v}_{\perp 2}} + v_\parallel \hat{\mathbf{e}}_{\mathbf{v}_\parallel}$. Eulerian three-dimensional velocity-space grids of size $N_{v_{\perp 1}} \times N_{v_{\perp 2}} \times N_{v_\parallel}$ are generated within each spatial cell. Grid cells of index triplet $(\tilde{v}_{\perp 1},\ \tilde{v}_{\perp 2},\ \tilde{v}_\parallel)$, where $\tilde{v}_{\perp 1} \in \begin{bmatrix} 1 & N_{v_{\perp 1}} \end{bmatrix}$, $\tilde{v}_{\perp 2} \in \begin{bmatrix} 1 & N_{v_{\perp 2}} \end{bmatrix}$, and $\tilde{v}_\parallel \in \begin{bmatrix} 1 & N_{v_\parallel} \end{bmatrix}$, have lower limits $(v_{\perp 1_L},\ v_{\perp 2_L},\ v_{\parallel_L})$, center values $(v_{\perp 1_C},\ v_{\perp 2_C},\ v_{\parallel_C})$, and upper limits $(v_{\perp 1_H},\ v_{\perp 2_H},\ v_{\parallel_H})$. Eulerian velocity-space volume elements in local gyro-frames are

$$d^3v(\tilde{v}_{\perp 1}, \tilde{v}_{\perp 2},\ \tilde{v}_\parallel) = h_{v_{\perp 1}} h_{v_{\perp 2}} h_{v_\parallel}\ dv_{\perp 1}\ dv_{\perp 2}\ dv_\parallel, \tag{2.8}$$

where scale factors assume those of Cartesian basis such that $h_i(\tilde{v}_{\perp 1}, \tilde{v}_{\perp 2}, \tilde{v}_\parallel) = 1$ and $dv_i(\tilde{v}_{\perp 1}, \tilde{v}_{\perp 2}, \tilde{v}_\parallel) \approx \left| v_{i_H}(\tilde{v}_{\perp 1}, \tilde{v}_{\perp 2},\ \tilde{v}_\parallel) - v_{i_L}(\tilde{v}_{\perp 1}, \tilde{v}_{\perp 2},\ \tilde{v}_\parallel) \right|\ \forall i = v_{\perp 1},\ v_{\perp 2},\ v_\parallel$. Eulerian velocity-space vectors have the form

$$\mathbf{v}_C(\tilde{v}_{\perp 1}, \tilde{v}_{\perp 2},\ \tilde{v}_\parallel) = v_{\perp 1_C}\hat{\mathbf{e}}_{\mathbf{v}_{\perp 1}} + v_{\perp 2_C}\hat{\mathbf{e}}_{\mathbf{v}_{\perp 2}} + v_{\parallel_C}\hat{\mathbf{e}}_{\mathbf{v}_\parallel}. \tag{2.9}$$

2.1.4 Lagrangian Macro-Particle Velocity Initialization

Transverse ion temperature, $T_\perp$, is comprised of temperature in the transverse plane, $T_{\perp 1}$ and $T_{\perp 2}$, as $T_\perp = T_{\perp 1}/2 + T_{\perp 2}/2$. For parallel ion temperature, $T_\parallel$, the total ion temperature is $T_i = 2T_\perp/3 + T_\parallel/3 = T_{\perp 1}/3 + T_{\perp 2}/3 + T_\parallel/3$ [Shunk and Nagy, 2000]. Transverse and parallel ion energy is $w_\perp = k_B T_\perp = 3k_B T_i/4$ and $w_\parallel = k_B T_\parallel/2 = 3k_B T_i/4$, respectively, where two transverse thermal energies are $w_{\perp 1} = k_B T_{\perp 1}/2$ and $w_{\perp 2} = k_B T_{\perp 2}/2$ such that $w_\perp = w_{\perp 1} + w_{\perp 2}$. Total thermal energy is $w_i = w_\perp + w_\parallel = 3k_B T_i/2$. All ions are initialized with three-dimensional Maxwellian velocity distributions sampled as normal (Gaussian) distributions generated from uniform distributions via Box-Muller transforms. With velocity components in global Cartesian coordinates the Box-Muller transform gives, $\forall i = x,\ y,\ z$,

$$v_{i0}(\tilde{j}) = \cos(2\pi\gamma_{v_{i0}})\sqrt{-2\log(\gamma_{v_{i0}})}, \tag{2.10}$$

where $\gamma_{v_{i0}}(\tilde{j}) \in U\begin{pmatrix}0 & 1\end{pmatrix}$ are random numbers generated from uniform distributions and $v_{i0}(\tilde{j})$ are associated random numbers of normal distributions. Ions are initially temperature isotropic such that ion temperature is $T_i = T_{\perp 1} = T_{\perp 2} = T_\parallel$. Initial three-dimensional Cartesian velocity components, $[v'_{x0}(\tilde{j}),\ v'_{y0}(\tilde{j}),\ v'_{z0}(\tilde{j})]$, result from Equation 2.10 with standard deviations $\sigma_i = \left|\sqrt{k_B T_i/m}\right|$, $\forall i = x,\ y,\ z$:

$$v'_{i0}(\tilde{j}) = \sigma_i v_{i0}.$$

Cartesian velocity components, $[v'_{x0}(\tilde{j}),\ v'_{y0}(\tilde{j}),\ v'_{z0}(\tilde{j})]$, are transformed to dipole velocity components, $[v'_{p0}(\tilde{j}),\ v'_{q0}(\tilde{j}),\ v'_{\phi 0}(\tilde{j})]$, via transformations outlined in Appendix .10. Translational velocity components are field-aligned, i.e., $v_{\parallel 0} = v'_{q0}$, and perpendicular velocity components are transverse, i.e., $v_{\perp 10} = v'_{p0}$ and $v_{\perp 20} = v'_{\phi 0}$, according to Figure 2.2. Provided initial spherical particle positions, $[r_0(\tilde{j}),\ \theta_0(\tilde{j}),\ \phi_0(\tilde{j})]$, initial field-aligned (translational) velocity components along $\hat{\mathbf{e}}_\mathbf{q}$ are

$$v_{\parallel 0}(\tilde{j}) = \frac{3\cos(\theta_0)\sin(\theta_0)}{\sqrt{\ell_0}}\left[v'_{x0}\cos(\phi_0) + v'_{y0}\sin(\phi_0)\right] + \frac{v'_{z0}\left[3\cos^2(\theta_0) - 1\right]}{\sqrt{\ell_0}}, \tag{2.11}$$

where $\ell_0 = 1 + 3\cos^2(\theta_0)$. Ion trajectories follow curved magnetic field lines in gyro-centered frames such that they are inherently three-dimensional in global Cartesian coordinates:

$$v_{x0}(\tilde{j}) = \frac{\cos(\phi_0)}{\sqrt{\ell_0}}\left[3v_{\parallel 0}\cos(\theta_0)\sin(\theta_0)\right], \quad v_{y0}(\tilde{j}) = \frac{\sin(\phi_0)}{\sqrt{\ell_0}}\left[3v_{\parallel 0}\cos(\theta_0)\sin(\theta_0)\right],$$
$$v_{z0}(\tilde{j}) = \frac{v_{\parallel 0}\left[3\cos^2(\theta_0) - 1\right]}{\sqrt{\ell_0}}. \tag{2.12}$$

Initial transverse velocity components along $\mathbf{\hat{e}_p}$ and $\mathbf{\hat{e}_\phi}$ are

$$v_{\perp 10}(\tilde{j}) = \frac{1 - 3\cos^2(\theta_0)}{\sqrt{\ell_0}}\left[v'_{x0}\cos(\phi_0) + v'_{y0}\sin(\phi_0)\right] + \frac{3v'_{z0}\cos(\theta_0)\sin(\theta_0)}{\sqrt{\ell_0}},$$
$$v_{\perp 20}(\tilde{j}) = -v'_{x0}\sin(\phi_0) + v'_{y0}\cos(\phi_0). \tag{2.13}$$

Particle velocities are updated by the kinetic solver detailed in Appendix .7.

2.2 Ion Kinetics

2.2.1 Boundary Conditions

Particles are initialized from hydrostatic temperature and density approximations subject to gravitational and self-consistent ambipolar forces. Maxwellian populations of cold ionospheric ions of lower boundary hydrostatic density are injected into computational domains on time-steps equal to mean thermal ion transit times through lower boundary ghost cells, τ_i. Mean thermal velocities are much less than Alfvén wave speeds. Low-altitude injections of thermal ion populations with flux-tube footprint reference densities of Equation 2.2 are sampled from Maxwellian velocity distributions according to Equations 2.12 and 2.13. Successive macro-particle injections are on time-steps equal to

$$\tau_i = \sqrt{\frac{m}{k_B T_\parallel}} h_q(\tilde{q}) d_q(\tilde{q})\Big|_{\tilde{q}=0}, \tag{2.14}$$

where all functions dependent on space are evaluated at lower boundary ghost cells of index $\tilde{q} = 0$. Macroscopic plasma parameters, such as ion distribution functions and moments, are extracted at statistical time-steps of index $\tilde{n}' \in \left[1 \quad N'_t + 1\right]$, $\tilde{n}' \in \mathbb{Z}^+$ a total of $N'_t + 1$ times throughout the simulation, that is, at initial times (i.e., $\tilde{n} = 1$) and at integer multiples of statistical time-steps, $n_{df}h = N_t h / N'_t$, thereafter (i.e., $\tilde{n} = [\tilde{n}' - 1]n_{df}$). Distribution functions and moments are computed on statistical time-steps equal to τ_i such that $n_{df}h = \tau_i$. Ion macro-particles are free to exit and re-enter lower and upper altitude boundaries within τ_i time-scales; total simulated particle numbers, N_s, are re-computed on τ_i time-steps to account for particle loss and injection. Computational time-steps, h, are set to resolve ion cyclotron interaction times, $\tau_\perp$, such that $h < \tau_\perp$ sets the upper bounds on h and the lower limit is set by tolerance to numerical noise. Gyro-centers and translational ion phase-space components are advanced per RK4 iterations outlined in Appendix .7 on computational time-steps $f_g^{-1} \leq h \leq \tau_\perp$, where f_g is gyro-frequency and $\tau_\perp$ is determined by the flux-tube arc length traversing the electromagnetic turbulence wave-field as detailed in Subsection 2.2.5. Net field-aligned acceleration components of all macro-particles are recast into global Cartesian coordinates to avoid time-dependent unit bases. Acceleration components are position dependent in the global spherical coordinate basis as given by Equation 69:

$$a_i = a_i(r,\ \theta,\ \phi) \neq a_i(v_r,\ v_\theta,\ v_\phi), \tag{2.15}$$

where $(r,\ \theta,\ \phi)$ and $(v_r,\ v_\theta,\ v_\phi)$ are position and velocity coordinates $\forall i = x,\ y,\ z$.

2.2.2 Gravitational Force

Earth exerts a radially inward gravitational force on each macro-particle given by

$$\mathbf{a}_G = \frac{-GM_\oplus}{r_C^2}\hat{\mathbf{e}}_\mathbf{r}, \tag{2.16}$$

where $G \approx 6.674 \times 10^{-11}$ N $\cdot$ kg^{-2} $\cdot$ m^2 is the universal gravitational constant and $M_\oplus \approx 5.972 \times 10^{24}$ kg is Earth's mass. Projecting Equation 2.16 onto magnetic flux-tubes by coordinate transformations of Equation 92, where $a_{G_p} = a_{G_\phi} = 0$, gravitational acceleration takes the form

$$\mathbf{a}_G = \frac{-2GM_\oplus \cos(\theta_C)}{r_C^2\sqrt{\ell_C}}\hat{\mathbf{e}}_\mathbf{q}. \tag{2.17}$$

According to hydrostatic equilibria between ambipolar electric field and gravitational forces as discussed in Appendix .6 gravitational force is computed at centers of spatial cells and interpolated to individual particle positions on every computational time-step. Equation 95 renders Cartesian components where $\mathbf{a}_G = a_G\hat{\mathbf{e}}_\mathbf{q}$:

$$
\begin{aligned}
a_{G_x} &\approxeq a_G \left[\frac{3\cos(\theta)\sin(\theta)\cos(\phi)}{\sqrt{\ell}} \right], \\
a_{G_y} &\approxeq a_G \left[\frac{3\cos(\theta)\sin(\theta)\sin(\phi)}{\sqrt{\ell}} \right], \\
a_{G_z} &\approxeq a_G \left[\frac{3\cos^2(\theta)-1}{\sqrt{\ell}} \right].
\end{aligned}
\tag{2.18}
$$

2.2.3 Ambipolar Electric Field

Diffuse aurorae extend around the auroral oval as belts of sub-visual weak emissions primarily generated by collisions of atmospheric atoms with electrons that follow magnetic field lines from the central plasma sheet [Ni et al., 2016] [Lui et al., 1977] [Meng et al., 1979]. $\sim$ 100 eV-10 keV electrons precipitate to ionospheric altitudes after energized by resonant interactions with plasma sheet electron cyclotron harmonic (ECH) or whistler-mode chorus waves [Anderson and Maeda, 1977] [Inan et al., 1992] [Schulz, 1998]. Auroral precipitation generally increases with geomagnetic activity [Petrinec et al., 1999] and acts to produce ionospheric ions by ionization and heat ionospheric electrons directly by Coulomb collisions or indirectly by wave interactions [Ni et al., 2016] [Moore and Horwitz, 2007].

Ambipolar fields- electric fields generated by slight ion-electron charge separation- become significant for high electron temperatures and are primary drivers of Type 2 ion upflows [Su et al., 1999] [Moore and Horwitz, 2007]. Analyses of Dynamics Explorer 2 (DE-2) observations demonstrated that large auroral electron precipitation energy fluxes correlate with increased ionospheric electron temperatures [Seo et al., 1997] [Moore and Horwitz, 2007]. Low-energy, or "ultrasoft", precipitating electrons are unable to reach low-altitudes and are most efficient in heating topside ionospheric electrons and, consequently, serve to enhance ambipolar electric fields and produce large outward fluxes [Seo et al., 1997] [Moore and Horwitz, 2007].

A quasi-neutral ($n_e = n$) thermal electron fluid with supersonic (non-adiabatic) parallel drift ($v_e = u_\parallel$) consistent with ideal gas equation of state is employed to compute the ambipolar electric field, $\mathbf{E}_A$. Contributions of electron fluids on ambipolar electric fields originate from field-aligned gradients of scalar electron pressures, p_e. Relevant electron fluid momentum conservation equations of classical magnetohydrodynamics take the form [Shunk and Nagy, 2000]

$$
\mathcal{D}\left(u_\parallel \hat{\mathbf{e}}_\mathbf{q}\right) = \frac{q_e}{m_e}\left(\mathbf{E}_A + u_\parallel \hat{\mathbf{e}}_\mathbf{q} \times \mathbf{B}\right) - \left(m_e n\right)^{-1} \nabla p_e - \sum{}_s \nu^{es}\left(v_e - v_s\right), \tag{2.19}
$$

where $\mathcal{D} = \partial_t + \left(\mathbf{v_e} \cdot \nabla\right) = \partial_t + \left(u_\parallel \hat{\mathbf{e}}_\mathbf{q} \cdot \nabla\right)$ are inertial convective derivatives, and $\sum{}_s \nu^{es}\left(v_e - v_s\right) =$

0 are electron-ion collision terms where $v_e = u_\parallel$. $\mathbf{B} = B\hat{\mathbf{e}}_\mathbf{q}$ such that $u_\parallel \hat{\mathbf{e}}_\mathbf{q} \times \mathbf{B} = 0$ and Equation 2.19 reduces to

$$\mathcal{D}\left(u_\parallel \hat{\mathbf{e}}_\mathbf{q}\right) = \frac{q_e}{m_e}\mathbf{E}_A - \left(m_e n\right)^{-1} \nabla p_e. \tag{2.20}$$

Ambipolar electric field $\mathbf{E}_A$ takes the form $\mathbf{E}_A = \mathcal{I}_e + \mathcal{P}_e$, where

$$\mathcal{I}_e = \frac{m_e}{q_e}\mathcal{D}\left(u_\parallel \hat{\mathbf{e}}_\mathbf{q}\right), \quad \mathcal{P}_e \equiv \left(q_e n\right)^{-1} \nabla p_e, \tag{2.21}$$

Owing to small electron mass, m_e, electron inertial term, $\mathcal{I}_e$, is safely neglected and electron scalar pressure term, $\mathcal{P}_e$, dominates $\mathbf{E}_A$. In absence of self-consistent fluid electron energy equation solvers constant electron temperature is assumed in ideal gas law equation of state such that $\mathcal{P}_e = \left(q_e n\right)^{-1} k_B T_e \nabla n$. Electron temperatures may increase at set rates when modeling soft electron precipitation. $\mathbf{E}_A$ takes the form

$$\mathbf{E}_A = \frac{k_B T_e}{q_e n h_q}\partial_q (n)\, \hat{\mathbf{e}}_\mathbf{q}. \tag{2.22}$$

Self-consistent ambipolar electric fields update densities, n, in space and time such that active ambipolar electric fields respond to quasi-neutral density gradients along the flux-tube and drive ions to regions of low density. Spatial derivatives of Equation 2.22 are treated by five-point stencil quadratures and $\mathbf{E}_A$ has field-aligned ion acceleration, $\mathbf{a}_A = \mathbf{E}_A q/m$. Ambipolar electric field magnitudes are computed between successive configuration-space grid cell centers and interpolated to particle positions on every computational time-step. Equation 95 gives Cartesian coordinates of ambipolar electric field accelerations, where $\mathbf{a}_A = a_A \hat{\mathbf{e}}_\mathbf{q}$:

$$\begin{aligned} a_{A_x} &\approxeq a_A \left[\frac{3\cos(\theta)\sin(\theta)\cos(\phi)}{\sqrt{\ell}}\right], \\ a_{A_y} &\approxeq a_A \left[\frac{3\cos(\theta)\sin(\theta)\sin(\phi)}{\sqrt{\ell}}\right], \\ a_{A_z} &\approxeq a_A \left[\frac{3\cos^2(\theta)-1}{\sqrt{\ell}}\right]. \end{aligned} \tag{2.23}$$

2.2.4 Magnetic Mirror Force

Magnetic mirror force occurs when charged particles interact with cylindrically-symmetric magnetic fields, $\mathbf{B}$, with field-aligned spatial variations much larger than particle gyro-radii, ρ_g, such that first adiabatic invariants of particle motion are conserved. Ion macro-particles accelerate towards the magnetic equator by the mirror force acceleration given by [Shunk and Nagy, 2000]

$$\mathbf{a}_M = \frac{-\mu}{m}\frac{\partial|\mathbf{B}|}{\partial s}\hat{\mathbf{e}}_{\mathbf{q}}, \tag{2.24}$$

where $\mu = mv_\perp^2/(2|\mathbf{B}|)$ is the charge magnetic moment. Figure 2.2 illustrates the local cylindrical coordinate system of the geomagnetic field of the form $\mathbf{B} = B(z)\hat{\mathbf{e}}_{\mathbf{z}} + B_r(z,\ r)\hat{\mathbf{e}}_{\mathbf{r}}$, where $\hat{\mathbf{e}}_{\mathbf{z}} = \hat{\mathbf{e}}_{\mathbf{z}}^{\mathbf{v}} = \hat{\mathbf{e}}_{\mathbf{q}}$, $\hat{\mathbf{e}}_{\mathbf{r}} = \hat{\mathbf{e}}_{\mathbf{v}_\perp}$ and $B_\theta = 0$. Field-aligned magnetic flux densities are assumed to exceed radial components such that $B(z) \gg B_r(z,\ r)$. Functional forms of the dipole magnetic field are derived in Appendix .1:

$$|\mathbf{B}| \approx B(z) = \frac{M_0}{r^3}\sqrt{\ell}, \tag{2.25}$$

where $\ell = 1 + 3\cos^2(\theta)$, $M_0 = B_E R_E^3$ is the Earth's magnetic moment, and $B_E = \mu_0 M_0/3$ is the dipole magnetic field magnitude at the equator (i.e., $\theta = \pi/2$). Divergence of $\mathbf{B}$ gives

$$\nabla \cdot \mathbf{B} = r^{-1}\frac{\partial[rB(z,\ r)]}{\partial r} + \frac{\partial B(z)}{\partial z} = 0. \tag{2.26}$$

Field-aligned differential elements ∂s along $\mathbf{B} = B(z)\hat{\mathbf{e}}_{\mathbf{q}}$ are expressed in spherical coordinates [Shunk and Nagy, 2000]:

$$\frac{\partial}{\partial s} = \hat{\mathbf{e}}_{\mathbf{q}} \cdot \nabla = \frac{2\cos(\theta)}{\sqrt{\ell}}\frac{\partial}{\partial r} + \frac{\sin(\theta)}{r\sqrt{\ell}}\frac{\partial}{\partial \theta}, \tag{2.27}$$

where $\nabla = \hat{\mathbf{e}}_{\mathbf{r}} h_r^{-1}\partial_r + \hat{\mathbf{e}}_{\boldsymbol{\theta}} h_\theta^{-1}\partial_\theta$, $h_r = 1$, and $h_\theta = r$. Dipolar magnetic field gradients are given by Equations 2.27 and 2.25:

$$\frac{\partial|\mathbf{B}|}{\partial s} = \frac{-6M_0\cos(\theta)}{r^4} - \frac{3M_0\cos(\theta)\sin^2(\theta)}{r^4\ell}. \tag{2.28}$$

Field-aligned ion accelerations by the mirror force follow from Equation 2.24:

$$\mathbf{a}_M = \frac{-\mu}{m}\left\{\frac{-6M_0\cos(\theta)}{r^4} - \frac{3M_0\cos(\theta)\sin^2(\theta)}{r^4\ell}\right\}\hat{\mathbf{e}}_{\mathbf{q}}. \tag{2.29}$$

Cartesian components transform by Equation 95, where $\mathbf{a}_M = a_M\hat{\mathbf{e}}_{\mathbf{q}}$:

$$
\begin{aligned}
a_{M_x} &= a_M \left[\frac{3\cos(\theta)\sin(\theta)\cos(\phi)}{\sqrt{\ell}} \right], \\
a_{M_y} &= a_M \left[\frac{3\cos(\theta)\sin(\theta)\sin(\phi)}{\sqrt{\ell}} \right], \\
a_{M_z} &= a_M \left[\frac{3\cos^2(\theta) - 1}{\sqrt{\ell}} \right].
\end{aligned}
\tag{2.30}
$$

2.2.5 Wave-Particle Interactions

Transverse energization of charged particles by cyclotron resonance was first studied in laboratory plasmas [Hooke and Rothman, 1964] [Eldridge, 1972] [Golovato et al., 1985]. In most applications a narrow frequency band of cyclotron waves is used to energize the charged particles. Wave energization by ion cyclotron resonance is thought to be a primary driver of ion outflows [Bouhram et al., 2002] [Wu et al., 1999] [Bouhram et al., 2003a] [Bouhram et al., 2003b] [Crew et al., 1990] [Chang and Crew, 1986]. Broadband extremely low-frequency (BBELF) and very low-frequency (VLF) wave generation is thought to be driven by superthermal electron beam instabilities, ion beam instabilities, and velocity shear [Wu et al., 2002] [Ganguli et al., 1994]. Spatial (temporal) variations of waves comparable to particle gyro-radii (gyro-frequencies) may produce variations in particle magnetic moments on sub-gyro-period time-scales and violate the first adiabatic invariant [Schulz and Lanzerotti, 1974].

Wave heating occurs if the gyro-frequency is larger than the collision frequency and the gyro-radius is smaller than the transverse wavelength, $\lambda_\perp$, [Wu et al., 2002] [Barakat and Barghouthi, 1994] [Bouhram et al., 2003a] [Zeng et al., 2006]. Cyclotron resonance occurs over the ion transit time through regions of left-hand polarized VLF wave turbulence with frequencies at resonant particle gyro-frequencies. Ions have smaller interaction times, $\tau_\perp$, resonating with waves within a large frequency bandwidth, Δf, about the gyro-frequency, f_g. In this study ion macro-particles are energized independently in the $\hat{\mathbf{e}}_{\perp 1}$ and $\hat{\mathbf{e}}_{\perp 2}$ directions by electrostatic VLF and BBELF ion cyclotron waves with electric field power spectral density, $S_\perp(\omega_g)$ in units of $[\mathrm{V}^2 \cdot \mathrm{m}^{-2} \cdot \mathrm{Hz}^{-1}]$, left-hand circularly polarized and centered at reference gyro-frequency, ω_{g0}, with spectral index, $\chi_\perp$. In the absence of wave-particle interactions the gyro-center approximation of particle motion renders constraints on the computational time-step restricted primarily by numerical noise.

Wave power is transferred to particles on time-scales equal to wave-particle interaction times, $\tau_\perp$, which depend on scale size, ds, of wave activity regions within frequency bandwidths, Δf, of gyro-frequency, f_g, [Schulz and Lanzerotti, 1974]. During $\tau_\perp$ waves energize ions by imparting gyro-tropic Gaussian velocity kicks, $\delta v_{\perp 1}$ and $\delta v_{\perp 2}$, along $\hat{\mathbf{e}}_{\perp \mathbf{1}}$ and $\hat{\mathbf{e}}_{\perp \mathbf{2}}$ directions independently on each simulation time-step, h. Due to currently limited information on ion cyclotron resonance interaction region variations in space and time, ds is assumed to span the entire computational flux-tube. As transverse velocity kick magnitudes correspond to those on $\tau_\perp$ time-scales the computational time-step, h, is set to resolve $\tau_\perp$ such that perpendicular velocity diffusion occurs at appropriate rates on time-scales of h. First adiabatic invariants are violated during transverse energization and ion cyclotron resonance interaction time-steps are $h < \tau_\perp$.

Wave power spectral density along $\hat{\mathbf{e}}_{\perp \mathbf{1}}$ and $\hat{\mathbf{e}}_{\perp \mathbf{2}}$ components, $S_{\perp i}(\omega_g)$, is related to the total energy density, $E_{\perp i}^2$, as $E_{\perp i}^2 = S_{\perp i}(\omega_g)\Delta f$, where $\Delta f = 1/\tau_\perp$ is the frequency bandwidth about the local gyro-frequency over which the wave power is transferred, $\forall i = 1,\ 2$ [Chang and Crew, 1986]. [Schulz and Lanzerotti, 1974] provide an expression for the interaction time, $\tau_\perp$, for sharp resonance, i.e., small Δf, as $\Delta f = \sqrt{\epsilon} f_g$, where $f_g = \omega_g/(2\pi)$ is the gyro-frequency in [Hz], $\epsilon = \langle v_\parallel/(\omega_g ds)\rangle$, $ds = h_q dq$ is the flux-tube arc length of the wave activity region, $v_\parallel$ is the particle's translational velocity, and angle brackets denote values averaged over particle orbits. This expression requires that gyro-radii are much less than flux-tube arc lengths (i.e., $\rho_g \ll ds$). For radiation belt particles with GeV kinetic energies, such as protons, alpha particles, other light ions, and relativistic electrons, the condition $|\epsilon| \ll 1$ is satisfied in a distinction from high-energy particles, such as galactic cosmic rays, where gyro-radii are comparable to the size of the magnetosphere itself [Schulz and Lanzerotti, 1974]. Simulation time-steps are selected to resolve wave-particle interaction times such that $h < \tau_\perp$. Where ds is flux-tube arc length of the ion cyclotron resonance interaction region the interaction time takes the form [Schulz and Lanzerotti, 1974]

$$\tau_\perp = \sqrt{\frac{2\pi\, ds}{f_g v_\parallel}}. \tag{2.31}$$

Transverse velocity diffusion in $\hat{\mathbf{e}}_{\perp \mathbf{1}}$ and $\hat{\mathbf{e}}_{\perp \mathbf{2}}$ directions is quantified by anomalous velocity diffusion coefficients, $D_{\perp i}$, defined as half the rate $\langle|\Delta v_{\perp i}|^2\rangle$ grows with time, that is, $D_{\perp i} = \langle|\Delta v_{\perp i}|^2\rangle/(2\tau_\perp)$, $\forall i = 1,\ 2$ in units of [$\mathrm{m}^2 \cdot \mathrm{s}^{-3}$] [Schulz and Lanzerotti, 1974]. Transverse velocity diffusion variances are

$$\langle|\Delta v_{\perp 1}|^2\rangle = 2D_{\perp 1}\tau_\perp, \quad \langle|\Delta v_{\perp 2}|^2\rangle = 2D_{\perp 2}\tau_\perp. \tag{2.32}$$

Perpendicular velocity kick magnitudes over $\tau_\perp$ time-scales are $\gamma_{\perp 1}\Delta v_{\perp 1}$ and $\gamma_{\perp 2}\Delta v_{\perp 2}$ in $\hat{\mathbf{e}}_{\perp \mathbf{1}}$ and $\hat{\mathbf{e}}_{\perp \mathbf{2}}$ directions, respectively. Transverse velocity kick magnitudes, $|\delta v_{\perp i}|$, imparted on computational time-steps, h, are scaled to those on $\tau_\perp$ such that $\delta v_{\perp i} = \left(h/\tau_\perp\right)\gamma_{\perp i}\sqrt{2D_{\perp i}\tau_\perp}$ $\forall i = 1,\ 2$. Velocity diffusion is iteratively pushed on ion cyclotron resonance interaction time-steps, $h < \tau_\perp$, as $v_{\perp i}(\tilde{n}+1) = v_{\perp i}(\tilde{n}) + \delta v_{\perp i}$:

$$v_{\perp 1}(\tilde{n}+1) = v_{\perp 1}(\tilde{n}) + \frac{h}{\tau_\perp}\gamma_{\perp 1}\sqrt{2D_{\perp 1}\tau_\perp}, \quad v_{\perp 2}(\tilde{n}+1) = v_{\perp 2}(\tilde{n}) + \frac{h}{\tau_\perp}\gamma_{\perp 2}\sqrt{2D_{\perp 2}\tau_\perp}, \tag{2.33}$$

where $\left[v_\perp(\tilde{n}+1)\right]^2 = \left[v_{\perp 1}(\tilde{n}+1)\right]^2 + \left[v_{\perp 2}(\tilde{n}+1)\right]^2$. $\gamma_{\perp 1},\ \gamma_{\perp 2} \in N\begin{pmatrix}-1 & 1\end{pmatrix}$ are random numbers from normal distributions generated uniform distributions via Box-Muller transforms:

$$\gamma_{\perp 1} = \cos(2\pi\gamma'^{1}_{\perp 1})\sqrt{-2\log(\gamma'^{2}_{\perp 1})}, \quad \gamma_{\perp 2} = \cos(2\pi\gamma'^{1}_{\perp 2})\sqrt{-2\log(\gamma'^{2}_{\perp 2})}, \tag{2.34}$$

where $\gamma'^{j}_{\perp i} \in U\begin{pmatrix}0 & 1\end{pmatrix}$ are random numbers generated from uniform distributions and $\gamma_{\perp i}$ are associated random numbers of the Gaussian distributions $\forall i,\ j = 1,\ 2$. Sampling of $\gamma_{\perp 1}$ and $\gamma_{\perp 2}$ determines the direction of two-dimensional transverse Gaussian velocity kicks. To derive perpendicular velocity diffusion coefficients, $D_{\perp 1}$ and $D_{\perp 2}$, it is noted the momentum transfer in the i^{th} transverse direction, $\hat{\mathbf{e}}_{\perp\mathbf{i}}$, over the interaction time, $\tau_\perp$, $\forall i = 1,\ 2$, abides by Newton's second law [Crew et al., 1990] [Chang and Crew, 1986]:

$$\dot{p}_{\perp i} = m\frac{\Delta v_{\perp i}}{\tau_\perp} = E_{\perp i}q, \tag{2.35}$$

where $\dot{p}_{\perp i}$ are wave momentum time derivatives and $E_{\perp i}$ are plasma wave electric fields in $[\mathrm{V}\cdot\mathrm{m}^{-1}]$ along $\hat{\mathbf{e}}_{\perp\mathbf{i}}$. By use of diffusion variances in Equation 2.32 Equation 2.35 gives [Bouhram et al., 2003a] [Wu et al., 1999]

$$D_{\perp 1} = \left(\frac{q^2}{2m^2}\right)S_{\perp 1}(\omega_g), \quad D_{\perp 2} = \left(\frac{q^2}{2m^2}\right)S_{\perp 2}(\omega_g), \tag{2.36}$$

where $S_{\perp 1}(\omega_g) = E^2_{\perp 1}\tau_\perp$ and $S_{\perp 2}(\omega_g) = E^2_{\perp 2}\tau_\perp$ are left-hand polarized power spectral densities along $\hat{\mathbf{e}}_{\perp\mathbf{1}}$ and $\hat{\mathbf{e}}_{\perp\mathbf{2}}$. Fraction of reference electric field spectral energy density, S_0, circularly left-hand polarized is $\eta_{LH} \in \begin{bmatrix}0 & 1\end{bmatrix}$ of which $\xi_{\perp 1}$ and $\xi_{\perp 2}$ are the fractions along $\hat{\mathbf{e}}_{\perp\mathbf{1}}$ and $\hat{\mathbf{e}}_{\perp\mathbf{2}}$ directions, respectively. $S_{\perp 1}(\omega_g) = E^2_{\perp 1}\tau_\perp$ and $S_{\perp 2}(\omega_g) = E^2_{\perp 2}\tau_\perp$ are left-hand polarized power spectral densities along $\hat{\mathbf{e}}_{\perp\mathbf{1}}$ and $\hat{\mathbf{e}}_{\perp\mathbf{2}}$ centered at reference gyro-frequency, ω_{g0}, with spectral indices, $\chi_{\perp 1}$ and $\chi_{\perp 2}$. Spectral energy densities are recast [Chang and Crew, 1986] [Wu et al., 1999]:

$$S_{\perp 1}(\omega_g) = \xi_{\perp 1}\eta_{LH}S_0\left(\frac{\omega_g}{\omega_{g0}}\right)^{-\chi_{\perp 1}}, \quad S_{\perp 2}(\omega_g) = \xi_{\perp 2}\eta_{LH}S_0\left(\frac{\omega_g}{\omega_{g0}}\right)^{-\chi_{\perp 2}}. \tag{2.37}$$

Perpendicular velocity diffusion coefficients of Equation 2.36 depend on altitude via gyro-frequency as $D_{\perp i} = \left[q^2/(2m^2)\right]S_{\perp i}(\omega_g)$, $\forall i = 1,\ 2$ [Chang and Crew, 1986] [Wu et al., 1999]. Ion gyro-radii, ρ_g, become comparable and may exceed electromagnetic turbulence transverse wavelengths, $\lambda_\perp$, for sufficiently low gyro-frequencies and/or high transverse velocities. Such is the case for high-altitude wave-energized ions. In the short wavelength limit (i.e., $\rho_g \sim \lambda_\perp$) diffusion coefficients inherit velocity dependence by ρ_g [Barghouthi, 2008] [Barghouthi and Atout, 2006] [Barghouthi et al., 1998]. Velocity-dependent diffusion coefficients, $D_{\perp i}$, that accommodate $\lambda_\perp \leq \rho_g$ follow from formalism of [Barghouthi, 2008] [Barghouthi and Atout, 2006] and investigations of [Barghouthi et al., 1998] and [Curtis, 1985] on wave heating for different values of $\rho_g/\lambda_\perp$. Transverse velocity diffusion coefficients $\forall i = 1,\ 2$ become

$$D_{\perp i} = \sigma_\perp^{-3} \left(\frac{q^2}{2m^2}\right) \xi_{\perp i} \eta_{LH} S_0 \left(\frac{\omega_g}{\omega_{g0}}\right)^{-\chi_{\perp i}}, \quad \sigma_\perp = \begin{cases} 1 & \text{for } 2\pi\rho_g < \lambda_\perp \\ 2\pi v_\perp/(\lambda_\perp \omega_g) & \text{for } 2\pi\rho_g \geq \lambda_\perp. \end{cases} \tag{2.38}$$

Total wave power transferred to ions by $S_\perp(\omega_g)$, or, the ion heating rate, $\dot{W}_\perp$, in units of [J $\cdot$ s^{-1}], abides by the quadrature sum of diffusion variances in $\hat{\mathbf{e}}_{\perp 1}$ and $\hat{\mathbf{e}}_{\perp 2}$ directions such that $\langle|\Delta \mathbf{v}_\perp|^2\rangle = \langle|\Delta v_{\perp 1}|^2\rangle + \langle|\Delta v_{\perp 2}|^2\rangle$ [Bouhram et al., 2003b] [Chang and Crew, 1986] [Crew et al., 1990] [Bouhram et al., 2002] and $\dot{W}_\perp = \Delta W_\perp/\tau_\perp = m\langle|\Delta \mathbf{v}_\perp|^2\rangle/(2\tau_\perp)$. Transverse heating rates follow from Equation 2.32: $\dot{W}_\perp = m\left(D_{\perp 1} + D_{\perp 2}\right)$ and $\dot{W}_\perp = 2mD_\perp$ for $D_{\perp 1} = D_{\perp 2}$ [Bouhram et al., 2003a] [Chang and Crew, 1986] [Crew et al., 1990]. Heating rates in the gyro-frame with diffusion coefficients Equation 2.38 are

$$\dot{W}_{\perp 1} = \sigma_\perp^{-3} \left(\frac{q^2}{2m}\right) \xi_{\perp 1} \eta_{LH} S_0 \left(\frac{\omega_g}{\omega_{g0}}\right)^{-\chi_{\perp 1}}, \quad \dot{W}_{\perp 2} = \sigma_\perp^{-3} \left(\frac{q^2}{2m}\right) \xi_{\perp 2} \eta_{LH} S_0 \left(\frac{\omega_g}{\omega_{g0}}\right)^{-\chi_{\perp 2}}. \tag{2.39}$$

2.2.6 Parallel Electric Field

Ion traps in ionospheric pressure cookers are responsible for producing dense superthermal ion outflows with high-energy conic and bowl distributions observed in regions of low wave-power [Bouhram et al., 2003a] [Wu et al., 2002] [Jasperse, 1998] [Gorney et al., 1985] [Bouhram et al., 2003b]. Temperature anisotropies of hot magnetospheric plasmas are thought to produce parallel electric fields [Alfvén and Falthammar, 1963]. Parallel electric fields are established to ensure charge balance when ions and electrons of different pitch-angle distributions and mirror point locations generate unrealistically large space-charge densities [Wu et al., 2002]. Information is limited on potential structure variations in space and time such that an ad hoc scalar potential is applied across modeled magnetic flux-tubes from reference or incomplete data sets of the auroral acceleration region, such as ion precipitation average energy. Scalar potential drops, $\Delta\Phi_{\|}$, in [V] are computed over successive spatial cells of arc length, $dq(\tilde{q})h_q(\tilde{q})$, according to a reference parallel electric field, $E_{\|0}$, in [V $\cdot$ m^{-1}]:

$$\Delta\Phi_{\|}(\tilde{q}) = E_{\|0} \sum_{1}^{\tilde{q}} dq(\tilde{q})h_q(\tilde{q}), \tag{2.40}$$

where $\tilde{q}$ is configuration-space bin index. Parallel electric fields are electrostatic: $\mathbf{E}_{\|} = -\nabla_{\|}\Delta\Phi_{\|}$. By Equation 2.27 $\nabla_{\|} = \hat{\mathbf{e}}_{\mathbf{q}} h_q^{-1}\partial_q$ such that $\mathbf{E}_{\|} = -h_q^{-1}\partial_q\Delta\Phi_{\|}\hat{\mathbf{e}}_{\mathbf{q}}$ where spatial derivatives are treated by common finite-difference quadratures. Parallel electric fields, $\mathbf{E}_{\|}$, are interpolated to macro-particle positions on each computational time-step. Particle accelerations take the form $\mathbf{a}_{\|} = \mathbf{E}_{\|}q/m$ and Equation 95 gives global Cartesian coordinates of parallel electric field accelerations, where $\mathbf{a}_{\|} = a_{\|}\hat{\mathbf{e}}_{\mathbf{q}}$:

$$\begin{aligned} a_{\|_x} &\approxeq a_{\|}\left[\frac{3\cos(\theta)\sin(\theta)\cos(\phi)}{\sqrt{\ell}}\right], \\ a_{\|_y} &\approxeq a_{\|}\left[\frac{3\cos(\theta)\sin(\theta)\sin(\phi)}{\sqrt{\ell}}\right], \\ a_{\|_z} &\approxeq a_{\|}\left[\frac{3\cos^2(\theta)-1}{\sqrt{\ell}}\right]. \end{aligned} \tag{2.41}$$

2.3 Ion Fluid Dynamics

2.3.1 Ion Distribution Functions

Ion distribution functions and low-order moments are computed on statistical time-steps equal to mean thermal ion transit times through the lower boundary ghost cells, τ_i, as given by Equation 2.14. Ion number densities in spatial cells of index $\tilde{q}$ are given by

$$\mathcal{N}_q(\tilde{q}) = \mathcal{N}'_q\left(\frac{\mu}{d^3x}\right), \tag{2.42}$$

where μ are macro-particle normalization constants, $d^3x(\tilde{q})$ are field-aligned volume elements, and $\mathcal{N}'_q(\tilde{q})$ are numbers of ion macro-particles in spatial bin of index $\tilde{q}$. Eulerian velocity-space vector is given by Equation 2.9. Of the $\mathcal{N}'_q(\tilde{q})$ macro-particles in spatial cell of index $\tilde{q}$ exist $\mathcal{N}'(\tilde{q}, \tilde{v}_{\perp 1}, \tilde{v}_{\perp 2}, \tilde{v}_{\|})$ macro-particles in each three-dimensional velocity-space grid cell. The number of ions, $\mathcal{N}(\tilde{q},\ \tilde{v}_{\perp 1},\ \tilde{v}_{\perp 2},\ \tilde{v}_{\|})$, in each three-dimensional velocity-space grid cell within each spatial cell is

$$\mathcal{N}(\tilde{q},\ \tilde{v}_{\perp 1},\ \tilde{v}_{\perp 2},\ \tilde{v}_{\|}) = \mathcal{N}'\mu. \tag{2.43}$$

Ion distribution functions in units of $[\mathrm{s}^3 \cdot \mathrm{m}^{-6}]$ are formed for each phase-space grid cell by Equations 2.43 and 2.8:

$$f(\tilde{q},\ \tilde{v}_{\perp 1},\ \tilde{v}_{\perp 2},\ \tilde{v}_{\|}) = \frac{\mathcal{N}}{d^3x d^3v}. \tag{2.44}$$

2.3.2 Ion Moments

The m^{th} moment of the ion distribution function, f, is the integral over velocity-space:

$$\mathcal{M}^m(\tilde{q}) = \int\int\int f\mathbf{v}_C^m\, d^3v, \quad d^3v(\tilde{v}_{\perp 1},\ \tilde{v}_{\perp 2},\ \tilde{v}_{\|}) = \ dv_{\perp 1}\, dv_{\perp 2}\, dv_{\|}, \tag{2.45}$$

where $\mathbf{v}_C^m$ is the m^{th} power of the grid-centered velocity vector of Equation 2.9 and $h_{v_{\perp 1}} = h_{v_{\perp 2}} = h_{v_{\|}} = 1$ by Equation 2.8. Zeroth moments of ion distribution functions, or plasma densities $n(\tilde{q})$ in $[\mathrm{m}^{-3}]$, have integrands $\mathcal{I}^0$:

$$n(\tilde{q}) = \int\int\int \mathcal{I}^0\, dv_{\perp 1}\, dv_{\perp 2}\, dv_{\|}, \quad \mathcal{I}^0(\tilde{q},\ \tilde{v}_{\perp 1},\ \tilde{v}_{\perp 2},\ \tilde{v}_{\|}) = f. \tag{2.46}$$

First moments of ion distribution functions, or bulk plasma velocities in $[\mathrm{m}\cdot\mathrm{s}^{-1}]$, are normalized by zeroth moments and split into perpendicular and parallel components $\mathbf{u}_{\perp\mathbf{1}}(\tilde{q})$, $\mathbf{u}_{\perp\mathbf{2}}(\tilde{q})$, and $\mathbf{u}_{\|}(\tilde{q})$, with integrands $\mathcal{I}^1_{\perp 1}$, $\mathcal{I}^1_{\perp 2}$, and $\mathcal{I}^1_{\|}$:

$$\mathbf{u}_{\perp\mathbf{1}}(\tilde{q}) = n^{-1}\int\int\int \mathcal{I}^1_{\perp 1}\, dv_{\perp 1}\, dv_{\perp 2}\, dv_{\|}\hat{\mathbf{e}}_{\mathbf{p}}, \quad \mathcal{I}^1_{\perp 1}(\tilde{q},\ \tilde{v}_{\perp 1},\ \tilde{v}_{\perp 2},\ \tilde{v}_{\|}) = v_{\perp 1_C} f, \tag{2.47}$$

$$\mathbf{u}_{\perp\mathbf{2}}(\tilde{q}) = n^{-1}\int\int\int \mathcal{I}^1_{\perp 2}\, dv_{\perp 1}\, dv_{\perp 2}\, dv_{\|}\hat{\mathbf{e}}_{\boldsymbol{\phi}}, \quad \mathcal{I}^1_{\perp 2}(\tilde{q},\ \tilde{v}_{\perp 1},\ \tilde{v}_{\perp 2},\ \tilde{v}_{\|}) = v_{\perp 2_C} f, \tag{2.48}$$

$$\mathbf{u}_{\|}(\tilde{q}) = n^{-1}\int\int\int \mathcal{I}^1_{\|}\, dv_{\perp 1}\, dv_{\perp 2}\, dv_{\|}\hat{\mathbf{e}}_{\mathbf{q}}, \quad \mathcal{I}^1_{\|}(\tilde{q},\ \tilde{v}_{\perp 1},\ \tilde{v}_{\perp 2},\ \tilde{v}_{\|}) = v_{\|_C} f. \tag{2.49}$$

Second moments of ion distribution functions, $w(\tilde{q})$, are total thermal energies in [J], where m is ion mass and $\hat{\mathbf{e}}_{\mathbf{v_i}} \cdot \hat{\mathbf{e}}_{\mathbf{v_j}} = 0$ for $i \neq j\ \forall i,\ j = \perp 1,\ \perp 2,\ \|$. Accordingly

$$w(\tilde{q}) = \frac{m}{2n} \int\int\int \mathcal{I}^2 \, dv_{\perp 1} \, dv_{\perp 2} \, dv_{\parallel},$$
$$\mathcal{I}^2(\tilde{q},\ \tilde{v}_{\perp 1},\ \tilde{v}_{\perp 2},\ \tilde{v}_{\parallel}) = \left(v^2_{\perp 1_C} + v^2_{\perp 2_C} + v^2_{\parallel_C}\right) f. \tag{2.50}$$

Eulerian velocity-space grid coordinates are centered by first parallel moments such that $v_{\parallel_C} \rightarrow \left(v_{\parallel_C} - u_{\parallel}\right)$ and $\mathcal{I}^2$ from Equation 2.50 becomes

$$\mathcal{I}^2(\tilde{q},\ \tilde{v}_{\perp 1},\ \tilde{v}_{\perp 2},\ \tilde{v}_{\parallel}) = v^2_{\perp 1_C} f + v^2_{\perp 2_C} f + \left(v_{\parallel_C} - u_{\parallel}\right)^2 f. \tag{2.51}$$

Total ion thermal energy, $w(\tilde{q})$, is split into perpendicular and parallel components:

$$w_{\perp 1}(\tilde{q}) = \frac{m}{2n} \int\int\int \mathcal{I}^2_{\perp 1} \, dv_{\perp 1} \, dv_{\perp 2} \, dv_{\parallel}, \quad \mathcal{I}^2_{\perp 1}(\tilde{q},\ \tilde{v}_{\perp 1},\ \tilde{v}_{\perp 2},\ \tilde{v}_{\parallel}) = v^2_{\perp 1_C} f, \tag{2.52}$$

$$w_{\perp 2}(\tilde{q}) = \frac{m}{2n} \int\int\int \mathcal{I}^2_{\perp 2} \, dv_{\perp 1} \, dv_{\perp 2} \, dv_{\parallel}, \quad \mathcal{I}^2_{\perp 2}(\tilde{q},\ \tilde{v}_{\perp 1},\ \tilde{v}_{\perp 2},\ \tilde{v}_{\parallel}) = v^2_{\perp 2_C} f, \tag{2.53}$$

$$w_{\parallel}(\tilde{q}) = \frac{m}{2n} \int\int\int \mathcal{I}^2_{\parallel} \, dv_{\perp 1} \, dv_{\perp 2} \, dv_{\parallel}, \quad \mathcal{I}^2_{\parallel}(\tilde{q},\ \tilde{v}_{\perp 1},\ \tilde{v}_{\perp 2},\ \tilde{v}_{\parallel}) = v^2_{\parallel_C} f, \tag{2.54}$$

where $w = w_{\perp 1} + w_{\perp 2} + w_{\parallel}$. Perpendicular temperature is $T_{\perp}(\tilde{q}) = w_{\perp}/k_B$, where $T_{\perp 1}(\tilde{q}) = 2w_{\perp 1}/k_B$ and $T_{\perp 2}(\tilde{q}) = 2w_{\perp 2}/k_B$, and parallel temperature is $T_{\parallel}(\tilde{q}) = 2w_{\parallel}/k_B$ such that total ion temperature in [K] is $T_i(\tilde{q}) = 2T_{\perp}/3 + T_{\parallel}/3 = T_{\perp 1}/3 + T_{\perp 2}/3 + T_{\parallel}/3$ [Shunk and Nagy, 2000].

2.3.3 Three-Dimensional Velocity-Space Integrator

m^{th} moment integrands, $\mathcal{I}^m$, of ion velocity distribution functions, f, are integrated over velocity-space by three-dimensional quadrature of order $\mathcal{O}[\Delta v^4_{\perp 1}] + [\Delta v^4_{\perp 2}] + \mathcal{O}[\Delta v^4_{\parallel}]$. m^{th} moments, $\mathcal{M}^m(\tilde{q})$, are numerically approximated for integrands $\mathcal{I}^m$ of Equations 2.46, 2.47, 2.48, 2.49, 2.51, 2.52, 2.53, and 2.54:

$$\int\int\int \mathcal{I}^m \, dv_{\perp 1} \, dv_{\perp 2} \, dv_{\parallel} \approxeq \sum\sum\sum \mathcal{I}^m \, \Delta v_{\perp 1} \, \Delta v_{\perp 2} \, \Delta v_{\parallel}. \tag{2.55}$$

Discrete ion velocity differential elements, $\forall i = \perp 1, \perp 2, \parallel$, are $\Delta v_i(\tilde{v}_{\perp 1}, \tilde{v}_{\perp 2}, \tilde{v}_{\parallel}) = \left|v_{i_H} - v_{i_L}\right|$.

Chapter 3

MODEL VALIDATION

In this Chapter ionospheric and magnetospheric plasmas are modeled in one field-aligned dipole spatial coordinate and three dipole velocity coordinates where several particle trajectories are tracked in three-dimensional global Cartesian coordinates along the dipole curvature of a given L-shell. O^+ ions are subject to gravitational and self-consistent ambipolar electric forces once initialized from hydrostatic density profiles of Equation 2.2 and sampled from Maxwellian velocity distributions according to Equations 2.12 and 2.13. Temperature distributions achieve kinetic equilibrium with gravitational and self-consistent ambipolar electric forces as responses from cold lower boundary injection. Kinetic equilibrium incurs expected departure from hydrostatic approximation, particularly at high altitude. In kinetic equilibrium anisotropic Maxwellian distributions drift in time and gyro-center approximations render the computational time-step, h, free of constraints that would otherwise exist due to wave-particle interaction times. Comparisons are made with previous computational investigations of finite gyro-radius effects on ion cyclotron resonance heating with implications of parallel potential structures on wave-heated plasmas. High-altitude wave-particle interactions are simulated for $L = 5\ R_E$ and $L = 15\ R_E$ to emphasize effects of different L-shells on ion outflows. Limited discussion exists in literature concerning ion cyclotron resonance interaction times, $\tau_\perp$, such that variations of this open parameter are quantified within bounds of the model framework. We quantify dependence of upflowing/outflowing ion distributions on: 1) BBELF wave-field transverse wavelength, $\lambda_\perp$, 2) ion cyclotron resonance interaction time-step, h, 3) reference parallel electric field, $E_{\|0}$, and, 4) simulated altitudes of ionospheric and magnetospheric potential structures. Drifting Maxwellian distributions, Type 2 ion upflows, and pressure cookers are modeled, non-Maxwellian distributions features are characterized, and implications of future parametric constraints are considered.

3.1 Kinetic Equilibrium & Self-Consistent Ambipolar Electric Field

Ions are initially distributed along curved magnetic field lines with hydrostatic density profiles according to Equation 2.2 with initial Maxwellian velocity components given by Equations 2.12 and 2.13. Ion macro-particles are pushed by three-dimensional Cartesian RK4 as detailed in Appendix .7 and distribution functions with associated moments are computed along flux-tubes in three-dimensional dipole velocity coordinates as detailed in Sections 2.3.1 and 2.3.2. Hydrostatic density and thermal equilibrium is ensured at lower boundaries by injecting lower boundary density Maxwellian populations of ionospheric ions on time-steps of τ_i as outlined in Section 2.2.1. At all other altitudes parallel energies respond to cold injected ionospheric populations and generate thermal distributions in kinetic equilibrium.

Fluid plasma descriptions treat pressure gradients as forces in the ion momentum equation of classical magnetohydrodynamics. In kinetic theory pressure gradients result from thermal motion of individual particles and are not imposed as kinetic forces. As temperature profiles respond to cold injections and reach steady-state the resulting thermal distribution subject to gravitational and ambipolar electric forcing is said to be in kinetic equilibrium. Kinetic equilibria are achieved following propagations of transient phenomena out of computational domains as systems depart from hydrostatic, or fluid, descriptions. Initial transient effects motivate the capability to begin or continue kinetic simulations from previously modeled output conditions. The continuation of a previous simulation requires input plasma density, temperature, and self-consistent ambipolar electric field magnitude from a previous simulation. Kinetic equilibrium is obtained before the introduction of additional particle forcing. In this section relative departures from hydrostatic approximations of plasmas in kinetic equilibria subject to static and active (self-consistent) ambipolar electric fields are discussed and drifting Maxwellian distributions are modeled for various initial density and temperature distributions. Type 2 ion upflows driven by plasma sheet electron precipitation are modeled as monotonic increases of electron temperature in time with associated self-consistent ambipolar electric field enhancements in the auroral zone.

3.1.1 Drifting Maxwellian Distributions

Table 3.1: Numerical equilibrium simulations with static or active ambipolar electric field, reference density, n_0, at lower boundary, $r_0 = 133$ km, and initial ion temperature, T_i.

Simulation	Ambipolar Electric Field	n_0 [m^{-3}]	T_i [K]
A1	Static	1×10^{11}	1000
A2	Active	1×10^{11}	1000
A3	Active	2×10^{11}	1000
A4	Active	2×10^{11}	1200

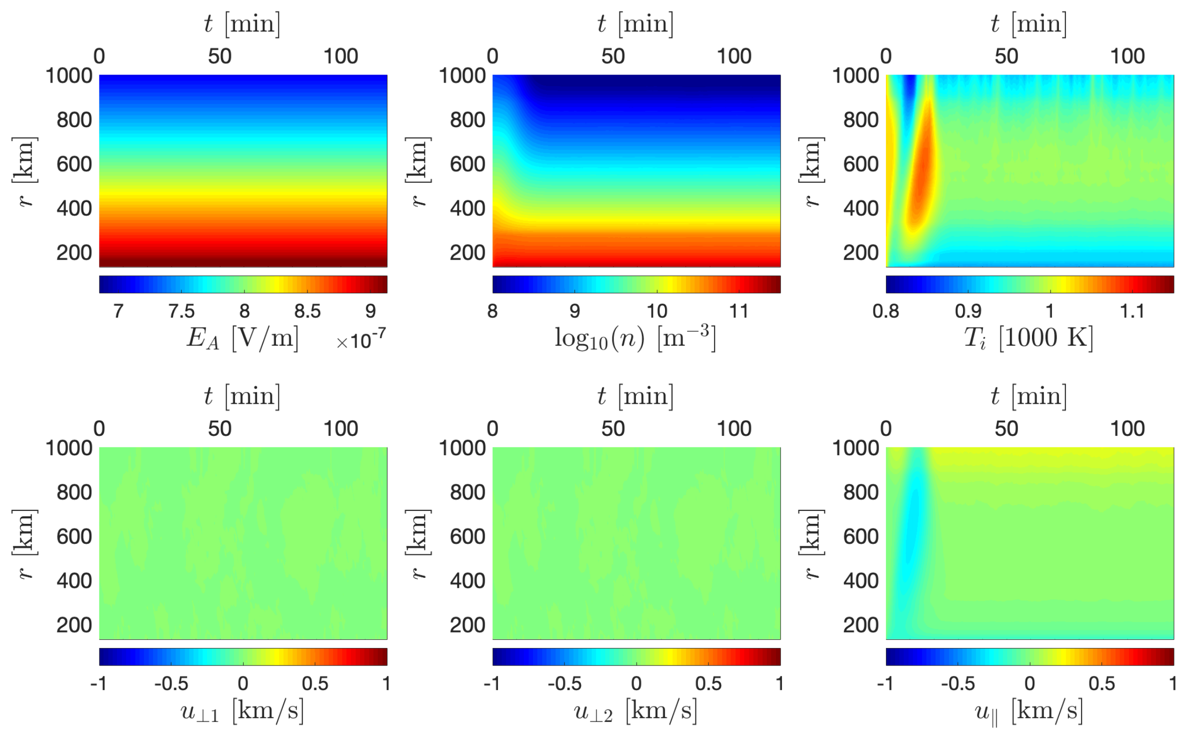

Figure 3.1: Plasma density, ion temperature, and bulk velocity flows along $\hat{\mathbf{e}}_{\mathbf{v}_{\perp 1}}$, $\hat{\mathbf{e}}_{\mathbf{v}_{\perp 2}}$, and $\hat{\mathbf{e}}_{\mathbf{v}_{\parallel}}$ directions with static ambipolar electric field magnitude and initial temperature and density of Simulation A1 of Table 3.1.

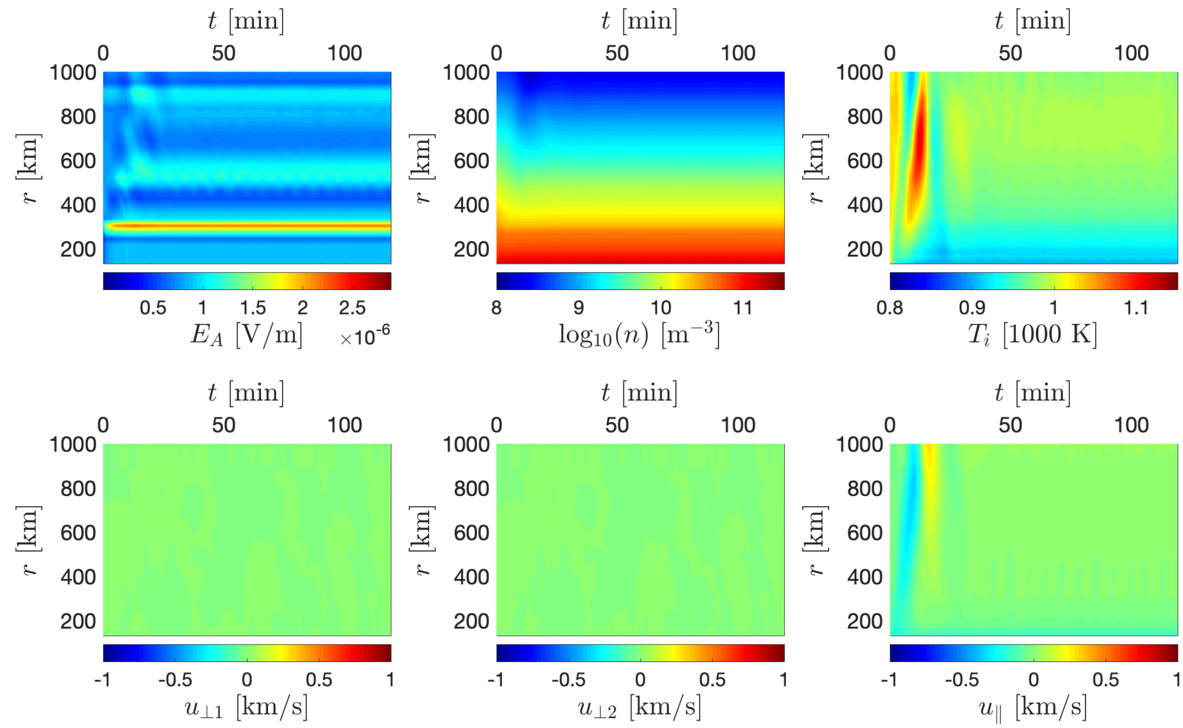

Figure 3.2: Plasma density, ion temperature, and bulk velocity flows along $\hat{\mathbf{e}}_{\mathbf{v}_{\perp 1}}$, $\hat{\mathbf{e}}_{\mathbf{v}_{\perp 2}}$, and $\hat{\mathbf{e}}_{\mathbf{v}_{\|}}$ directions with self-consistent ambipolar electric field magnitude and initial temperature and density of Simulation A2 of Table 3.1.

Evolution of O^+ ion plasmas initially in hydrostatic equilibrium subject to gravitational forcing and ionospheric injection are discussed with static and active ambipolar electric fields, E_A. Kinetic equilibrium corresponds to a drifting Maxwellian distribution of ion temperature, T_i, that has responded to the injection of cold ionospheric ions. Although hydrostatic equilibria applies to plasmas above the F region at $r \sim 300$ km the lower boundary of $r_0 = 133$ km serves to represent a non-reactive equilibrium distribution of plasma that allows us to test our code. Conditions are not representative of realistic ionospheres such that in what follows is a numerical experiment of model validation. Ion moments with static and active ambipolar electric fields are illustrated in Figures 3.1 and 3.2. Similar cases with varying lower boundary reference densities and initial temperatures are tabulated in Table 3.1 for electron temperature $T_e = 1500$ K on $L = 8$ R_E. Evolution of total macro-particle numbers, N_s, are shown in Figure 3.3. As opposed to the static ambipolar electric field case of Figure 3.1, which takes the initial density gradient for all time, the self-consistent ambipolar electric field case of Figure 3.2 actively forces particles to regions of low density such that significant density gradients are reduced and the system tends closer towards the hydrostatic solution. Particles initially fall under gravity which generates a density gradient that pulls plasma up in altitude by the self-consistent ambipolar field in a feature absent in the static analog.

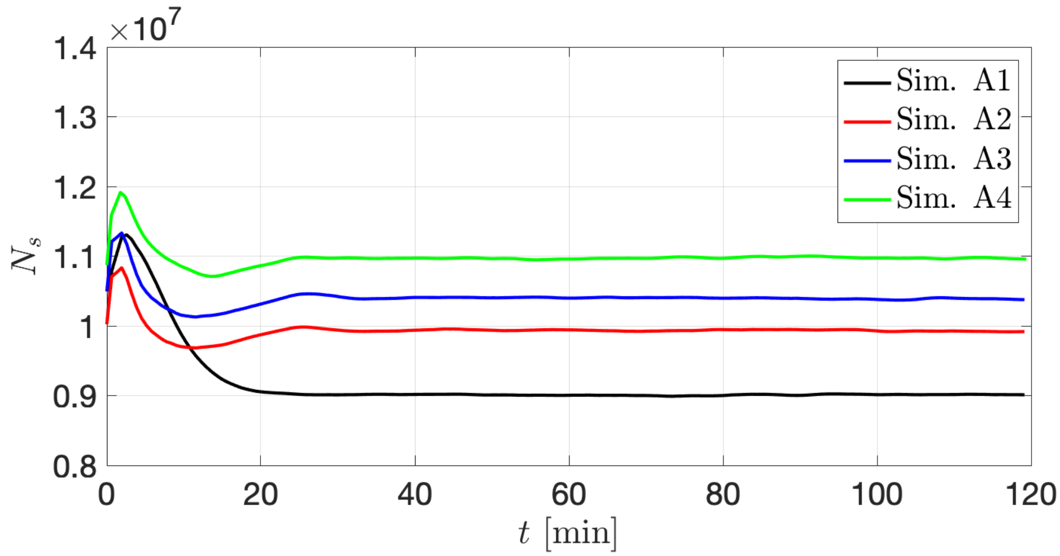

Figure 3.3: Total number of simulated ion macro-particles, N_s, as a function of time for initial conditions outlined in Table 3.1.

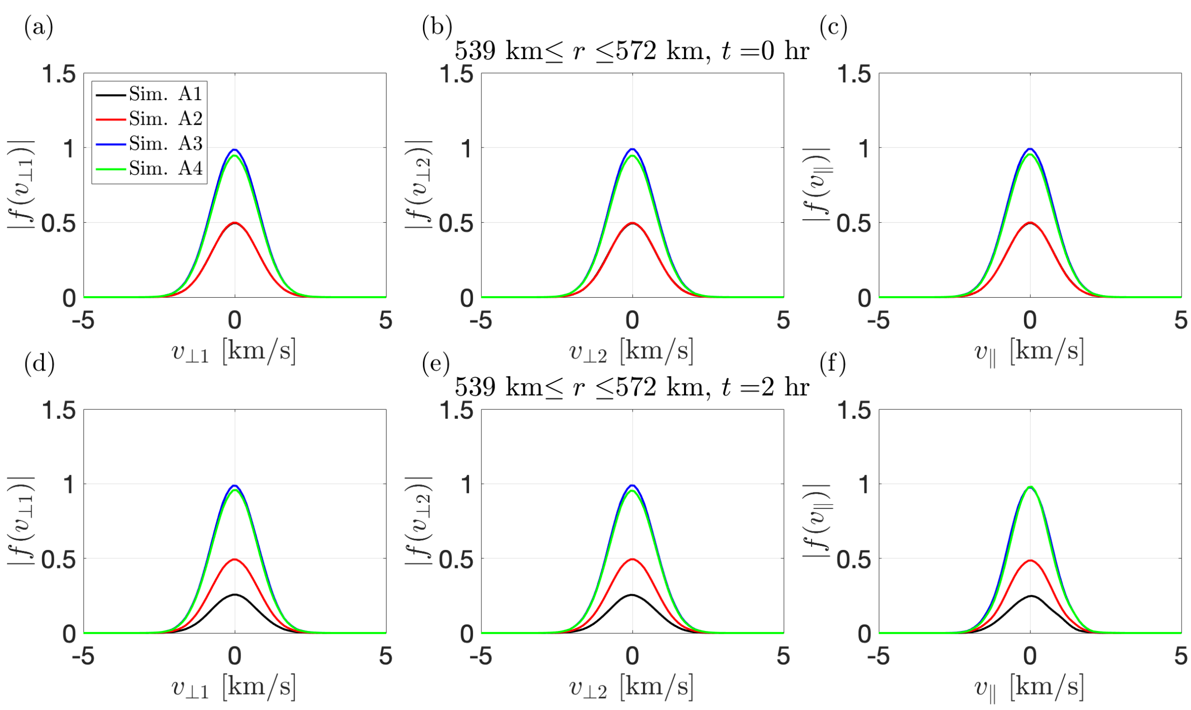

Figure 3.4: Reduced ion distribution functions along $v_{\perp 1}$, $v_{\perp 2}$, and $v_{\parallel}$ at initial time and $t = 2$ hours for initial hydrostatic plasma conditions tabulated in Table 3.1.

Active ambipolar electric field enhancements near lower boundaries form density gradients produced by the collection of cold injected ions. In both static and active cases transient effects have propagated out of the system by $t \sim 30$ minutes and total numbers of simulated macro-particles stabilize. Self-consistent ambipolar electric fields are instrumental in obtaining kinetic equilibria in close agreement to hydrostatic equilibria. Three-dimensional distributions are reduced to single dimensions by integration along two remaining components. The result is shown in Figure 3.4 corresponding to moments of Simulation A2 of Figure 3.2. Integration along two dimensions gives normalized phase-space distributions functions, $|f(v_i)|$, where $f(v_i)$ is in units of [s $\cdot$ m^{-4}], $\forall i = \perp 1, \perp 2, \parallel$. Of the cases tabulated in Table 3.1, Simulations A3 and A4 have stronger cold thermal cores due to greater reference densities at flux-tube footprints. Simulation A3 is an ion population at $T_i = 1000$ K with parallel standard deviations $\sigma = \sqrt{k_B T_i/m} = 0.72$ km $\cdot$ s^{-1}. Simulation A4 has $T_i = 1200$ K and $\sigma = 0.79$ km $\cdot$ s^{-1}. Thermal distributions are nearly indistinguishable for the two cases in the one-dimensional velocity distributions of Figure 3.4. Total simulated macro-particle numbers are greater for higher temperature owing to larger ion scale heights. Simulations A1 and A2 share initial conditions yet total particle numbers and thermal core distributions dominate for active ambipolar electric fields of Simulation A2 due to reduced lower boundary escape flux. Appendix .8 contains energy-pitch-angle distribution transformations and derivations of differential number and energy fluxes.

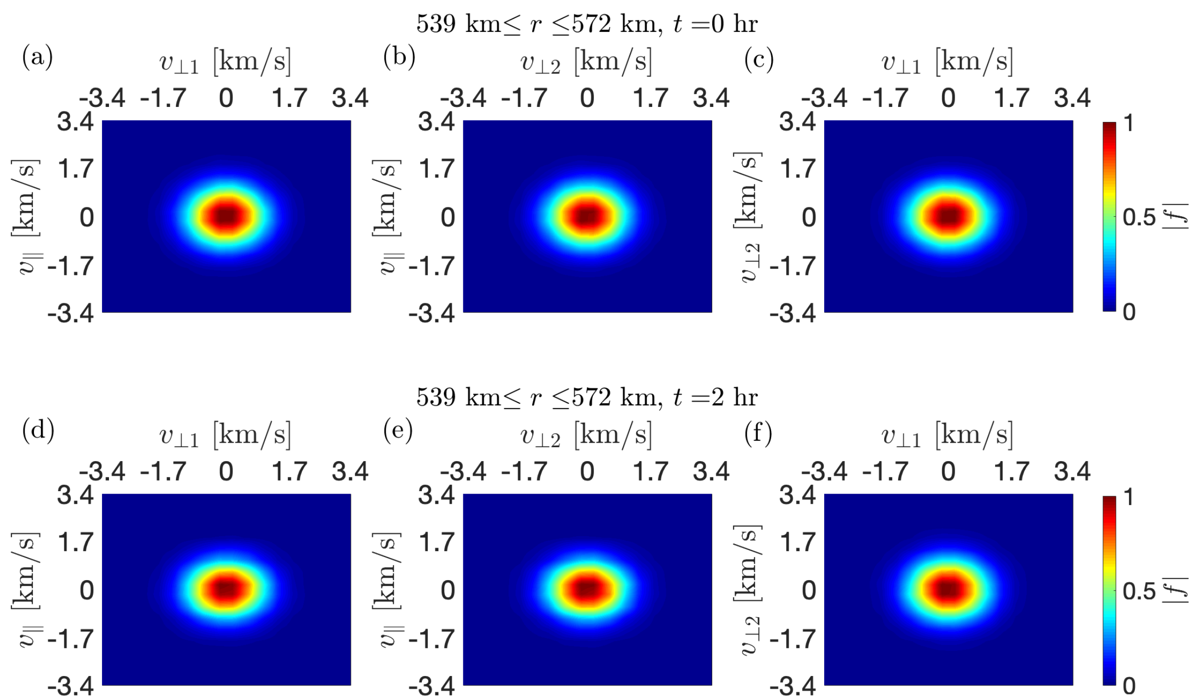

Figure 3.5: Normalized distribution functions in $(v_{\perp 1}, v_{\parallel})$, $(v_{\perp 2}, v_{\parallel})$, and $(v_{\perp 1}, v_{\perp 2})$ planes at initial state and $t = 2$ hours in altitude range 539 km $\leq r \leq$ 572 km with self-consistent ambipolar electric field and initial conditions pertaining to Simulation A2 of Table 3.1.

Normalized drifting phase-space Maxwellian ion distribution functions, $|f(v_{\perp 1}, v_{\perp 2}, v_{\parallel})|$, and normalized energy-pitch-angle distribution functions, $|f_E(E, \alpha, \theta)|$, where E is energy, α is pitch-angle, and θ is gyro-angle, associated with plasma moments of Figures 3.1 and 3.2 are shown in Figures 3.5 and 3.6. Phase-space distribution isotropy in the $(v_{\perp 1},\ v_{\perp 2})$ plane generates zero bulk flows along $\hat{\mathbf{e}}_{\mathbf{v}_{\perp 1}}$ and $\hat{\mathbf{e}}_{\mathbf{v}_{\perp 2}}$ directions. Pitch-angles are measured from outward components of $\mathbf{B}$ such that low pitch-angles correspond to outflowing directions. Kinetic equilibria of Maxwellian distributions entail retention of isotropy in α and θ, as seen in Panels (a), (b), (d), and (e) of Figure 3.6, and conservation of zero-mean distribution functions for positive and negative values of $(v_{\perp 1},\ v_{\perp 2},\ v_{\parallel})$, as seen in Figure 3.5.

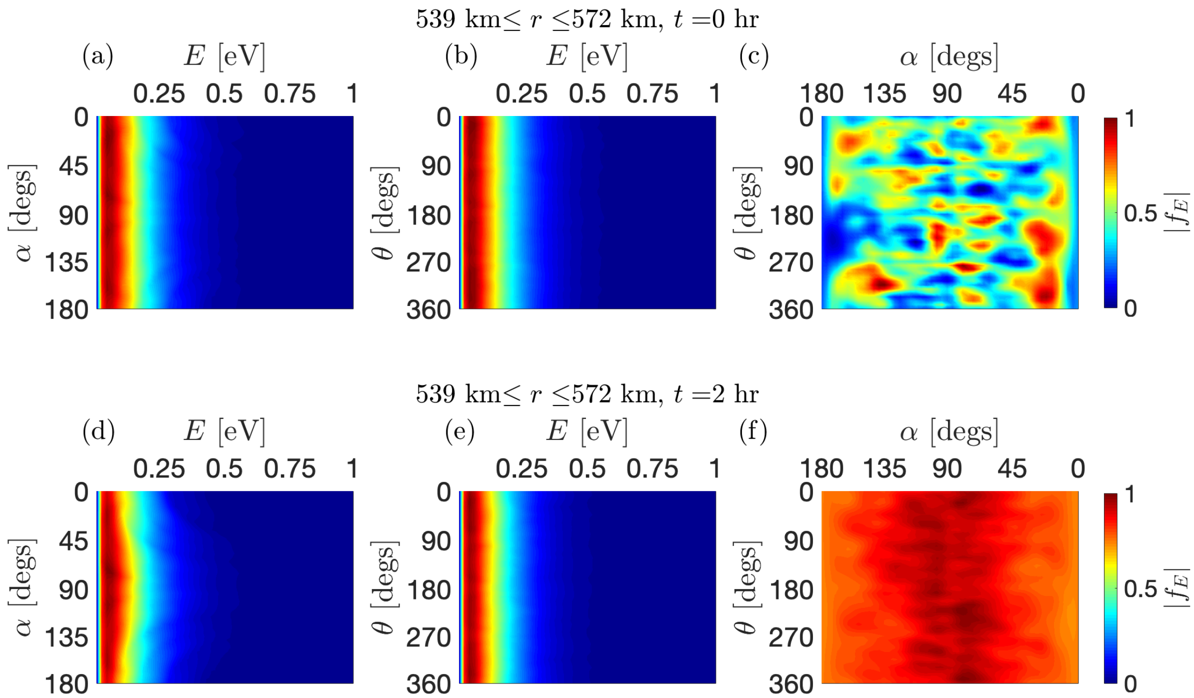

Figure 3.6: Normalized distribution functions in $(E,\ \alpha)$, $(E,\ \theta)$, and $(\alpha,\ \theta)$ planes at initial state and $t = 2$ hours in altitude range 539 km $\leq r \leq$ 572 km with self-consistent ambipolar electric field and initial conditions pertaining to Simulation A2 of Table 3.1. Upwards (downwards) motion for $\alpha < 90°$ ($\alpha > 90°$).

Cold thermal cores within ~ 0.5 eV exist for all α and θ in three degrees-of-freedom according to the equipartition of total energy, $w_i = k_B T_{\perp 1}/2 + k_B T_{\perp 2}/2 + k_B T_{\parallel}/2$, for ion temperature $T_i = T_{\perp 1}/3 + T_{\perp 2}/3 + T_{\parallel}/3$. Distribution functions are drifting Maxwellians constant in time as kinetic responses to thermal, gravitational, and ambipolar forces of hydrostatic equilibrium. Initial irregularities in $(\alpha,\ \theta)$ (Figure 3.6) dissipate while isotropy permeates the $(\alpha,\ \theta)$ plane at the final time. Magnetic moments are defined by initial perpendicular velocities sampled by Maxwellian distributions in three-dimensional global Cartesian coordinates for all time in the absence of adiabatic cooling and transverse wave heating. Evolution to kinetic solutions purely concerns translational, or parallel, particle motion. Slight departures from initial hydrostatic parallel velocity distributions of Panel (c) in Figure 3.4 exist when the system reaches kinetic equilibrium at $t = 2$ hours, as seen in Panel (f) of Figure 3.4. Transverse components remain Maxwellian throughout as magnetic moments are conserved on gyro-periods, as seen in Panels (a), (b), (d), and (e) in Figure 3.4. Since the active ambipolar case more closely approximates hydrostatic equilibrium from 133 km $\leq r \leq$ 1000 km self-consistent ambipolar fields are adopted for the remainder of this work.

3.1.2 Type 2 Ion Upflows

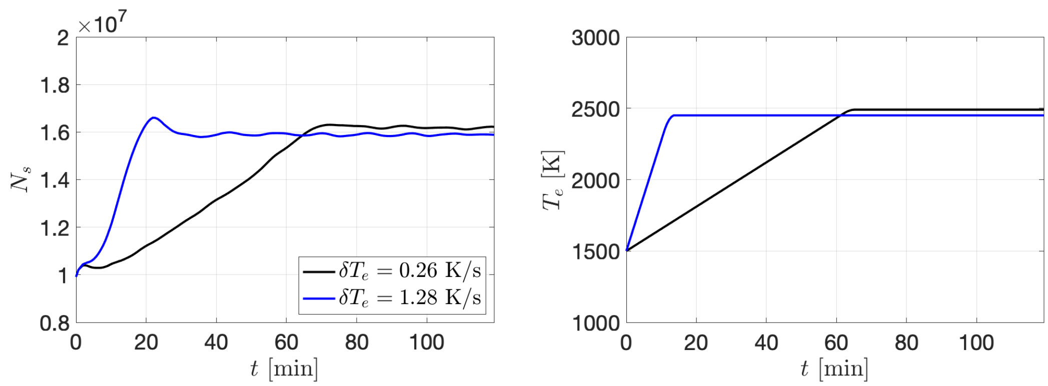

Figure 3.7: Total number of ion macro-particles simulated, N_s, and electron temperature, T_e, as functions of time for soft magnetospheric electron precipitation driven Type 2 ion upflows with cases of $\delta T_e = 0.26\ \mathrm{K} \cdot \mathrm{s}^{-1}$ and $\delta T_e = 1.28\ \mathrm{K} \cdot \mathrm{s}^{-1}$.

Type 2 ion upflows are thought to be central in lifting ions to altitudes of significant wave heating resulting in transversely energized ion outflows [Strangeway et al., 2005] [Zheng et al., 2005] [Su et al., 1999]. Observed ion upflows in the topside ionosphere have been correlated with soft auroral electron precipitation [Seo et al., 1997] [Wu et al., 2002]. Effects of self-consistent ambipolar electric field enhancements on upflowing plasma from auroral precipitation of magnetospheric electrons of plasma sheet origin are modeled as monotonic increases in electron temperature, T_e, by rates δT_e until T_e surpasses a given threshold in time. To ensure all transient effects have propagated out of the computational domain all simulations of the remainder of this work are subject to re-initialization with initial conditions corresponding to a system in kinetic equilibrium. In what follows Type 2 ion upflow simulations are initialized from the final plasma density, ion temperature, and active ambipolar electric field of Simulation A2 of Table 3.1. All other parameters carry on from the previous section. Two ion upflow environments are simulated for initial electron temperatures $T_e = 1500$ K increasing at rates: $\delta T_e = 0.26\ \mathrm{K} \cdot \mathrm{s}^{-1}$ and $\delta T_e = 1.28\ \mathrm{K} \cdot \mathrm{s}^{-1}$, that is by 10 K and 50 K per 39 seconds, respectively, while T_e does not exceed 2500 K. Evolution of total macro-particle numbers, N_s, and electron temperature, T_e, are shown in Figure 3.7, where $E_A \propto T_e$ according to Equation 2.22. Moments for the moderate and enhanced electron precipitation cases of $\delta T_e = 0.26\ \mathrm{K} \cdot \mathrm{s}^{-1}$ and $\delta T_e = 1.28\ \mathrm{K} \cdot \mathrm{s}^{-1}$ are illustrated in Figures 3.8 and 3.9. Self-consistent ambipolar electric field enhancements are produced by cold injections of ionospheric ions and associated low-altitude density gradients for all time, while ion ambipolar accelerations increase linearly with electron temperature according to Equation 2.22.

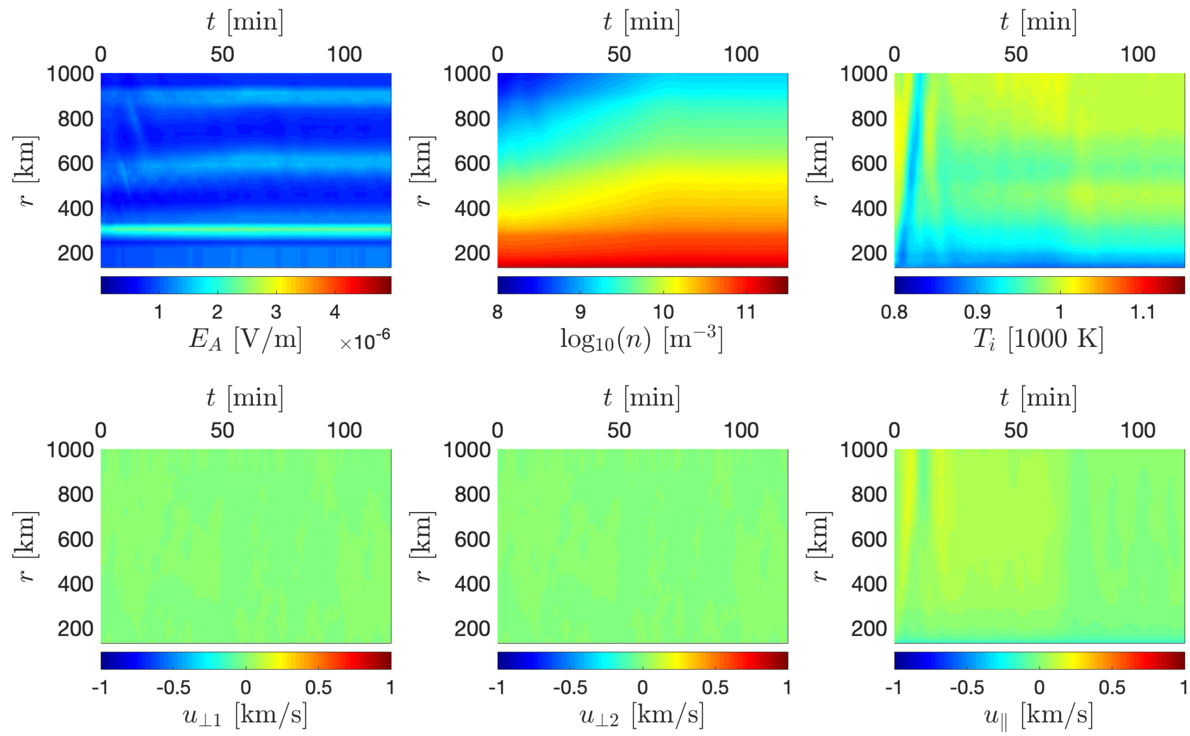

Figure 3.8: Plasma density, ion temperature, and bulk velocity flows along $\hat{\mathbf{e}}_{\mathbf{v}_{\perp 1}}$, $\hat{\mathbf{e}}_{\mathbf{v}_{\perp 2}}$, and $\hat{\mathbf{e}}_{\mathbf{v}_{\parallel}}$ directions for Type 2 ion upflow cases with self-consistent ambipolar electric field magnitude, flux-tube footprint reference density $n_0 = 1 \times 10^{11}\ \mathrm{m}^{-3}$ at $r_0 = 133$ km, initial ion temperature $T_i = 1000$ K, initial electron temperature $T_e = 1500$ K increased at rate of $\delta T_e = 0.26\ \mathrm{K} \cdot \mathrm{s}^{-1}$.

Transverse populations are drifting Maxwellians in the absence of mirror force induced relaxation of magnetic moments and wave heating such that first adiabatic invariants are comfortably conserved. It is apparent from moments of the two upflow cases of Figures 3.8 and 3.9 that active ambipolar electric field enhancements result in upwards thermal plasma expansions that settle at $t \sim 70$ minutes for $\delta T_e = 0.26\ \mathrm{K} \cdot \mathrm{s}^{-1}$ and $t \sim 20$ minutes for $\delta T_e = 1.28\ \mathrm{K} \cdot \mathrm{s}^{-1}$. Moderate upflow occurs for the case of $\delta T_e = 0.26\ \mathrm{K} \cdot \mathrm{s}^{-1}$ where the system is able to thermally respond to increase in T_e such that ion temperature remains relatively unchanged. An initial upflow plume appears in the first $t \sim 25$ minutes with upward drifts of $u_{\parallel} \sim 0.5\ \mathrm{km \cdot s^{-1}}$ leaving behind cold ion populations at $T_i \sim 900$ K, as seen in Figure 3.9. Consistent with moments in Figure 3.9, the enhanced outward ambipolar diffusion and upflow plume at $t \sim 15.6$ minutes from $r \sim 539$-572 km is characterized by the normalized one and two-dimensional velocity distributions of Figures 3.10 and 3.11, respectively, with energy-pitch-angle distributions in Figure 3.12. Velocity distribution departures from Maxwellian occur parallel to the field line from net negative lower boundary escape fluxes by active ambipolar electric field lifting and associated Type 2 ion upflow. Positive $v_{\parallel}$ values correspond to outflowing directions.

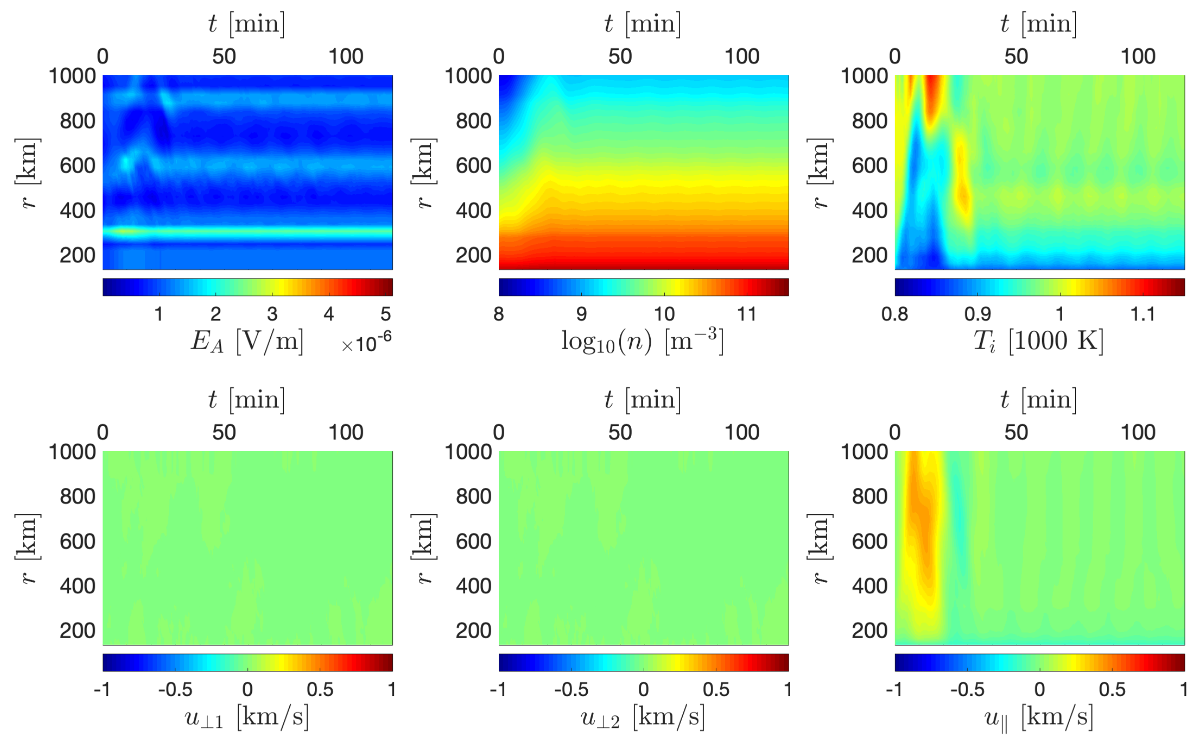

Figure 3.9: Plasma density, ion temperature, and bulk velocity flows along $\hat{\mathbf{e}}_{\mathbf{v}_{\perp 1}}$, $\hat{\mathbf{e}}_{\mathbf{v}_{\perp 2}}$, and $\hat{\mathbf{e}}_{\mathbf{v}_{\parallel}}$ directions for Type 2 ion upflow cases with self-consistent ambipolar electric field magnitude, flux-tube footprint reference density $n_0 = 1 \times 10^{11}\ \mathrm{m^{-3}}$ at $r_0 = 133$ km, initial ion temperature $T_i = 1000$ K, initial electron temperature $T_e = 1500$ K increased at rate of $\delta T_e = 1.28\ \mathrm{K \cdot s^{-1}}$.

Until electron temperatures saturate in time ion thermal cores deepen and assume non-Maxwellian upward parallel drifts while conserving adiabatic invariants of orbital motion. Initial transverse Maxwellian velocity distributions drift intact in time as seen in Panels (c) and (f) of Figure 3.5. At $t = 15.6$ minutes the total number of particles, N_s, for the enhanced upflow case $\delta T_e = 1.28\ \mathrm{K \cdot s^{-1}}$, exceeds that of the moderate $\delta T_e = 0.26\ \mathrm{K \cdot s^{-1}}$ analog by $\sim 84\%$. Parallel drifts up to $u_{\parallel} \sim 0.4\ \mathrm{km \cdot s^{-1}}$ are seen in moments of Figure 3.9.

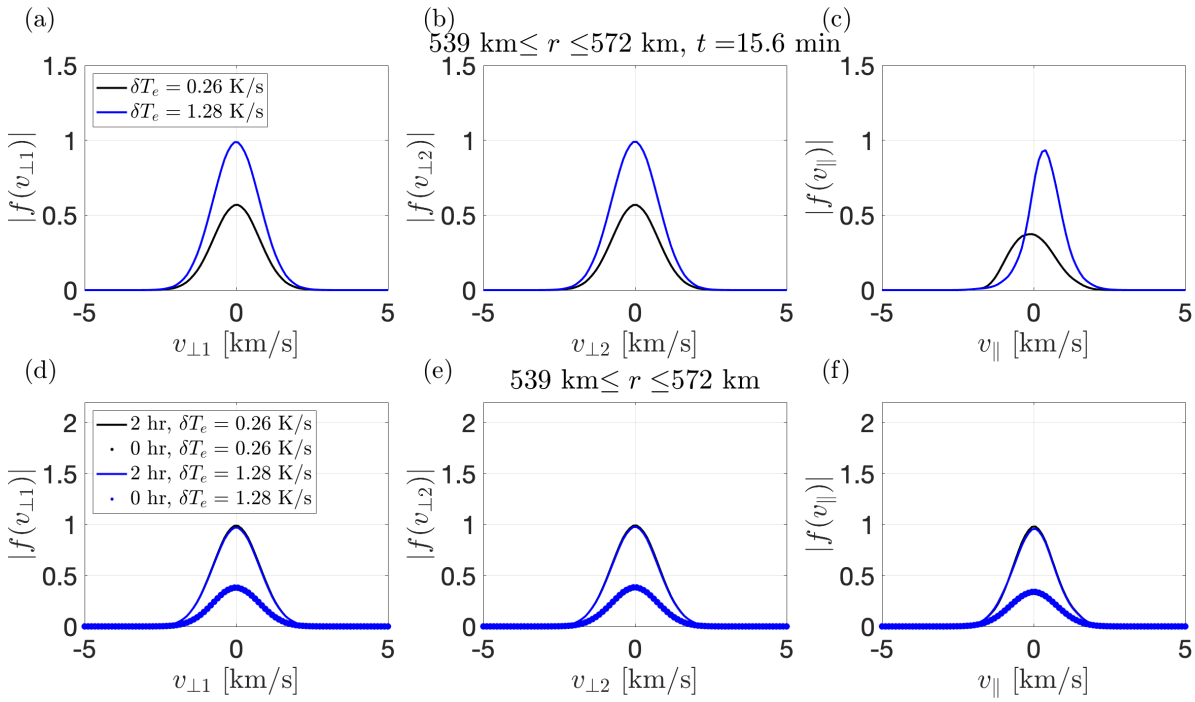

Figure 3.10: Reduced ion distribution functions along $v_{\perp 1}$, $v_{\perp 2}$, and $v_{\parallel}$ for Type 2 ion upflows with initial electron temperature $T_e = 1500$ K increased at rates of $\delta T_e = 0.26$ K $\cdot$ s^{-1} and $\delta T_e = 1.28$ K $\cdot$ s^{-1}.

Thermal distribution peaks shift towards $+v_{\parallel}$ as seen in Panel (c) of Figure 3.10 at $t = 15.6$ minutes. At 2 hours simulation time both upflow cases obtain new thermal distributions corresponding to larger densities and drifting ion temperatures. Distribution functions remain isotropic and amplitudes increase by nearly $\sim 60\%$ initial values by $t = 2$ hours consistent with growth in N_s. Parallel velocity distributions at 2 hours in Panel (f) of Figure 3.10 obtain equilibrium and recover from auroral electron precipitations and associated ambipolar upward diffusion at $t = 15.6$ minutes, as seen in Panel (c) of Figure 3.10. Self-consistent ambipolar electric fields associated with increases in electron temperature by magnetospheric electron precipitation drive Maxwellian velocity distributions upward in altitude generating parallel distributions shifted outwards as seen in Panels (a) and (b) of Figure 3.5. This behavior is apparent by the outward diffusion of thermal distributions towards low pitch-angles, as seen in Panels (a), (b), and (c) of Figure 3.12, where upwards motion corresponds to $\alpha < 90°$. Distributions drop off above $\alpha \sim 90°$ in the initial upflow plume and energies are gyro-tropic in θ in the absence of transversely anisotropic wave heating.

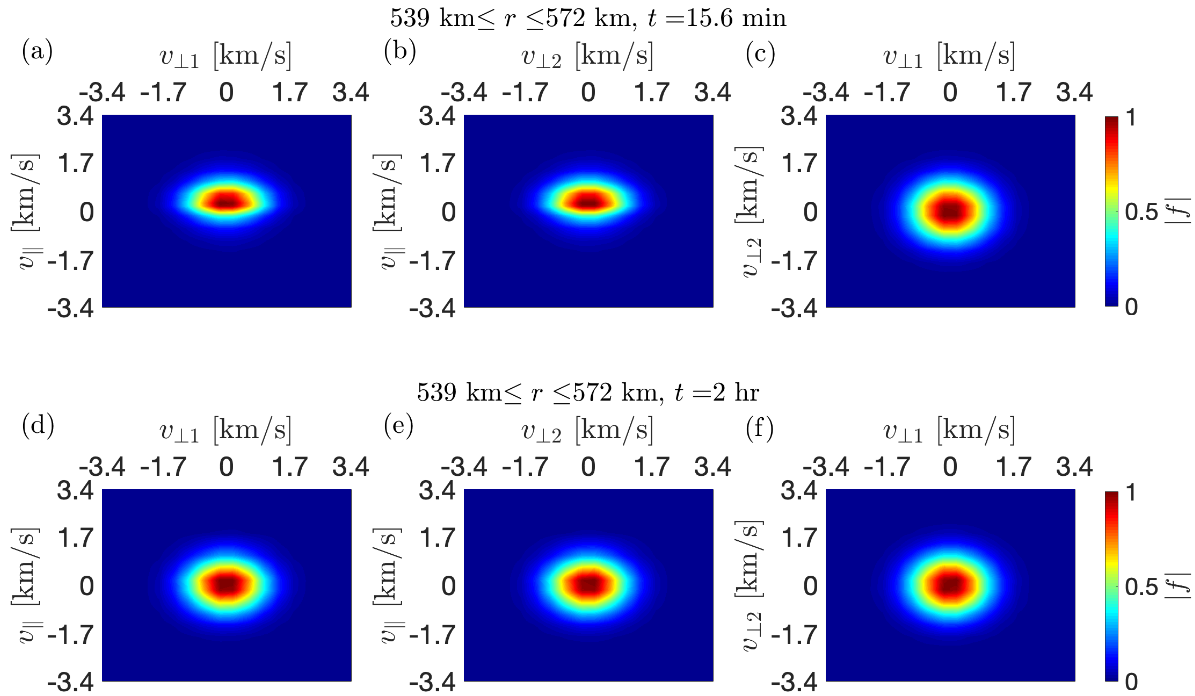

Figure 3.11: Normalized distribution functions in ($v_{\perp 1}$, $v_{\parallel}$), ($v_{\perp 2}$, $v_{\parallel}$), and ($v_{\perp 1}$, $v_{\perp 2}$) planes at $t = 15.6$ minutes and $t = 2$ hours in altitude range 539 km $\leq r \leq$ 572 km for Type 2 ion upflows with initial electron temperature $T_e = 1500$ K increased at rate of $\delta T_e = 1.28\ \mathrm{K \cdot s^{-1}}$.

Gyro-tropic transverse velocity distributions are conserved with amplitudes that reflect increase in total particle number, N_s, as seen in Panels (d) and (e) of Figure 3.10. Panels (c) and (f) of Figure 3.11 illustrate isotropy of drifting Maxwellian distributions in gyro-angle, θ. Parallel Maxwellian distributions are fully recovered by 2 hours from the upward expansion of ions. At this time total energy, E, is uniformly distributed in pitch-angle, α, as seen in Panel (d) of Figure 3.12. Relaxed thermal ion populations are isotropic in α and θ for energies below $E \sim 0.5$ eV, as seen in Panels (d), (e), and (f) of Figure 3.12. Plasma is thermalized by $t \sim 70$ minutes and $t \sim 20$ minutes after precipitation events for $\delta T_e = 0.26\ \mathrm{K \cdot s^{-1}}$ and $\delta T_e = 1.28\ \mathrm{K \cdot s^{-1}}$ cases, respectively.

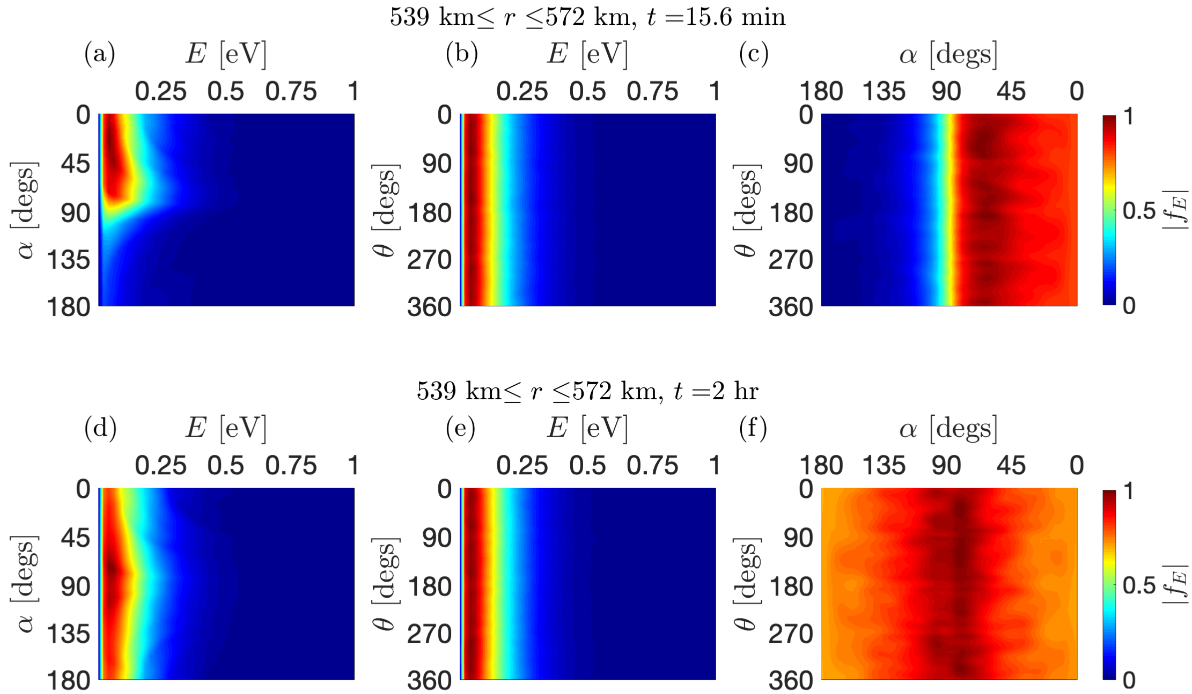

Figure 3.12: Normalized distribution functions in $(E,\ \alpha)$, $(E,\ \theta)$, and $(\alpha,\ \theta)$ planes at $t = 15.6$ minutes and $t = 2$ hours in altitude range 539 km $\leq r \leq$ 572 km for Type 2 ion upflows with initial electron temperature $T_e = 1500$ K increased at rate of $\delta T_e = 1.28$ K $\cdot$ s^{-1}.

3.2 Wave Heating & Parallel Potential Drops

3.2.1 Wave Heating With Electron Precipitation

Orbital particle motion is averaged over gyro-periods such that, until this point, no constraints exist on computational time-steps, h, beyond numerical noise incurred by approximations of curved particle trajectories. Computational time-steps must resolve ion cyclotron resonance interaction times, $\tau_\perp$, when magnetic moments are not conserved, as for the case of wave-particle interactions discussed in Subsection 2.2.5. It is selected such that $h \leq \tau_\perp$ where choices of h are linearly proportional to transverse velocity kick magnitudes per Equation 2.33. Wave power spectral densities within narrow frequency passbands, Δf, centered at ion gyro-frequencies, f_g, diffuse transverse velocities of wave-heated ions as overviewed in Subsection 2.2.5. Interaction times of wave resonance at frequencies within Δf of f_g with particles at gyro-frequency f_g is $\tau_\perp = 1/\Delta f$. Particle transit times across localized wave-fields are limited by durations of phase-coherence between particle gyro-frequencies and resonant wave spectrum Fourier components [Schulz and Lanzerotti, 1974]. Wave heating intensity varies along and across auroral field lines and information on variations in altitude and time is sparse [Wu et al., 1999] [Wu et al., 2002] [Huddleston et al., 2000] [Winningham and Burch, 1984b]. Limited constraints on $\tau_\perp$ for gyro-centered approximations lead to computational time-steps $f_g^{-1} < h < \tau_\perp$. Although $h \to \tau_\perp$ is desirable to properly scale transverse velocity kick magnitudes, $\delta v_\perp$, performed on computational time-scales of h to kicks on interaction time-scales of $\tau_\perp$ in Equation 2.33 tolerances on numerical noise become critical when equating h to large values of $\tau_\perp$.

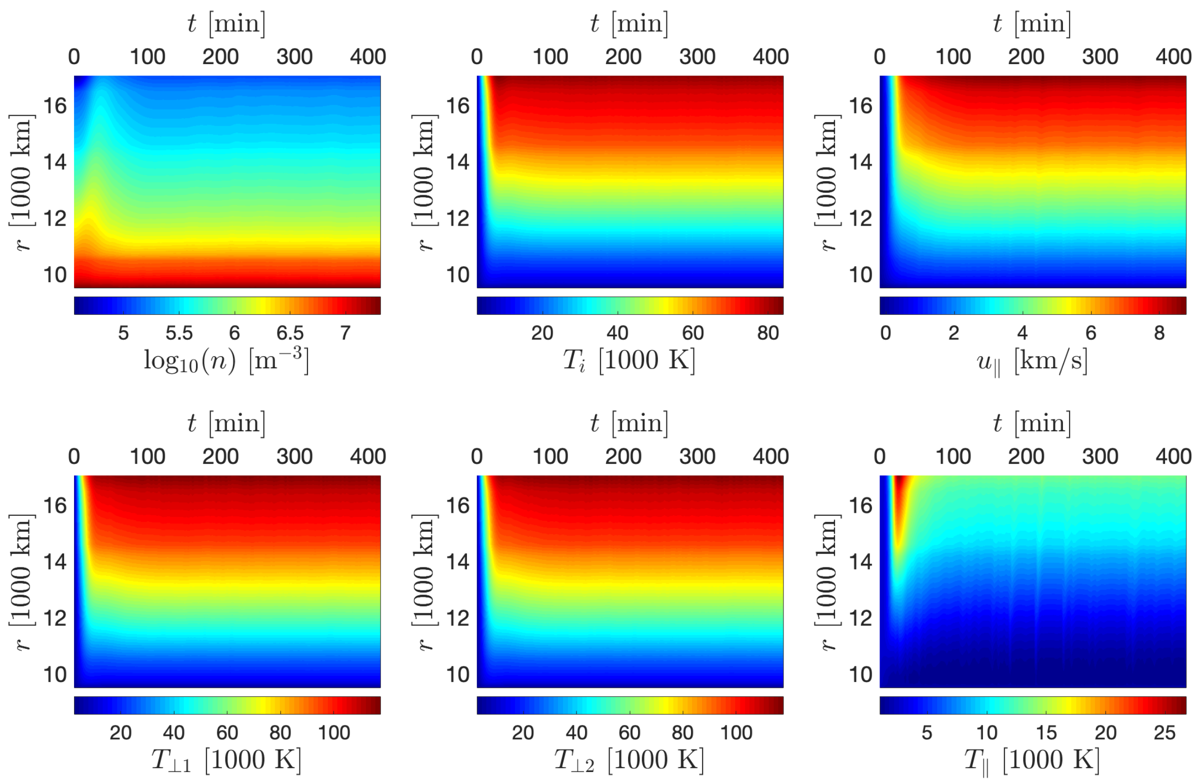

Figure 3.13: Plasma density, ion temperature, parallel plasma flow, and temperatures for high-altitude ion cyclotron wave-induced outflows with active ambipolar electric field and heating parameterization from [Wu et al., 1999].

Elevated ion conic, beam, and toroidal distributions of suprathermal ion populations up to tens or hundreds of eV are commonly observed along active auroral field lines [Wu et al., 2002] [Klumpar et al., 1984] [Hirahara, 1998]. Mirror force effects and ion cyclotron resonance heating by BBELF waves on plasmas in kinetic equilibrium under gravitational and active ambipolar forcing are modeled and discussed in this section. Generation and characterization of highly non-Maxwellian ion distribution functions driven by wave-particle interactions- such as winged conic, or bowl distributions, and ring, or toroidal distributions- are contrasted to other investigations. Several studies exist for characterizations of wave-inducing ion outflows [Barakat and Barghouthi, 1994] [Barghouthi et al., 1998] [Barghouthi, 2008] [Wu et al., 1999] [Wu et al., 2002] [Glocer et al., 2018].

Model differences are noted as disparities are apparent and similar plasma phenomena are elucidated. Open heating parameters unconstrained by observations are interaction time-steps, h, and transverse wavelengths, $\lambda_\perp$. Values of h and $\lambda_\perp$ are adopted ad hoc to best represent observations or modeling efforts and remain within bounds of prudent numerical approximation. A qualitative analysis is what follows of wave-driven ionospheric outflows and minor attempts are made to reconcile background conditions.

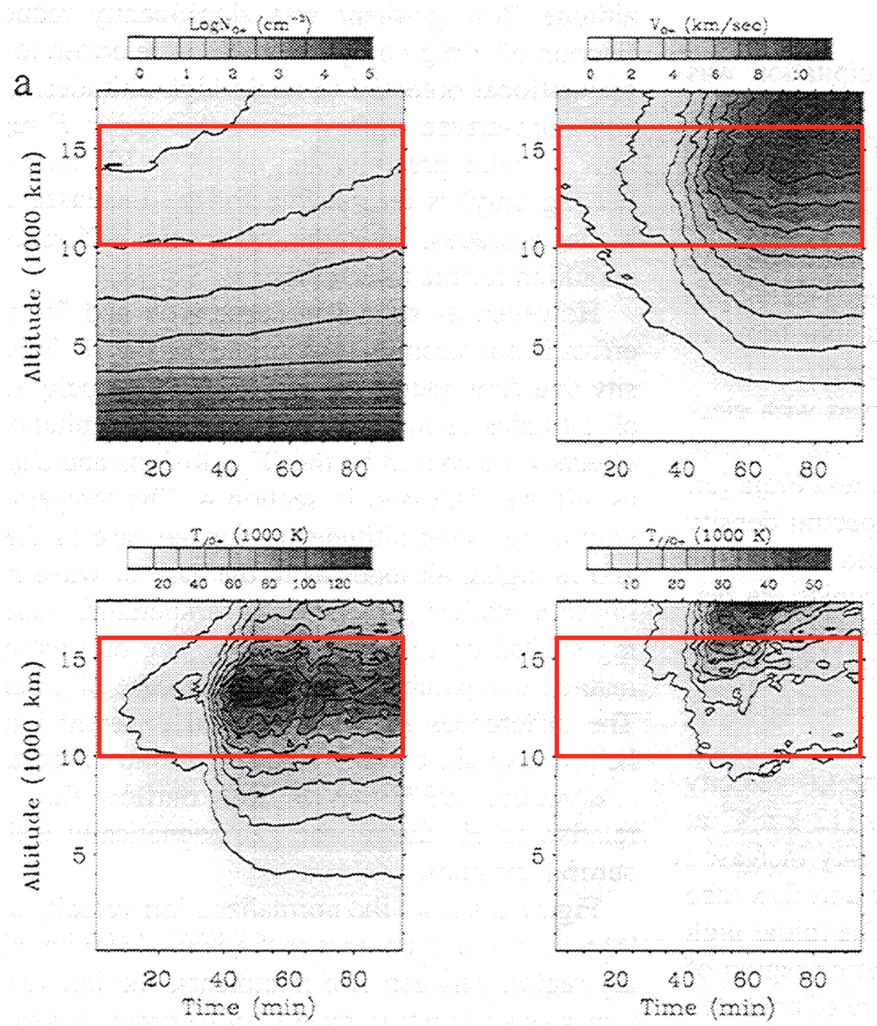

Figure 3.14: Plasma density, parallel flow, and energies for the auroral event of wave-induced heating as modeled by DyFK [Wu et al., 1999]. Red squares indicate regions of comparison.

Moments in Figures 3.13 and 3.15 correspond to transverse wave heating conditions along $L = 7.88\ R_E$ with $r_0 = 340$ km altitude footprint corresponding to reference density $n_0 = 6 \times 10^{10}$ m^{-3}, ionospheric ion injection temperature $T_i = 4400$ K, and electron temperature $T_e = 2400$ K. Wave-heated outflows of Figure 3.13 have turbulent wave-field parameters selected from [Wu et al., 1999] with reference electric field power spectral density $S_0 = 1 \times 10^{-7}\ \mathrm{V}^2 \cdot \mathrm{m}^{-2} \cdot \mathrm{Hz}^{-1}$ at reference gyrofrequency $f_{g0} = 6.5$ Hz, $\eta_{LH} = 0.125$ as the fraction of left-hand polarized wave power [Chang and Crew, 1986], $\xi_{\perp 1} = \xi_{\perp 2} = 0.5$, and $\chi_{\perp 1} = \chi_{\perp 2} = 1.7$. As compared to DyFK efforts of [Wu et al., 1999] illustrated in Figure 3.14 perpendicular energies with interaction time-steps $h = 2.5$ seconds produce perpendicular temperatures $T_\perp \sim 1\times10^5$ K and parallel temperatures $T_\parallel \sim 2\times10^4$ K consistent with levels seen in Figure 3.13. Parallel drifts exceed $u_\parallel \sim 5$ km $\cdot$ s^{-1} in both models and densities reside near $n \sim 1 \times 10^7$ m^{-3} at $r \sim 10000$ km altitude.

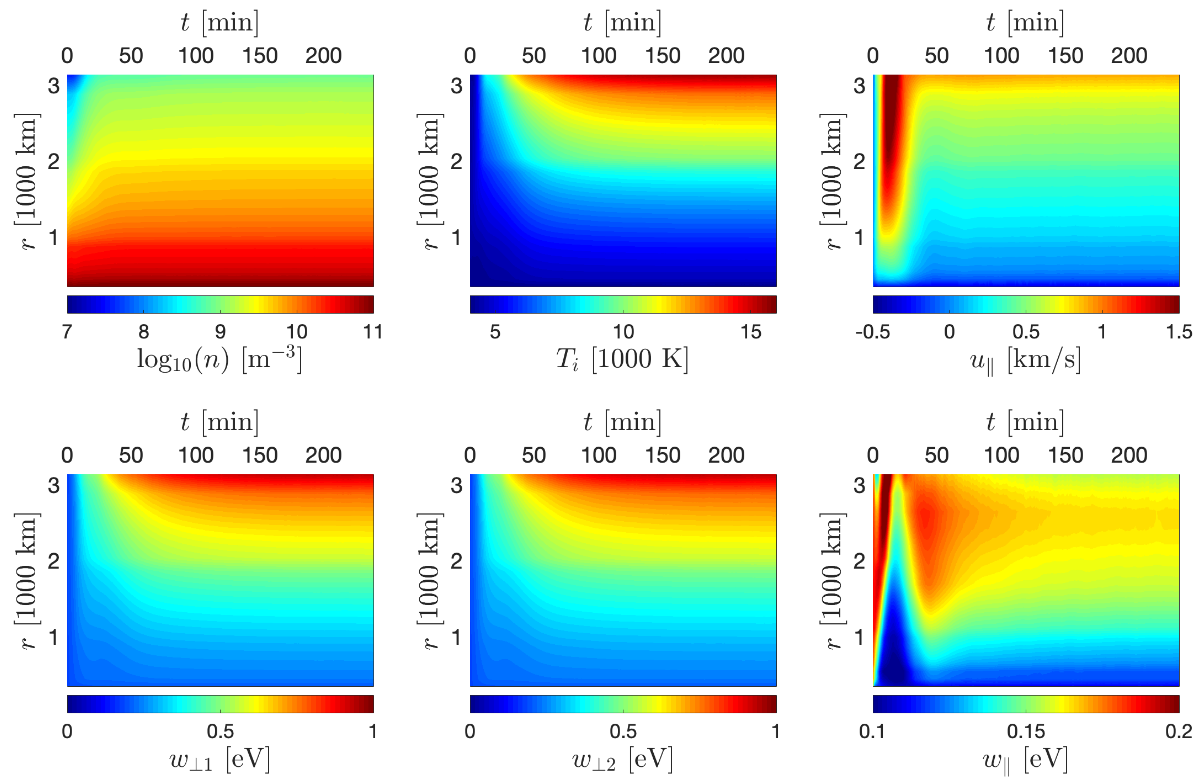

Figure 3.15: Plasma density, ion temperature, parallel plasma flow, and energies along $\hat{\mathbf{e}}_{\mathbf{v}_{\perp 1}}$, $\hat{\mathbf{e}}_{\mathbf{v}_{\perp 2}}$, and $\hat{\mathbf{e}}_{\mathbf{v}_\parallel}$ directions for low-altitude ion cyclotron wave-induced outflows with active ambipolar electric field, heating parameterization from [Zeng et al., 2006], and soft electron precipitation with $\delta T_e = 8.06$ K $\cdot$ s^{-1}.

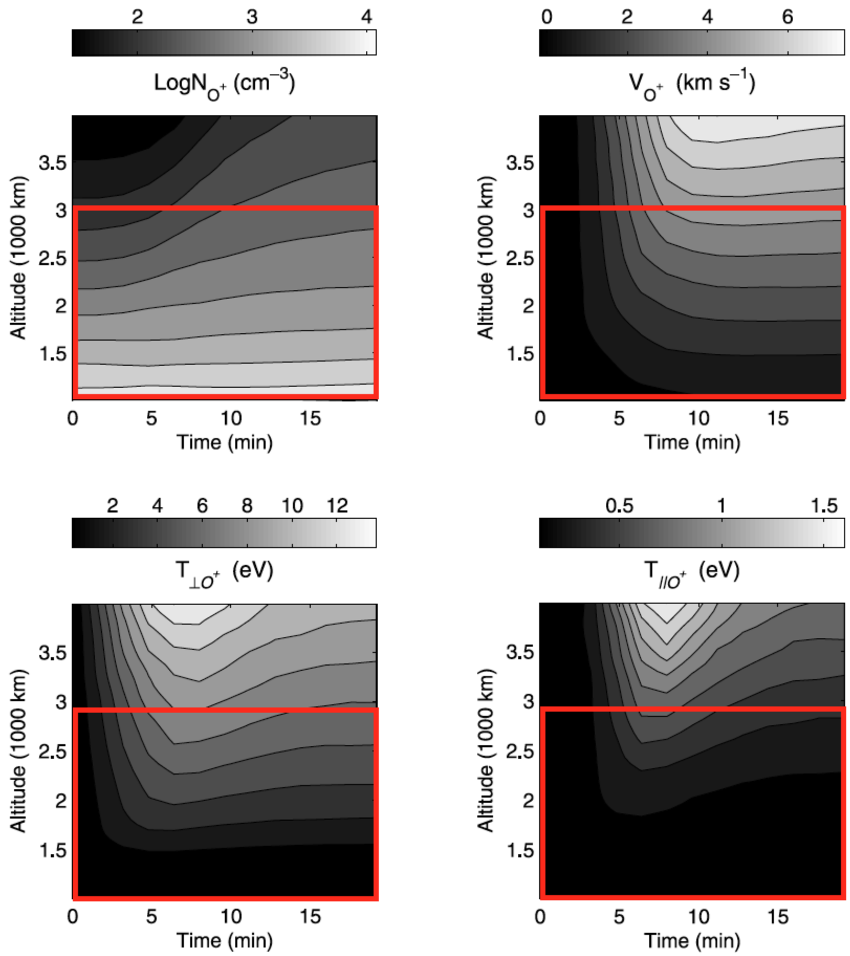

Figure 3.16: Plasma density, parallel flow, and energies for the auroral event of wave-induced heating and soft electron precipitation as modeled by DyFK [Zeng et al., 2006]. Red squares indicate regions of comparison.

Wave heating parameters from DyFK efforts of [Zeng et al., 2006] are selected for moments in Figure 3.15 where transverse velocity diffusion coefficients of Equation 2.38 assume infinite perpendicular wavelength (i.e., $\lambda_\perp \gg \rho_g$). [Zeng et al., 2006] models an auroral event subject to wave heating with soft electron precipitation of characteristic energy 100 eV and energy flux $1.0\ \text{ergs}\cdot\text{cm}^{-2}\cdot\text{s}^{-1}$. Electron precipitation is modeled in our study as monotonic increases in electron temperature, T_e, by rates $\delta T_e = 8.06\ \text{K}\cdot\text{s}^{-1}$, that is, by 500 K increments every 62 seconds. Reference electric field power spectral densities $S_0 = 3\times10^{-7}\ \text{V}^2\cdot\text{m}^{-2}\cdot\text{Hz}^{-1}$ at reference gyrofrequency $f_{g0} = 6.5$ Hz with spectral index $\chi_{\perp1} = \chi_{\perp2} = 1.7$ are employed. $\eta_{LH} = 0.125$ [Chang and Crew, 1986] is the fraction of left-hand polarized wave power isotropically distributed in gyrophase, i.e., $\xi_{\perp1} = \xi_{\perp2} = 0.5$. Plasma density computed by DyFK at $t \sim 17$ minutes at $r \sim 2000$ km is $n \sim 1\times10^9\ \text{m}^{-3}$ with $u_\parallel \sim 1-3\ \text{km}\cdot\text{s}^{-1}$ and $w_\parallel \leq 0.5$ eV. At $r \sim 2000$ km and $t = 4$ hours

Figure 3.15 denotes plasma densities $n \sim 1 \times 10^9$ m^{-3} with $u_\parallel \sim 0.5 - 0.8$ km $\cdot$ s^{-1} and $w_\parallel \sim 0.17$ eV.

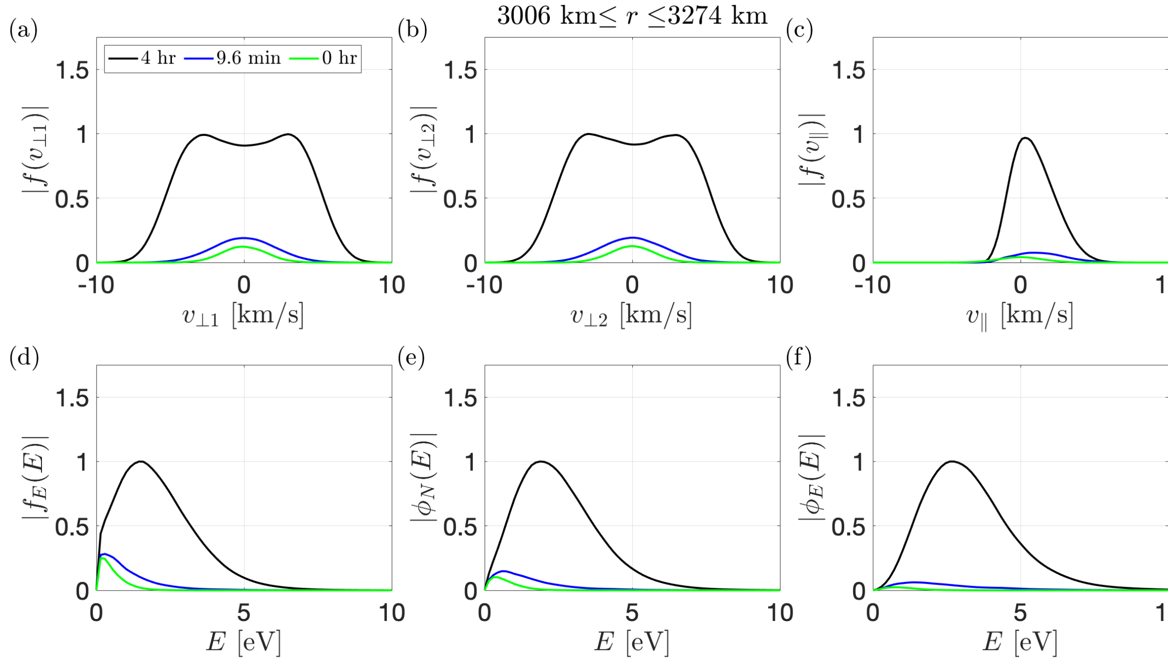

Figure 3.17: Normalized reduced ion distribution functions, $|f(v_{\perp 1})|$, $|f(v_{\perp 2})|$, and $|f(v_\parallel)|$, and normalized reduced energy-pitch-angle distribution functions, $|f_E(E)|$, and differential number and energy fluxes, $|\phi_N|$ and $|\phi_E|$, for ion cyclotron heating parameterization from [Zeng et al., 2006] and soft electron precipitation with $\delta T_e = 8.06$ K $\cdot$ s^{-1}.

Transverse thermal cores widen under stochastic wave heating exciting charge magnetic moments while perpendicular energy is converted to parallel energy via the mirror force. First adiabatic invariants are violated as both transverse directions are independently tracked for all macro-particles subject to velocity diffusion with Gaussian kick variances given by Equation 2.32. Relaxing magnetic moments convert wave energy to parallel energy to extend upward velocity tails of $|f(v_\parallel)|$ as seen in Figure 3.17. Early wave-induced ion outflow plume fronts are apparent at $t = 9.6$ minutes where plasma lifts from $r \sim 1000$ km and thermal distributions are energized significantly in the transverse directions as seen in Panels (a) and (b) of Figure 3.17 and Panels (a) and (b) of Figure 3.18. Ion velocity distributions recast into normalized energy-pitch-angle distributions, $|f_E(E)|$, differential number flux, $|\phi_N(E)|$, and differential energy flux, $|\phi_E(E)|$, as functions of total energy, E, as detailed in Appendix .8, are shown in Panels (d), (e), and (f) of Figure 3.17.

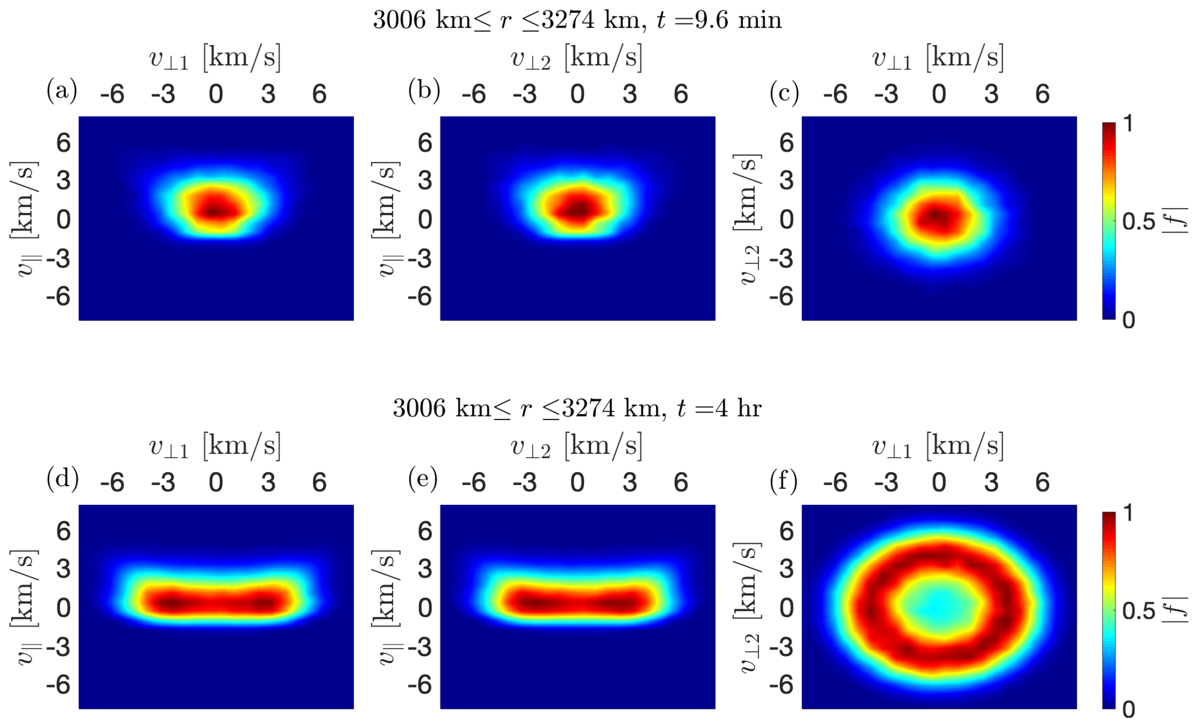

Figure 3.18: Normalized distribution functions in ($v_{\perp 1}$, $v_{\parallel}$), ($v_{\perp 2}$, $v_{\parallel}$), and ($v_{\perp 1}$, $v_{\perp 2}$) planes for altitude range 3006 km $\leq r \leq$ 3274 km at $t = 9.6$ minutes and $t = 4$ hours with ion cyclotron heating parameterization from [Zeng et al., 2006] and soft electron precipitation with $\delta T_e = 8.06$ $\mathrm{K \cdot s^{-1}}$.

During the early plume front at $t = 9.6$ minutes near $r \sim 3000$ km ion distribution transverse wings form and outwards diffusion occurs in the perpendicular plane. Conic distributions up to $E \sim 4$ eV peak near $\alpha \sim 45°$-$90°$ with strong upward components while energy decreases above $\alpha \sim 90°$. Low transverse velocity bins are vacated as thermal cores increase in energy and thermal populations $f(v_{\perp 1})$ and $f(v_{\perp 2})$ are split into bi-modal populations, seen in Panel (f) of Figure 3.18, defining the ion toroid cores in Panels (d) and (e) of Figure 3.18. Conics elevate into bowl distributions with altitude and detach from thermal cores to produce high-energy toroids, typically at the front of outflow plumes [Wu et al., 2002] [Brown et al., 1995]. Similarly, the initial outflow plume front at $t = 9.6$ minutes consists of conics which evolve into toroid distributions seen in Figure 3.18. Due to the variation of background and simulation parameters employed by the DyFK study of [Zeng et al., 2006] it would have to be verified that modeled energetics correspond to the outflow plume occurring at $t = 9.6$ minutes since conics typical of steady-state flows are shown in Figure 3.19.

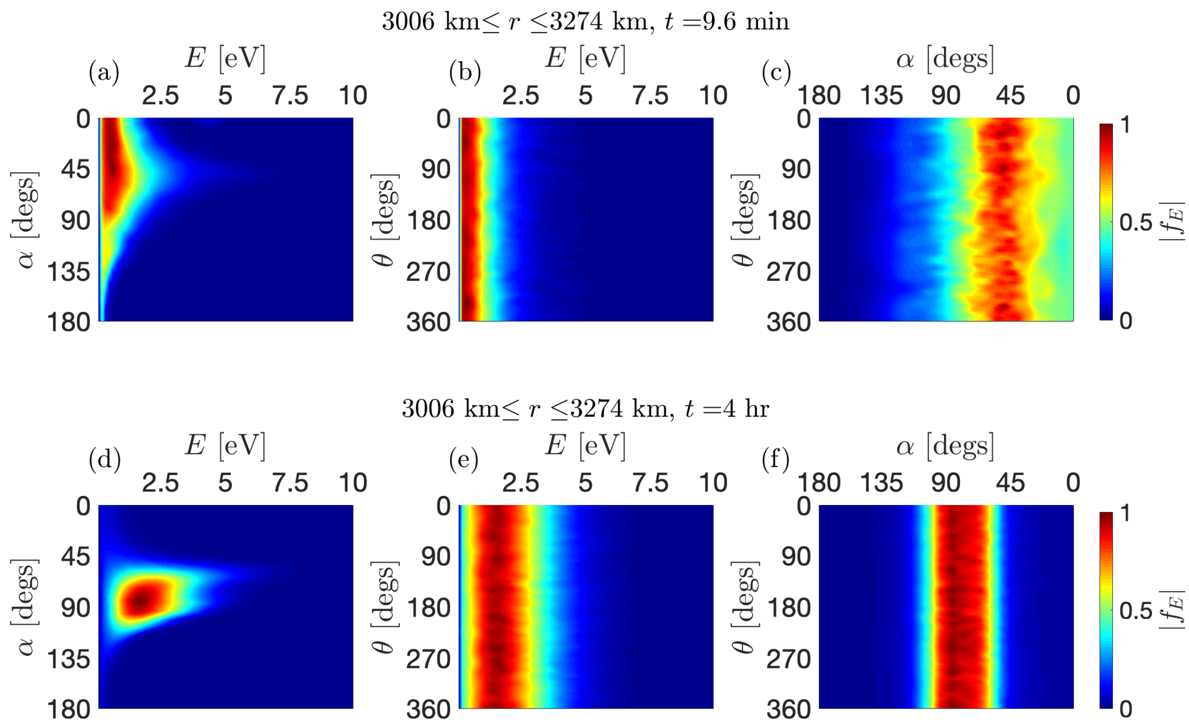

Figure 3.19: Normalized distribution functions in $(E,\ \alpha)$, $(E,\ \theta)$, and $(\alpha,\ \theta)$ planes for altitude range 3006 km $\leq r \leq$ 3274 km at $t = 9.6$ minutes and $t = 4$ hours with ion cyclotron heating parameterization from [Zeng et al., 2006] and soft electron precipitation with $\delta T_e = 8.06\ \mathrm{K} \cdot \mathrm{s}^{-1}$.

Low-energy thermal populations isotropic in α and θ subject to wave heating diffuse transversely and energize to outflows concentrated to $\alpha \sim 45°$-$100°$. Upwards (downwards) motion corresponds to $\alpha < 90°$ ($\alpha > 90°$). Initial thermal ions are uniformly distributed in α with preferential transverse orientation to $\alpha \sim 60°$ by the outflow plume front at $t = 9.6$ minutes. By $t = 4$ hours low-energy cores are hollowed and particles are focused between $E = 1$-4 eV at transverse values of $\alpha \sim 45°$-$100°$ to form rings and toroids of Panels (d), (e), and (f) of Figure 3.18. Three-dimensional velocity distribution functions, $f = f(v_{\perp 1},\ v_{\perp 2},\ v_{\parallel})$, reduced along two perpendicular planes in Panels (a) and (b) of Figure 3.17, are in agreement between 3014-3083 km with two-dimensional analogs of [Zeng et al., 2006] presented in Figure 3.20.

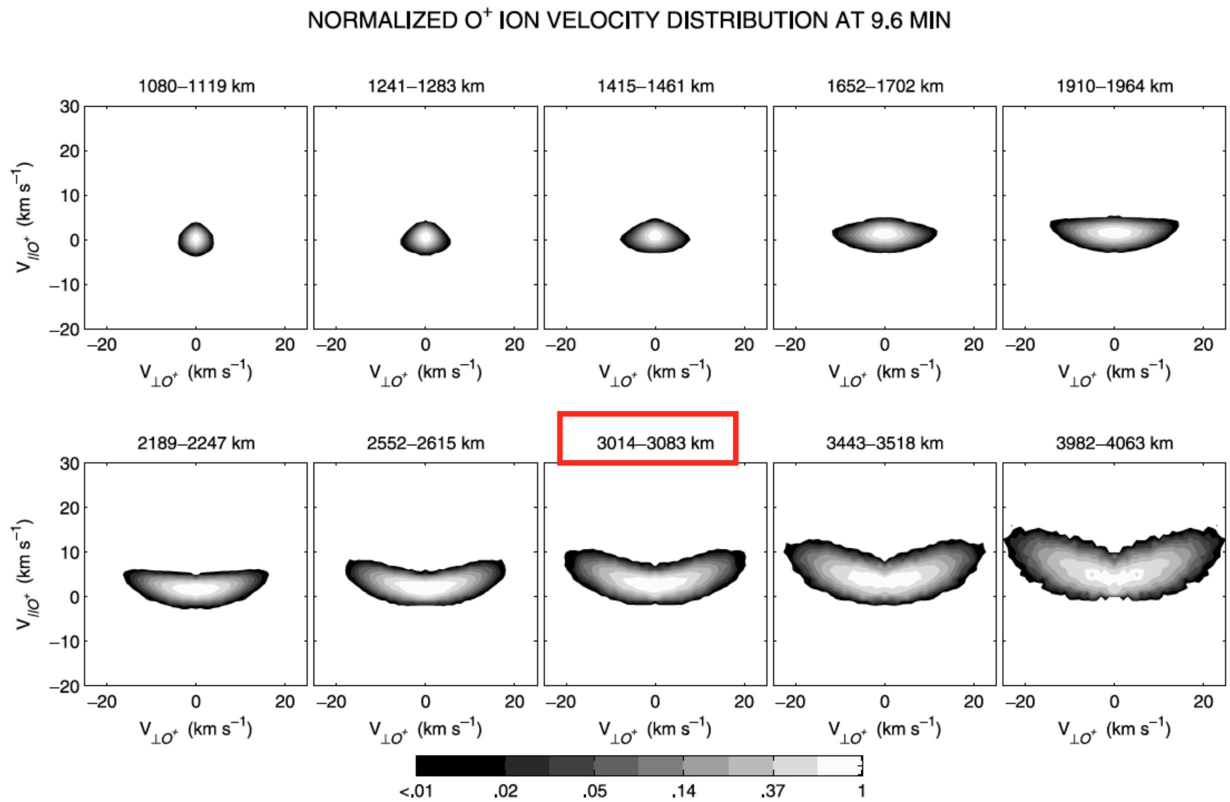

Figure 3.20: Normalized ion velocity distribution functions for the auroral event of wave-induced heating, soft electron precipitation and gravitational and ambipolar forces as modeled by DyFK [Zeng et al., 2006].

Outward field-aligned motion shifts zero-mean parallel velocity distributions positive as core energy populations shift toward $E \sim 2$ eV consistent with energy anisotropies at $r \sim 3000$ km seen in Figure 3.15. Wave-heated ions fill the flux-tube and overwhelm initial thermal populations until low-energy tails of energy distributions fall quickly below $E \sim 2$ eV as seen in Panel (d) of Figure 3.17. High-energy outflowing populations produce transversely bi-modal distributions over thermal background levels as seen in Panels (a) and (b) of Figure 3.17. Ions are uniformly distributed in gyro-angle in the absence of gyro-bunching effects due to transverse heating anisotropies (i.e., $\xi_{\perp 1} = \xi_{\perp 2}$). Ions populate $\alpha \sim 45°$-$70°$ during early plume expansion at $t = 9.6$ minutes and diffuse outwards in the transverse velocity plane such that core populations reside within $\alpha \sim 45°$-$100°$ by $t = 4$ hours as seen in Panel (c) and (f) of Figure 3.19. Gyro-tropic elevated conic distributions at $t = 9.6$ minutes transform into ring distributions with elevated wings at $t = 4$ hours as seen in Figure 3.18.

3.2.2 L-Shell Dependent Wave Heating

Two simulations are performed in this section to illustrate effects of different curved dipole magnetic field lines on wave-heated ion outflows. Two field lines are selected to emphasize the dependence of outflow energetics on L-shell simulated. Figure 3.21 depicts moments of the ion distribution function for a configuration-space binned along $L = 5\ R_E$. In contrast Figure 3.22 shows moments for $L = 15\ R_E$. Ion cyclotron wave heating is applied onto a system in kinetic equilibrium in the absence of electron precipitation and parallel potentials with reference wave spectral energy density $S_0 = 5 \times 10^{-7}\ \mathrm{V}^2 \cdot \mathrm{m}^{-2} \cdot \mathrm{Hz}^{-1}$ at reference gyro-frequency $f_{g0} = 6.5$ Hz at spectral index $\chi_\perp = 2.1$ with ion cyclotron resonance interaction time-step $h = 1.3$ seconds. Local O^+ gyro-frequency at $r \sim 14000$ km along $L = 15\ R_E$ is $f_g \sim 1.67$ Hz while $f_g \sim 1.32$ Hz corresponds to $r \sim 14000$ km along $L = 5\ R_E$. Accordingly, higher wave powers exist at $r \sim 14000$ km along $L = 5\ R_E$ for given reference wave power spectral density and frequency than at $r \sim 14000$ km along $L = 15\ R_E$.

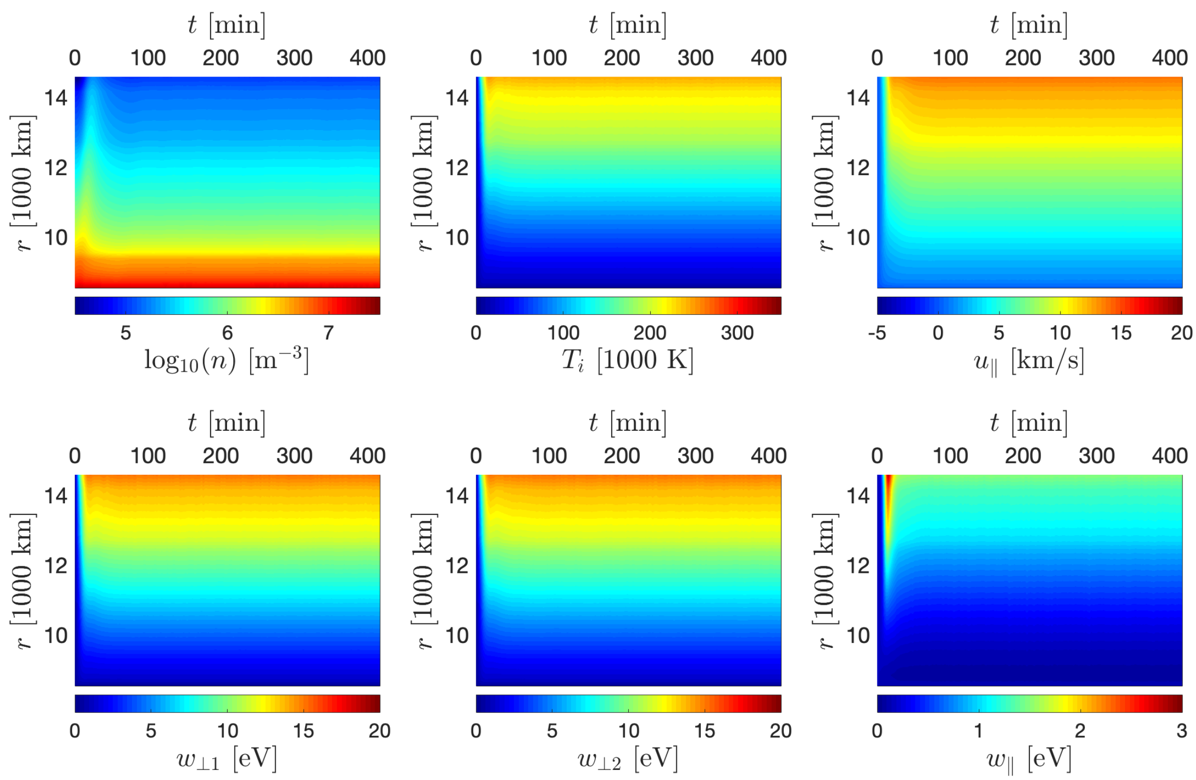

Figure 3.21: Plasma density, ion temperature, parallel plasma flow, and energies along $\hat{\mathbf{e}}_{\mathbf{v}_{\perp 1}}$, $\hat{\mathbf{e}}_{\mathbf{v}_{\perp 2}}$, and $\hat{\mathbf{e}}_{\mathbf{v}_\parallel}$ directions with high-altitude wave heating along $L = 5\ R_E$.

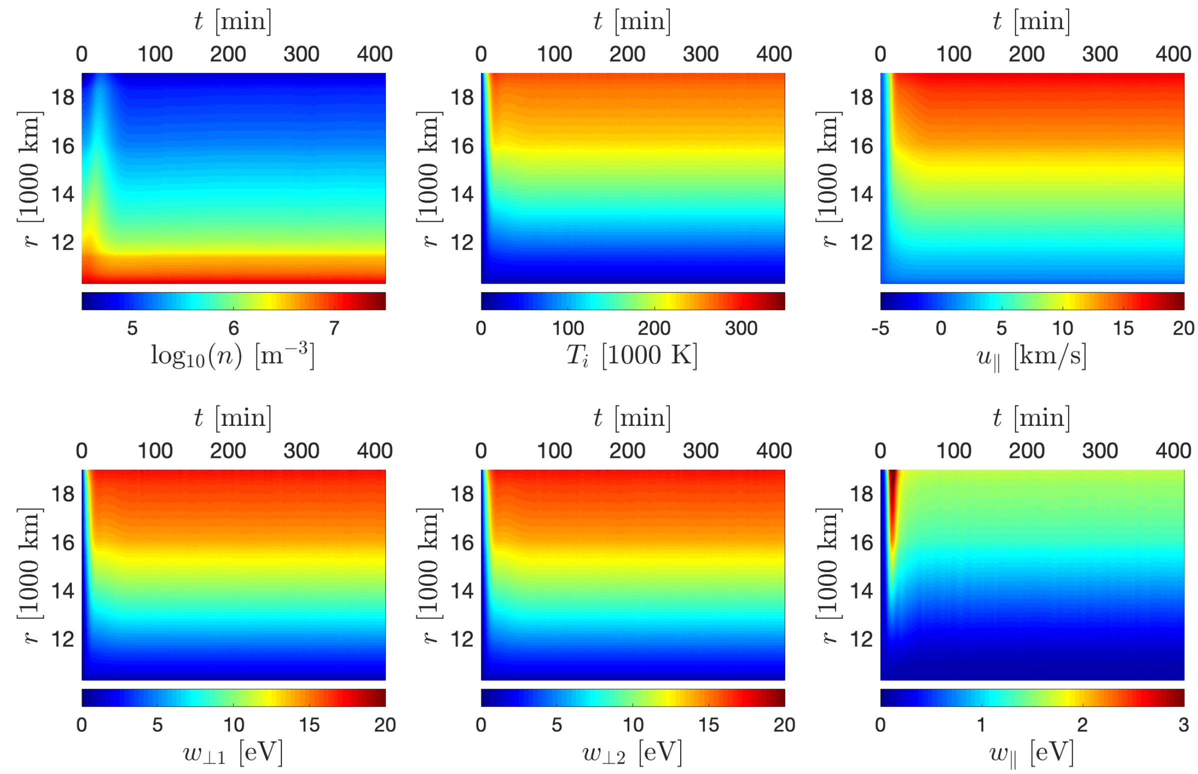

Figure 3.22: Plasma density, ion temperature, parallel plasma flow, and energies along $\hat{\mathbf{e}}_{\mathbf{v}_{\perp 1}}$, $\hat{\mathbf{e}}_{\mathbf{v}_{\perp 2}}$, and $\hat{\mathbf{e}}_{\mathbf{v}_\parallel}$ directions with high-altitude wave heating along $L = 15\ R_E$.

As seen from Figure 3.21 at $r \sim 14000$ km along $L = 5\ R_E$ the density is $n \sim 1 \times 10^{5.4}$ m^{-3} with ion temperature $T_i \sim 220000$ K, positive parallel drift near $u_\parallel \sim$ 11-12 km $\cdot$ s^{-1}, and total transverse energies $w_\perp = w_{\perp 1} + w_{\perp 2} \sim 24$ eV with parallel energies $w_\parallel \sim$ 1.3-1.5 eV. Figure 3.22 at $r \sim 14000$ km along $L = 15\ R_E$ denotes a density of $n \sim 1 \times 10^6$ m^{-3} with ion temperature $T_i \sim 200000$ K, positive parallel drift near $u_\parallel \sim$ 8-10 km $\cdot$ s^{-1}, and total transverse energies $w_\perp = w_{\perp 1} + w_{\perp 2} \sim$ 20-22 eV with parallel energies $w_\parallel \sim$ 0.8-1 eV. Magnetic field strengths at $r \sim 14000$ km along $L = 15\ R_E$ are greater than along $L = 5\ R_E$ such that gyro-frequencies are less for $L = 5\ R_E$ than for $L = 15\ R_E$; wave powers are greater for $L = 5\ R_E$ resulting in increased transverse and parallel energetics seen in moments of Figures 3.21 and 3.22.

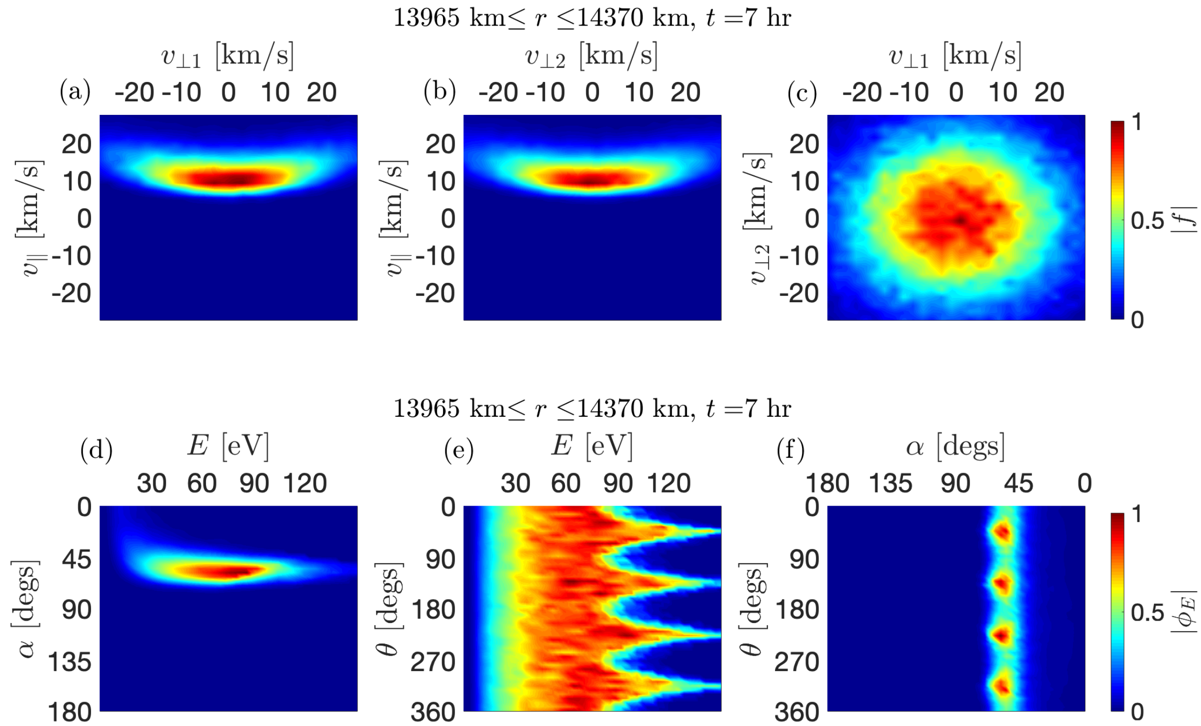

Figure 3.23: Normalized distribution functions in $(v_{\perp 1},\, v_{\parallel})$, $(v_{\perp 2},\, v_{\parallel})$, and $(v_{\perp 1},\, v_{\perp 2})$ planes at $t = 7$ hours in Panels (a), (b), and (c), and normalized differential energy flux, $|\phi_E|$, in $(E,\ \alpha)$, $(E,\ \theta)$, and $(\alpha,\ \theta)$ planes in Panels (d), (e), and (f) with high-altitude wave heating along $L = 5\ R_E$.

Increased wave powers at low O^+ gyro-frequencies at $r \sim 14000$ km along $L = 5\ R_E$ over the $L = 15\ R_E$ are apparent by levels of transverse energization of their distribution functions seen in Figures 3.23 and 3.24. For $L = 5\ R_E$ near $r \sim 14000$ km ion bowl distributions are deeper with greater elevated conic wings over $L = 15\ R_E$ owing to enhanced wave heating and more rapid adiabatic cooling rates. Ion populations congregate near $\alpha \sim 55°$-$60°$ for both cases with energy cores near $E \sim 50$-100 eV for $L = 5\ R_E$ and near $E \sim 30$-90 eV for $L = 15\ R_E$. Energies are isotropically distributed in gyro-angle, θ, such that all gyro-phases encounter particles from $E \sim 15$-150 eV for $L = 5\ R_E$ as seen in Panel (e) of Figure 3.23. Particles collect near $E \sim 10$-120 eV for $L = 15\ R_E$ as seen in Panel (e) of Figure 3.24. Two simulations performed in this section serve to quantify effects of curved dipole magnetic field approximations on wave-heated ion outflows. It is apparent that altering the L-shell to more severe values acts to increase the local magnetic field strength at a given altitude thus increasing the ion gyro-frequency and subjecting resonant particles to low-power waves. Effects of low versus high wave powers are apparent in moments for $L = 5\ R_E$ and $L = 15\ R_E$ seen in Figures 3.21 and 3.22, respectively. Normalized phase-space distribution functions and normalized differential energy fluxes are seen in Figures 3.23 and 3.24.

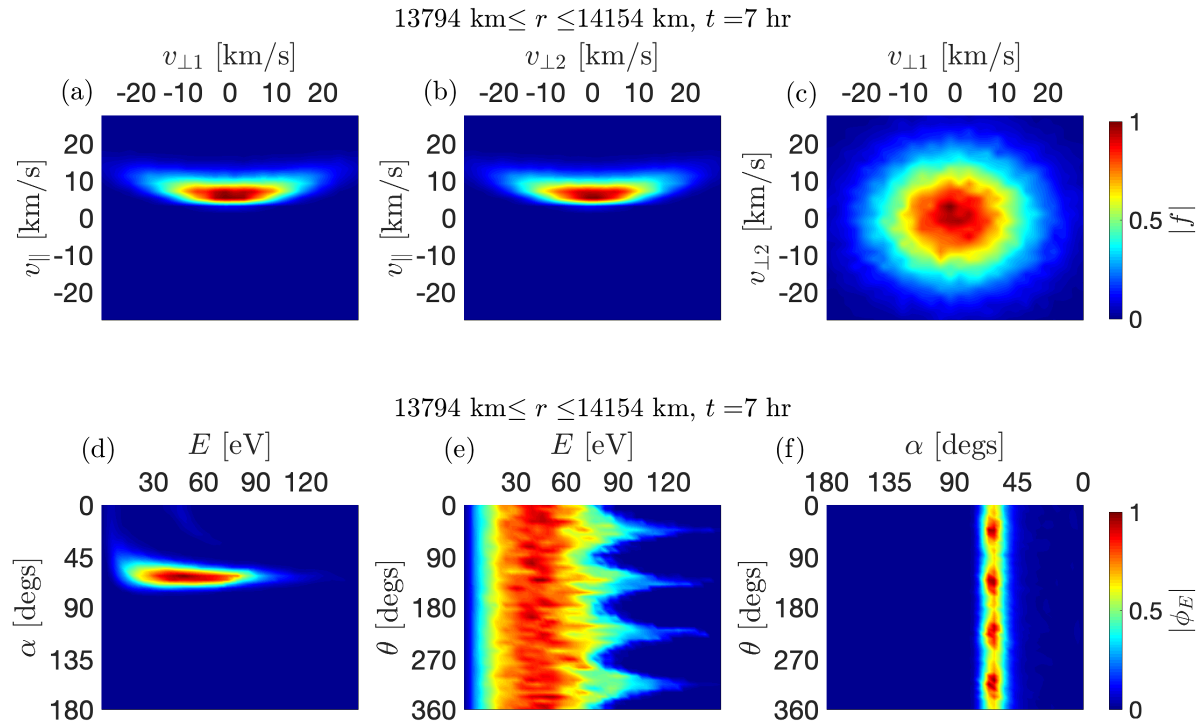

Figure 3.24: Normalized distribution functions in $(v_{\perp 1},\ v_{\parallel})$, $(v_{\perp 2},\ v_{\parallel})$, and $(v_{\perp 1},\ v_{\perp 2})$ planes at $t = 7$ hours in Panels (a), (b), and (c), and normalized differential energy flux, $|\phi_E|$, in $(E,\ \alpha)$, $(E,\ \theta)$, and $(\alpha,\ \theta)$ planes in Panels (d), (e), and (f) with high-altitude wave heating along $L = 15\ R_E$.

3.2.3 Wave Heating at Small Transverse Wavelengths

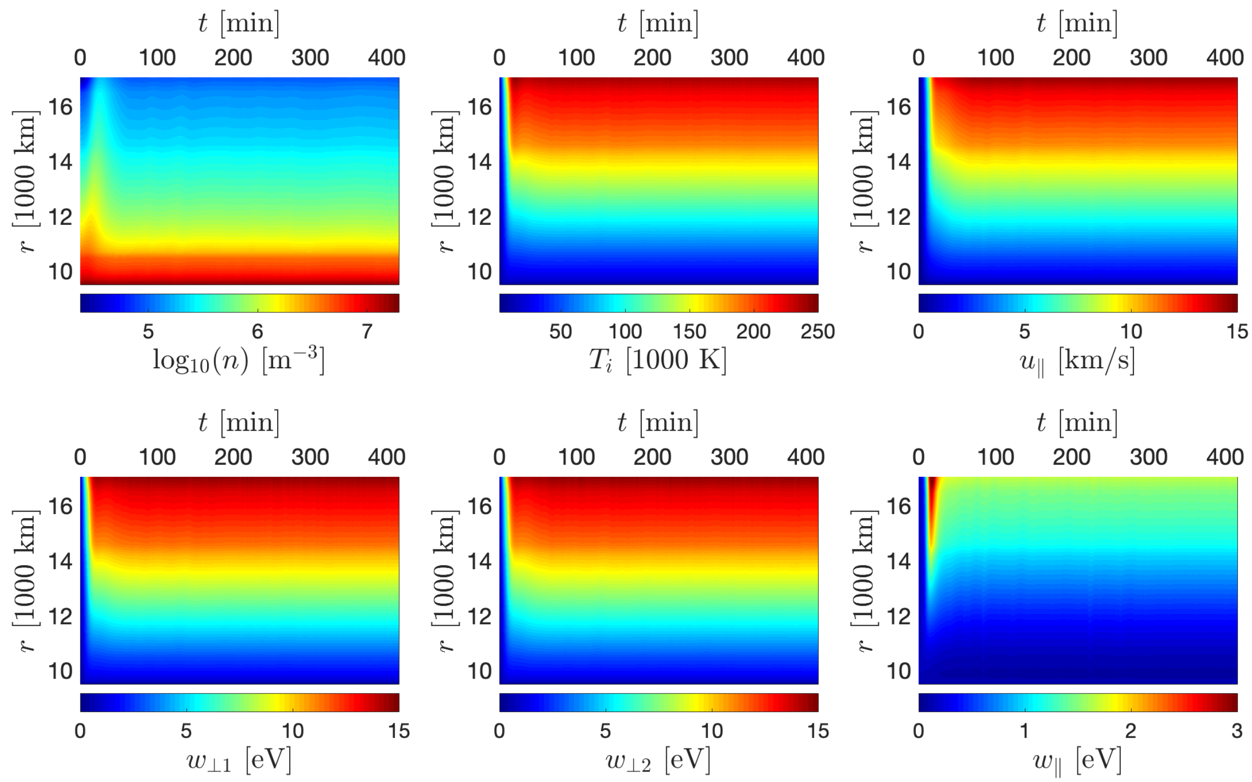

Figure 3.25: Plasma density, ion temperature, parallel plasma flow, and energies along $\hat{\mathbf{e}}_{\mathbf{v}_{\perp 1}}$, $\hat{\mathbf{e}}_{\mathbf{v}_{\perp 2}}$, and $\hat{\mathbf{e}}_{\mathbf{v}_\parallel}$ directions for high-altitude ion cyclotron wave-induced outflows with active ambipolar electric field and heating parameterization from [Barghouthi and Atout, 2006] with $\lambda_\perp = \infty$.

Particles are subject to high-powered wave heating at high altitude according to power law scaling of wave power spectral density, $S_\perp$, with gyro-frequency seen in transverse velocity diffusion coefficients of Equation 2.38. Transverse velocity kicks are governed by diffusion coefficients and ion cyclotron interaction times, $\tau_\perp$. For wave-particle resonance in a sufficiently narrow frequency band about the local gyro-frequency, Δf, $\tau_\perp$ assumes a value larger than the gyro-period. In the absence of further parameterization of $\tau_\perp$ it is assumed that the region of resonant wave power spectral components extends the computational flux-tube such that $\tau_\perp \gg h$ and $\Delta f \to 0$ and constraints on h imposed by $\tau_\perp$ are relaxed. Gaussian transverse velocity kicks on computational time-steps, h, along $\hat{\mathbf{e}}_{\perp 1}$ and $\hat{\mathbf{e}}_{\perp 2}$ directions are scaled to $\tau_\perp$ time-scales according to Equation 2.33. Wave spectra total energy density at reference power spectral density, S_0, reference gyro-frequency, ω_{g0}, and spectral index, $\chi_\perp$, increases at high-altitude via dependence of ω_g on field strength, $\mathbf{B}$.

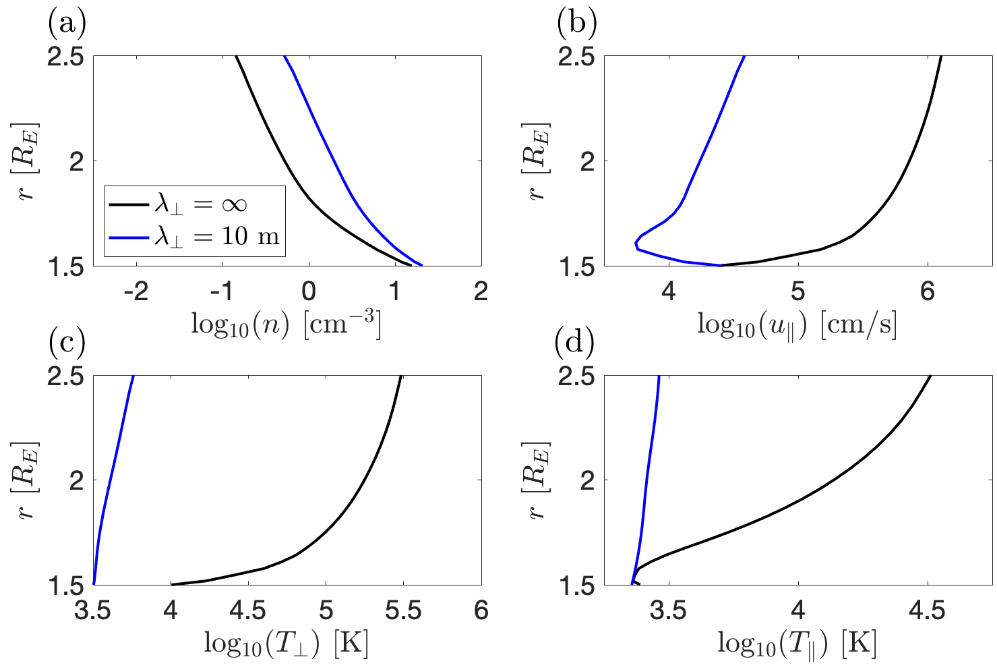

Figure 3.26: Plasma density, parallel plasma flow, and perpendicular and parallel temperatures for high-altitude ion cyclotron wave-induced outflows with active ambipolar electric field and heating parameterization from [Barghouthi and Atout, 2006] for $\lambda_\perp = \infty$ and $\lambda_\perp = 10$ m.

As particles are transversely energized to gyro-radii, $\rho_g = v_\perp / f_g$, greater than perpendicular wavelengths, $\lambda_\perp$, diffusion coefficient magnitudes decrease as $(\lambda_\perp/\rho_g)^3$ resulting in self-limited heating mechanisms of short-wavelength regimes of velocity-dependent ion cyclotron wave heating. Transverse velocity-dependent diffusion coefficients Equation 2.38 assume $\sigma_\perp = 1$ for long-wavelength approximations (i.e., $\lambda_\perp > \rho_g$). Between 1.5-2.5 R_E ion gyro-radii may exceed perpendicular wavelengths with sufficient transverse energization resulting in heating rate saturation. Characterization of $\lambda_\perp$ is primarily observational where short wavelengths that saturate heating rates to produce perpendicular energies associated with observed values are selected as values of $\lambda_\perp$ [Huddleston et al., 2000]. Long-wavelength wave-heated ions form elevated conics typical at high-altitude [Huddleston et al., 2000] [Winningham and Burch, 1984b] [Glocer et al., 2018] [Bouhram et al., 2003a] [Bouhram et al., 2003b] [Barakat and Barghouthi, 1994]. This section models two cases of Maxwellian plasmas in kinetic equilibrium subject to gravitational and active ambipolar forcing with finite gyro-radius wave heating pertaining to heating parameters employed by [Barghouthi and Atout, 2006].

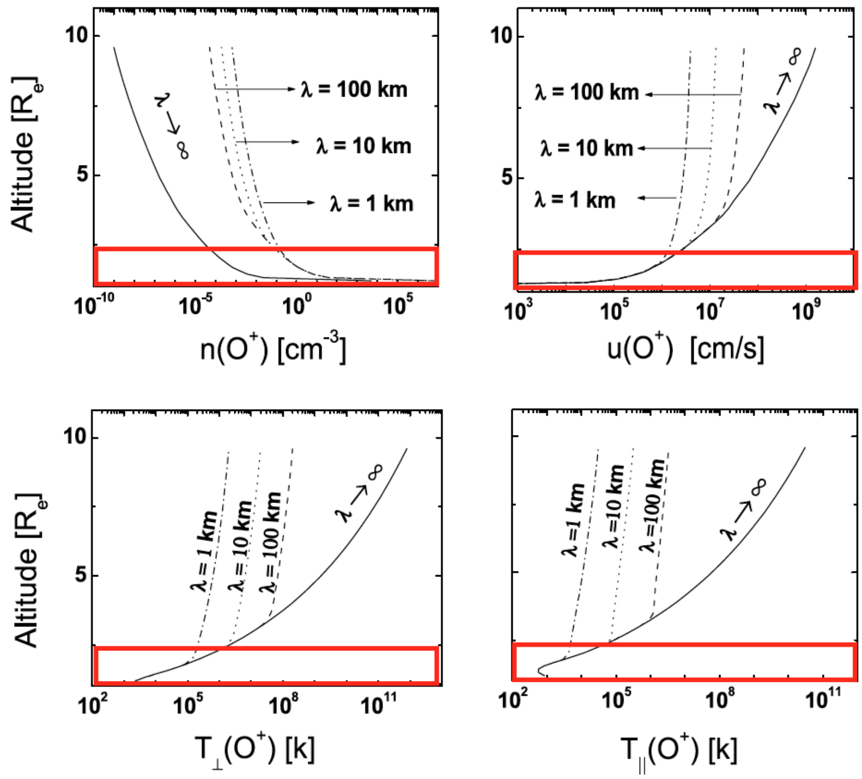

Figure 3.27: Plasma density, parallel flow, and perpendicular and parallel temperatures for finite gyro-radius wave-induced heating for $\lambda_\perp = \infty$, $\lambda_\perp = 100$ km, $\lambda_\perp = 10$ km, and $\lambda_\perp = 1$ km as modeled by [Barghouthi and Atout, 2006]. Red squares indicate regions of comparison.

It has been demonstrated by [Barghouthi and Atout, 2006] that characteristic electromagnetic turbulence wavelengths of $\lambda_\perp \sim 10$ km correspond to observed O^+ ion temperatures of 200 eV [Huddleston et al., 2000] at 4.8 R_E equator-ward of the cusp. Owing to linearity of $\rho_g \propto B^{-1}$ for constant $v_\perp$ and power law scaling of power spectral density with ω_g it is natural to assume wavelengths $\lambda_\perp < 10$ km heat ions at sufficiently low wave powers and/or altitudes. Short-wavelength regimes below $\lambda_\perp = 10$ km are explored in our study and used in conjunction with long-wavelength results of [Barghouthi and Atout, 2006]. Accommodation of background conditions and model parameters simulated by [Barghouthi and Atout, 2006] are secondary to finite gyro-radius wave heating effects. Short-wavelength ion energetics serve to characterize heated plasmas at low-altitudes or high-altitude regions of reduced resonant wave activity. Effects of finite gyro-radius are elucidated in contrast to long-wavelength approximations and implications of altitude constraints on $\lambda_\perp$ are discussed.

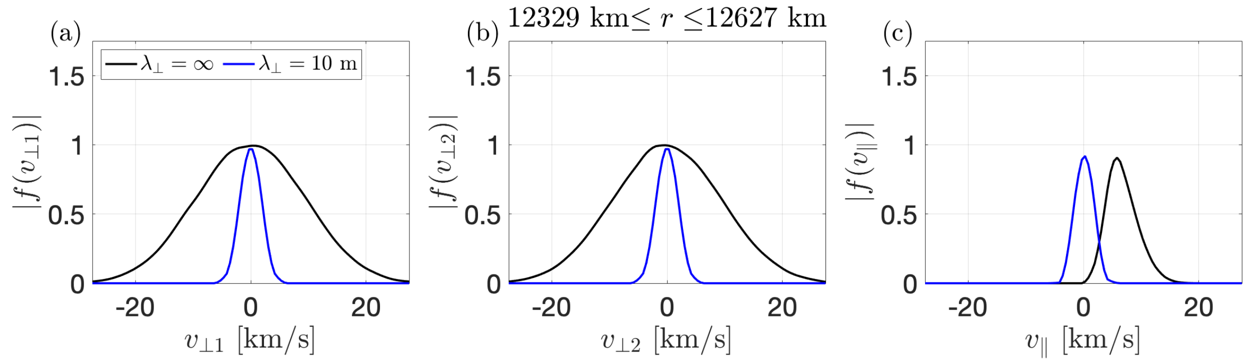

Figure 3.28: Normalized reduced ion distribution functions, $|f(v_{\perp 1})|$, $|f(v_{\perp 2})|$, and $|f(v_{\|})|$, for high-altitude ion cyclotron wave-induced outflows with active ambipolar electric field and heating parameterization from [Barghouthi and Atout, 2006] for $\lambda_\perp = \infty$ and $\lambda_\perp = 10$ m at $t = 7$ hours.

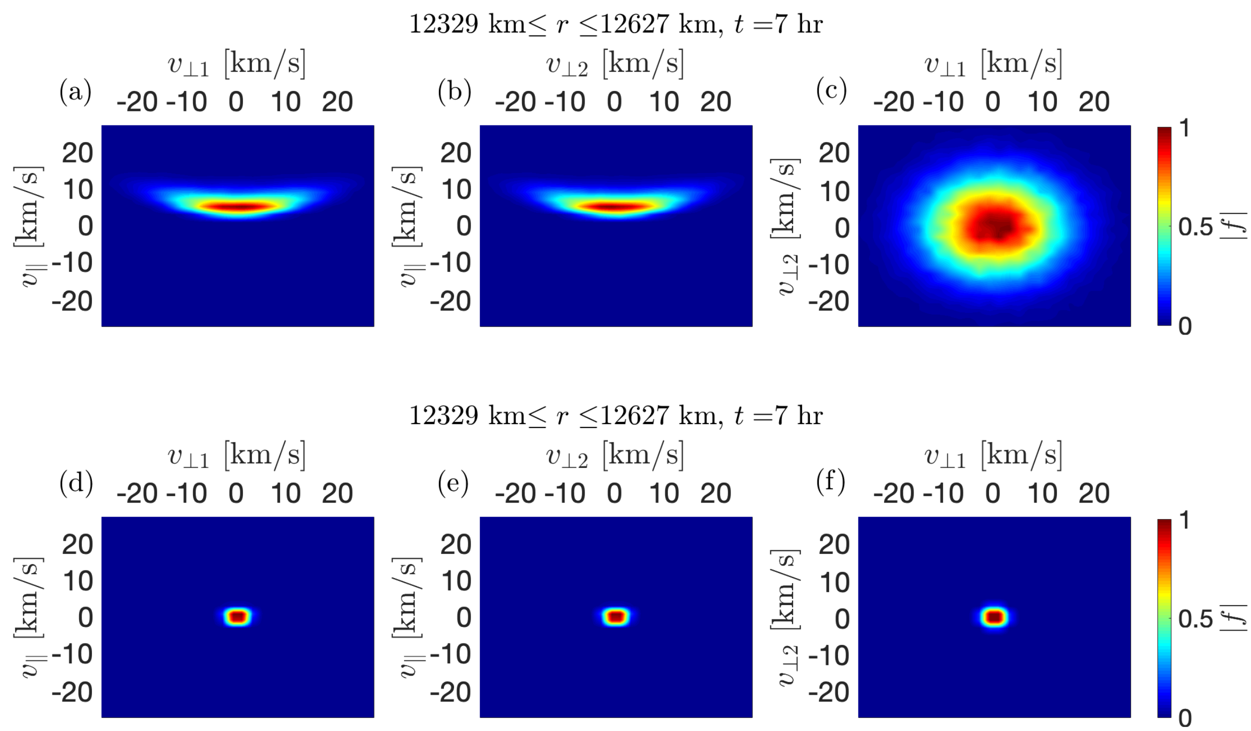

Figure 3.29: Normalized distribution functions in $(v_{\perp 1},\ v_{\|})$, $(v_{\perp 2},\ v_{\|})$, and $(v_{\perp 1},\ v_{\perp 2})$ planes for altitude range 12329 km $\leq r \leq$ 12627 km at $t = 7$ hours and velocity-dependent ion cyclotron resonance heating parameterization from [Barghouthi and Atout, 2006] for perpendicular wavelength $\lambda_\perp = \infty$ in Panels (a), (b), and (c) and $\lambda_\perp = 10$ m in Panels (d), (e), (f).

To characterize plasma responses to short and long-wavelength approximations of wave heating two cases are selected: $\lambda_\perp = \infty$ and $\lambda_\perp = 10$ m. Ion populations at $T_i = 2500$ K with reference density $n_0 = 1 \times 10^7$ m^{-3} at lower boundary altitude $r_0 = 9500$ km and electron temperature $T_e = 2500$ K are initialized in kinetic equilibrium along $L = 7.88\ R_E$. Plasmas extending larger altitude ranges relax into steady-state conditions over longer time-scales such that simulations run to seven hours ensure conditions representative of steady-state outflows. Heating conditions adopted from [Barghouthi and Atout, 2006] pertain to reference wave power spectral density $S_0 = 1.2\times10^{-6}$ $V^{-2} \cdot m^{-2} \cdot Hz^{-1}$ at reference gyro-frequency $f_{g0} = 5.6$ Hz, spectral index $\chi_{\perp1} = \chi_{\perp2} = 1.7$. $\eta_{LH} = 0.125$ [Chang and Crew, 1986] is the fraction of left-hand polarized wave power isotropically distributed in gyro-phase, θ, such that $\xi_{\perp1} = \xi_{\perp2} = 0.5$ in Equation 2.38.

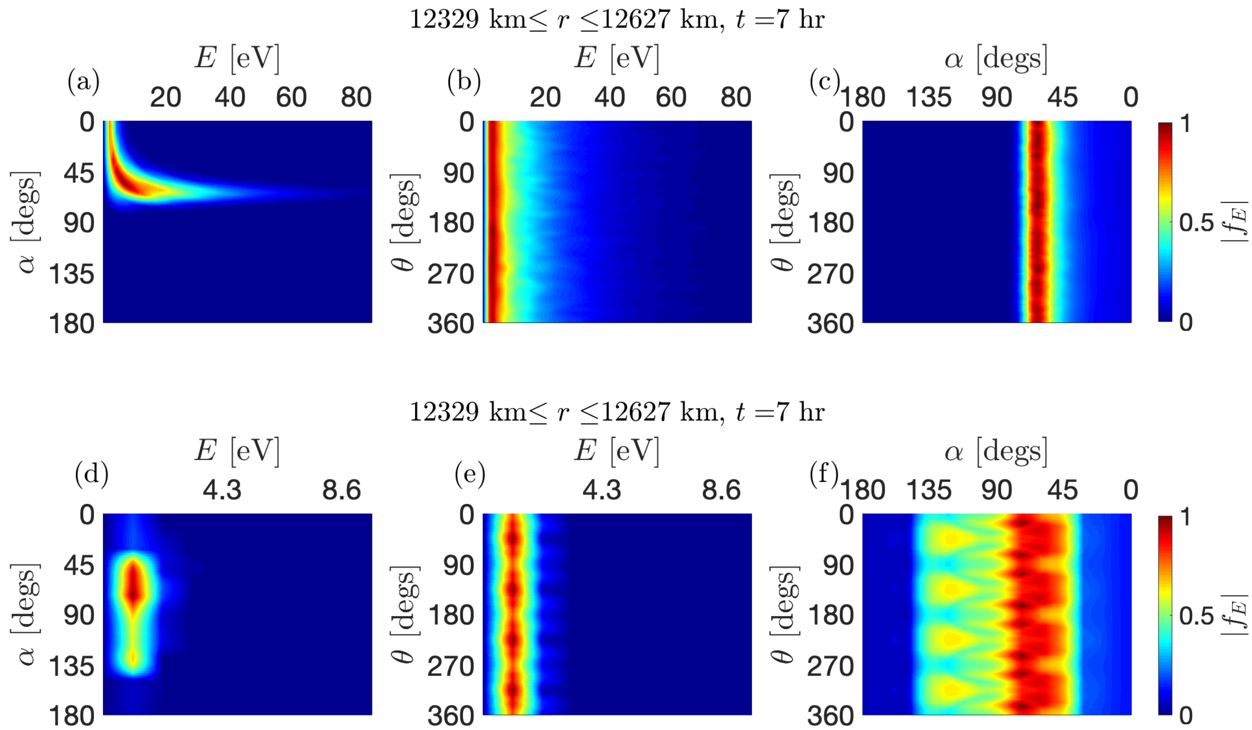

Figure 3.30: Normalized distribution functions in $(E,\ \alpha)$, $(E,\ \theta)$, and $(\alpha,\ \theta)$ planes for altitude range 12329 km $\leq r \leq$ 12627 km at $t = 7$ hours and velocity-dependent ion cyclotron resonance heating parameterization from [Barghouthi and Atout, 2006] for perpendicular wavelength $\lambda_\perp = \infty$ in Panels (a), (b), and (c) and $\lambda_\perp = 10$ m in Panels (d), (e), (f).

Moments are presented in Figure 3.25 for $\lambda_\perp = \infty$. As upward-flowing population densities exceed injection densities at the lower boundary upper boundary escape fluxes are enhanced above $r \sim 10000$ km. Transverse energy is converted to parallel energy via ion magnetic moment adiabatic cooling while perpendicular energies exceed parallel energies by $\sim$ 10 eV. According to Figure 3.26 which contrasts $\lambda_\perp = \infty$ and $\lambda_\perp = 10$ m cases less plasma is evacuated at mid-altitudes of the domain through the upper boundary for $\lambda_\perp = 10$ m since upward wave-heated flux is comparable to lower boundary thermal flux. Transverse wave energizations account for field-aligned drifts of $u_\parallel \sim 10$ km $\cdot$ s^{-1} and $u_\parallel \sim 0.3$ km $\cdot$ s^{-1} for $\lambda_\perp = \infty$ and $\lambda_\perp = 10$ m cases, respectively, as seen in Panel (b) of Figure 3.26. Perpendicular temperatures for $\lambda_\perp = \infty$ exceed those of $\lambda_\perp = 10$ m by over sixty times and parallel temperatures are in excess by an order of magnitude. Relative transverse energization levels of $\lambda_\perp = \infty$ and $\lambda_\perp = 10$ m wave-heated plasmas are suitable representatives of conditions modeled by [Barghouthi and Atout, 2006] in Figure 3.27.

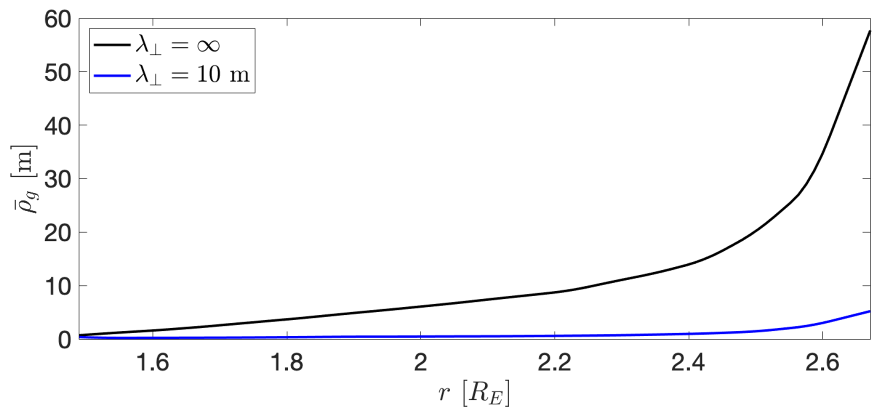

Figure 3.31: Mean ion gyro-radii, $\bar{\rho}_g$, computed from perpendicular ion velocity moments as a function of altitude, r, for velocity-dependent transverse diffusion of wave-heated ions with perpendicular wavelength cases $\lambda_\perp = \infty$ and $\lambda_\perp = 10$ m.

Energies remain isotropic in gyro-phase and transverse energizations are significantly higher for $\lambda_\perp = \infty$ than for $\lambda_\perp = 10$ m as seen in Figure 3.29. Pitch-angle distributions concentrate near $\alpha \sim 60°$ for both cases with extended energy tails to $E \sim 80$ eV for $\lambda_\perp = \infty$. Ions do not receive adequate energy transfer via magnetic moments to populate low pitch-angles and contribute to energized ion outflows for $\lambda_\perp = 10$ m. Parallel flows tend outward from counter-streaming thermal populations for $\lambda_\perp = 10$ m as seen in the Panel (d) of Figure 3.30 and Panel (c) of Figure 3.28. Transverse components remain nearly thermal for $\lambda_\perp = 10$ m as seen in Panels (a) and (b) in Figure 3.28 while the transverse tails broaden and parallel flows shift towards $+v_\parallel$ for $\lambda_\perp = \infty$.

Significant reduction in transferrable wave power occurs for transverse wavelengths less than the gyro-radius. For conditions simulated in absence of velocity-dependent diffusion coefficients ions are energized until mean gyro-radii computed from perpendicular ion velocity moments $\bar{\rho}_g \geq 50$ m for $\lambda_\perp = \infty$. Figure 3.31 demonstrates that $\bar{\rho}_g \leq 10$ m for $\lambda_\perp = 10$ m. Since $\bar{\rho}_g \sim 55$ m for $\lambda_\perp = \infty$ reducing to $\lambda_\perp = 10$ m sets an upper limit on mean gyro-radii before transverse heating rate saturation. $\bar{\rho}_g = \lambda_\perp = 10$ m gyro-radii at $r \sim 12476$ km correspond to $f_g = 1.945$ Hz and $v_\perp = 19.45$ km $\cdot$ s^{-1}. Consistent with reduced transverse distribution functions of Panels (a) and (b) in Figure 3.28 ions are energized until $\bar{\rho}_g$ exceeds $\lambda_\perp$ near $v_\perp \sim 19.45$ km $\cdot$ s^{-1} for $r \sim 12476$ km. Although wave intensity is known to vary along and across field lines information on wave power variations in space and time is limited and constraints on $\lambda_\perp$ are empirically established by observations [Wu et al., 2002] [Huddleston et al., 2000] [Winningham and Burch, 1984b]. Constraints on wave powers, resonance interaction times, and perpendicular wavelengths are central to properly parameterized sources of ion cyclotron resonance heating.

3.2.4 Pressure Cookers

Evolution of plasmas in kinetic equilibrium subject to gravitational and active ambipolar forcing, diverging magnetic field lines, with parameterized sources of ion cyclotron resonance heating have thus far been considered. Responses of self-limited wave heating mechanisms in short-wavelength approximations have been modeled and discussed. In this section a downwards parallel electric field is introduced to the flux-tube as a pressure cooker environment where wave-heated ions are continuously spread in altitude according to parallel energy and ability to overcome reflection by the potential barrier.

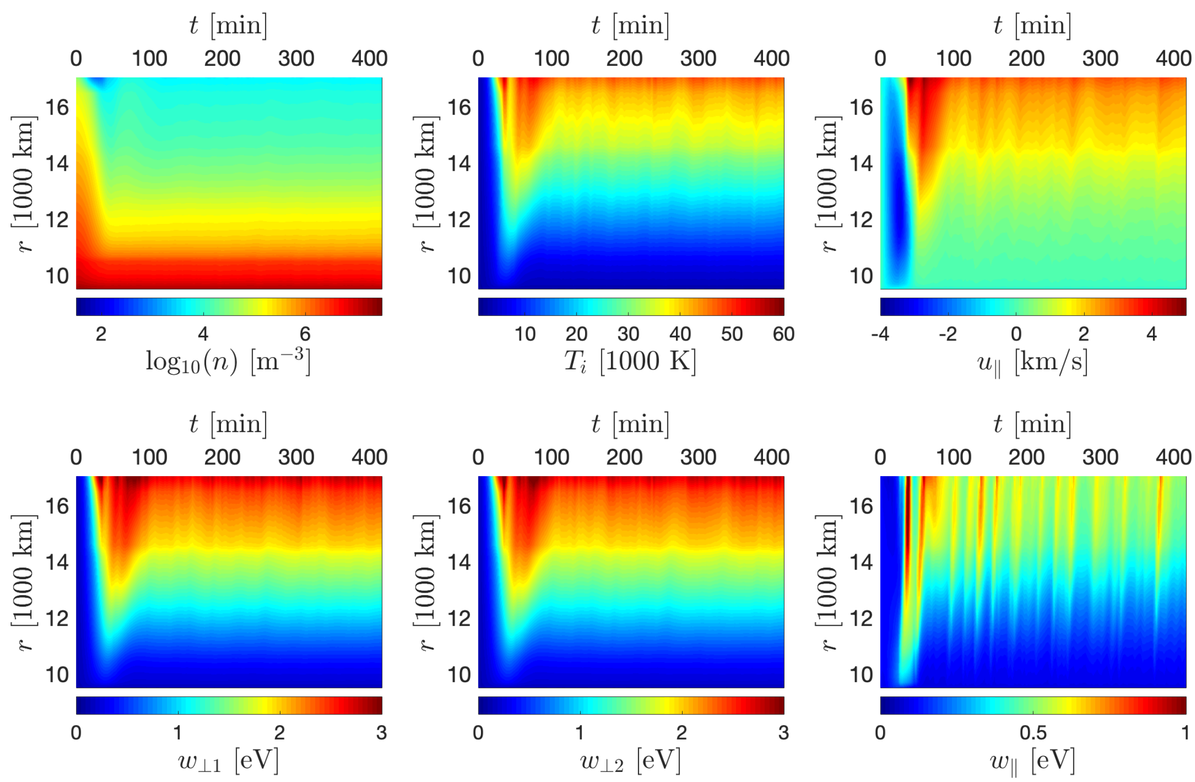

Figure 3.32: Plasma density, ion temperature, parallel plasma flow, and energies along $\hat{\mathbf{e}}_{\mathbf{v}_{\perp 1}}$, $\hat{\mathbf{e}}_{\mathbf{v}_{\perp 2}}$, and $\hat{\mathbf{e}}_{\mathbf{v}_{\parallel}}$ directions for high-altitude pressure cooker cases with active ambipolar electric field and heating parameterization from [Wu et al., 2002] with $E_{\parallel 0} = 5 \times 10^{-7}$ V $\cdot$ m^{-1} for interaction time-step $h = 2.5$ seconds.

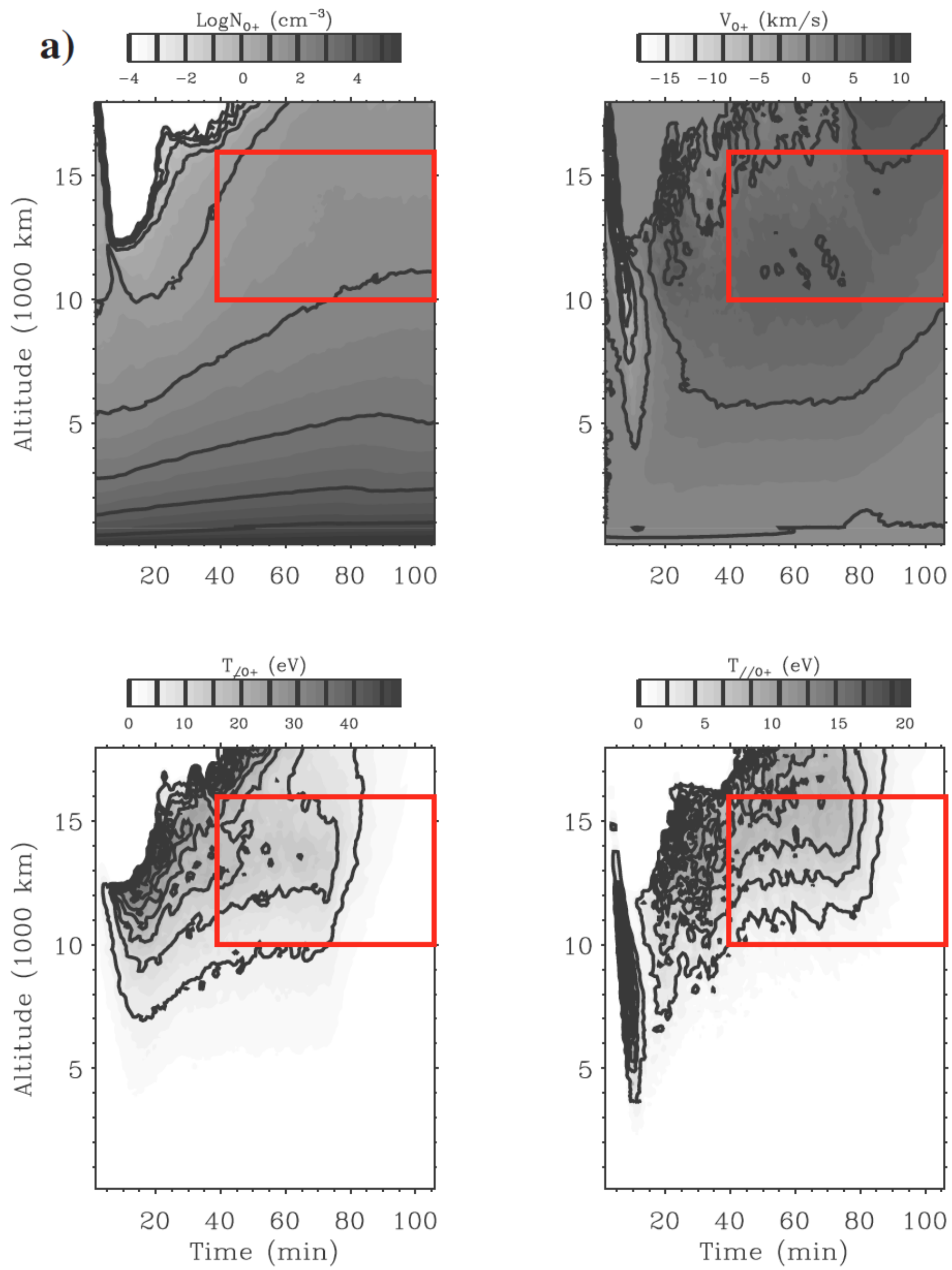

Figure 3.33: Plasma density, parallel drift, and ion energies for pressure cookers with self-consistently computed parallel electric fields and wave-induced particle heating as modeled by DyFK by [Wu et al., 2002]. Red squares indicate regions of comparison.

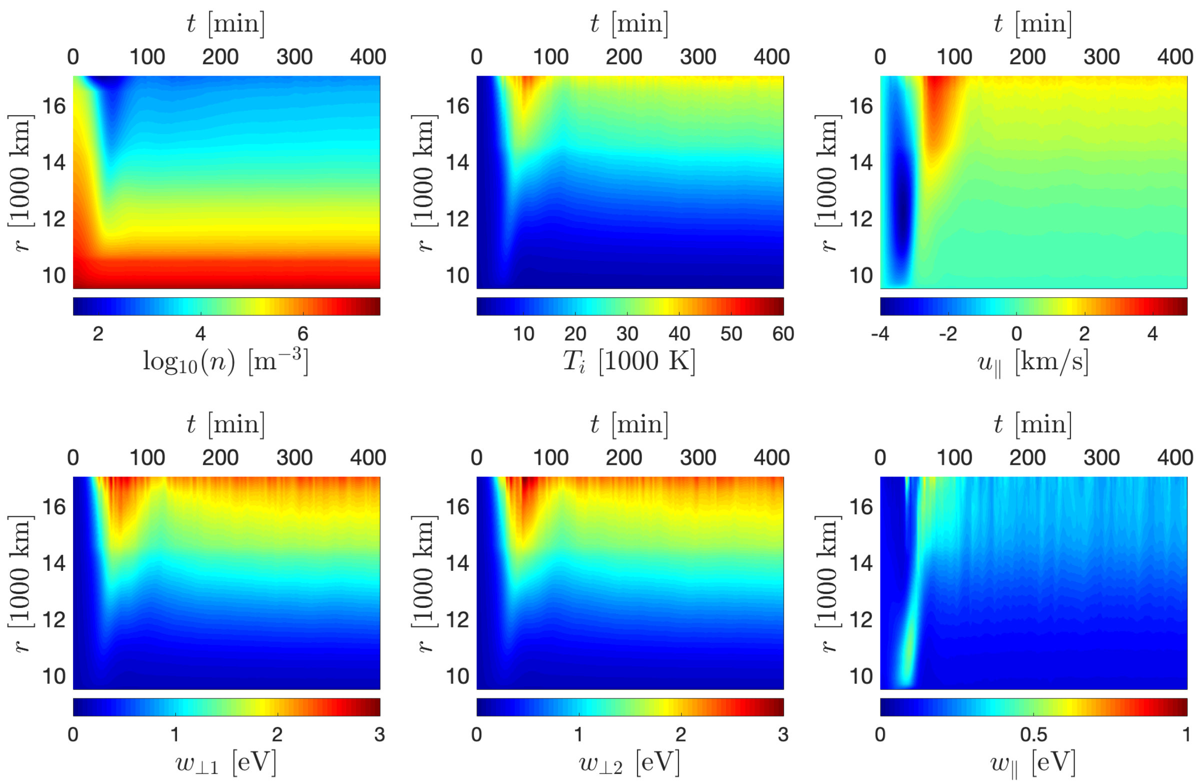

Figure 3.34: Plasma density, ion temperature, parallel plasma flow, and energies along $\hat{\mathbf{e}}_{\mathbf{v}_{\perp 1}}$, $\hat{\mathbf{e}}_{\mathbf{v}_{\perp 2}}$, and $\hat{\mathbf{e}}_{\mathbf{v}_{\parallel}}$ directions for high-altitude pressure cooker cases with active ambipolar electric field and heating parameterization from [Wu et al., 2002] with $E_{\|0} = 5 \times 10^{-7}$ V $\cdot$ m^{-1} for interaction time-step $h = 0.84$ seconds.

Several studies exist to investigate the ability of pressure cookers to bring wave-heated ions to low altitude by downward parallel electric fields [Bouhram et al., 2003a] [Bouhram et al., 2003b] [Wu et al., 2002]. Potential barriers in pressure cooker ion traps have the ability to produce observed conic and bowl distributions of few hundred eV in the absence of high-power resonant waves; high-altitude energized conics are pushed downward by parallel electric fields to observed low wave-power altitudes [Wu et al., 2002] [Jasperse, 1998] [Gorney et al., 1985]. Electron and ion temperature anisotropies give rise to the differential anisotropy ratio (DAR) as defined in [Brown et al., 1995], where values of DAR $>$ 1 (DAR $<$ 1) correspond to downward (upward) electric fields. In absence of constraints on potential drop ad hoc non-localized electrostatic barriers with potential energy profiles comparable to outflowing parallel energies are applied across magnetic flux-tubes in what follows.

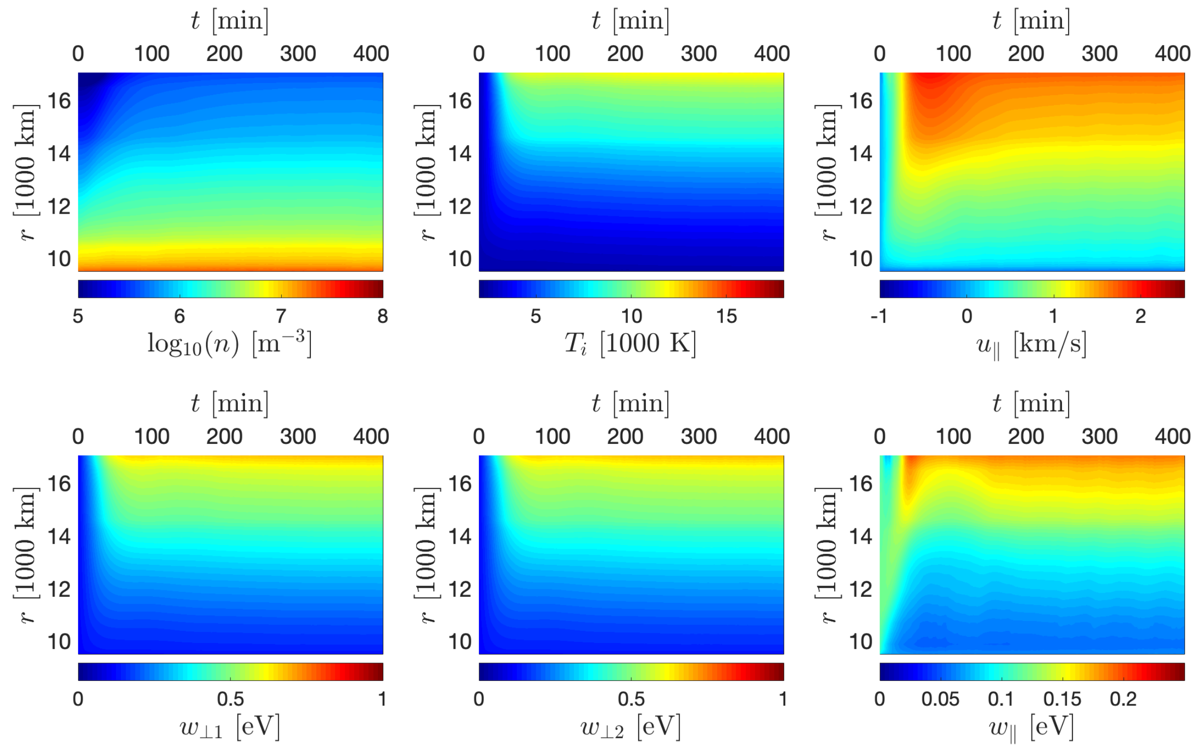

Figure 3.35: Plasma density, ion temperature, parallel plasma flow, and energies along $\hat{\mathbf{e}}_{\mathbf{v}_{\perp 1}}$, $\hat{\mathbf{e}}_{\mathbf{v}_{\perp 2}}$, and $\hat{\mathbf{e}}_{\mathbf{v}_{\parallel}}$ directions for high-altitude pressure cooker cases with active ambipolar electric field and heating parameterization from [Wu et al., 2002] with $E_{\parallel 0} = 0 \text{ V} \cdot \text{m}^{-1}$ for interaction time-step $h = 0.84$ seconds.

Figure 3.33 denotes moments of wave-heated plasmas subject to downward parallel electric fields self-consistently computed from DAR values modeled in DyFK by [Wu et al., 2002]. Consistent with pressure cookers modeled in Figure 3.32 plasma densities reaches $n \sim 1 \times 10^5 \text{ m}^{-3}$ with counter-streaming flows within $\sim 5 \text{ km} \cdot \text{s}^{-1}$ as seen in Figure 3.33. Since computational domain of [Wu et al., 2002] covers greater altitude range than modeled here pressure cookers produce low-altitude ion conics consisting of particles unable to escape the ion trap with transverse energies typical of high-altitude regions of increased wave power at low frequencies. Maximum energetics at $t \sim$ 40-60 minutes are seen in Figure 3.33 which coincide with downward energetic plumes at $t \sim 40$ minutes seen in Figure 3.34. Owing to higher altitude ranges modeled and self-consistent localized parallel potential drops, which increase at high altitude as a hard reflection points for outflowing ions, the perpendicular energies of [Wu et al., 2002] exceed those of this study by several eV. Modulation of parallel potential profiles in altitude by ion observations and/or varying reference electric field values cause variations in ion temperature, particularly in the transverse plane due to ion trap wave heating.

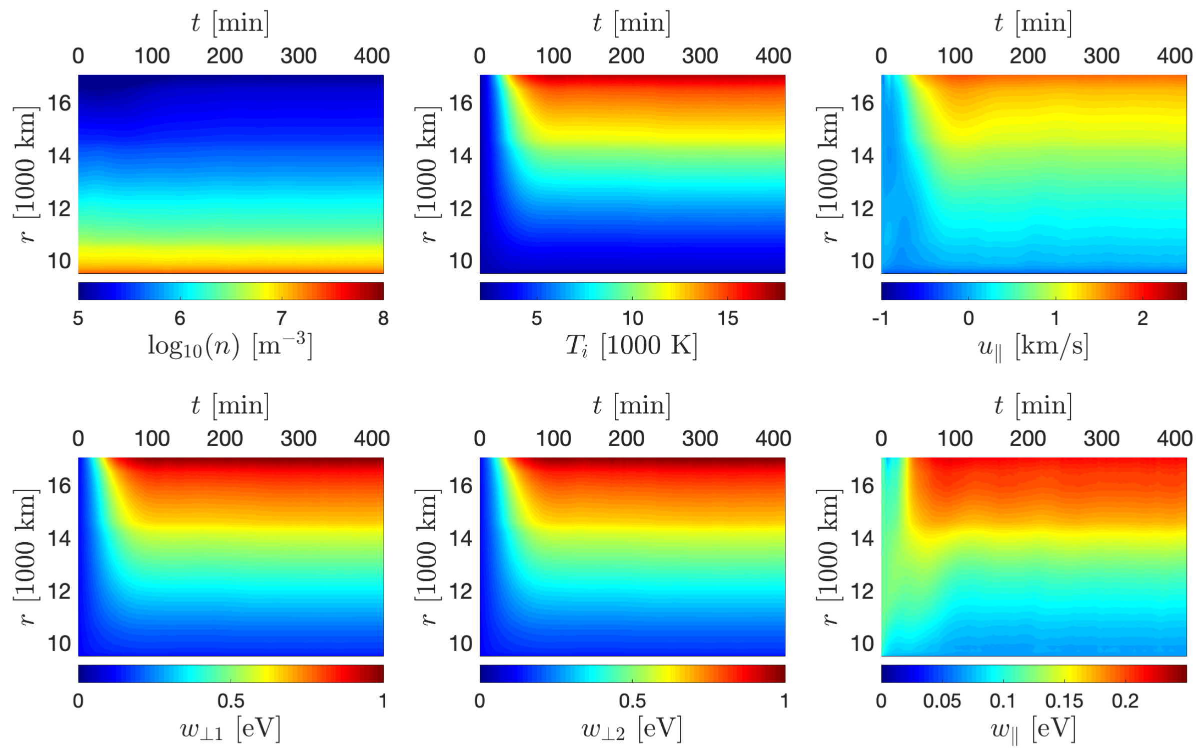

Figure 3.36: Plasma density, ion temperature, parallel plasma flow, and energies along $\hat{\mathbf{e}}_{\mathbf{v}_{\perp 1}}$, $\hat{\mathbf{e}}_{\mathbf{v}_{\perp 2}}$, and $\hat{\mathbf{e}}_{\mathbf{v}_{\parallel}}$ directions for high-altitude pressure cooker cases with active ambipolar electric field and heating parameterization from [Wu et al., 2002] with $E_{\parallel 0} = 1 \times 10^{-7}$ V $\cdot$ m^{-1} for interaction time-step $h = 0.84$ seconds.

Computational time-step employed by DyFK in [Wu et al., 2002] is selected to be less than local mean collision and ion gyro-periods, that is, in the range of $h \sim 0.5$-4 seconds for O^+ ions from 800 km to 3 R_E [Wu et al., 1999]. Since particles experience two-dimensional perpendicular velocity kicks of magnitude proportional to the ratio of computational time-step, h, to resonance interaction time, $\tau_{\perp}$, the degree of transverse heating depends on the proper parameterization of $\tau_{\perp}$ and selection of interaction time-step, h. For direct comparison to kinetic time-scales modeled by DyFK in [Wu et al., 1999] and [Wu et al., 2002] a pressure cooker scenario with $E_{\parallel 0} = 5 \times 10^{-7}$ V $\cdot$ m^{-1} is generated as seen in Figure 3.32 for computational time-step $h = 2.5$ seconds as opposed to $h = 0.84$ second for Figure 3.34. Greater computational interaction time-steps result in enhanced wave-heated ion outflows according to Equation 2.33. Constraints on wave power localization in space and time and interaction time-steps are lax ($h < \tau_{\perp}$) according to observations [Wu et al., 1999] [Wu et al., 2002] [Huddleston et al., 2000] [Winningham and Burch, 1984b]. Total thermal ion energy is $w_{\perp} = w_{\perp 1} + w_{\perp 2} \sim 5$ eV at $r \sim 15000$ km per Figure 3.32 in agreement with transverse energies of Figure 3.33 considering enhanced pressure cooker transverse energization levels by the self-consistently localized potential barrier computed by [Wu et al., 2002].

Parallel energies exceed the case of Figure 3.32 by several eV due to enhanced ambipolar forcing by soft auroral electron precipitation. With $h = 2.5$ seconds the perpendicular energies of Figure 3.32 exceed those of $h = 0.84$ seconds in Figure 3.34 by $\sim$ 0.5 eV. Given open parameter space of ion cyclotron resonance region interaction time-step, h, and transverse BBELF wavelengths, $\lambda_\perp$, qualitative features of ionospheric outflows in what follows are characterized by variations of reference parallel electric fields, $E_{\|0}$, for $h = 0.84$ seconds and $\lambda_\perp = \infty$.

Plasmas are initialized in kinetic equilibrium for reference density $n_0 = 1 \times 10^7$ m^{-3} at lower boundary altitude $r_0 = 9500$ km, initial ion temperature $T_i = 2500$ K, and electron temperature $T_e = 2500$ K along $L = 7.88$ R_E. Ions are heated with reference wave power spectral density $S_0 = 1 \times 10^{-8}$ V$^2 \cdot$ m$^{-2} \cdot$ Hz^{-1} at reference frequency $f_{g0} = 6.5$ Hz, and spectral index $\chi_{\perp 1} = \chi_{\perp 2} = 1.7$. $\eta_{LH} = 0.125$ [Chang and Crew, 1986] is the fraction of left-hand polarized wave power isotropically distributed in gyro-phase (i.e., $\xi_{\perp 1} = \xi_{\perp 2} = 0.5$) and the long-wavelength limit is assumed such that $\lambda_\perp = \infty$. Three simulations are presented with potential barriers corresponding to reference potential electric fields $E_{\|0} = 0$ V $\cdot$ m^{-1}, $E_{\|0} = 1 \times 10^{-7}$ V $\cdot$ m^{-1}, and $E_{\|0} = 5 \times 10^{-7}$ V $\cdot$ m^{-1} with sources of ion cyclotron resonance heating parameterized by [Wu et al., 2002]. Soft electron precipitation with Maxwellian electron distribution peaks at 100 eV with energy fluxes of 3 erg $\cdot$ cm$^{-2} \cdot$ s^{-1} at 800 km altitude is included in [Wu et al., 2002] results in a feature absent in our study.

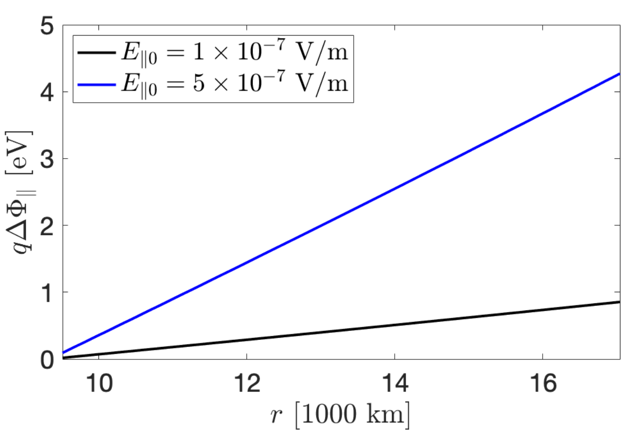

Figure 3.37: Potential energy drops in altitude for pressure cooker simulations with heating parameterization from [Wu et al., 2002] and reference parallel electric fields $E_{\|0} = 1 \times 10^{-7}$ V $\cdot$ m^{-1} and $E_{\|0} = 5 \times 10^{-7}$ V $\cdot$ m^{-1} for interaction time-step $h = 0.84$ seconds.

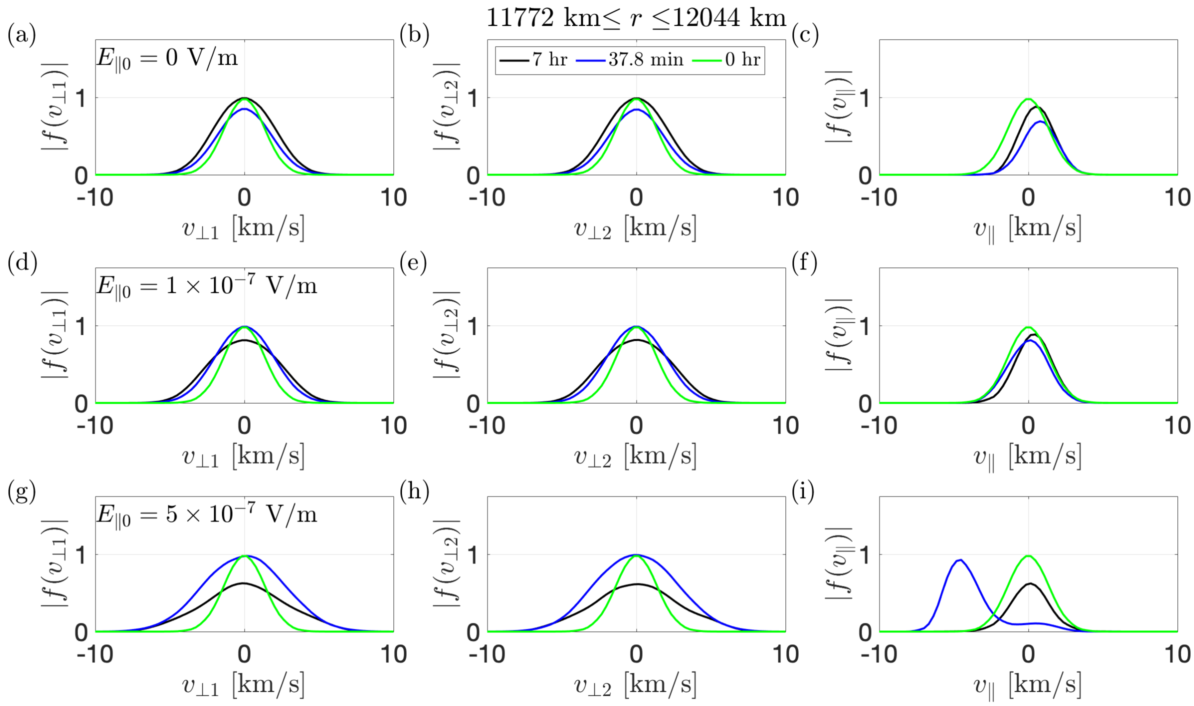

Figure 3.38: Normalized reduced ion distribution functions, $|f(v_{\perp 1})|$, $|f(v_{\perp 2})|$, and $|f(v_{\|})|$, for altitude range 11772 km $\leq r \leq$ 12044 km at initial time, $t = 37.8$ minutes, and $t = 7$ hours with ion cyclotron resonance heating parameterization from [Wu et al., 2002] and $E_{\|0} = 0 \text{ V} \cdot \text{m}^{-1}$, $E_{\|0} = 1 \times 10^{-7} \text{ V} \cdot \text{m}^{-1}$, and $E_{\|0} = 5 \times 10^{-7} \text{ V} \cdot \text{m}^{-1}$ for interaction time-step $h = 0.84$ seconds.

Balance between wave-heated outflows and potential barriers reflections are possible with fine tuning of heating parameters and reference potential drops. Introduction of an electrostatic barrier with reference parallel electric field $E_{\|0} = 1 \times 10^{-7} \text{ V} \cdot \text{m}^{-1}$ on the purely heated system of Figure 3.35 results in the striation of ion population in altitude according to parallel energy and ability to penetrate potential barriers. Although plasmas are compressed downward by potential barriers high-altitudes are populated with ions of sufficient energy to overcome ion traps. In purely heated case of Figure 3.35 ion temperature reaches $T_i \sim 10000$ K where ion temperatures exceed $T_i = 15000$ K for $E_{\|0} = 1 \times 10^{-7} \text{ V} \cdot \text{m}^{-1}$ at $r \sim 16000$ km. Parallel energies for the former case are at $w_{\|} \sim 0.17$ eV and $w_{\|} \sim 0.22$ eV for the latter at $r \sim 16000$ km altitudes. Low-energy particles are vacated from high-altitude grid cells by the potential barrier leaving a high-energy population of outflowing ions.

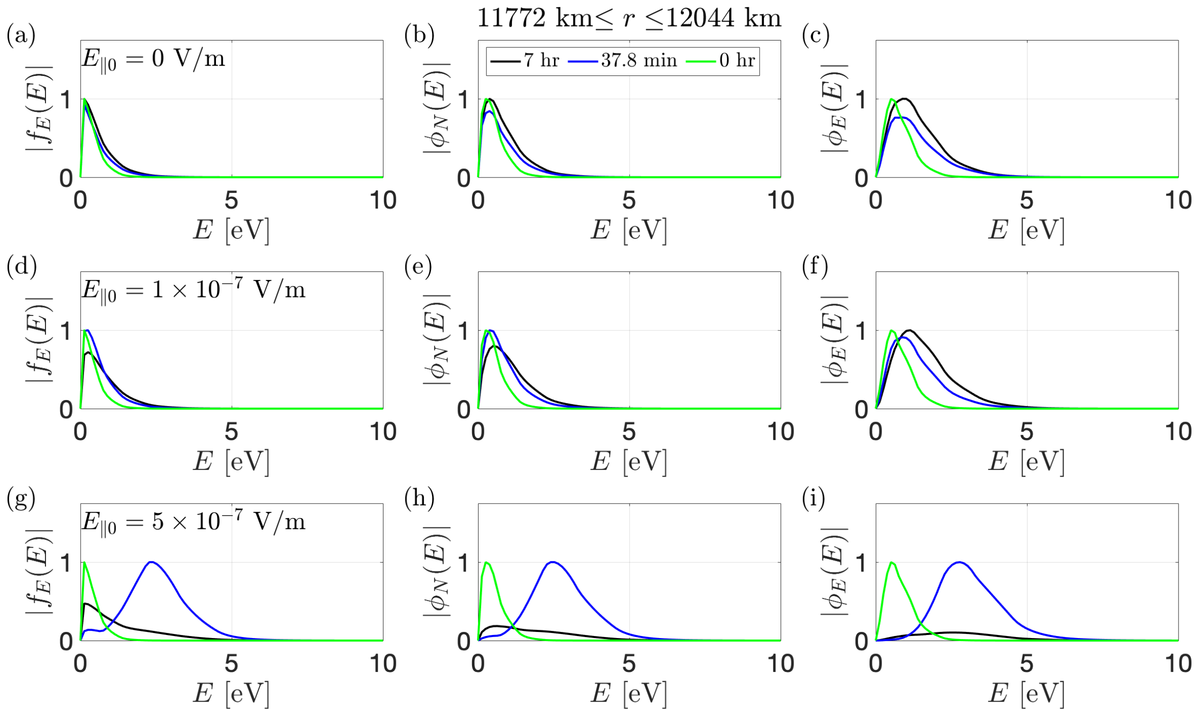

Figure 3.39: Normalized reduced energy-pitch-angle ion distribution functions, $|f_E(E)|$, and differential number and energy fluxes, $|\phi_N(E)|$ and $|\phi_E(E)|$, for altitude range 11772 km $\leq r \leq$ 12044 km at initial time, $t = 37.8$ minutes, and $t = 7$ hours with ion cyclotron resonance heating parameterization from [Wu et al., 2002] and $E_{\|0} = 0$ V $\cdot$ m^{-1}, $E_{\|0} = 1 \times 10^{-7}$ V $\cdot$ m^{-1}, and $E_{\|0} = 5 \times 10^{-7}$ V $\cdot$ m^{-1} for interaction time-step $h = 0.84$ seconds.

As reference parallel electric fields are increased to $E_{\|0} = 5 \times 10^{-7}$ V $\cdot$ m^{-1} plasma is further compressed in altitude leaving vestiges of high-energy populations in abandoned high-altitude spatial cells with reduced statistic fidelity as seen in Figure 3.34. Downward plumes of high-altitude ($r \sim 15000$ km) wave-energized plasmas form within $t \sim 40$ minutes transporting elevated conics downward at $u_\| \sim 4$ km $\cdot$ s^{-1} to $r \sim 11000$ km. Upper boundary escape fluxes relax and numerical noise increases due to poor statistics in sparsely populated spatial cells as seen in texturized energy moments near upper flux-tube boundaries. Figure 3.37 shows potential barrier energy profiles in eV versus altitude for $E_{\|0} = 1 \times 10^{-7}$ V $\cdot$ m^{-1} and $E_{\|0} = 5 \times 10^{-7}$ V $\cdot$ m^{-1}, where q denotes ion charge and $\Delta\Phi_\|$ is field-aligned potential drop according to Equation 2.40. Particles may reach high-altitude if they have parallel energies greater than $w_\| \sim 1$ eV since ion traps repel anything less energetic for $E_{\|0} = 1 \times 10^{-7}$ V $\cdot$ m^{-1}. This is consistent with $\sim$ 0.2-0.3 eV parallel energies above $r \sim 14000$ km as seen in Figure 3.36. $E_{\|0} = 5 \times 10^{-7}$ V $\cdot$ m^{-1} keeps all particles below $w_\| \sim 4.15$ eV at lower altitudes.

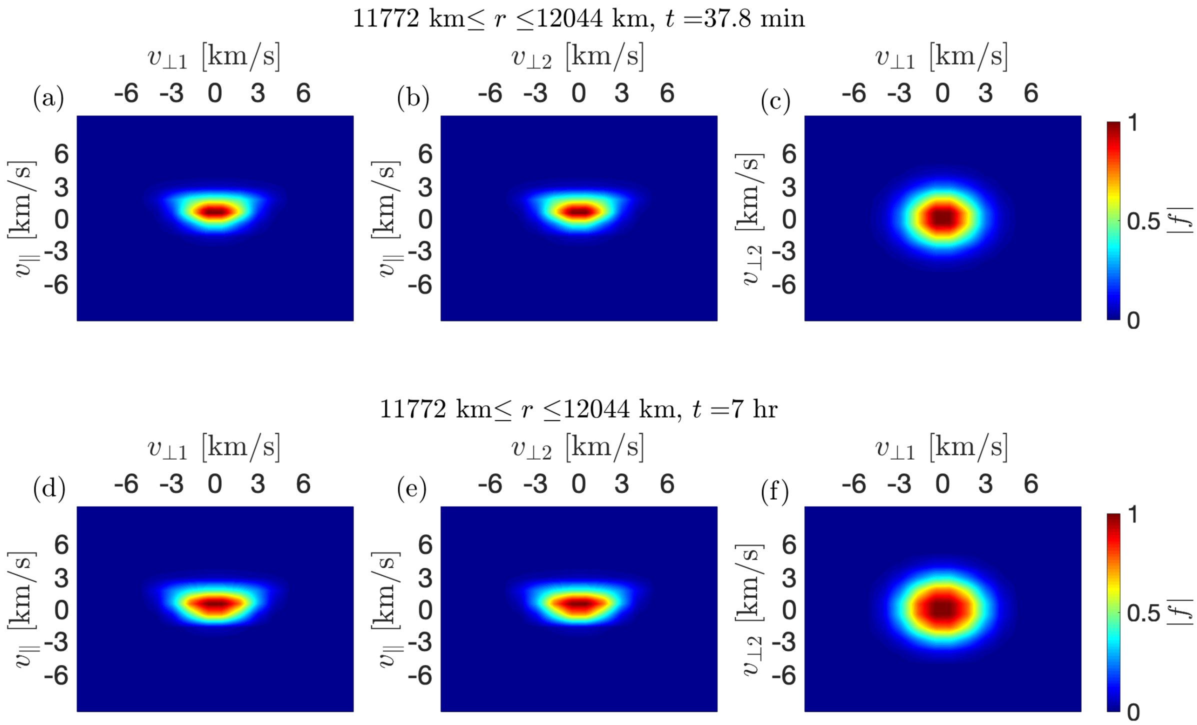

Figure 3.40: Normalized distribution functions in ($v_{\perp 1}$, $v_{\parallel}$), ($v_{\perp 2}$, $v_{\parallel}$), and ($v_{\perp 1}$, $v_{\perp 2}$) planes for altitude range 11772 km $\leq r \leq$ 12044 km at $t = 37.8$ minutes and $t = 7$ hours for ion cyclotron resonance heating parameterization from [Wu et al., 2002] and $E_{\parallel 0} = 0$ V $\cdot$ m^{-1} for interaction time-step $h = 0.84$ seconds.

Notable pressure cookers form at $t = 37.8$ minutes where descending ion conics transport plasmas of magnetospheric origin to low altitude via parallel electric fields of reference electric field $E_{\parallel 0} = 5 \times 10^{-7}$ V $\cdot$ m^{-1} as seen in Figure 3.41. Ion velocity distribution functions begin Maxwellian and evolve into broadened transverse distributions at zero-mean and outward parallel drifts for $E_{\parallel 0} = 0$ V $\cdot$ m^{-1} at both $t = 37.8$ minutes and $t = 7$ hours as seen in Figure 3.38. Parallel drifts are reduced at $t = 37.8$ minutes and $t = 7$ hours for $E_{\parallel 0} = 1 \times 10^{-7}$ V $\cdot$ m^{-1} and downward flows of cores near $E \sim 3$ eV at $t = 37.8$ minutes exist for $E_{\parallel 0} = 5 \times 10^{-7}$ V $\cdot$ m^{-1}. Prolonged interactions of transversely energized ions with regions of resonant wave heating produce transversely accelerated distributions with cores energized beyond those of the purely heated case.

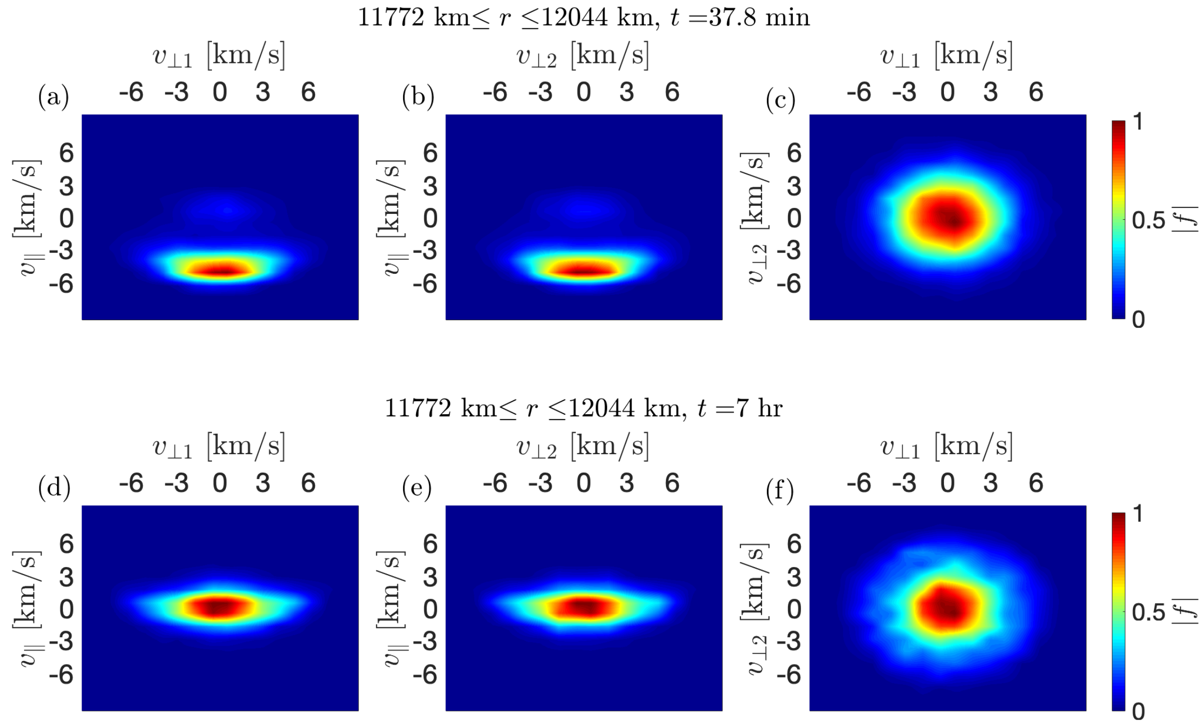

Figure 3.41: Normalized distribution functions in ($v_{\perp 1}$, $v_{\parallel}$), ($v_{\perp 2}$, $v_{\parallel}$), and ($v_{\perp 1}$, $v_{\perp 2}$) planes for altitude range 11772 km $\leq r \leq$ 12044 km at t = 37.8 minutes and t = 7 hours for ion cyclotron resonance heating parameterization from [Wu et al., 2002] and $E_{\parallel 0} = 5{\times}10^{-7}$ V $\cdot$ m^{-1} for interaction time-step h = 0.84 seconds.

According to Panels (a) and (g) of Figure 3.39 ion distributions reach $E \sim 3$ eV for $E_{\parallel 0} = 5{\times}10^{-7}$ V $\cdot$ m^{-1} and remain below $E \sim 1$ eV for $E_{\parallel 0} = 0$ V $\cdot$ m^{-1}. Increased transverse energization levels in pressure cookers exceed $\sim$ 2 eV over purely heated counterparts as seen in Panels (a), (b), (g), and (h) in Figure 3.38. Elevated ion conic distributions with upward folded wings below $E \sim 1$ eV form between 11772 km and 12044 km for zero potential drop. Core populations are transversely energized to $E \sim 3$ eV and slightly counter-streaming for $E_{\parallel 0} = 5 \times 10^{-7}$ V $\cdot$ m^{-1} as seen in Figures 3.40 and 3.41. Descending ion conics near $u_{\parallel} \sim 5$ km $\cdot$ s^{-1} are accompanied by secondary populations of pronounced transverse and upward components at t = 37.8 minutes which eventually strengthen to become the primary conics seen in Panel (d) of Figure 3.41. Pressure cookers at t = 37.8 minutes are characterized by downward $E \sim 3$ eV ion conics for $E_{\parallel 0} = 5{\times}10^{-7}$ V $\cdot$ m^{-1} and moderately outward-drifting conics by t = 7 hours as seen in Figure 3.41.

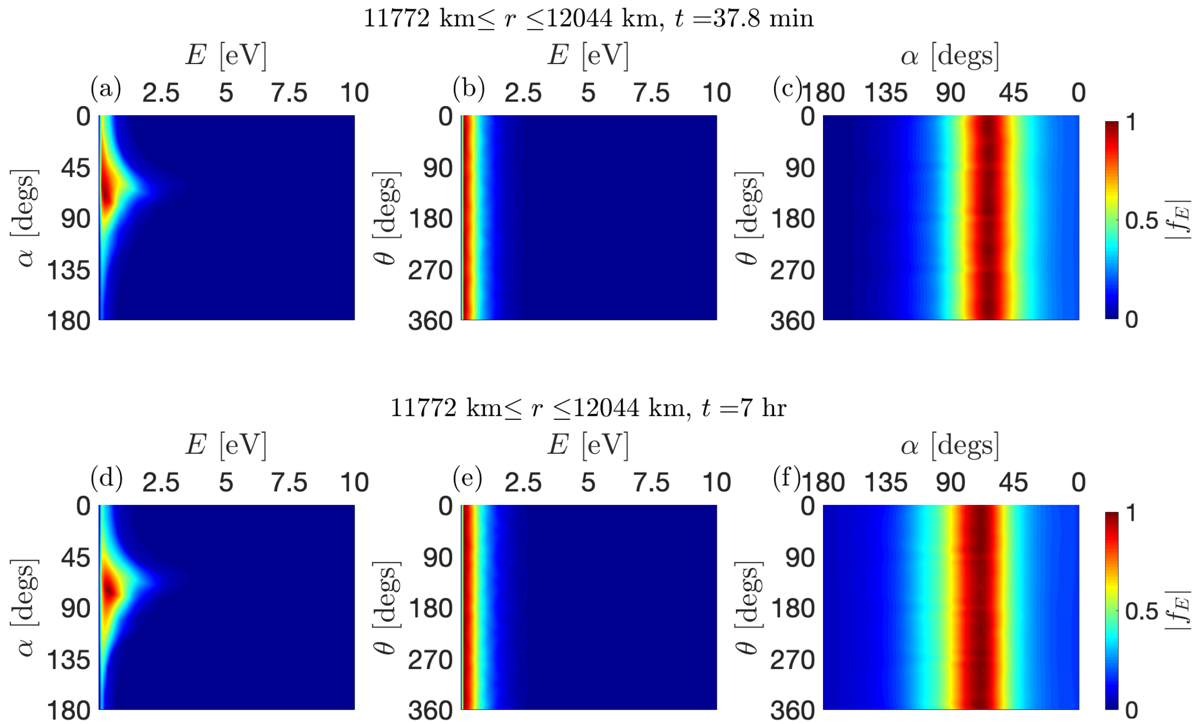

Figure 3.42: Normalized distribution functions in $(E,\ \alpha)$, $(E,\ \theta)$, and $(\alpha,\ \theta)$ planes for altitude range 11772 km $\leq r \leq$ 12044 km at t = 37.8 minutes and t = 7 hours for ion cyclotron resonance heating parameterization from [Wu et al., 2002] and $E_{\parallel 0} = 0\ \mathrm{V \cdot m^{-1}}$ for interaction time-step $h = 0.84$ seconds.

Moderately counter-streaming conics have enhanced upward components for zero potential drop denoted by pitch-angle distributions peaking near $\alpha \sim 60°$. At $t = 37.8$ minutes distributions above $\alpha \sim 135°$ form near $E \sim 2.5$ eV. Core populations are unable to contribute to upper boundary escape fluxes as they are repeatedly subjected to heating regions by $E_{\parallel}$. Pressure cooker effects reach equilibrium between competing forces and produce counter-streaming ion populations with upward-folded wings from adiabatic cooling with peaks at $E \sim 4.5$ eV near $\alpha \sim 90°$.

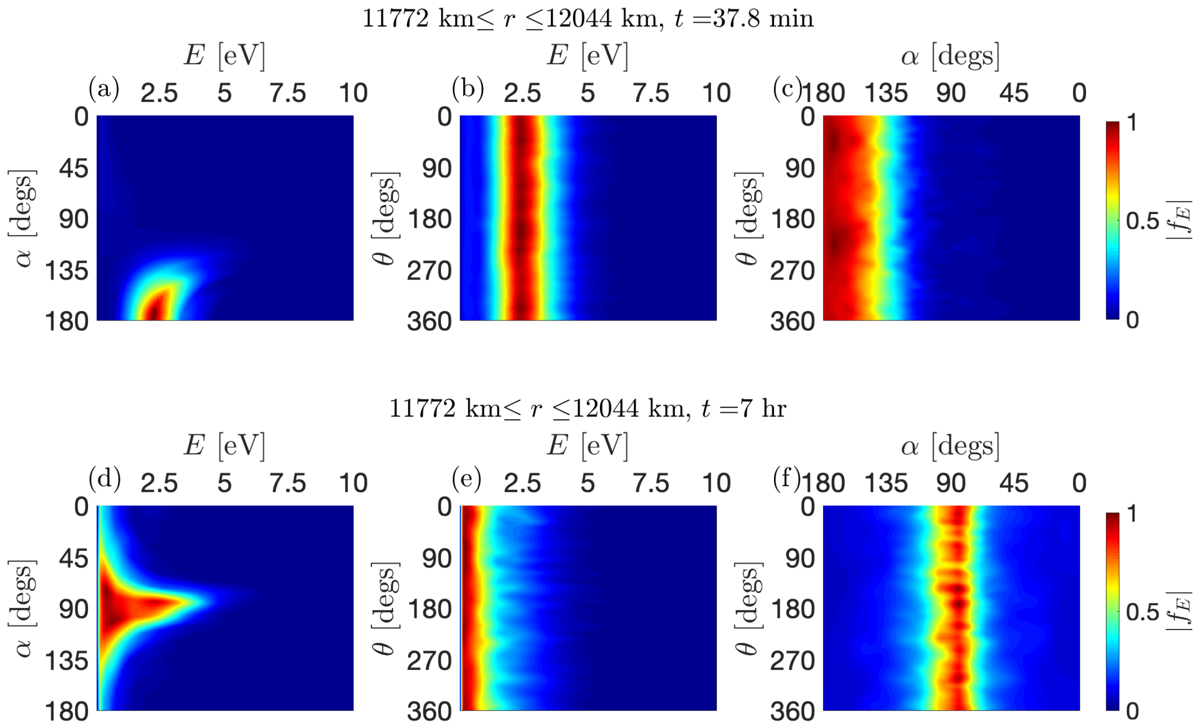

Figure 3.43: Normalized distribution functions in $(E,\ \alpha)$, $(E,\ \theta)$, and $(\alpha,\ \theta)$ planes for altitude range 11772 km $\leq r \leq$ 12044 km at $t = 37.8$ minutes and $t = 7$ hours for ion cyclotron resonance heating parameterization from [Wu et al., 2002] and $E_{\|0} = 5{\times}10^{-7}$ V $\cdot$ m^{-1} for interaction time-step $h = 0.84$ seconds.

Chapter 4

VISIONS-1 CASE STUDY

The VISIONS-1 (VIsualizing Ion Outflow via Neutral atom imaging during a Substorm) sounding rocket was launched from Poker Flat, AK, on February 7, 2013, at 08:21 UTC into the expansion phase of an auroral substorm to study the drivers of low-altitude ion outflow. It was equipped with instrumentation to remotely observe ion outflow by imaging energetic neutral atoms (ENAs) and to directly measure ion differential energy fluxes by in-situ detections. VISIONS-1 carried two Miniaturized Imagers for Low-Energy Neutral Atoms (MILENA) to remotely sense ion outflow from imaging ENAs from 50 eV to 3 keV energies, an Electrostatic Electron Analyzer (EEA) from 3 eV to 30 keV, an Electrostatic Ion Analyzer (EIA) from 1.5 eV to 15 keV, a four-channel visible imager in 6300 Å, 3914 Å, H-beta, and 8446 Å, and a Fields and Thermal Plasma (FTP) instrument that measured DC electric fields, magnetic fields, electron temperatures, and electron densities [Collier et al., 2015]. The Electrostatic Ion Analyzer (EIA) does not discriminate between ion species. The MILENA imagers remotely sensed source locations of ions that have charge-exchanged with neutral particles along the imager's line-of-sight to produce observed ENA fluxes. Modeling of ENA production from ionospheric outflows is subject of future work. Wave-heated pressure cookers parameterized by VLF wave heating detections by VISIONS-1 and PFISR radar observations of plasma density and temperature during rocket flight are modeled for different perpendicular wavelengths, $\lambda_\perp$, ion cyclotron resonance interaction time-steps, h, and reference parallel electric fields, $E_{\|0}$. Implications of altitude ranges are considered with respect to 1) ability of wave-heated ions to penetrate potential barriers, and 2) pressure cooker reflection regions for various parallel energy distributions. Modeled ion differential energy fluxes are compared directly to ion flux detections by the EIA instrument aboard VISIONS-1. Modeled energy flux levels coincide with observations for descending magnetospheric conic and bowl distributions originating above the rocket. Highly transversely energized descending conic and bowls have the capability to transport plasma heated at high wave-power to low altitude.

4.1 Model Parameterization

4.1.1 Plasma Density & Temperature Initialization

As the VISIONS-1 sounding rocket traversed several L-shells during flight instantaneous conditions are modeled with ion dynamics along the given magnetic field line. Conditions corresponding to time-of-flight $t_{of} = 591.3$ seconds near apogee $r = 718.9$ km at $L = 7.88$ R_E are modeled. VISIONS-1 is sent into the expansion phase of an auroral substorm with trajectory in altitude and co-latitude shown in Figure 4.1. Initial plasma temperatures and flux-tube footprint reference densities are parameterized from Poker Flat Incoherent Scatter Radar (PFISR) observations at the location and time of rocket apogee. High plasma temperatures enable the ability to model large altitude ranges with relatively low computational expense due to enhanced plasma scale heights. Ionospheric plasma is injected at the magnetic flux-tube footprint with reference density and temperature corresponding to observed values by PFISR at $t_{of} = 591.3$ seconds. All theoretical machinery described in Chapter 2 is employed for simulating VISIONS-1 conditions.

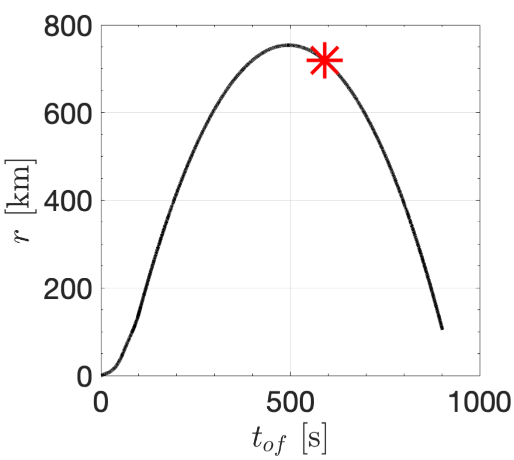

Figure 4.1: VISIONS-1 flight trajectory as a function of time-of-flight t_{of} (left), and tilted dipole co-latitude θ (right) consistent with Figure 1 of Appendix .2. The L-shell $L = 7.88$ R_E simulated corresponds to the location of significant VLF wave heating power at $t_{of} = 591.3$ seconds.

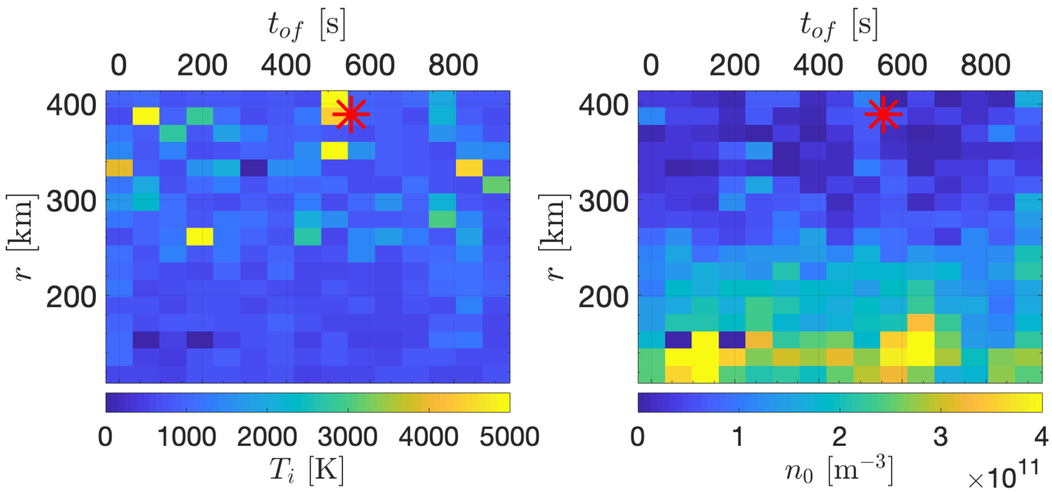

Figure 4.2: Ion temperature (left) and quasi-neutral plasma density (right) for the PFISR radar beam at the time of the VISIONS-1 flight at co-latitude $\theta = 158°$. Reference temperature and density used to initialize the model corresponds to PFISR data at the closest time to rocket time-of-flight $t_{of} = 591.3$ seconds.

Reference electron temperature $T_e = 2415$ K is selected from PFISR radar observations at the closest time to the VISIONS-1 event time-of-flight, $t_{of} = 555$ seconds, at $r \sim 370.78$ km. Although electron temperature varies in altitude and time it is considered constant. According to Figure 4.2 the ion temperature, $T_i = 4392$ K, and reference plasma density, $n_0 = 6 \times 10^{10}$ m^{-3}, corresponding to $r \sim 370.78$ km is obtained from PFISR at $t_{of} = 555$ seconds. 19 spatial bins span from 340-3100 km. Kinetic equilibria is achieved prior to mirror forcing, wave heating, and/or parallel electric forcing by employing lead-in simulations as discussed in Section 3.1. Cold Maxwellian ionospheric populations corresponding to the magnetic flux-tube footprint density and isotropic ion temperature are injected at the lower boundary grid cell on time scales τ_i equal to the mean thermal ion transit time through the lower boundary ghost cell as detailed in Section 2.2.1. Ion distributions and moments are computed on $\tau_i \sim 62$ second time intervals.

4.1.2 Wave Power Spectral Density Parameterization

Wave power spectral density values vary in different modeling efforts; $S_0 = 1.5\times10^{-5}$ V$^2\cdot$ m$^{-2}\cdot$ Hz^{-1} at reference O$^+$ gyro-frequency 0.67 Hz [Klumpar et al., 1984], $S_0 = 1.2 \times 10^{-6}$ V$^2\cdot$ m$^{-2}\cdot$ Hz^{-1} at reference O$^+$ gyro-frequency 5.6 Hz [Winningham and Burch, 1984a], $S_0 = 8.8\times10^{-6}$ V$^2\cdot$ m$^{-2}\cdot$ Hz^{-1} at reference O$^+$ gyro-frequency 0.43 Hz [Coffey, 1982a] [Coffey, 1982b] [Coffey, 1982c], and $S_0 = 2.2 \times 10^{-8}$ V$^2\cdot$ m$^{-2}\cdot$ Hz^{-1} at reference O$^+$ gyro-frequency 45 Hz [Chang and Crew, 1986]. [Chang and Crew, 1986] investigated relative effects of ion heating from varying power spectral densities for fixed spectral index and reference gyro-frequency. Wave power spectral densities are fit to observed rocket wave spectra by polynomial fitting to produce a spectral index of $\chi_\perp = 2.1$ at $r \sim 718$ km and $t_{of} = 591.3$ seconds time-of-flight. Following sections constrain model parameter space to reproduce ion differential energy fluxes observed by VISIONS-1 and pressure cooker environments that may generate observed fluxes are described. Qualitative attributes of synergistic drivers of ionospheric outflows with model limitations are analyzed.

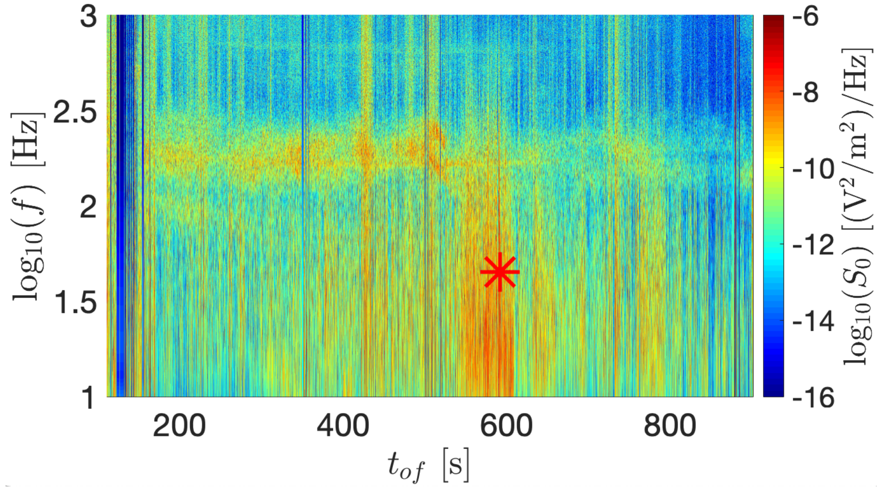

Figure 4.3: VLF spectrogram observed by VISIONS-1 throughout the flight. Near-apogee altitude of $r \sim 718.9$ km during enhanced wave power spectral density at reference O^+ gyro-frequency $f_{g0} = 72.53$ Hz and time-of-flight $t_{of} = 591.3$ seconds is marked by the red star.

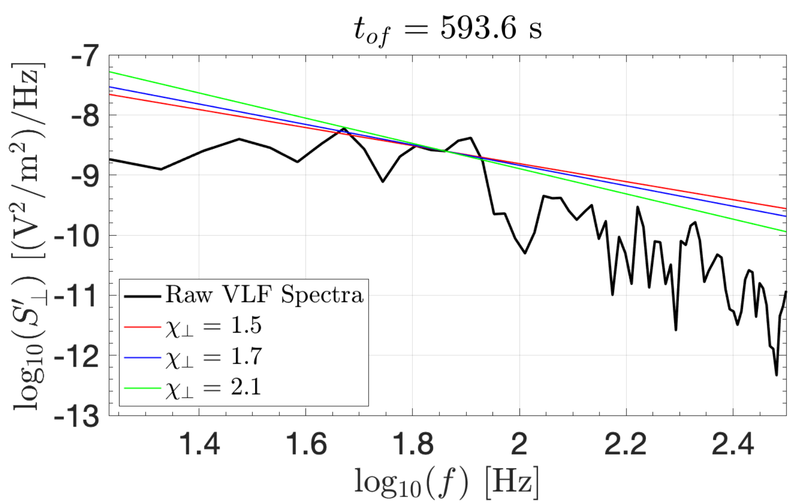

Figure 4.4: VLF wave spectra observed by VISIONS-1 at time-of-flight $t_{of} = 593.6$ seconds with power spectral densities for spectral indices $\chi_\perp = 1.5$, 1.7, and 2.1 at reference O^+ gyro-frequency $f_{g0} = 72.53$ Hz.

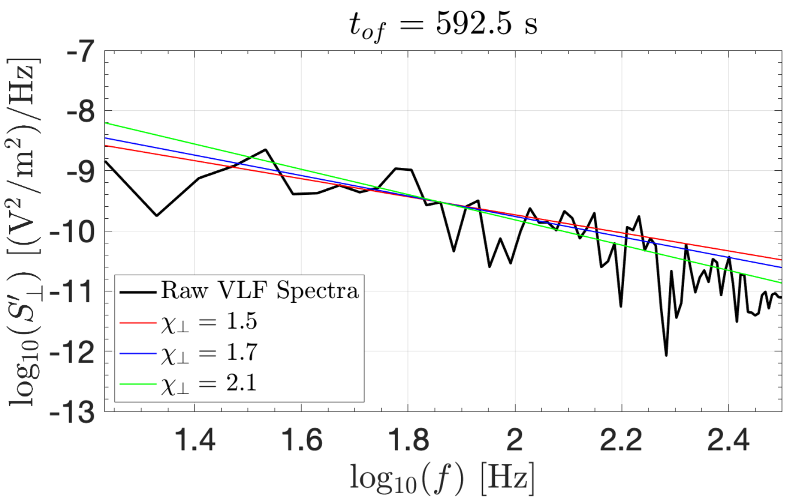

Figure 4.5: VLF wave spectra observed by VISIONS-1 at time-of-flight t_{of} = 592.5 seconds with power spectral densities for spectral indices $\chi_\perp$ = 1.5, 1.7, and 2.1 at reference O^+ gyro-frequency f_{g0} = 72.53 Hz.

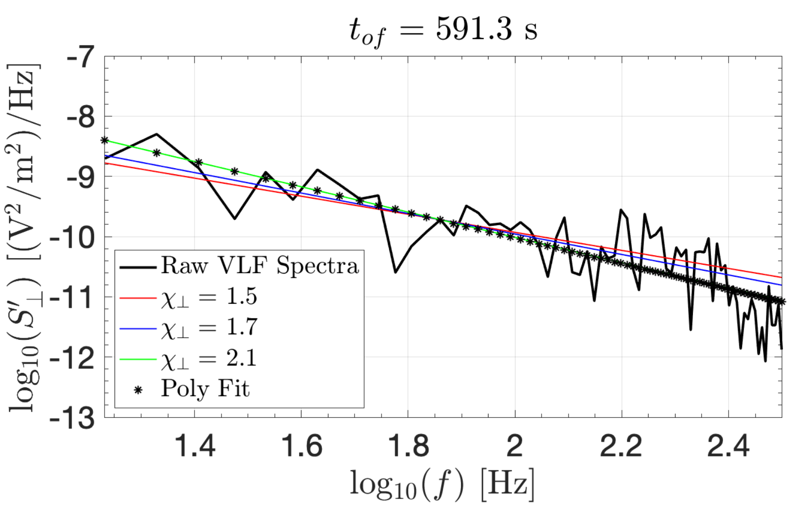

Figure 4.6: VLF wave spectra observed by VISIONS-1 at time-of-flight t_{of} = 591.3 seconds with power spectral densities for spectral indices $\chi_\perp$ = 1.5, 1.7, and 2.1 at reference O^+ gyro-frequency f_{g0} = 72.53 Hz. Linear fit to selected frequency range yields a heating spectral index of $\chi_\perp$ = 2.1.

VISIONS-1 detects significant VLF wave turbulence activity seen in Figure 4.3 at t_{of} = 591.3 seconds and r = 718.9 km. The time and location of maximum wave power varies as seen in the sequence of power spectral densities of Figures 4.6, 4.5, and 4.4. For instantaneous wave heating conditions general temperaments of O^+ populations are characterized subject to wave heating within various frequency bandwidths, Δf, about the ion cyclotron frequency. In this Chapter plasmas modeled from parameterized initial conditions are wave-heated with heating spectral index $\chi_\perp$ = 2.1 corresponding to the power law fit of power spectral density with reference value, S_0, at reference gyro-frequency, f_{g0}, to observed wave spectra of Figure 4.6. Velocity-dependent effects on transverse velocity diffusion coefficients are omitted to emphasize power spectral variations in frequency where $S'_\perp = S_0 \left(f_g/f_{g0}\right)^{-\chi_\perp}$ according to Equation 2.38. Synergistic effects of variations of the following open parameters in VISIONS-1 flight conditions are analyzed: perpendicular electromagnetic turbulence wavelength, $\lambda_\perp$, computational time-step scaled to ion cyclotron resonance interaction time, h, and reference parallel electric field values, $E_{\|0}$.

4.2 Modeling VISIONS-1 Flight Conditions

4.2.1 Finite Gyro-Radius Wave Heating

Table 4.1: VISIONS-1 case study finite gyro-radius simulations for initial conditions parameterized at the rocket flight for transverse BBELF wavelengths, $\lambda_\perp$, and reference parallel electric fields, $E_{\|0}$.

Simulation	$\lambda_\perp$ [m]	$E_{\|0}$ [V $\cdot$ m^{-1}]
B1	∞	0
B2	0.25	0
B3	∞	1×10^{-6}
B4	0.25	1×10^{-6}

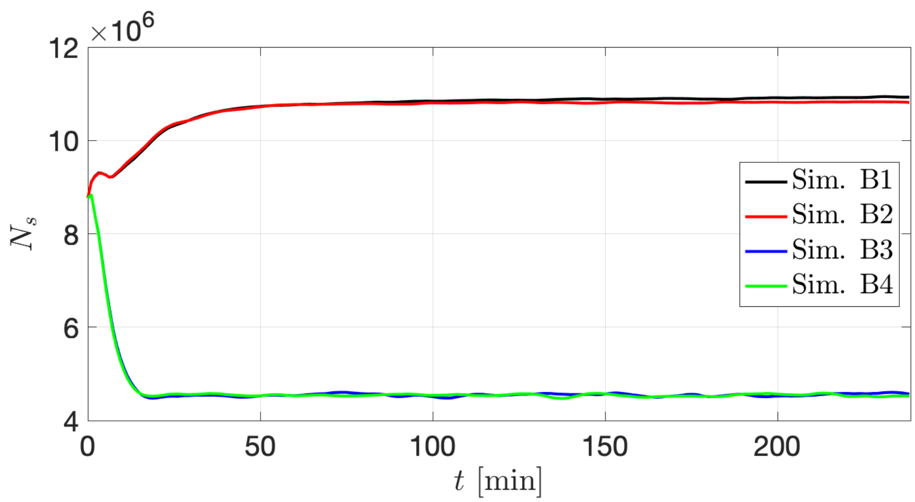

Figure 4.7: Total number of simulated ion macro-particles, N_s, as a function of time for pressure cooker conditions tabulated in Table 4.1.

Subsection 3.2.3 investigates effects of transverse turbulence wavelengths, $\lambda_\perp$, on heated ion distributions when the gyro-radius, ρ_g, exceeds $\lambda_\perp$. The short-wavelength limit, $\lambda_\perp < \rho_g$, results in self-limited heating mechanisms where velocity-dependent terms, $\sigma_\perp$, of the transverse velocity diffusion coefficients of Equation 2.38 become much less than unity for small values of $\lambda_\perp$ relative to ρ_g [Barghouthi and Atout, 2006]. Effects of finite gyro-radius are only apparent when ρ_g exceeds $\lambda_\perp$. This section scrutinizes the validity of short-wavelength approximations on wave-heated ionospheric outflows observed by VISIONS-1. Self-limited heating occurs when $\lambda_\perp \lesssim 0.25$ m for heating parameters and altitudes parameterized from the VISIONS-1 flight; saturation of the perpendicular heating rate occurs when $\lambda_\perp \lesssim 0.25$ m. Particles are not sufficiently heated to produce values of ρ_g that exceed wavelengths $\lambda_\perp \sim 10$ km such that characteristic electromagnetic turbulence wavelengths $\lambda_\perp \sim 10$ km corresponding to observed O^+ ion temperatures of 200 eV [Huddleston et al., 2000] at 4.8 R_E equator-ward of the cusp [Barghouthi and Atout, 2006] reside in the long-wavelength regime for the modeled environment of VISIONS-1.

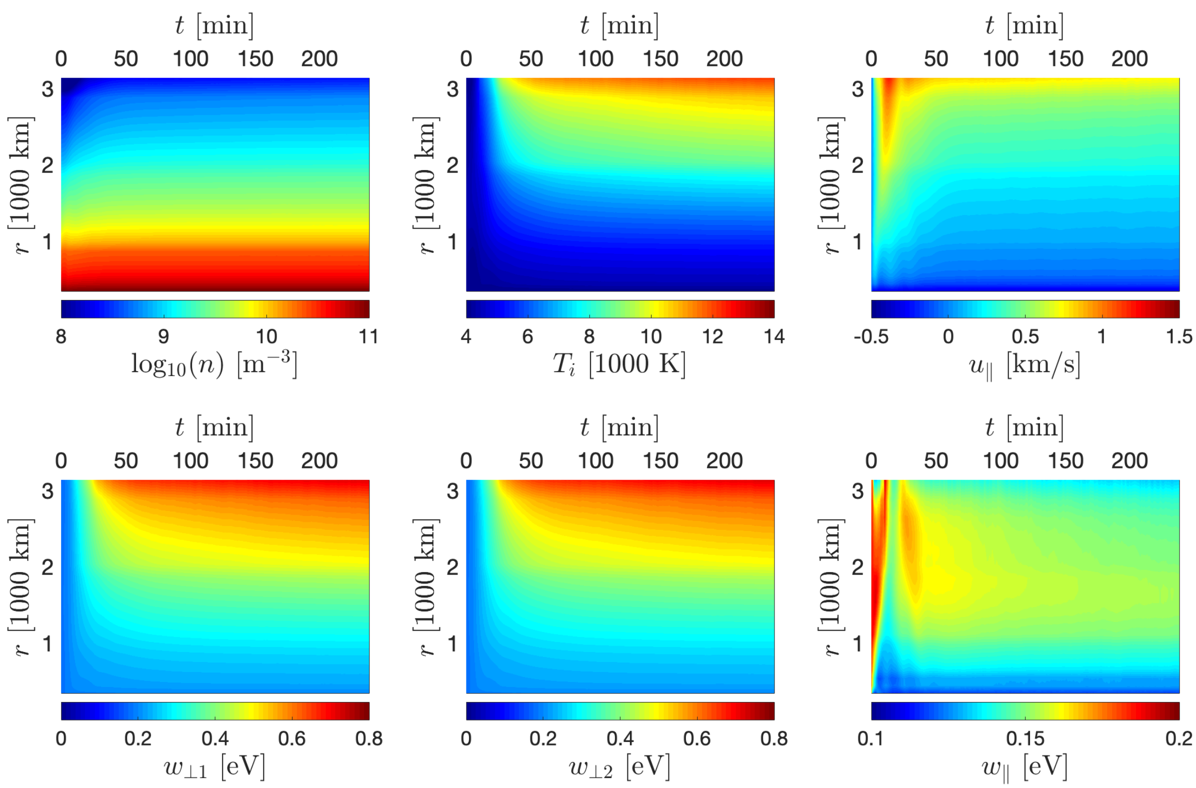

Figure 4.8: Plasma density, ion temperature, parallel plasma flow, and energies along $\hat{\mathbf{e}}_{v_{\perp 1}}$, $\hat{\mathbf{e}}_{v_{\perp 2}}$, and $\hat{\mathbf{e}}_{v_\parallel}$ directions with active ambipolar electric field and heating parameterization from the VISIONS-1 sounding rocket for Simulation B1 of Table 4.1.

This section scrutinizes the validity of short-wavelength approximations below $r \sim 3000$ km of wave-heated plasmas parameterized by the VISIONS-1 rocket observations as detailed in Subsection 4.1.2. Four simulations are performed to demonstrate wave heating at finite gyro-radii occurs for $\lambda_\perp \sim 0.25$ m for ion cyclotron resonance interaction time-step $h = 0.84$ seconds. Transverse wavelengths corresponding to saturations in transverse heating rates extend in length-scale with cyclotron interaction time-step, h; low-frequency wave heating ($\lambda_\perp > \rho_g$) acts to increase the upper limit of $\lambda_\perp$ in the short-wavelength regime for longer cyclotron interaction times-steps. Following plasmas modeled are unique to $h = 0.84$ seconds and ionospheric and magnetospheric responses to pressure-cooker-driven transverse energizations from cyclotron interaction time variations should be characterized qualitatively with respect to $h/\tau_\perp$. Moderate pressure cookers with long and short-wavelengths are modeled for reference parallel electric fields $E_{\|0} = 1 \times 10^{-6}$ V $\cdot$ m^{-1}, as tabulated in Table 4.1.

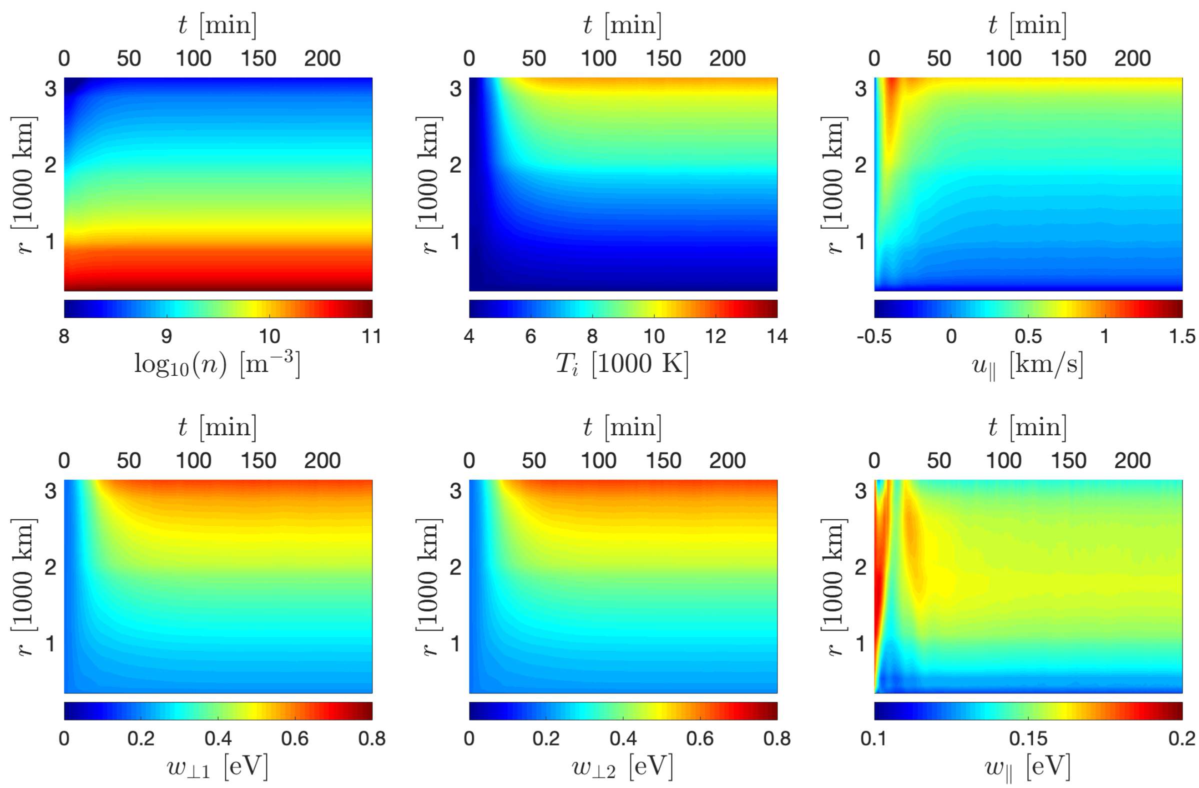

Figure 4.9: Plasma density, ion temperature, parallel plasma flow, and energies along $\hat{\mathbf{e}}_{\mathbf{v}_{\perp 1}}$, $\hat{\mathbf{e}}_{\mathbf{v}_{\perp 2}}$, and $\hat{\mathbf{e}}_{\mathbf{v}_\|}$ directions with active ambipolar electric field and heating parameterization from the VISIONS-1 sounding rocket for Simulation B2 of Table 4.1.

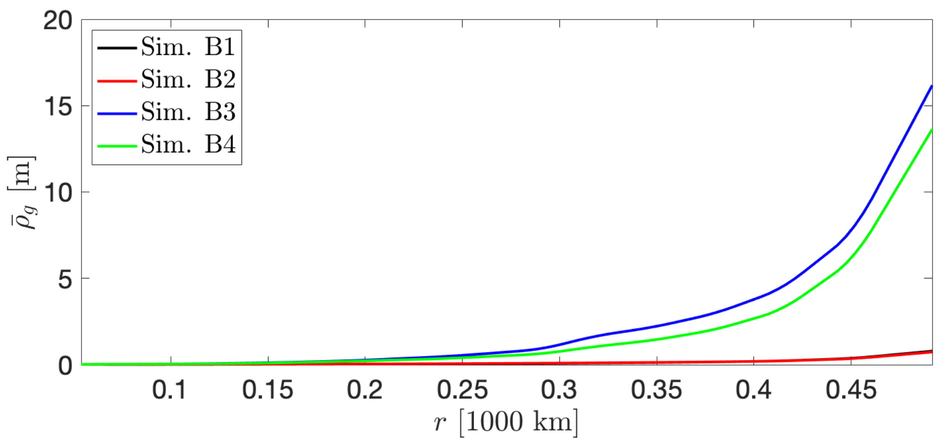

Figure 4.10: Mean ion gyro-radii, $\bar{\rho}_g$, computed from perpendicular ion velocity moments as a function of altitude, r, for velocity-dependent transverse diffusion of wave-heated ions with VISIONS-1 parameterized initial conditions and wave heating parameters and perpendicular wavelength cases $\lambda_\perp = \infty$ and $\lambda_\perp = 10$ m.

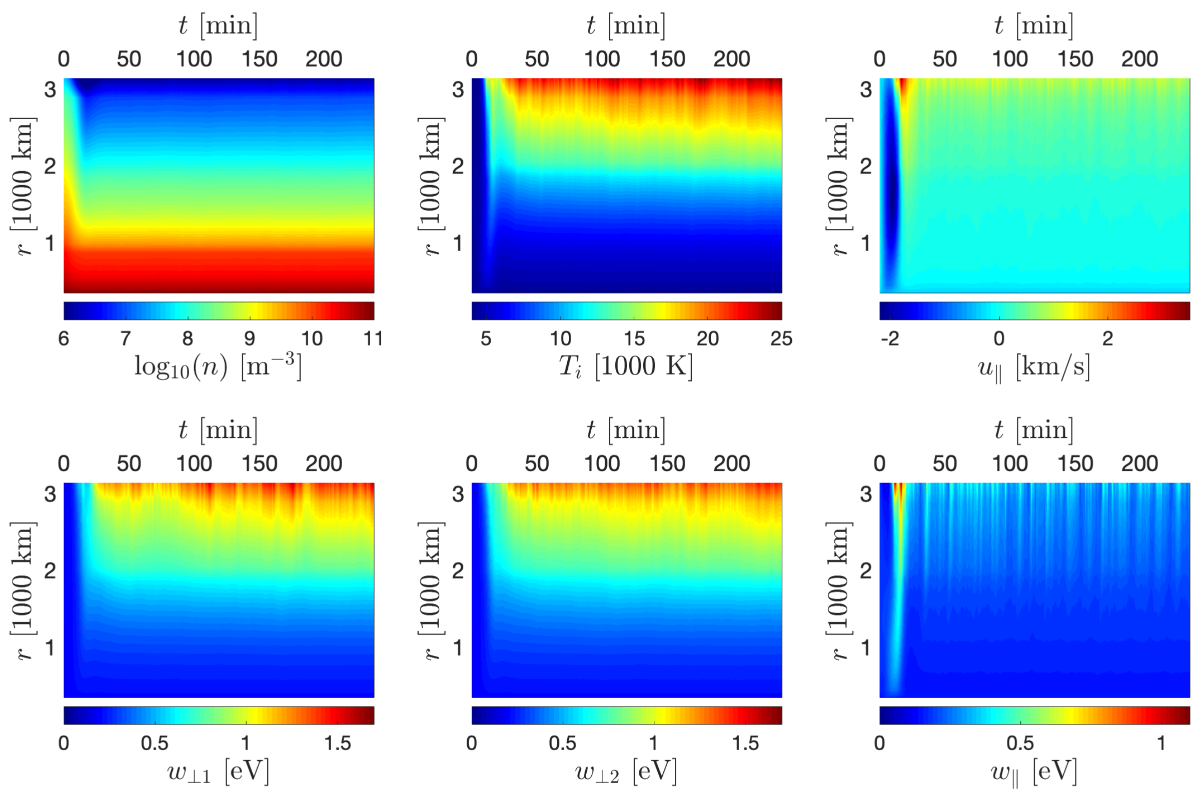

Figure 4.11: Plasma density, ion temperature, parallel plasma flow, and energies along $\hat{\mathbf{e}}_{\mathbf{v}_{\perp 1}}$, $\hat{\mathbf{e}}_{\mathbf{v}_{\perp 2}}$, and $\hat{\mathbf{e}}_{\mathbf{v}_\parallel}$ directions with active ambipolar electric field and heating parameterization from the VISIONS-1 sounding rocket for Simulation B3 of Table 4.1.

VLF wave power spectral density $S_0 = 1.91 \times 10^{-10}$ V$^2\cdot$ m$^{-2}\cdot$ Hz^{-1} at reference O$^+$ gyro-frequency $f_{g0} = 72.53$ Hz is observed by VISIONS-1 at time-of-flight $t_{of} = 591.3$ seconds, altitude $r = 718.6$ km, and tilted dipole co-latitude $\theta = 158.8°$ (70.91° N geographic latitude) as seen in Figures 4.1 and 4.3. Fraction of wave power that is left-hand polarized is $\eta_{LH} = 0.125$ [Chang and Crew, 1986]. Wave heating is assumed gyro-tropic such that equal fractions of $\eta_{LH} S_\perp$ are along the $\hat{\mathbf{e}}_{\perp 1}$ and $\hat{\mathbf{e}}_{\perp 2}$ directions such that $\xi_{\perp 1} = \xi_{\perp 2} = 0.5$ in the wave heating velocity diffusion coefficients of Equation 2.38 and $\chi_{\perp 1} = \chi_{\perp 2} = 2.1$ per Figure 4.6. Lower boundary ion escape fluxes are increased due to potential barriers impeding wave-heated outflows as seen in the evolution of total number of simulated macro-particles, N_s, in Figure 4.7. Lower boundary injection of thermal ions overwhelms lower boundary escape fluxes due to ion outflow by wave-heating as seen in Simulations B1 and B2 in Figure 4.7.

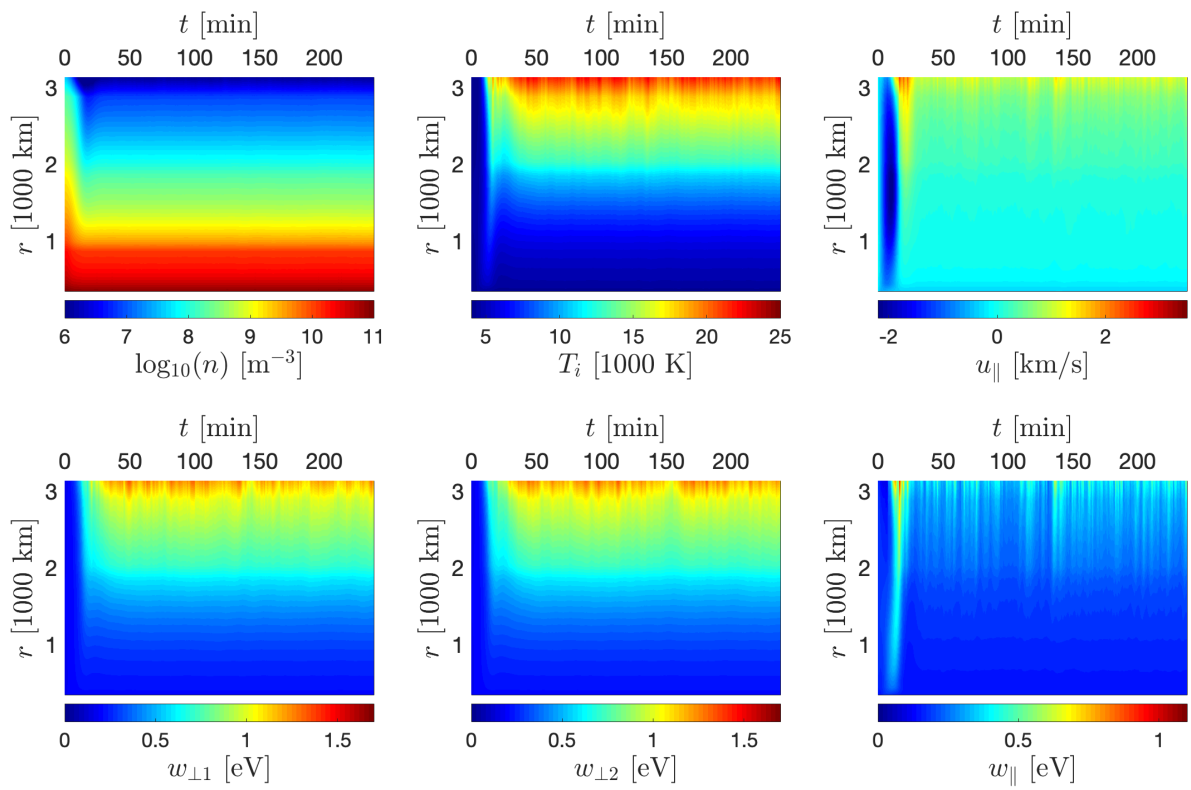

Figure 4.12: Plasma density, ion temperature, parallel plasma flow, and energies along $\hat{\mathbf{e}}_{\mathbf{v}_{\perp 1}}$, $\hat{\mathbf{e}}_{\mathbf{v}_{\perp 2}}$, and $\hat{\mathbf{e}}_{\mathbf{v}_\parallel}$ directions with active ambipolar electric field and heating parameterization from the VISIONS-1 sounding rocket for Simulation B4 of Table 4.1.

Figures 4.8 and 4.9 illustrate evolutions of ion moments in absence of parallel potential drops for $\lambda_\perp = \infty$ and $\lambda_\perp = 0.25$ m, that is, Simulations B1 and B2, respectively. Variations in transverse energization due to selections of $\lambda_\perp$ are primarily apparent above $r \sim 2500$ km since wave powers increase at lower resonant frequencies. Figure 4.8 for Simulation B1 denotes total transverse thermal energy $w_\perp = w_{\perp 1} + w_{\perp 2}$ increase by ~ 0.15 eV over the short-wavelength counterpart of Simulation B2 seen in Figure 4.9. Ions are isotropically heated in gyro-phase such that statistically equal enhancements of $w_{\perp 1}$ and $w_{\perp 2}$ are generated while bi-modal transverse fluxes balance such that $u_{\perp 1} \sim u_{\perp 2} \sim 0$. Adiabatic cooling by the relaxation of magnetic moments and conversion of transverse to parallel momentum via the mirror force is not sufficient to produce notable increases in parallel energy for $\lambda_\perp = \infty$ over $\lambda_\perp = 0.25$ m. Mean gyro-radii for Simulations B1 and B2 are less than $\bar{\rho}_g \sim 0.25$ m such that self-limited wave heating acts primarily on the high-energy tail of transverse distributions seen in Figure 4.14.

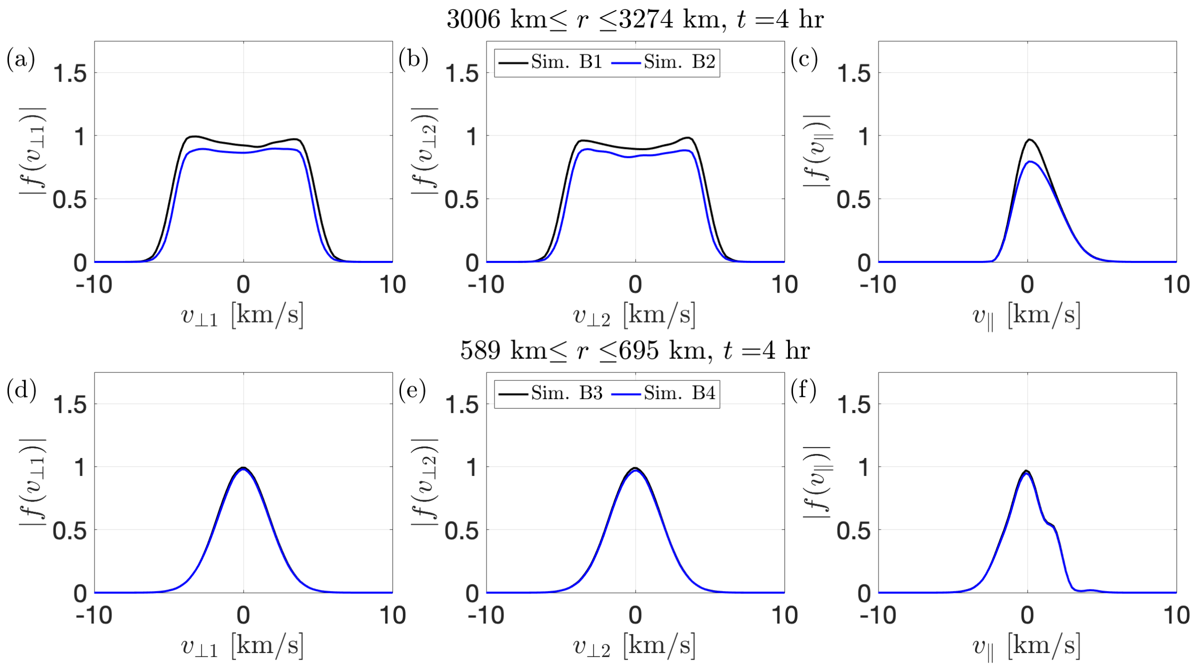

Figure 4.13: Normalized reduced ion distribution functions, $|f(v_{\perp 1})|$, $|f(v_{\perp 2})|$, and $|f(v_\parallel)|$, corresponding to VISIONS-1 flight conditions for altitude range 3006 km $\leq r \leq$ 3274 km at $t = 4$ hours for Simulations B1 and B2 of Table 4.1 on Panels (a), (b), and (c) and altitude range 589 km $\leq r \leq$ 695 km at $t = 4$ hours for Simulations B3 and B4 on Panels (d), (e), and (f).

Parallel potential drops characterized by a reference parallel electric field, $E_{\parallel 0}$, serve to striate ion populations by parallel energy in altitude; only particles with sufficient wave-induced parallel energy may overcome potential barriers and inhabit high altitudes. In spirit similar to Subsection 3.2.4 transverse energies in pressure cookers exceed purely wave-heated values for equal wave power as ions are reflected downwards according to parallel energy and $E_\parallel$ to repeatedly enter the ion cyclotron resonance wave-field on times-scales proportional to adiabatic cooling rates. Finite gyro-radius effects on wave-heated pressure cookers manifest as self-limited heating of plasmas above $r \sim 2500$ km as seen in Figures 4.11 and 4.12. For Simulations B2 and B4, above $\rho_g \sim 0.25$

m, the velocity-dependent factor, $\sigma_\perp$, in Equation 2.38 becomes greater than unity and ion cyclotron resonance velocity kicks decrease in magnitude at the $-3/2$ power of $\sigma_\perp$ according to Equation 2.33. Above $r \sim 2500$ km the turbulence perpendicular wavelength surpasses mean gyro-radii serving to saturate heating rates for low transverse energy ions.

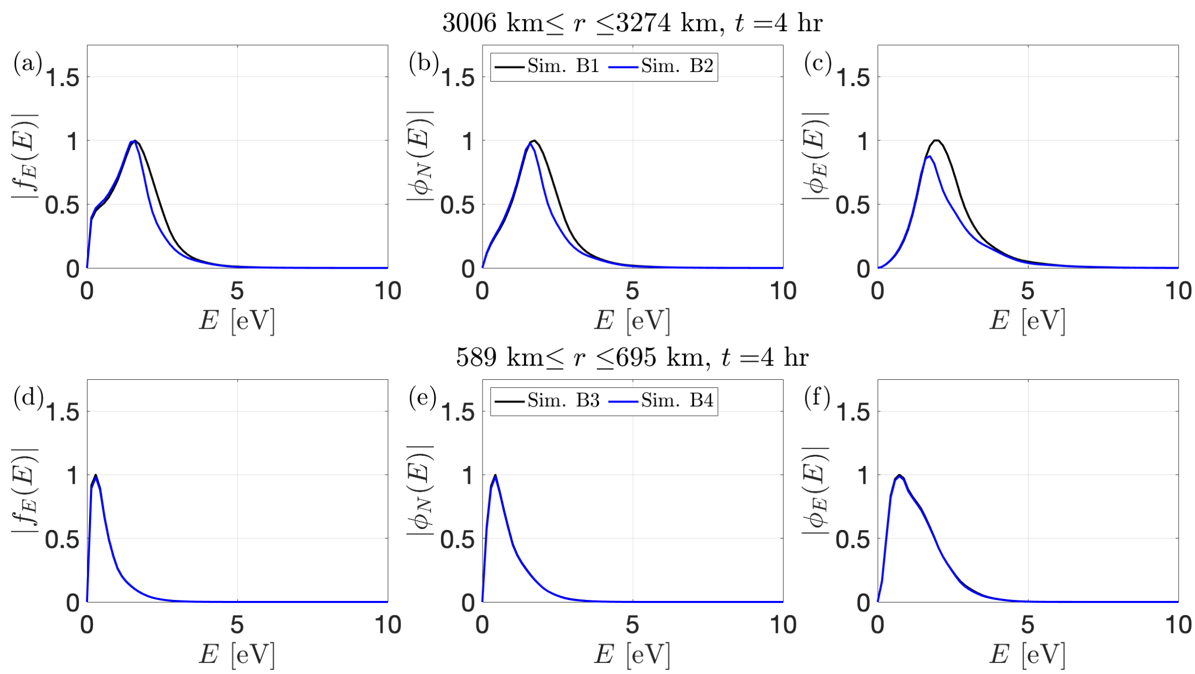

Figure 4.14: Normalized reduced energy-pitch-angle ion distribution functions, $|f_E(E)|$, and differential number and energy fluxes, $|\phi_N(E)|$ and $|\phi_E(E)|$, corresponding to VISIONS-1 flight conditions for altitude range 3006 km $\leq r \leq$ 3274 km at $t = 4$ hours for Simulations B1 and B2 of Table 4.1 on Panels (a), (b), and (c) and altitude range 589 km $\leq r \leq$ 695 km at $t = 4$ hours for Simulations B3 and B4 on Panels (d), (e), and (f).

In the absence of electrostatic parallel potential structures high altitude spatial cells are well-populated for wave-driven ion outflows. Toroids evolve from low-altitude ion bowl and conic distributions by $r \sim 3000$ km as low perpendicular velocity bins are evacuated by wave-particle interactions, as seen in Panels (a) and (b) of Figure 4.13. Finite gyro-radius effects on transverse velocity diffusion coefficients are apparent as high perpendicular velocity populations in Simulation B1 surpass those in Simulation B2; stochastic long transverse wavelength heating generates wider transverse velocity distributions than for short-wavelength approximations in consistent fashion with results presented by [Barghouthi and Atout, 2006] and analysis of Subsection 3.2.3. Parallel particle momenta transferred from wave-energized ion magnetic moments is greater for Simulation B1 than for Simulation B2. Simulations B1 and B2 show outward drifts of over $u_\parallel = 0.5$ km $\cdot$ s^{-1} as seen in Figures 4.8 and Figure 4.9 and Panel (c) of Figure 4.13.

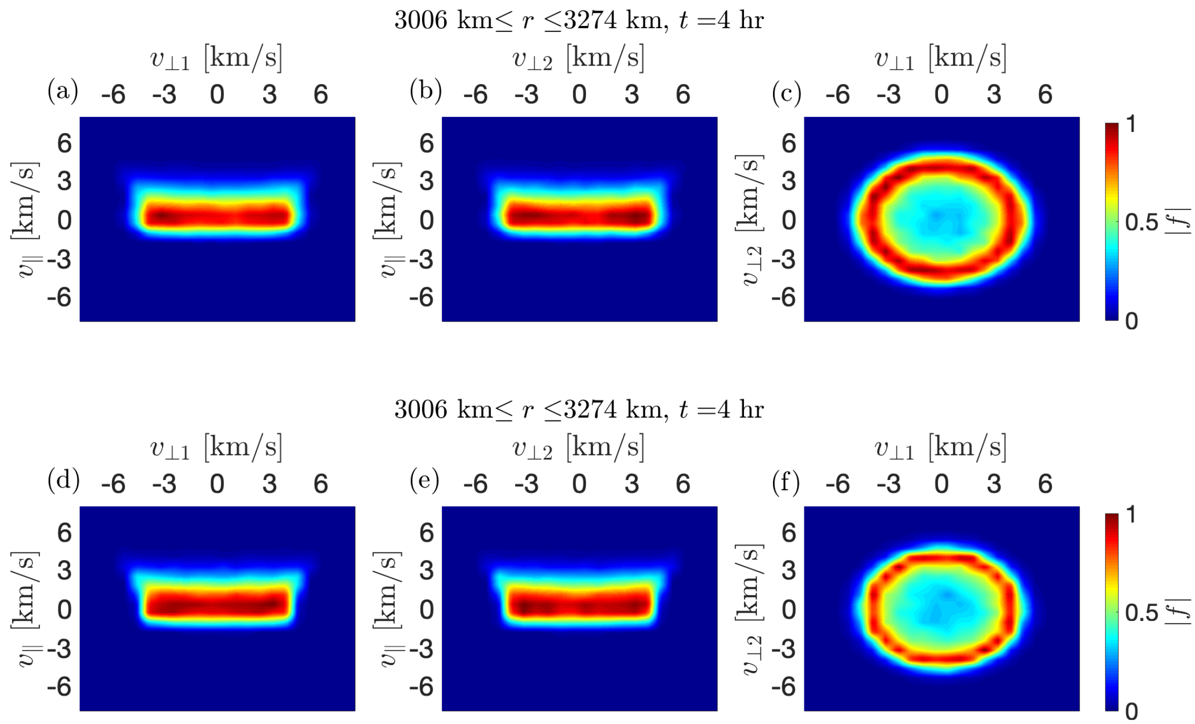

Figure 4.15: Normalized distribution functions in ($v_{\perp 1}$, $v_{\parallel}$), ($v_{\perp 2}$, $v_{\parallel}$), and ($v_{\perp 1}$, $v_{\perp 2}$) planes corresponding to VISIONS-1 flight conditions for altitude range 3006 km $\leq r \leq$ 3274 km at t = 4 hours for Simulation B1 on Panels (a), (b), and (c) and Simulation B2 on Panels (d), (e), and (f).

Elevated toroidal distributions with upward-folded wings at high transverse velocity bins for long and short-wavelength heating cases of Simulations B1 and B2 are apparent at $r \sim 3000$ km as seen in Figure 4.15. Low transverse velocity bins are evacuated due to wave-heating to form ring distributions in the perpendicular plane as seen for both choices of $\lambda_{\perp}$ in Panels (c) and (f) of Figure 4.15. Larger transverse velocity bins are inhabited at low parallel velocities for $\lambda_{\perp} = \infty$ over $\lambda_{\perp} = 0.25$ m. As seen in Figure 4.17 ion distributions have $E \sim 2$ eV cores near $\alpha \sim 90°$ with eV enhancements near $\alpha \sim 60°$ for outflowing populations. Core distributions span larger energy ranges for $\lambda_{\perp} = \infty$ than for $\lambda_{\perp} = 0.25$ m in consistent fashion with velocity-dependent wave-heating. Particles are isotropically energized in gyro-phase such that all values of gyro-angle, θ, contain $E \sim 2$ eV particles by $t = 4$ hours simulation duration. Slight enhancements of E in θ exist for Simulation B1 over Simulation B2 as seen in Panels (b) and (e) of Figure 4.17 owing to finite gyro-radius effects of ion cyclotron resonance heating.

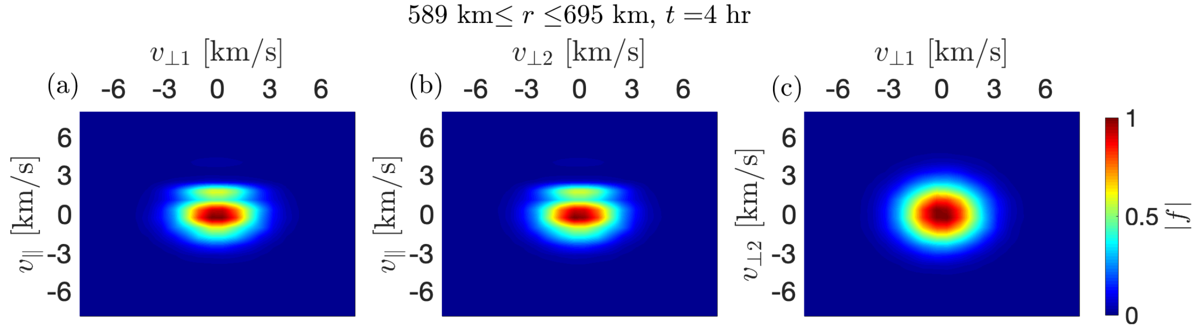

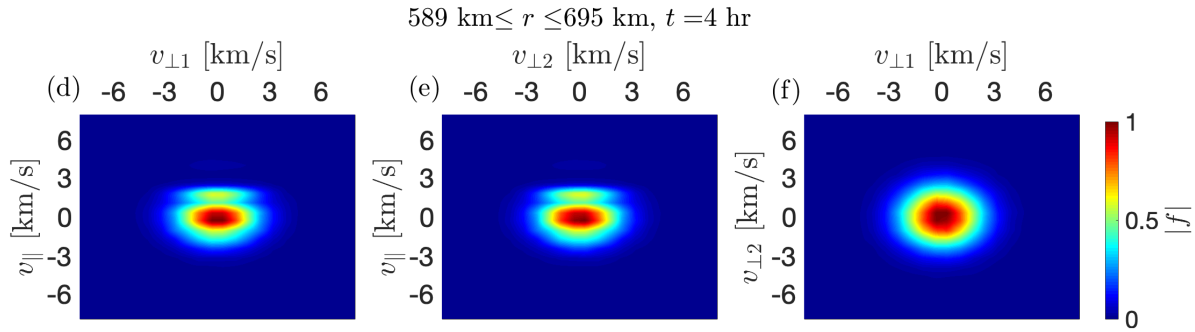

Figure 4.16: Normalized distribution functions in $(v_{\perp 1},\ v_{\parallel})$, $(v_{\perp 2},\ v_{\parallel})$, and $(v_{\perp 1},\ v_{\perp 2})$ planes corresponding to VISIONS-1 flight conditions for altitude range 589 km $\leq r \leq$ 695 km at t = 4 hours for Simulation B3 on Panels (a), (b), and (c) and Simulation B4 on Panels (d), (e), and (f).

Strong parallel potential structures impede ions from inhabiting high-altitudes such that statistical quality is reduced for low-populated spatial cells. At $r \sim 700$ km pressure cookers with reference parallel electric field $E_{\parallel 0} = 1 \times 10^{-6}\ \mathrm{V \cdot m^{-1}}$ energize ions to few eV counter-streaming conics with dominant downward components as seen in Panel (f) of Figure 4.13. Wave heating variations due to selections of $\lambda_\perp$ are more apparent at lower frequencies such that low-altitude energy differences between Simulations B3 and B4 are minimal as seen in Panels (d), (e), and (f) of Figure 4.14. Counter-streaming conic and bowl distributions exist for pressure cooker Simulations B3 and B4 with upward-tending asymmetries as seen in Panels (a), (b), (d), and (e) of Figure 4.16. Wave heating effects are reduced at VISIONS-1 altitudes due to scaling of reference power spectral density, S_0, to gyro-frequency by spectral index $\chi_\perp = 2.1$. Core ion populations of $E \sim 1$ eV reside around $\alpha \sim 90°$ and upward-drifting populations exist below $\alpha \sim 45°$. $E \sim 1$ eV particles isotropically inhabit all gyro-angles, θ, as seen in Panels (b) and (e) of Figure 4.18. All finite gyro-radius wave heating effects due to selections of $\lambda_\perp$ are minimal at VISIONS-1 altitudes such that the long wavelength approximation is consistent with pressure cooker transverse energization levels below $r \sim 1000$ km.

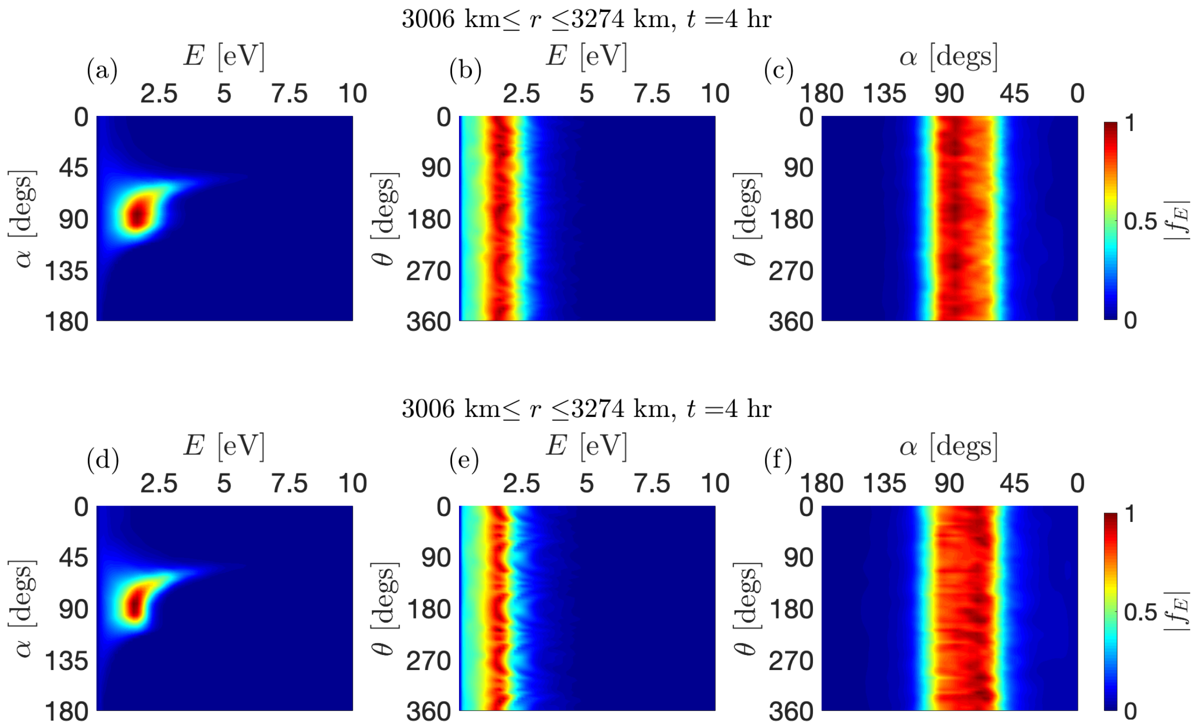

Figure 4.17: Normalized distribution functions in $(E,\ \alpha)$, $(E,\ \theta)$, and $(\alpha,\ \theta)$ planes corresponding to VISIONS-1 flight conditions for altitude range 3006 km $\leq r \leq$ 3274 km at $t = 4$ hours for Simulation B1 on Panels (a), (b), and (c) and Simulation B2 on Panels (d), (e), and (f).

It has been demonstrated in this section that transverse wavelengths exceed gyro-radii length-scales for $\lambda_\perp \sim 0.25$ m below $r \sim 2700$ km and self-limited heating occurs when $\lambda_\perp \lesssim 0.25$ m for heating parameters and altitudes parameterized from the VISIONS-1 flight. Although it has been verified theoretically by [Barghouthi and Atout, 2006] that characteristic electromagnetic turbulence wavelengths of $\lambda_\perp \sim 10$ km correspond to observed O^+ ion temperatures of 200 eV [Huddleston et al., 2000] at 4.8 R_E equator-ward the cusp, the validity of this value of $\lambda_\perp$ at low altitudes with different ion cyclotron interaction time-steps is not established. As seen in Figures 4.11 and 4.12 effects of finite gyro-radii are apparent above $r \sim 2700$ km where $\rho_g \sim \lambda_\perp$. Results presented here correspond to ion cyclotron resonance interaction time-steps $h = 0.48$ seconds. Increasing h results in more severe wave heating and serves to increase ρ_g for given wave powers and altitudes. It is expected that finite gyro-radius effects are enhanced for larger interaction time-steps owing to larger values of ρ_g relative to $\lambda_\perp$.

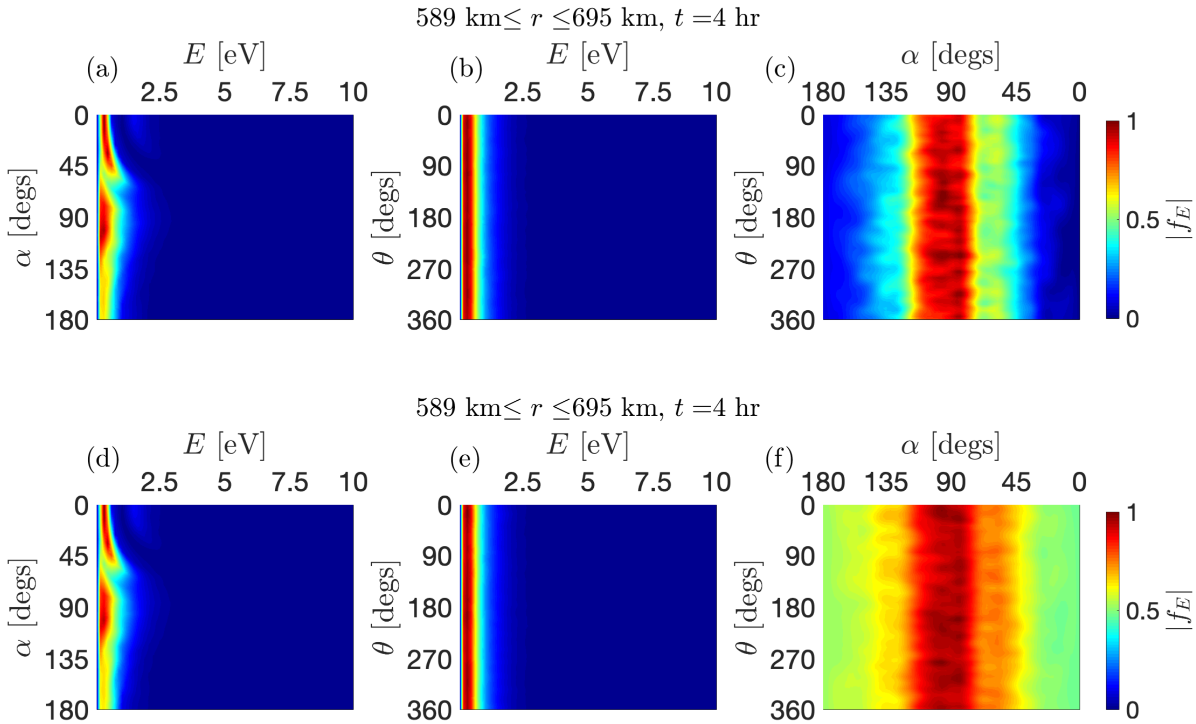

Figure 4.18: Normalized distribution functions in (E, α), (E, θ), and (α, θ) planes corresponding to VISIONS-1 flight conditions for altitude range 589 km $\leq r \leq$ 695 km at t = 4 hours for Simulation B3 on Panels (a), (b), and (c) and Simulation B4 on Panels (d), (e), and (f).

4.2.2 Modeling Observed Ionospheric Outflows

Table 4.2: VISIONS-1 case study pressure cooker simulations for initial conditions parameterized at the rocket flight for ion cyclotron resonance interaction time-steps, h, and reference parallel electric fields, $E_{\|0}$.

Simulation	h [s]	$E_{\|0}$ [$\mathrm{V \cdot m^{-1}}$]
C1	2.4	4×10^{-6}
C2	7.2	4×10^{-6}
C3	2.4	5×10^{-6}
C4	7.2	5×10^{-6}

At time-of-flight t_{of} = 591.3 seconds and altitude r = 718.9 km the VISIONS-1 sounding rocket detects enhanced VLF wave activity as seen in Figure 4.6. Wave heating parameters corresponding to this event consist of reference power spectral density $S_0 = 1.91 \times 10^{-10}\ \mathrm{V^2 \cdot m^{-2} \cdot Hz^{-1}}$ at reference gyro-frequency f_{g0} = 72.53 Hz and spectral index $\chi_\perp$ = 2.1 as discussed in Subsection 4.1.2.

Initial conditions are parameterized by PFISR radar plasma density and temperature measurements at the location and time of VISIONS-1 as discussed in Section 4.1. Subsection 4.2.1 demonstrates that modeled ion differential energy fluxes generated for S_0 and reference parallel electric fields, $E_{\|0}$, do not exceed 2-5 eV levels for long-wavelength ion cyclotron resonance approximations.

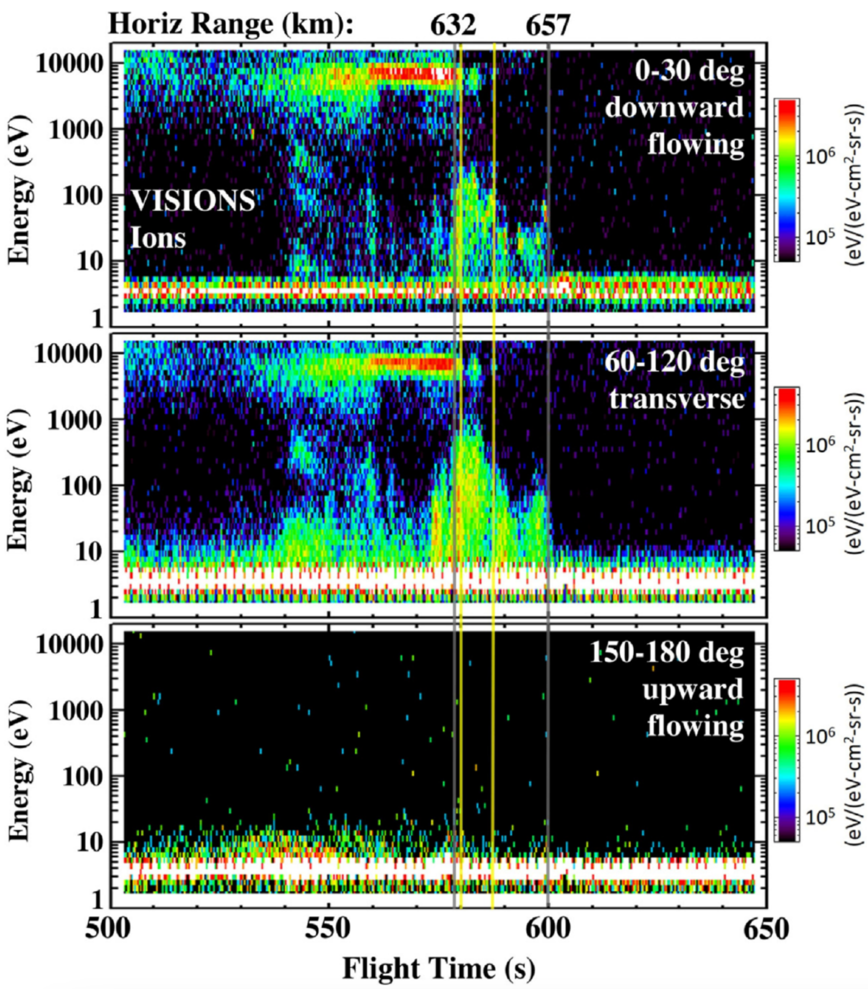

Figure 4.19: Differential ion energy flux observed by VISIONS-1 Electrostatic Ion Analyzer (EIA) during t_{of} = 500-650 seconds time-of-flight. Ion populations are sorted by pitch-angle to denote downward, transverse, and upward population components [Collier et al., 2015].

To model conditions pertaining to transverse and downward differential ion energy fluxes indicative of observed VISIONS-1 levels presented in Figure 4.19 the reference power spectral density is increased to $S_0 = 5 \times 10^{-7}$ V$^2 \cdot$ m$^{-2} \cdot$ Hz^{-1} at reference gyro-frequency $f_{g0} = 6.5$ Hz. These values are consistent with studies performed by [Wu et al., 2002] at high altitude and analyses in Section 3.2.4. Reference parallel electric fields are increased to $E_{\|0} = 4 \times 10^{-6}$ V $\cdot$ m^{-1} and $E_{\|0} = 5 \times 10^{-6}$ V $\cdot$ m^{-1} to generate reflection altitudes particular to parallel energy distributions.

Wave power spectral index $\chi_\perp = 2.1$ is employed per rocket VLF observations seen in Figure 4.6. In the absence of constraints on ion cyclotron resonance interaction time, $\tau_\perp$, selections of computational time-steps, h, set to resolve $\tau_\perp$ are linear in transverse heating rate, $\dot{W}_\perp$, as given by Equation 2.39. Perpendicular velocity kicks are performed on computational time-steps, h, with magnitudes scaled to those acting on interaction times, $\tau_\perp$; larger interaction time-steps result in larger perpendicular velocity kicks per Equation 2.33. In this section variations in transverse energization levels are modeled for four low-altitude pressure cookers with wave heating interaction time-steps $h = 2.4$ seconds and $h = 7.2$ seconds and reference parallel electric fields $E_{\parallel 0} = 4 \times 10^{-6}$ V $\cdot$ m^{-1} and $E_{\parallel 0} = 5 \times 10^{-6}$ V $\cdot$ m^{-1}. Parallel potential energy drop altitude profiles modeled are illustrated in Figure 4.20.

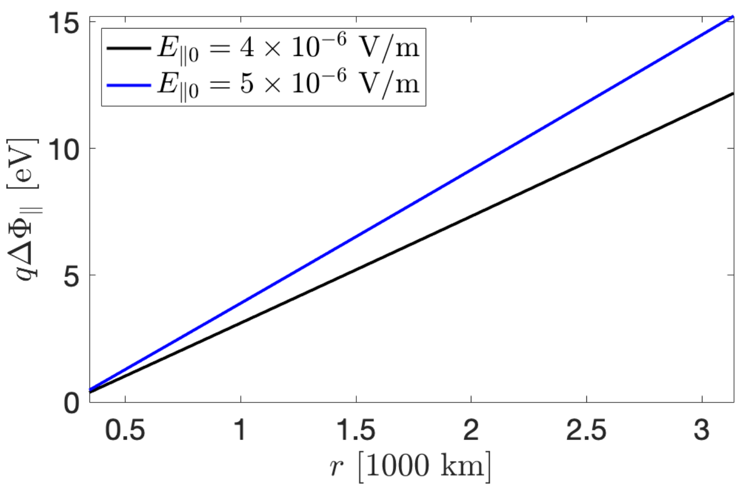

Figure 4.20: Potential energy drops in altitude for pressure cooker simulations with heating parameterization of VISIONS-1 flight and reference parallel electric fields $E_{\parallel 0} = 4 \times 10^{-6}$ V $\cdot$ m^{-1} and $E_{\parallel 0} = 5 \times 10^{-6}$ V $\cdot$ m^{-1}.

Four simulations, tabulated in Table 4.2, are performed to demonstrate transversely energized downward-drifting ion distributions, such as descending conics and bowls, exist limited to particle interaction times in potential structures and regions of resonant wave activity. Short pressure cooker altitude ranges inherit greater boundary escape fluxes and subsequent reductions in transverse energization levels. Observed ion distributions by VISIONS-1 at $r \sim 700$ km are transversely energized to levels characteristic of high wave power and/or high altitude. Below $r \sim 3000$ km simulated pressure cooker conditions produce downward and transverse ion populations characteristic of low-energy observations below $E \sim 25$ eV. Figures 4.21 and 4.22 illustrate ion moments for Simulations C1 and C4. Transverse energies of Simulation C4 exceed those of Simulation C1 by $E \sim 1$ eV owing to enhanced pressure cooker conditions from increased ion cyclotron interaction time-steps, h, and greater reference parallel electric fields, $E_{\parallel 0}$.

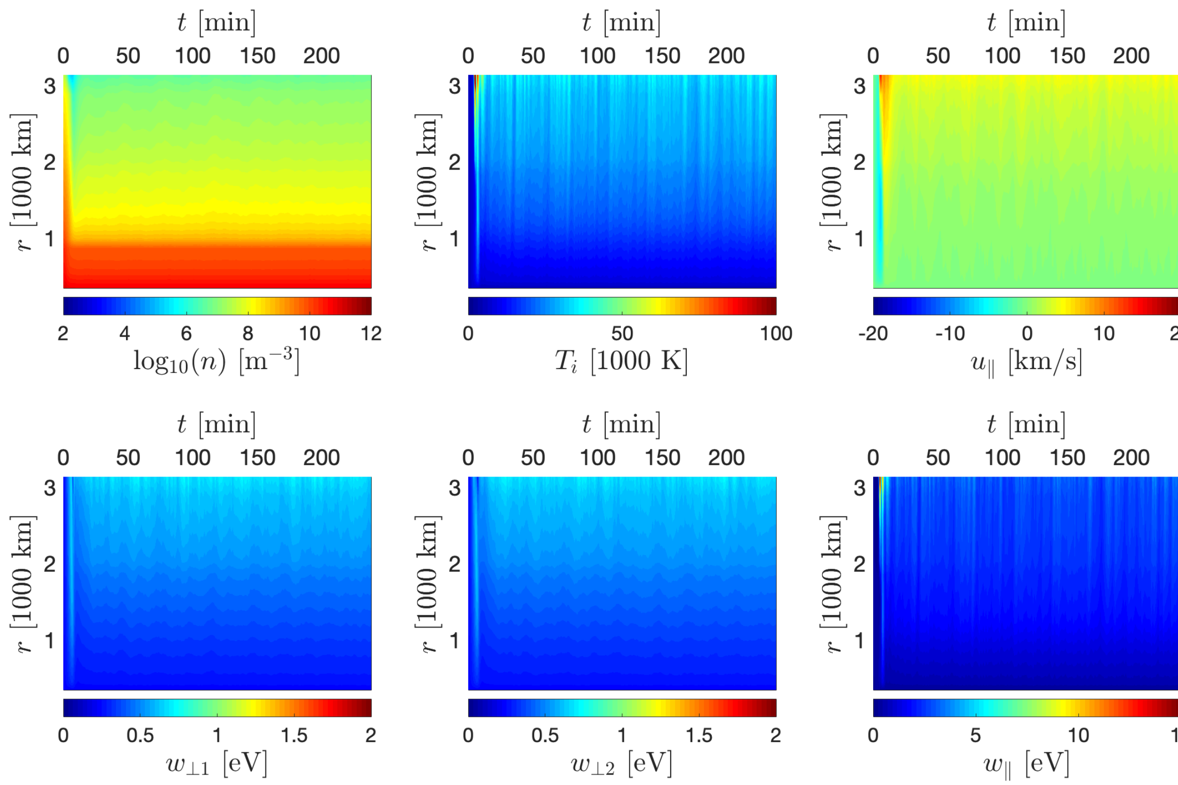

Figure 4.21: Plasma density, ion temperature, parallel plasma flow, and energies along $\hat{\mathbf{e}}_{\mathbf{v}_{\perp 1}}$, $\hat{\mathbf{e}}_{\mathbf{v}_{\perp 2}}$, and $\hat{\mathbf{e}}_{\mathbf{v}_{\|}}$ directions with pressure cooker conditions and wave heating parameterization from VISIONS-1 for Simulation C1 of Table 4.2.

Auroral acceleration region potential structures act to filter particles in altitude by parallel energy. High-velocity O^+ ions are able to overcome electrostatic barriers to inhabit high altitudes while cold injected ionospheric ions collect in regions of low resonant wave power below $r \sim 1000$ km as seen in Figure 4.22. Thermal populations of ions in kinetic equilibria closely approximating hydrostatic solutions are maintained at the lower boundary. Parallel energies exceed transverse energies for both Simulations C1 and C4 where strong parallel electric fields overwhelm adiabatic cooling rates of wave-driven magnetic moments. Downward-drifting plumes of wave-heated plasmas by parallel potential drops exist at $t = 5.2$ minutes, $t = 6.72$ minutes, $t = 5.2$ minutes, and $t = 5.76$ minutes for Simulations C1, C2, C3, and C4, respectively. Downward-drifting, or descending, conic distributions near $E \sim 10$ eV at plume events are apparent near $r \sim 700$ km as seen in Figures 4.23 and 4.24. Although parallel potential drops are considered to reside primarily at altitudes above those modeled [Bouhram et al., 2003a] [Wu et al., 2002] [Jasperse, 1998] [Gorney et al., 1985] [Bouhram et al., 2003b], for initial and background conditions simulate energized plumes in Figures 4.23 and 4.24 originate below $r \sim 3000$ km. High-altitude field-aligned potential structures act to more effectively heat ions as they are exposed to high-powered resonant wave-fields. Characteristic energies of descending conics presented in Figures 4.23 and 4.24 are particular to synergistic cooperations between altitude ranges, heating parameters, and reference parallel electric field values modeled.

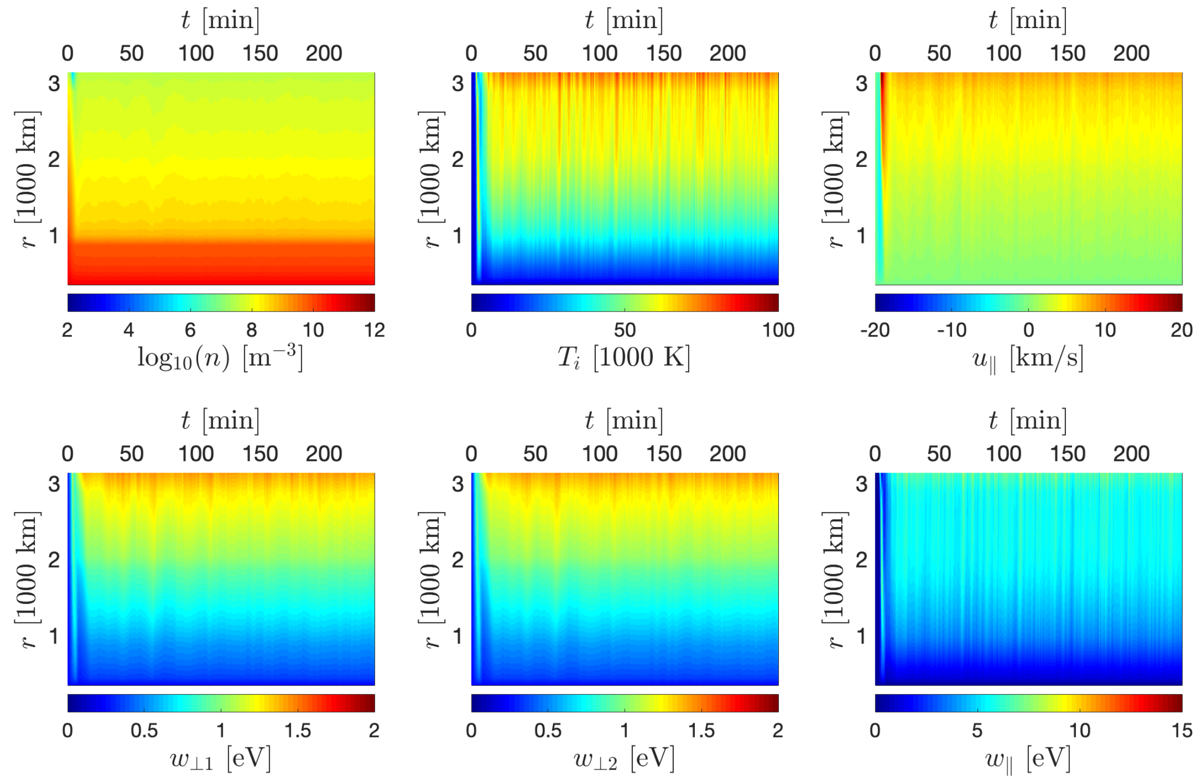

Figure 4.22: Plasma density, ion temperature, parallel plasma flow, and energies along $\hat{\mathbf{e}}_{\mathbf{v}_{\perp 1}}$, $\hat{\mathbf{e}}_{\mathbf{v}_{\perp 2}}$, and $\hat{\mathbf{e}}_{\mathbf{v}_\parallel}$ directions with pressure cooker conditions and wave heating parameterization from VISIONS-1 for Simulation C4 of Table 4.2.

Downward-drifting ion plumes energized by parallel potential drops exist for modeled pressure cooker environments of Table 4.2. Ion distribution functions range from moderately transversely energized thermal cores with strong downward components, seen in Panels (a), (b), and (c) of Figures 4.23 and 4.24, to elevated and descending conics distinctly separated by parallel velocity as seen in Panels (d), (e), and (f) of Figures 4.23 and 4.24. Particles are isotropically heated in gyro-phase such that distributions are symmetric in $v_{\perp 1}$ and $v_{\perp 2}$ directions as seen in Panels (c) and (f) of Figures 4.23 and 4.24. Sparse transverse and upward-drifting populations exist for low interaction time-steps while Simulations C2 and C4 incur counter-streaming ion conics. Greater values of $E_{\parallel 0}$ correspond to preferentially downward-drifting components of distributions shown in Figures 4.23 and 4.24.

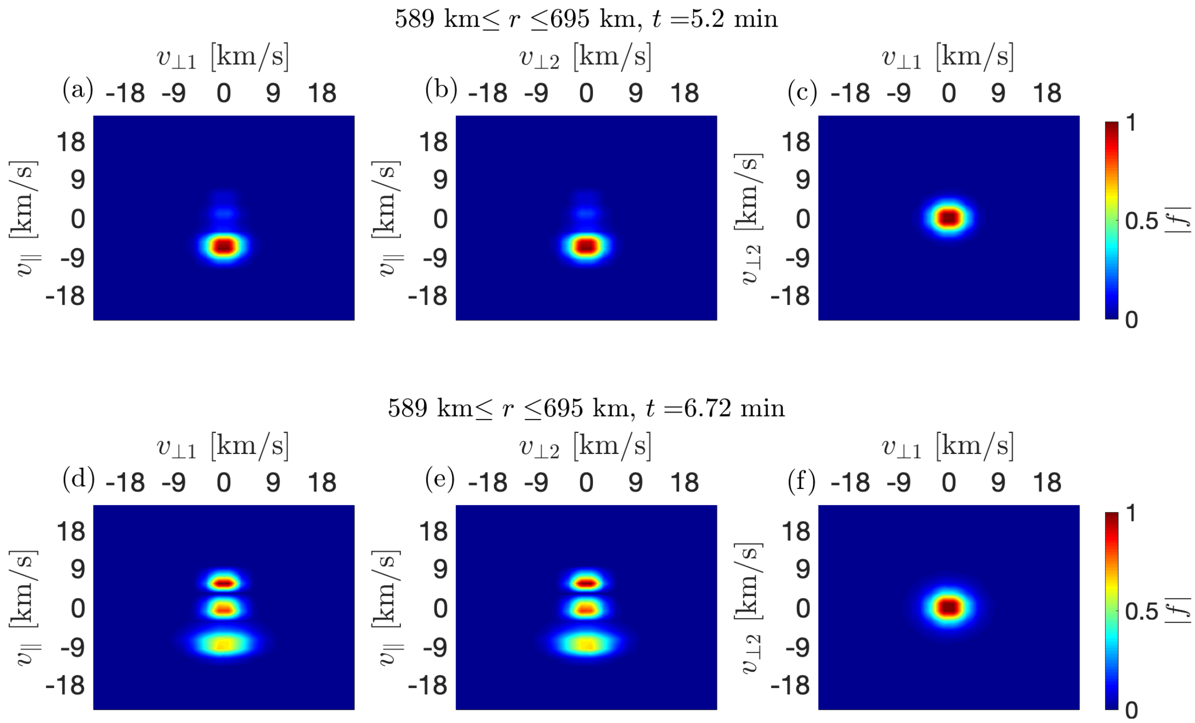

Figure 4.23: Normalized distribution functions in ($v_{\perp 1}$, $v_{\|}$), ($v_{\perp 2}$, $v_{\|}$), and ($v_{\perp 1}$, $v_{\perp 2}$) planes corresponding to VISIONS-1 flight conditions for altitude range 589 km $\leq r \leq$ 695 km at t = 5.2 minutes for Simulation C1 on Panels (a), (b), and (c) and t = 6.72 minutes for Simulation C2 on Panels (d), (e), and (f).

Ion differential energy fluxes recorded by the Electrostatic Ion Analyzer (EIA) aboard VISIONS-1 suggest that descending transversely energized ion populations exist at r = 718.9 km with $E \sim$ 10- 100 eV downward components and up to keV transverse components as seen in Figure 4.19 [Collier et al., 2015]. Downward ion fluxes peak near $E \sim$ 30-50 eV and transverse flux levels peak near $E \sim$ 30-100 eV as seen in Figure 4.19. Figures 4.26 and 4.26 show differential energy fluxes, ϕ_E, in units of [eV $\cdot$ eV^{-1} $\cdot$ m^{-2} $\cdot$ s^{-1} $\cdot$ sr^{-1}], sorted by pitch-angle, α, as measured from the outward direction of the local magnetic field, **B**. Phase-space distribution transformations to energy-pitch-angle distributions and field-aligned particle sorting is overviewed in Appendix .8. Normalized modeled energy fluxes emphasize relative populations in energy-space in general agreement to VISIONS-1 observations. At t = 6.72 minutes and $r \sim$ 700 km downward energy fluxes near $E \sim$ 10 eV exceed transverse components at these energies by roughly two orders-of-magnitude while upward components exceed transverse ones for Simulation C2 as seen in Figure 4.26.

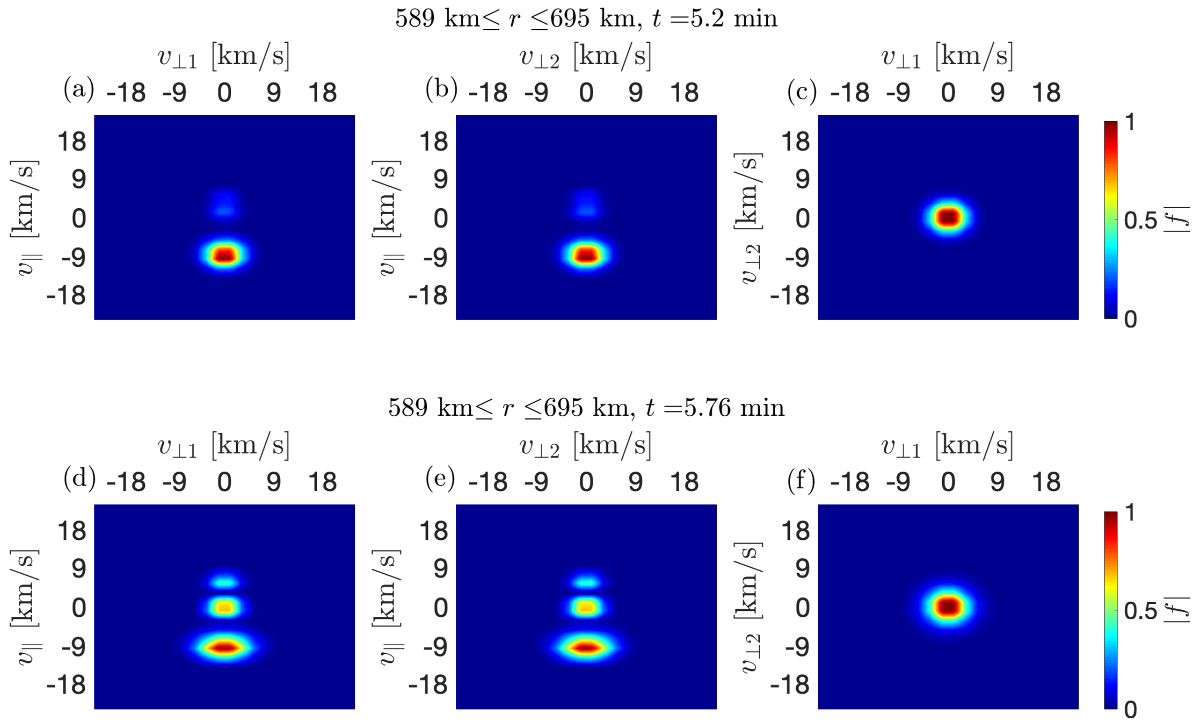

Figure 4.24: Normalized distribution functions in ($v_{\perp 1}$, $v_{\parallel}$), ($v_{\perp 2}$, $v_{\parallel}$), and ($v_{\perp 1}$, $v_{\perp 2}$) planes corresponding to VISIONS-1 flight conditions for altitude range 589 km $\leq r \leq$ 695 km at $t = 5.2$ minutes for Simulation C3 on Panels (a), (b), and (c) and $t = 5.76$ minutes for Simulation C4 on Panels (d), (e), and (f).

By $t = 4$ hours most low-energy plasma has escaped the lower boundary while wave-heated plasma produces transverse energy flux peaks near $E \sim$ 5-15 eV. Low transverse energy cores pertain to counter-streaming ions and high energies correspond to outflowing ions for Simulation C2 as seen in Panels (d) and (e) of Figure 4.23. With enhanced parallel potential drops of Simulation C4 the plume event at $t = 5.76$ minutes corresponds to dominant downward components as seen in Panels (a), (b), and (c) of Figure 4.27. Differential energy fluxes at low pitch-angles are prominent for lower reference parallel electric field selections and downward populations exist near $E \sim$ 5-15 eV for Simulations C2 and C4 as seen in Figure 4.25. Populated energy bins with suitable reference parallel electric fields are comparable to observations and transverse energy flux levels detected near $r \sim 700$ km by VISIONS-1 are greater than those produced by simulations of Table 4.2.

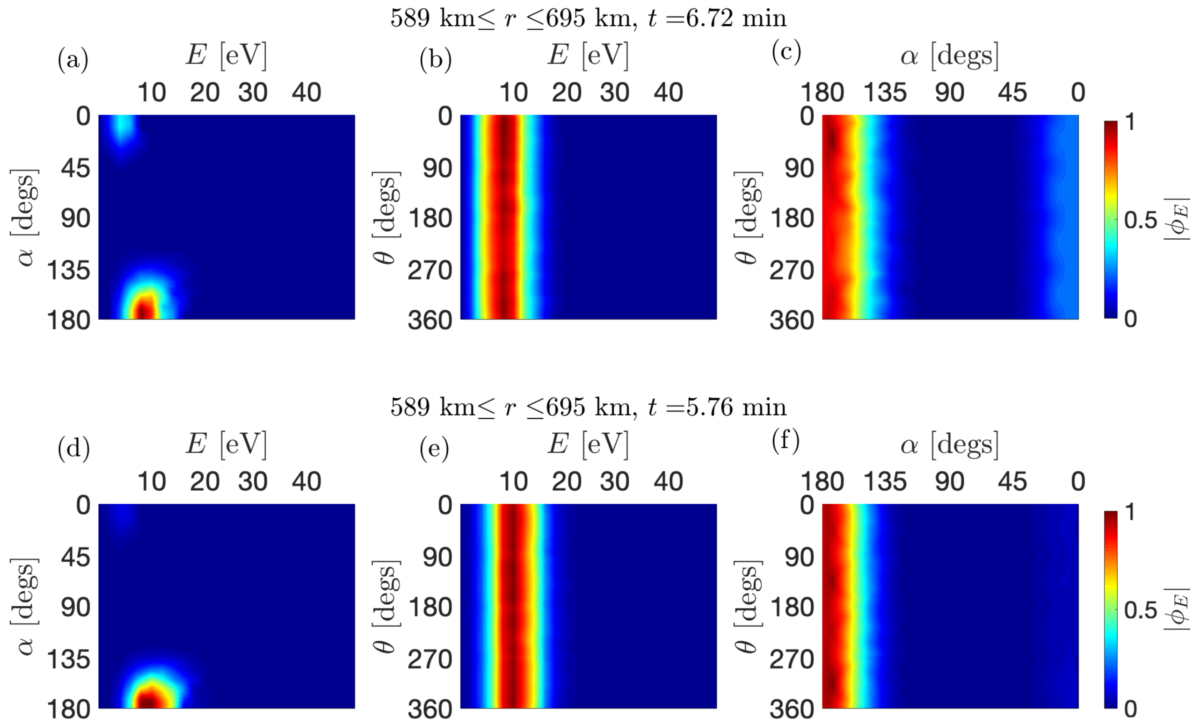

Figure 4.25: Normalized differential energy flux, $|\phi_E|$, in $(E,\ \alpha)$, $(E,\ \theta)$, and $(\alpha,\ \theta)$ planes corresponding to VISIONS-1 flight conditions for altitude range 589 km $\leq r \leq$ 695 km at $t = 5.2$ minutes for Simulation C2 on Panels (a), (b), and (c) and $t = 5.76$ minutes for Simulation C4 on Panels (d), (e), and (f).

In the absence of constrained transverse wavelengths, $\lambda_\perp$, ion cyclotron resonance interaction time-steps, h, pressure cooker altitude ranges, and reference parallel electric fields, $E_{\|0}$, simulations tabulated in Table 4.2 with wave heating parameters from VLF data of Figure 4.6 and initial conditions parameterized from PFISR radar data at the time and location of VISIONS-1 flight demonstrate that downward and transverse ion distributions modeled in non-localized $r \sim$ 400-3000 km altitude potential structures generate modeled differential energy fluxes of low-energy VISIONS-1 observations. Wave power spectral densities decrease at high frequencies at rates of $-\chi_\perp$ such that most significantly transversely energized ion distributions originate at high-altitude and are transported via parallel electric fields to VISIONS-1 altitudes of $r \sim$ 700 km. For $h = 7.2$ seconds and $E_{\|0} = 5 \times 10^{-6}$ V $\cdot$ m^{-1} of Simulation C4 the transition between upward and downward dominant conics resides between $r \sim$ 1100-1400 km as seen in Figure 4.28.

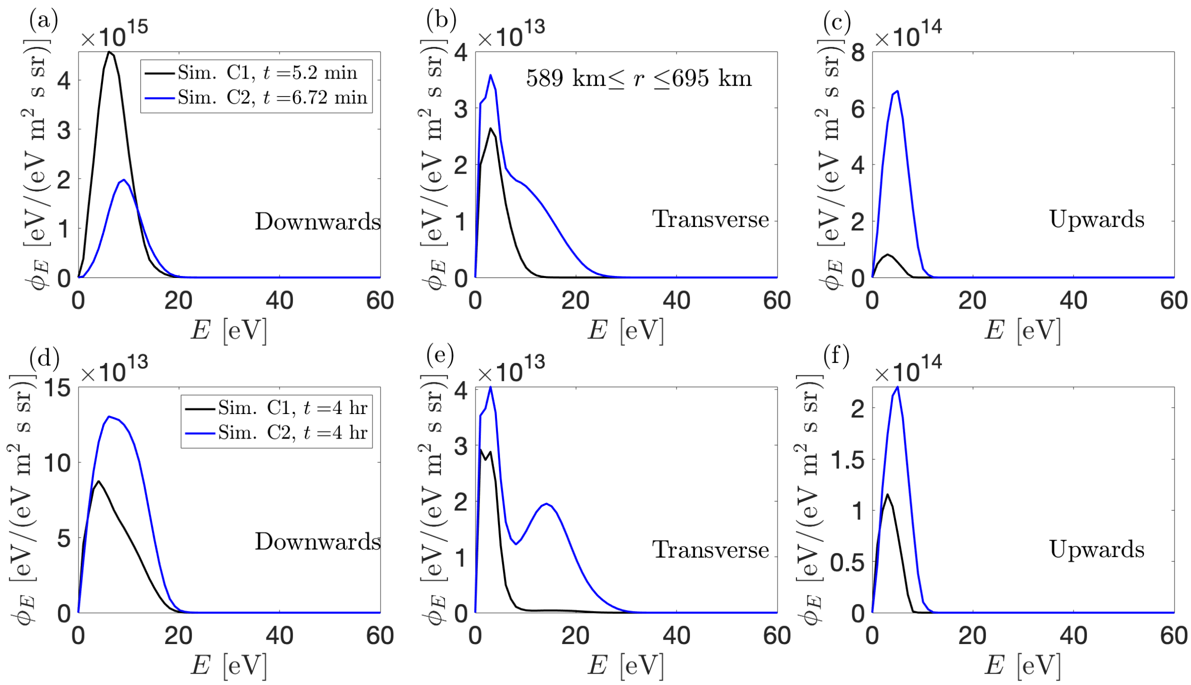

Figure 4.26: Reduced ion differential energy fluxes, ϕ_E, as a function of energy, E, for parameterized VISIONS-1 flight conditions corresponding to Simulations C1 and C2 as tabulated in Table 4.2.

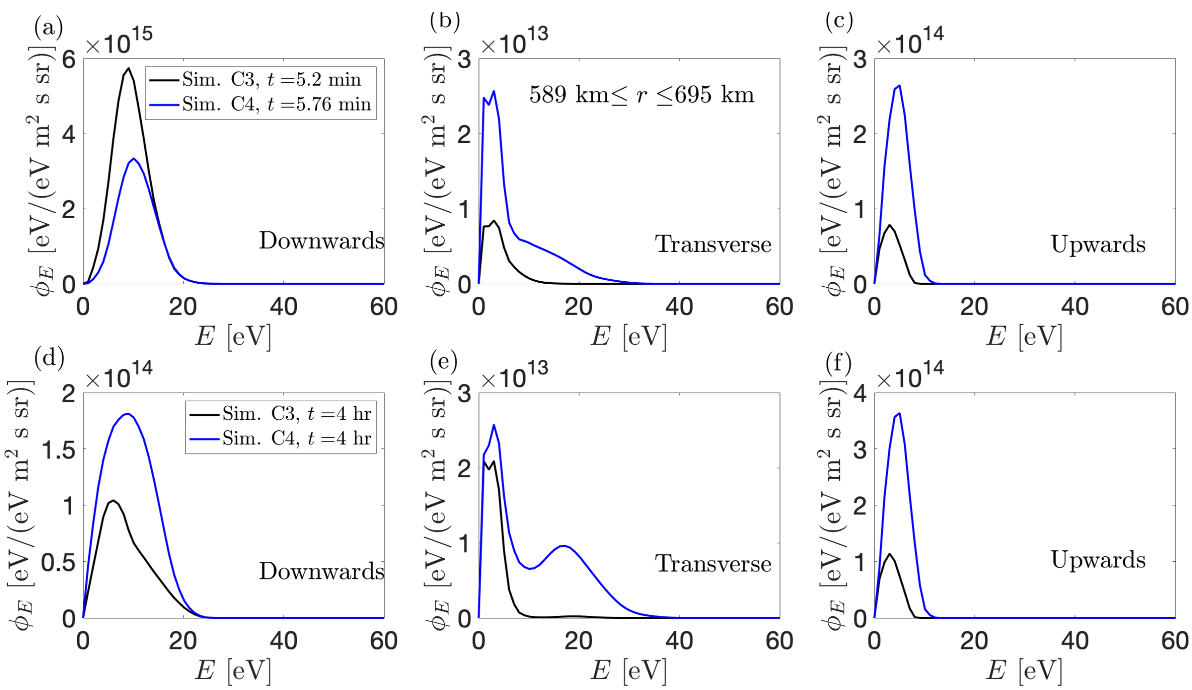

Figure 4.27: Reduced ion differential energy fluxes, ϕ_E, as a function of energy, E, for parameterized VISIONS-1 flight conditions corresponding to Simulations C3 and C4 as tabulated in Table 4.2.

Particles are preferentially lifted by wave-particle interactions or pushed down by parallel electric fields with few particles residing near zero parallel velocity from $r \sim$ 1100-1400 km. Below (above) this region reside downward (upward) drifting conics particular to parallel energy distributions- reflection points by parallel electric fields spread in altitude according to field-aligned momentum. Reflection regions correspond to approximately equal upward and downward forcing on ions of anisotropic temperature. Above pressure cooker reflection regions, as seen in Panels (a) and (b) of Figure 4.28, parallel motion is dominated by wave-particle interactions. Below this region parallel motion is driven by potential drops. Above the pressure cooker reflection region downward-drifting particles of wave-energized distributions lack the magnetic moments to overwhelm parallel potential drops and continue as descending conics until wave-driven mirror forces dominate and particles are reflected up to higher altitudes. Secondary ion populations form in pressure cooker reflection regions for given parallel energy distributions as seen in Panels (a) and (b) of Figure 4.28. Different reflection regions of pressure cooker conditions and parallel energy distributions are considered responsible for generating the multi-modal ion distributions seen in Figures 4.23, 4.24, and 4.28.

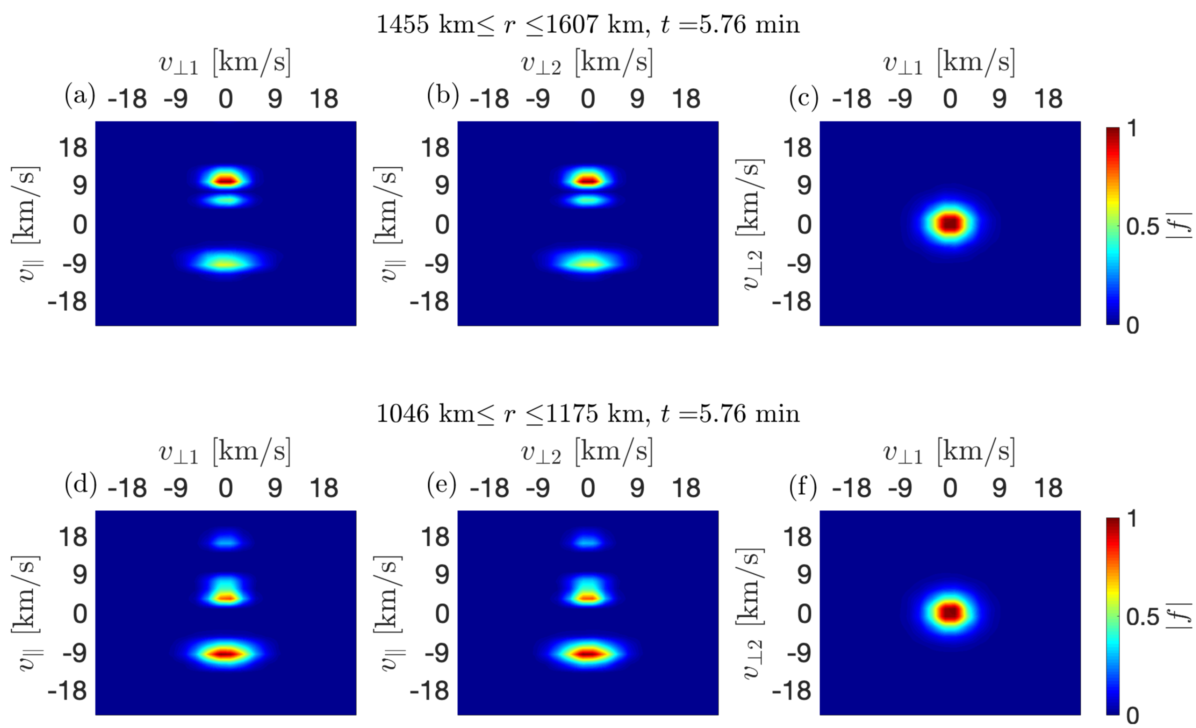

Figure 4.28: Normalized distribution functions in ($v_{\perp 1}$, $v_{\parallel}$), ($v_{\perp 2}$, $v_{\parallel}$), and ($v_{\perp 1}$, $v_{\perp 2}$) planes corresponding to VISIONS-1 flight conditions for altitude ranges 1046 km $\leq r \leq$ 1175 km and 1455 km $\leq r \leq$ 1607 km at t = 5.76 minutes for Simulation C4 of Table 4.2. The transition of upward and downward dominant ion conics denotes the pressure cooker reflection altitude.

Variations in parallel electric field magnitude and resonant wave power across flux-tubes and time determine relative counter-streaming populations and approximate outflow reflection regions. Pressure cooker reflection points limit wave power spectral density components resonant with ions by the dependence of $S_\perp$ on ω_g. This suggests that transversely energized ion populations may be transported from regions of increased wave power at low frequencies from high-altitude reflection regions that vary in time. Pressure cooker reflection regions- and approximate source locations of descending distributions- reside above the current magnetic flux-tube boundary for ion distributions with energies representative of VISIONS-1 observations. Initial hydrostatic density distributions may yield high quality statistics at high altitudes with sufficiently large initial plasma scale heights. Moderate scale heights with significant potential barriers produce poor statistics by the low number of macro-particles near upper boundaries. With expanded computational resources and suitable scale heights self-consistent modeling of magnetospheric wave-heated plasma transport to ionospheric altitudes by parallel potential structures beyond $r \sim 3000$ km is possible. This would enable the ability to self-consistently characterize source locations of highly energized descending ion conic distributions observed by VISIONS-1.

4.2.3 Localized Potential Structures

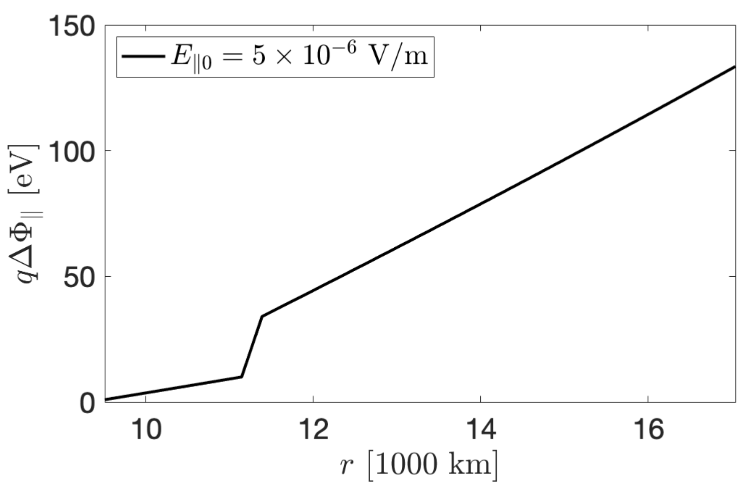

Figure 4.29: Potential energy drop in altitude localized above $r \sim 11000$ km for reference parallel electric field $E_{\|0} = 5 \times 10^{-6}$ V $\cdot$ m^{-1}.

A localized potential structure is imposed on wave-heated outflows where parallel electric field is enhanced by three times over nominal levels given by Equation 2.40 above $r \sim 11000$ km as seen in the potential energy profile of Figure 4.29. Ion cyclotron wave heating is applied onto plasmas in kinetic equilibrium in the absence of electron precipitation with reference wave spectral energy density $S_0 = 5 \times 10^{-7}$ V$^2 \cdot$ m$^{-2} \cdot$ Hz^{-1} at reference gyro-frequency $f_{g0} = 6.5$ Hz and spectral index $\chi_\perp = 2.1$ with ion cyclotron resonance interaction time-step of $h = 1.3$ seconds and transverse wavelength $\lambda_\perp = \infty$. Moments are seen in Figure 4.30. Ion populations are initially pushed downward at the initial pressure cooker plume event where wave-heated outward expansion lifts the system at $t \sim 20$ minutes. Cold injected ions generate large density gradients near $r \sim 11000$ km. As parallel electric fields increase by three times the original reference profile near $r \sim 11000$ km only particles with sufficient upward parallel velocity may inhabit regions above the potential localization. High potential drops at high altitudes produce low energy populations above $r \sim 15000$ km where maximum parallel energetics occur between $r \sim 12000$-15000 km as seen in Figure 4.30. High altitude populations have large parallel flows with counter-streaming populations consistent with low parallel energies between $r \sim 12000$-15000 km. Statistic fidelity at high altitude spatial cells is reduced for low particle counts.

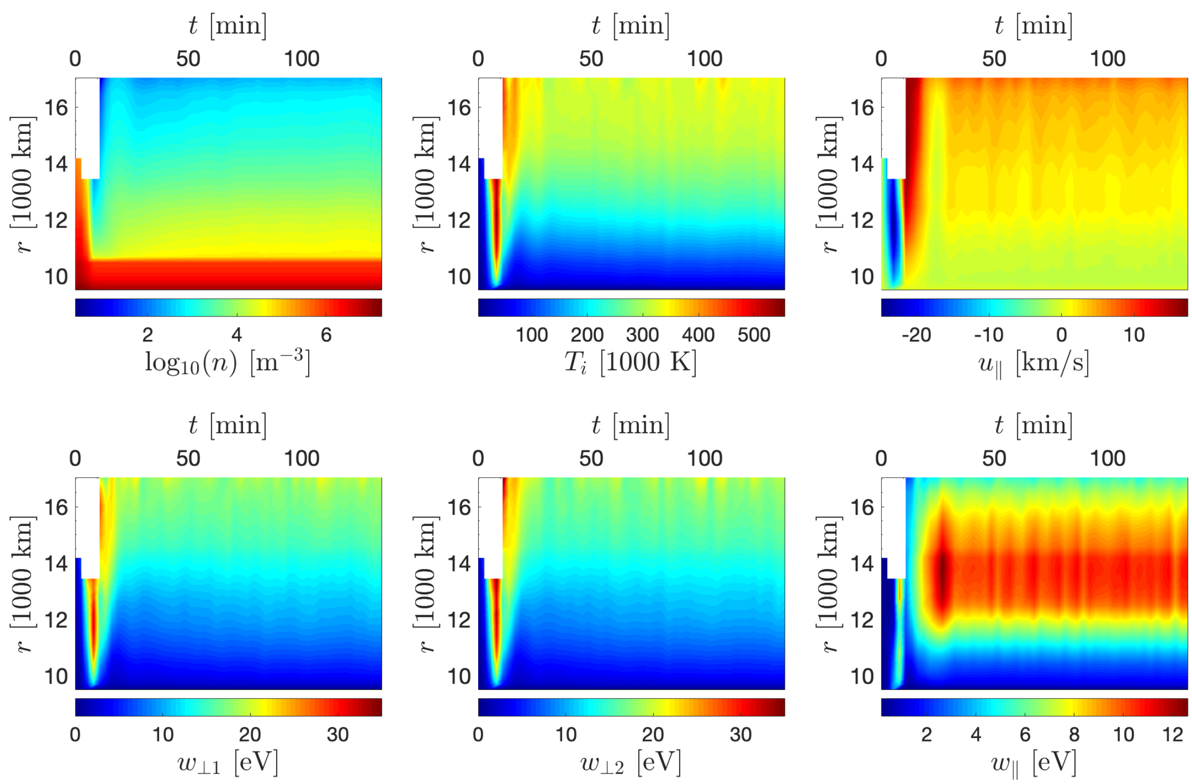

Figure 4.30: Plasma density, ion temperature, parallel plasma flow, and energies along $\hat{\mathbf{e}}_{\mathbf{v}_{\perp 1}}$, $\hat{\mathbf{e}}_{\mathbf{v}_{\perp 2}}$, and $\hat{\mathbf{e}}_{\mathbf{v}_\parallel}$ directions with high-altitude reference parallel electric field, $E_{\parallel 0} = 5 \times 10^{-6}$ V $\cdot$ m^{-1}, localized potential structure above $r \sim 11000$ km, wave heating parameterization from VISIONS-1 with wave power spectral index, $\chi_\perp = 2.1$, and ion cyclotron resonance interaction time-step $h = 1.3$ seconds.

Normalized ion distribution functions and differential energy fluxes in energy-pitch-angle space are illustrated in Figure 4.31. Near localized potential structure enhancements at $r \sim 11000$ km ion populations are separated by parallel velocity where core populations drifting upward near ~ 10 km $\cdot$ s^{-1} exist for pitch-angles less than $\alpha \sim 50°$ from $E \sim$ 10-40 eV. This primary population has the energy to overcome the potential barrier near $r \sim 11000$ km. A secondary population exists at higher energies ($E \sim$ 40-120 eV) near $\alpha \sim 90°$ as seen in Panel (d) of Figure 4.31. Particle energies are isotropically distributed in gyro-angle, θ, as seen in Panel (e) of Figure 4.31. It is noted that altering the potential drop profile in altitude results in different reflection altitudes for parallel ion energy distributions.

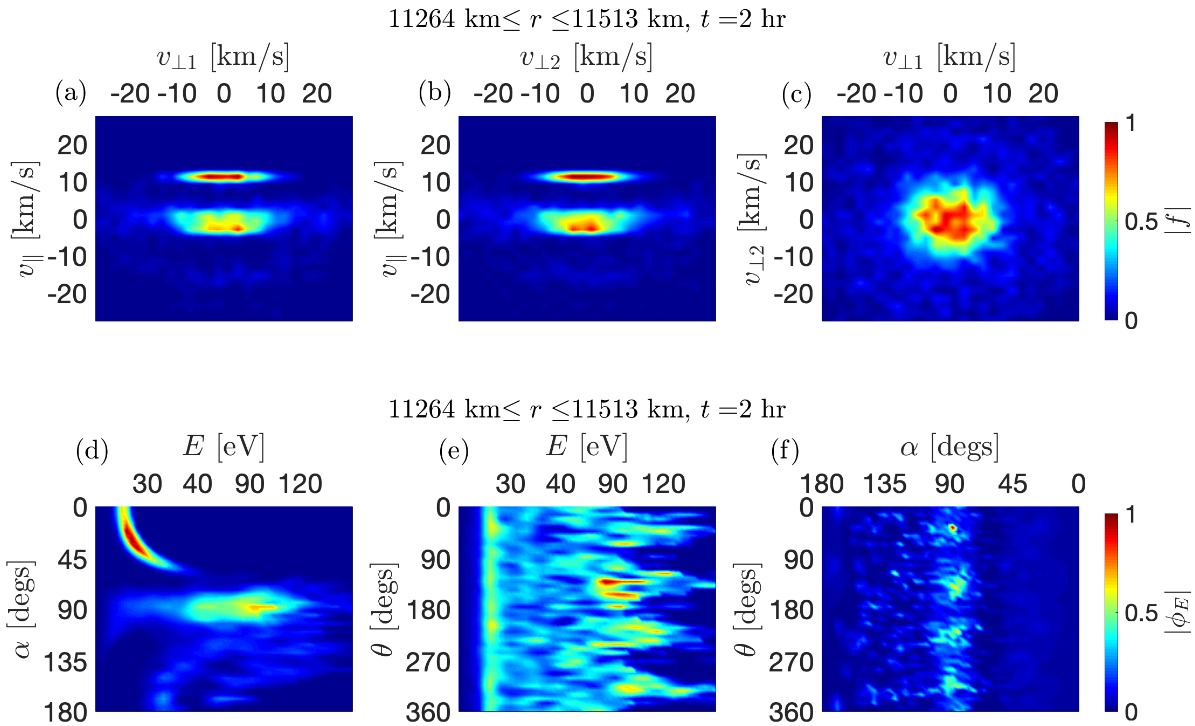

Figure 4.31: Normalized distribution functions in $(v_{\perp 1},\ v_{\|})$, $(v_{\perp 2},\ v_{\|})$, and $(v_{\perp 1},\ v_{\perp 2})$ planes at $t = 8.03$ minutes in Panels (a), (b), and (c), and normalized differential energy flux, $|\phi_E|$, in $(E,\ \alpha)$, $(E,\ \theta)$, and $(\alpha,\ \theta)$ planes in Panels (d), (e), and (f) with high-altitude reference parallel electric field $E_{\|0} = 5 \times 10^{-6}$ V $\cdot$ m^{-1} localized potential structure above $r \sim 11000$ km, wave heating parameterization from VISIONS-1 with wave power spectral index $\chi_{\perp} = 2.1$, and ion cyclotron resonance interaction time-step $h = 1.3$ seconds.

4.2.4 Magnetospheric Plasma Transport

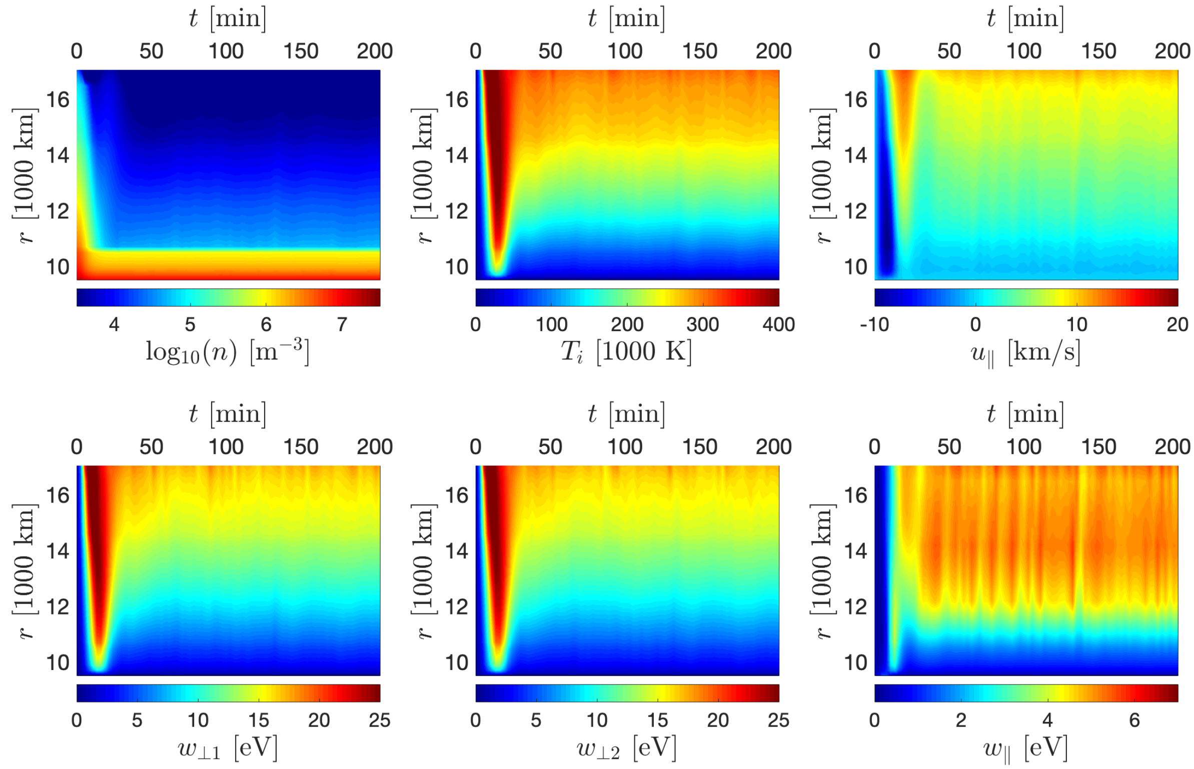

Figure 4.32: Plasma density, ion temperature, parallel plasma flow, and energies along $\hat{\mathbf{e}}_{\mathbf{v}_{\perp 1}}$, $\hat{\mathbf{e}}_{\mathbf{v}_{\perp 2}}$, and $\hat{\mathbf{e}}_{\mathbf{v}_{\parallel}}$ directions with high-altitude reference parallel electric field $E_{\parallel 0} = 5 \times 10^{-6}$ V · m^{-1}, wave heating parameterization from VISIONS-1 with wave power spectral index $\chi_\perp = 2.1$, and ion cyclotron resonance interaction time-step $h = 1.3$ seconds.

In this section high-altitude ($r \sim$ 1.5-2.5 R_E) pressure cookers are modeled to qualify the transport of descending ion conic and bowl distributions with observed differential energy fluxes to low altitudes ($r \sim$ 700 km) measured by the VISIONS-1 sounding rocket. Three high-altitude pressure cooker simulations are performed to generate high-altitude wave-heated ion conics drifting to low altitude by parallel electric fields with potential energy profiles of Figure 4.20. Initial thermal distributions are overwhelmed by pressure cooker environments and Maxwellian distributions morph into highly energized bowls and conics. Wave reference power spectral density is $S_0 = 5 \times 10^{-7}$ V^2 · m^{-2} · Hz^{-1} at reference gyro-frequency $f_{g0} = 6.5$ Hz. Reference parallel electric field $E_{\parallel 0} = 5 \times 10^{-6}$ V · m^{-1} is adopted with ion cyclotron resonance interaction time-step variations of $h = 1.3$ seconds (Figure 4.32), $h = 2.5$ seconds (Figure 4.33), and $h = 3.1$ seconds (Figure 4.34). Ion distributions and moments are computed on $\tau_i \sim 160$ seconds time intervals.

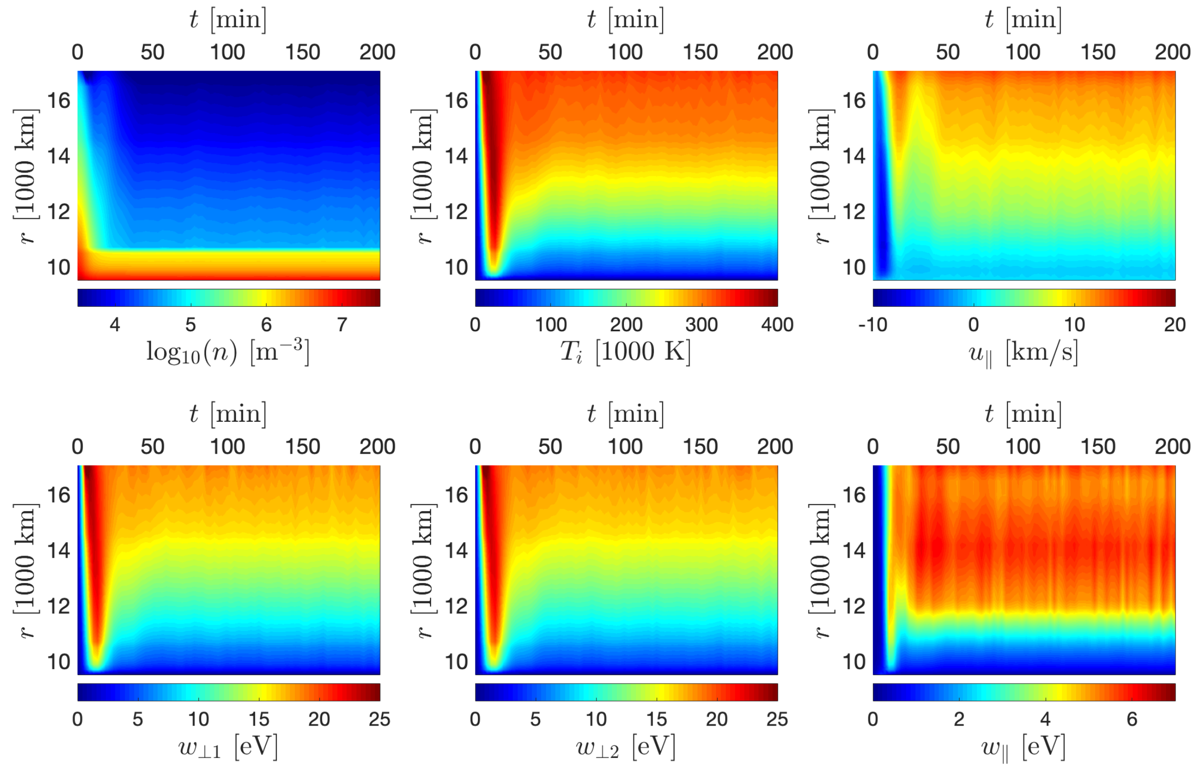

Figure 4.33: Plasma density, ion temperature, parallel plasma flow, and energies along $\hat{\mathbf{e}}_{\mathbf{v}_{\perp 1}}$, $\hat{\mathbf{e}}_{\mathbf{v}_{\perp 2}}$, and $\hat{\mathbf{e}}_{\mathbf{v}_{\parallel}}$ directions with high-altitude reference parallel electric field $E_{\parallel 0} = 5 \times 10^{-6}$ V · m^{-1}, wave heating parameterization from VISIONS-1 with wave power spectral index $\chi_{\perp} = 2.1$, and ion cyclotron resonance interaction time-step $h = 2.5$ seconds.

Initial downward-drifting plasma plumes appear at $t = 8.13$ seconds for $h = 1.3$ seconds, at $t = 8.06$ seconds for $h = 2.5$ seconds, and at $t = 8.03$ seconds for $h = 3.1$ seconds. With increased interaction time-step, h, particles are more effectively heated and above $r \sim 14000$ km, perpendicular energies, $w_{\perp 1}$ and $w_{\perp 2}$, exceed ~ 17 eV for $h = 3.1$ seconds. The $h = 1.3$ second case incurs perpendicular energies below ~ 17 eV above $r \sim 14000$ km. Plasma is initially pushed down by parallel potentials and wave-heated ions respond with outward expansion as seen by positive parallel drifts following initial downward plume events in Figures 4.32, 4.33, and 4.34. Parallel energy levels increase with selection of h due to adiabatic cooling. Low altitude ($r \lesssim 12000$ km) regions collect cold injected ions with moderate drifts. Lower boundary thermal injection generates significant density gradients below $r \sim 11000$ km. Due to the evacuation of particles from high altitudes from electrostatic ion traps statistical quality is reduced above $r \sim 14000$ km and moments should be accepted with discretion.

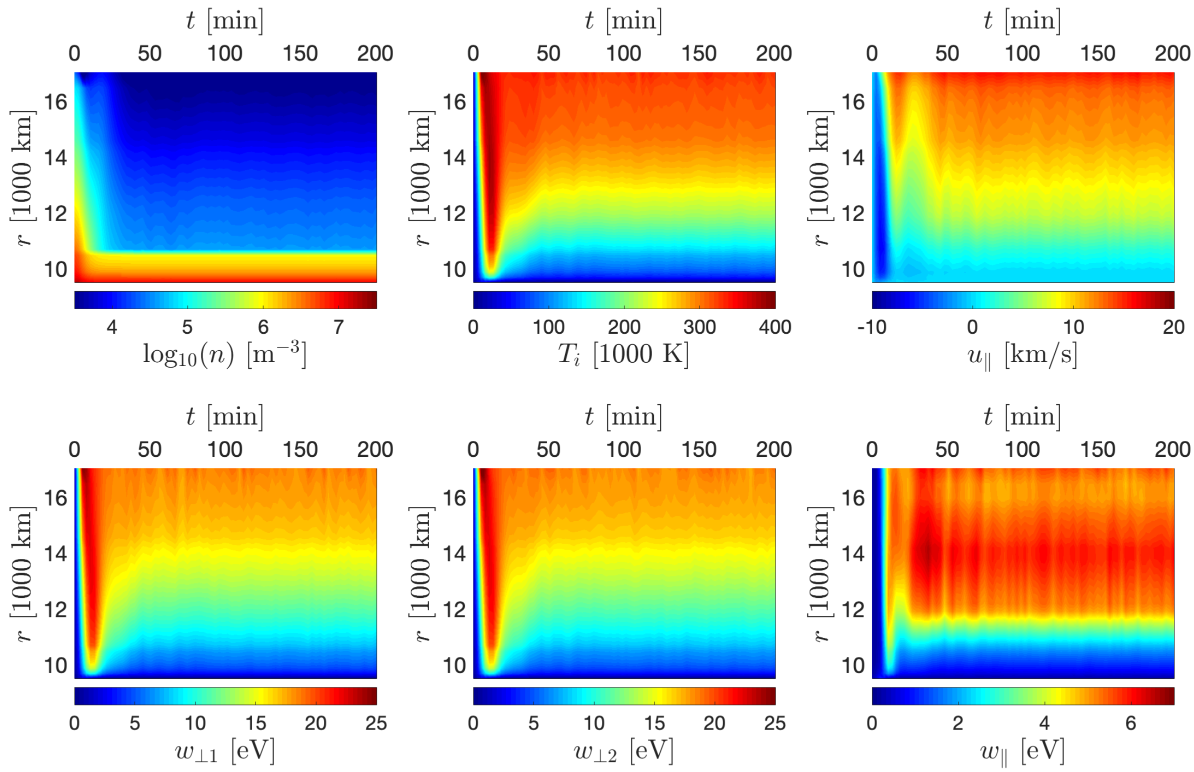

Figure 4.34: Plasma density, ion temperature, parallel plasma flow, and energies along $\hat{\mathbf{e}}_{\mathbf{v}_{\perp 1}}$, $\hat{\mathbf{e}}_{\mathbf{v}_{\perp 2}}$, and $\hat{\mathbf{e}}_{\mathbf{v}_{\parallel}}$ directions with high-altitude reference parallel electric field $E_{\parallel 0} = 5 \times 10^{-6}\ \mathrm{V} \cdot \mathrm{m}^{-1}$, wave heating parameterization from VISIONS-1 with wave power spectral index $\chi_{\perp} = 2.1$, and ion cyclotron resonance interaction time-step $h = 3.1$ seconds.

As wave-heated plasmas respond to initial downward plumes a moderate transversely energized population near zero parallel drift forms above highly transversely energized descending bowl distributions as seen in the normalized velocity distribution functions of Panels (a), (b), and (c) of Figures 4.35, 4.36, and 4.37. Adiabatic cooling by the mirror force folds conic wings upward to form ion bowl distributions. Parallel electric fields drive descending bowls in altitude. The extent of transverse energization of descending bowl and secondary thermal distributions is dictated by synergistic pressure cooker effects between wave heating parameters and potential drop magnitudes and altitude ranges. Velocity distributions are symmetric in the plane perpendicular due to non-preferentially heated transverse components as seen in Panels (c) of Figures 4.35, 4.36, and 4.37.

Normalized differential energy fluxes, $|\phi_E|$, in energy-pitch-angle space are shown in Panels (d), (e), and (f) of Figures 4.35, 4.36, and 4.37 for cases of $h = 1.3$ seconds, $h = 2.5$ seconds, and $h = 3.1$ seconds. High pitch-angle populations dominate during pressure cooker descending plume events with core distributions from $\alpha \sim 90°$-$180°$ at $E \sim 15$-70 eV for $h = 1.3$ seconds of Figure

4.35. Particles between $E \sim$ 15-40 eV are isotropically distributed in gyro-angle, θ, with extended high-energy tails. Most particles collect near $\alpha \sim 135°$ as seen in Panel (f) of Figure 4.35. For increased ion cyclotron resonance interaction time-steps bowl distributions have weak downward components relative to transverse. For h = 2.5 seconds core distributions form from $E \sim$ 15-80 eV primarily between α = 90°-135°. For h = 3.1 seconds core distributions at $E \sim$ 15-80 eV primarily reside between α = 90°-130°. Transverse energy enhancements serve to reduce high pitch-angle population numbers as seen in decreased energy fluxes at low energy and pitch-angles above $\alpha \sim 160°$ in Panels (d) of Figures 4.35, 4.36, and 4.37.

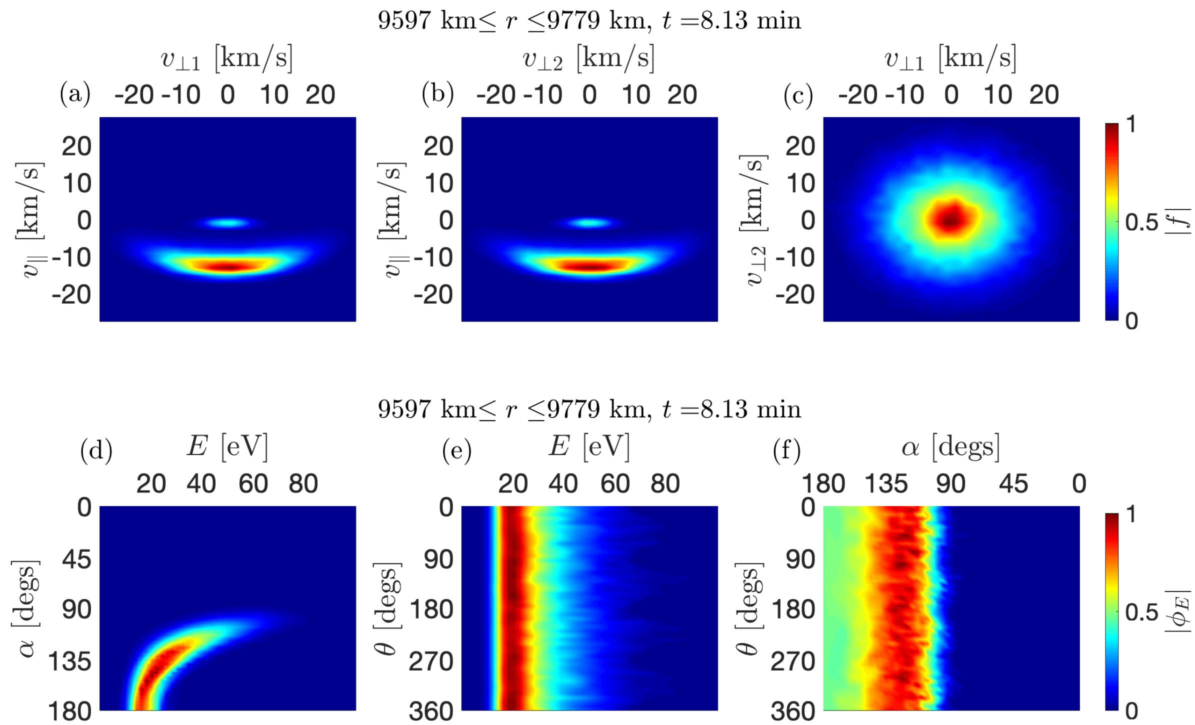

Figure 4.35: Normalized distribution functions in ($v_{\perp 1}$, $v_{\parallel}$), ($v_{\perp 2}$, $v_{\parallel}$), and ($v_{\perp 1}$, $v_{\perp 2}$) planes at t = 8.03 minutes in Panels (a), (b), and (c), and normalized differential energy flux, $|\phi_E|$, in (E, α), (E, θ), and (α, θ) planes in Panels (d), (e), and (f) with high-altitude reference parallel electric field $E_{\parallel 0} = 5 \times 10^{-6}$ V $\cdot$ m^{-1}, wave heating parameterization from VISIONS-1 with wave power spectral index $\chi_\perp$ = 2.1, and ion cyclotron resonance interaction time-step h = 1.3 seconds.

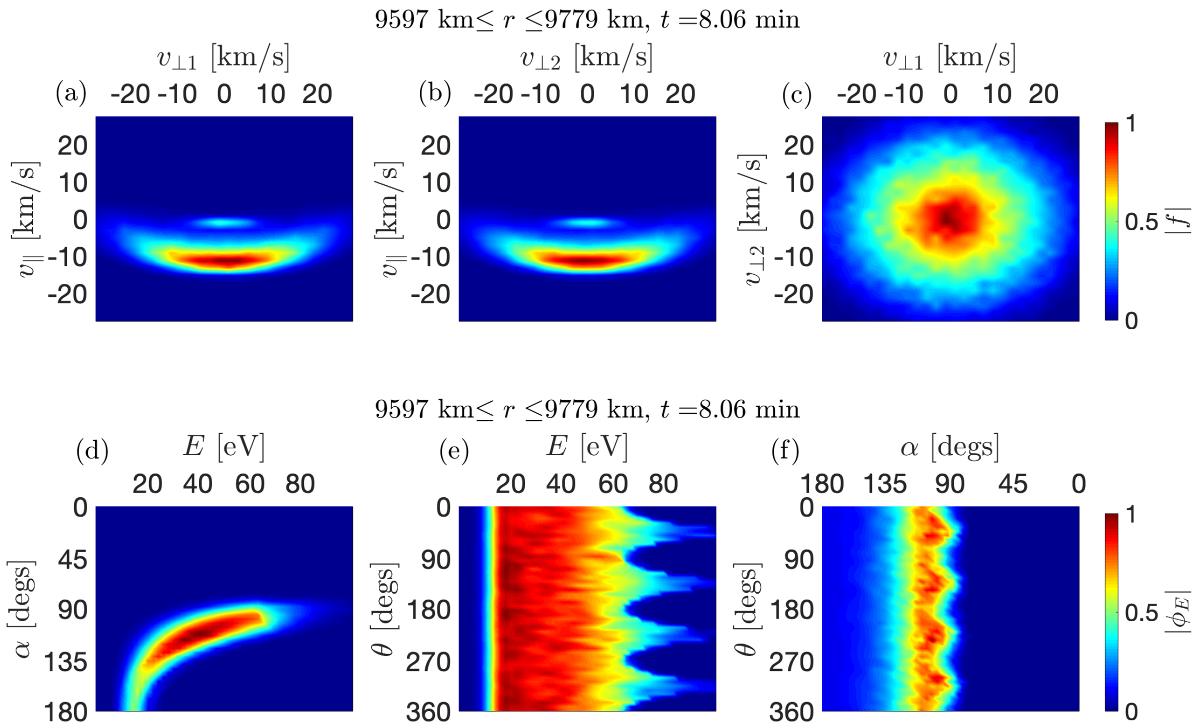

Figure 4.36: Normalized distribution functions in ($v_{\perp 1}$, $v_{\parallel}$), ($v_{\perp 2}$, $v_{\parallel}$), and ($v_{\perp 1}$, $v_{\perp 2}$) planes at $t = 8.03$ minutes in Panels (a), (b), and (c), and normalized differential energy flux, $|\phi_E|$, in (E, α), (E, θ), and (α, θ) planes in Panels (d), (e), and (f) with high-altitude reference parallel electric field $E_{\parallel 0} = 5 \times 10^{-6}$ V $\cdot$ m^{-1}, wave heating parameterization from VISIONS-1 with wave power spectral index $\chi_\perp = 2.1$, and ion cyclotron resonance interaction time-step $h = 2.5$ seconds.

Modeled differential energy fluxes for high-altitude pressure cookers parameterized to VISIONS-1 conditions denote core conic populations between $E \sim$ 20-80 eV near $r \sim 9500$ km of descending plasma plumes propagating in excess of $u_\parallel \sim 10$ km $\cdot$ s^{-1}. Descending bowl distributions from $E \sim$ 10-100 eV exist for $\alpha \sim 80°$-$180°$ for the $h = 3.1$ seconds case of Figure 4.37. Energy distributions sorted by pitch-angle denote transverse energies peaking near $E \sim 55$ eV at energy flux levels of $\phi_E \sim 2.4 \times 10^{12}$ eV $\cdot$ eV^{-1} $\cdot$ m^{-2} $\cdot$ s^{-1} $\cdot$ sr^{-1} for the case of $h = 3.1$ seconds as seen in Figure 4.39. Upward-drifting populations consist of particles with pitch-angles less than $\alpha = 30°$ such that $\phi_E = 0$ for plasma near the lower computational boundary at $r \sim 9600$ km as seen in Panels (c) and (f) of Figure 4.39. Descending low-altitude bowl distributions of magnetospheric origin are modulated by parallel energetics governed by competing wave-heated mirror forces and field-aligned potential drops. Since low-altitude resonance wave powers decrease at rates of $-\chi_\perp$ in frequency it is assumed that energized magnetospheric ion bowls and conics propagate downwards relatively unfettered from wave-driven upward expansion.

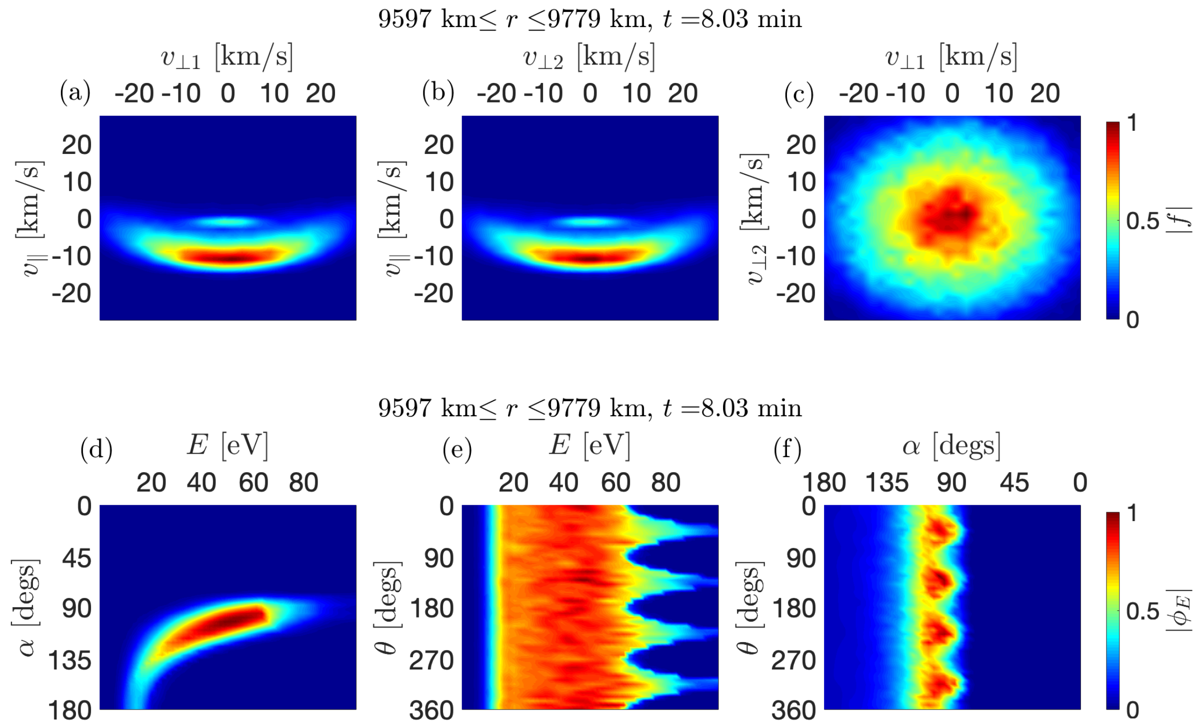

Figure 4.37: Normalized distribution functions in ($v_{\perp 1}$, $v_{\parallel}$), ($v_{\perp 2}$, $v_{\parallel}$), and ($v_{\perp 1}$, $v_{\perp 2}$) planes at $t = 8.03$ minutes in Panels (a), (b), and (c), and normalized differential energy flux, $|\phi_E|$, in (E, α), (E, θ), and (α, θ) planes in Panels (d), (e), and (f) with high-altitude reference parallel electric field $E_{\parallel 0} = 5 \times 10^{-6}$ V $\cdot$ m^{-1}, wave heating parameterization from VISIONS-1 with wave power spectral index $\chi_{\perp} = 2.1$, and ion cyclotron resonance interaction time-step $h = 3.1$ seconds.

Magnetospheric descending ion bowl distributions at the initial plume event at $r \sim 9600$ km have non-normalized levels of ϕ_E that exceed those observed at VISIONS-1 altitudes. During the initial plume event normalized transverse levels of ϕ_E account for the low-energy regime of observed VISIONS-1 ion fluxes from $E \sim$ 0-100 eV as seen in Figure 4.40 where the red square denotes area of comparison. Modeled downward components of ϕ_E during the initial plume peak near $E \sim$ 10-20 eV while observed downward components peak near $E \sim$ 30-40 eV as seen in Figure 4.40. Descending bowl distributions dissipate in time to become steady-state, moderately descending, downward-folded conics as seen in distribution functions and differential energy fluxes for $h = 3.1$ seconds in Figure 4.38.

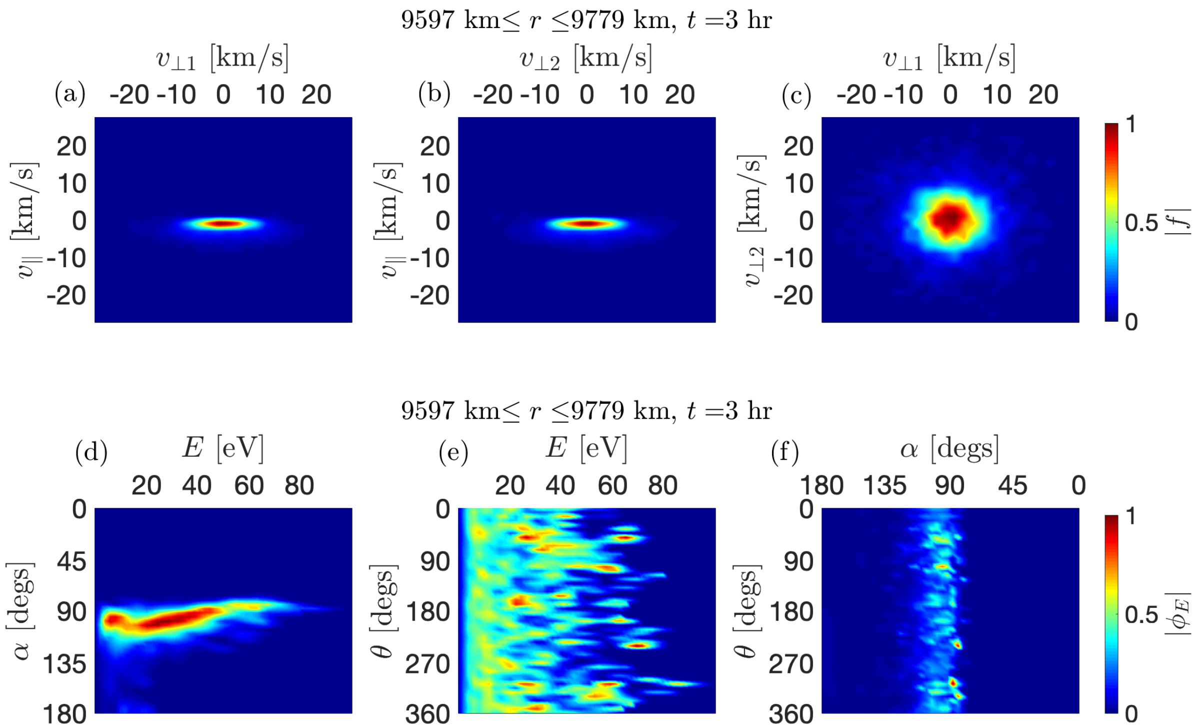

Figure 4.38: Normalized distribution functions in ($v_{\perp 1}$, $v_{\parallel}$), ($v_{\perp 2}$, $v_{\parallel}$), and ($v_{\perp 1}$, $v_{\perp 2}$) planes at $t = 3$ hours in Panels (a), (b), and (c), and normalized differential energy flux, $|\phi_E|$, in (E, α), (E, θ), and (α, θ) planes in Panels (d), (e), and (f) with high-altitude reference parallel electric field $E_{\parallel 0} = 5 \times 10^{-6}$ V · m^{-1}, wave heating parameterization from VISIONS-1 with wave power spectral index $\chi_{\perp} = 2.1$, and ion cyclotron resonance interaction time-step $h = 3.1$ seconds.

Steady-state descending conics at $t = 3$ hours correspond to differential energy fluxes in close agreement with VISIONS-1 observations as seen in Figures 4.39 and 4.40. By $t = 3$ hours three cases of h experience increases in downward energy flux near $E \sim$ 20-30 eV with peak fluxes at $\phi_E \sim 1 \times 10^{10}$ eV · eV^{-1} · m^{-2} · s^{-1} · sr^{-1} seen in Panel (d) of Figure 4.39. At this time the three cases generate peak transverse differential energy flux levels $\phi_E \sim 1.5 \times 10^{10}$-$2.6 \times 10^{10}$ eV · eV^{-1} · m^{-2} · s^{-1} · sr^{-1} from $E \sim$ 10-60 eV as seen in Panel (e) of Figure 4.39. At $r \sim 9600$ km transverse components of ϕ_E peak at higher energies than for downward components in consistent character with ion fluxes observed at $r \sim 700$ km by VISIONS-1.

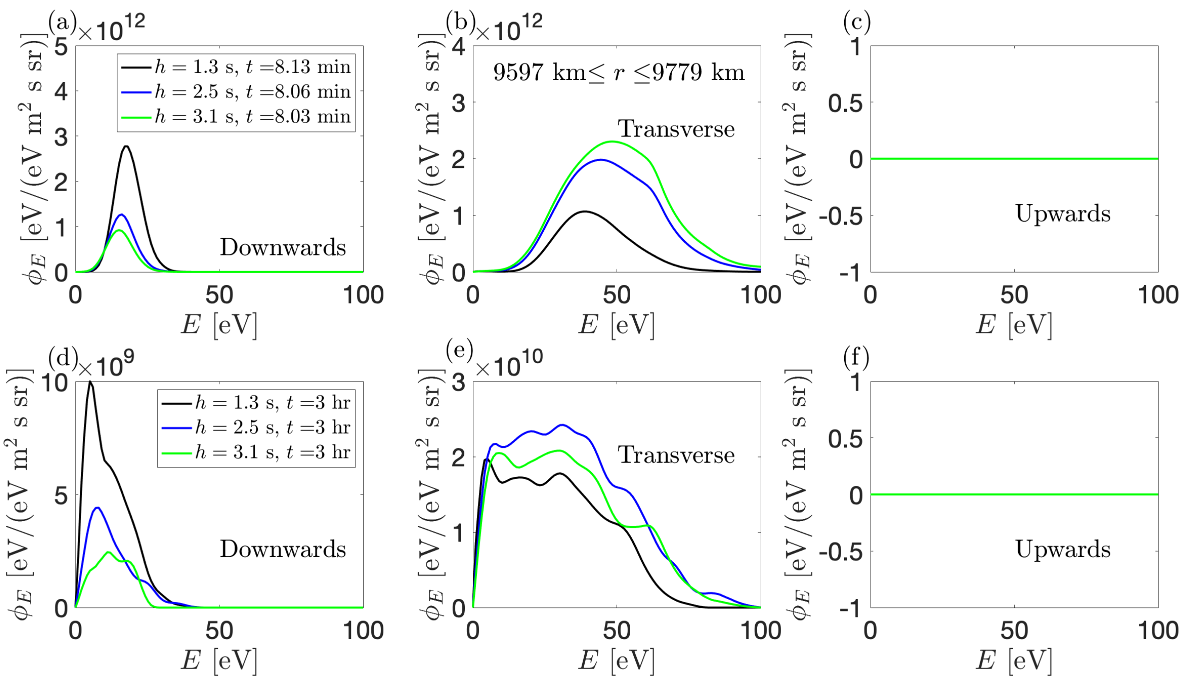

Figure 4.39: Reduced ion differential energy fluxes, ϕ_E, as a function of energy, E, with high-altitude reference parallel electric field $E_{\|0} = 5 \times 10^{-6}$ V $\cdot$ m^{-1} and wave heating parameterization from VISIONS-1.

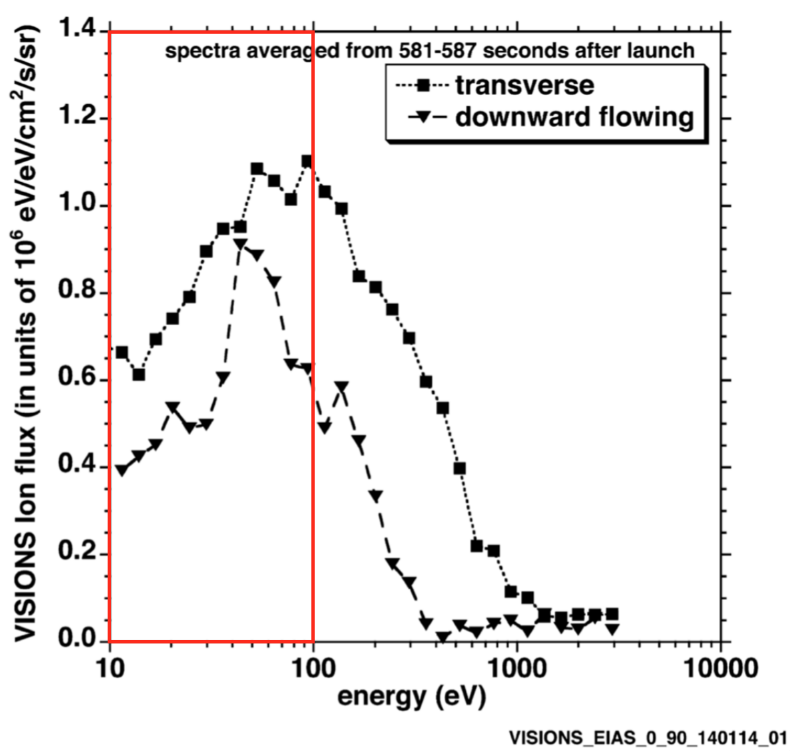

Figure 4.40: Differential ion energy flux observed by VISIONS-1 Electrostatic Ion Analyzer (EIA) from time-of-flight, t_{of} = 581-587 seconds [Collier et al., 2015].

Steady-state descending magnetospheric ion conic distributions modeled at $r \sim 9600$ km correspond closely to differential energy flux levels of transverse and downward ion populations observed by VISIONS-1 near $r \sim 700$ km as seen in Figures 4.39 and 4.40. This suggests the transport of transversely energized magnetospheric plasma to ionospheric altitudes by parallel electric fields. Parameterization of variations in parallel electric field structures and wave heating parameters- such as transverse wavelength, $\lambda_{\perp}$, and wave resonance interaction time-step, h- is required for the successful simulation of a discrete observation. Pressure cooker environments modeled in this study generate values of ϕ_E consistent with peak ion fluxes observed by VISIONS-1. Ions populating high-energy tails of transverse and downward parallel distributions are presumably exposed to more severe pressure cooker conditions. In actuality, pressure cooker parameters vary in space and time to produce a continuum of parallel particle energies and reflection regions resulting in energy flux ranges observed. It has been demonstrated in this section that, depending on parallel energy, transversely energized descending magnetospheric ion conics characteristic of detected VISIONS-1 ion energy flux levels are generated from pressure cooker reflection regions near or above $r \sim 9600$ km.

Chapter 5

CONCLUSION & FUTURE WORK

This dissertation introduces a fully kinetic direct simulation Monte Carlo (DSMC) model of ionospheric outflows subject to self-consistent ambipolar electric fields, gravitational and mirror forces, parallel potential drops, and parameterized sources of ion cyclotron resonance heating. Conditions of the VISIONS-1 sounding rocket flight are modeled and onboard differential ion energy flux measurements are reproduced via kinetic modeling of pressure cooker structures. O^+ ions are initialized in the model from Maxwellian velocity distributions corresponding to an input isotropic temperature with hydrostatic density profiles set by the plasma scale height. Thermal ion populations of hydrostatic initialization density and temperature are injected at the lower boundary on time-steps equal to the mean thermal ion transit time across the lower boundary ghost cell arc length. Particle trajectories are advanced via acceleration integration for position and velocity components in three-dimensional global Cartesian coordinates to account for local magnetic field line curvature. Three translational degrees-of-freedom exist for each particle in the global Cartesian system subject to field-aligned projections of self-consistent ambipolar electric, gravitational, and mirror forces, and parallel potential barriers. Two transverse degrees-of-freedom exist for each particle in the ion gyro-frame advanced by ion cyclotron resonance velocity diffusion or set to drift as transverse Maxwellian populations in the absence of resonant wave activity. Ion cyclotron interaction times, $\tau_\perp$, relative to computational time-steps, h, and self-limited wave heating mechanisms by gyro-radii surpassing transverse wavelengths, $\lambda_\perp$, are quantitatively analyzed as synergistic cooperations with parallel potential structures characterized by a reference parallel electric field, $E_{\|0}$. Guiding center approximations are valid until $r \sim 2.5\ R_E$ where particle trajectories should be described in a full Lorentz force formalism [Sauvaud and Delcourt, 1987] [Delcourt, 1985] [Delcourt et al., 1988] [Delcourt et al., 1989] [Delcourt et al., 1993] [Huddleston et al., 2005].

Validation of the kinetic model includes the capability to obtain kinetic equilibrium as a slight departure of the hydrostatic solution, particularly at collision-less high altitudes where fluid descriptions of non-thermalized plasmas break down [Schunk and Sojka, 1989] [Mitchell and Palmadesso, 1983]. Maxwellian distributions drift in three field-aligned velocity components- one parallel and two transverse- subject to gravitational and ambipolar forces. Self-consistent ambipolar electric fields are computed from actively updated moments of ion distribution functions and act to smooth significant density gradients. Soft magnetospheric electron precipitation-driven Type 2 ion upflows are simulated as periodic and monotonic electron temperature enhancements. Comparisons are made to finite gyro-radius modeling studies by [Barghouthi and Atout, 2006] and wave-heated pressure cooker simulations of the Dynamic Fluid Kinetic (DyFK) model by [Wu et al., 1999], [Wu et al., 2002], and [Zeng et al., 2006] are discussed. Introduction of wave-particle interactions includes considerations of ion cyclotron resonance interaction times, $\tau_\perp$. $\tau_\perp$ depends on particle parallel velocity, gyro-frequency, and the field-aligned extent of wave activity. Computational time-steps that resolve $\tau_\perp$ are referred to as ion cyclotron resonance interaction time-steps, $h < \tau_\perp$. Transverse wave-driven heating rates saturate when ion gyro-radii exceed perpendicular turbulence wavelengths, $\lambda_\perp$, such that self-limited heating mechanisms exist for velocity-dependent transverse diffusion coefficients. Since transverse diffusion variances are proportional to the root of $\tau_\perp$, particle distributions are transversely energized for larger interaction time-steps.

Electrostatic field-aligned potential barriers across regions of resonant wave activity produce pressure cooker environments where wave-heated plasmas rise by conversion of perpendicular to parallel energy and are separated in altitude according to parallel velocity- particles with high parallel energy overcome electrostatic potential barriers. Altitude ranges, heating parameters, and reference parallel electric fields of potential structures govern the ascent or descent of counter-streaming ion distributions. Sufficiently high parallel drops have the ability to generate downward-drifting populations with enhanced transverse energies and transfer high-altitude distributions to low altitudes. If modeled pressure cooker distributions produced by transverse heating rates at long wavelengths $\lambda_\perp > \rho_g$ correspond to observed ion fluxes then potential barrier altitude ranges and selections of $E_{\|0}$ must be constrained since stronger potential barriers have the ability to transfer energized ion populations down greater altitude ranges. The process is similar for short-wavelength analysis $\lambda_\perp < \rho_g$ where self-limited heating is more likely to occur at high-altitudes at moderate values of $E_{\|0}$ or sufficiently strong low-altitude pressure cookers. Altering the L-shell to more severe values acts to increase the local magnetic field strength at a given altitude thus increasing the ion gyro-frequency and subjecting particles to low-power waves.

The parameter space of reference wave power, S_0, transverse wavelength, $\lambda_\perp$, ion cyclotron interaction time-step, h, reference parallel electric field, $E_{\|0}$, and potential structure altitude profiles and ranges are thought to vary in space and time. In actuality, continuous values of these parameters exist to produce ranges of parallel energies and reflection altitudes. Realistic constraints on these parameters must be imposed to computationally reproduce particular ionospheric and magnetospheric conditions. Transverse energies, $w_\perp$, of wave-heated outflows in electrostatic potential structures are dictated primarily by particle interaction times and length-scales of potential barriers and regions of significant resonant wave activity. Ions exposed to high-power wave-energization in magnetospheric pressure cookers are spread by penetrating parallel energy along the flux-tube. Larger interaction time-steps, h, increase particle gyro-radii to longer transverse wavelength scale sizes and expose heating rate saturation levels to larger wavelength wave-fields. Information of wave interaction region scale sizes or transverse wavelength variations in space and time is required to constrain h and $\lambda_\perp$ parameters. Pressure cooker reflection points of wave-driven outflows depend on relative upward and downward forces. Low-altitude parallel energetics are governed by synergistic relations between two processes: the transfer of high-altitude ions heated at high-power to low altitudes by strong parallel electric fields, and the ability of particle magnetic moments to adiabatically convert perpendicular to upwards parallel energy. Both mechanisms depend on altitude ranges modeled- $w_\perp$ depends interaction length-scales of resonant wave-fields and electrostatic potential structures.

It has been shown by previous studies that characteristic electromagnetic turbulence wavelengths of $\lambda_\perp \sim 10$ km correspond to observed O^+ ion temperatures of 200 eV [Huddleston et al., 2000] at 4.8 R_E equator-ward of the cusp [Barghouthi and Atout, 2006]. Perpendicular heating levels from ion cyclotron resonance sources parameterized from VISIONS-1 flight conditions generate ion conics with mean gyro-radii below the transverse wave turbulence wavelength. Self-limiting perpendicular heating rates do not saturate for $\lambda_\perp \sim 0.25$ m and pressure cooker altitudes and/or reference potentials do not produce heating levels corresponding to $\rho_g > \lambda_\perp$ for modeled VISIONS-1 conditions. For considered wave heating levels at rocket altitudes near $r \sim 700$ km the long wavelength approximation of velocity-dependent wave heating is applicable and $\rho_g < \lambda_\perp$. Ion energy fluxes observed by VISIONS-1 correspond to plasmas transported from high-altitude wave-energized distributions to rocket altitudes by strong parallel electric fields. Observed ion fluxes correspond to low-altitude bowl and conics with energies characteristic of high-altitude magnetospheric descending bowl and conic distributions. This study demonstrates that ion differential energy fluxes recorded by the Electrostatic Ion Analyzer (EIA) instrument aboard VISIONS-1 at $r \sim 700$ km correspond to descending magnetospheric ion conic distributions originating from pressure cooker reflection regions near or above $r \sim 9600$ km. In order to reproduce differential ion energy flux levels near $E \sim 50$ eV as observed by VISIONS-1 the following conditions are required: 1) ion cyclotron wave heating of ions well-above the VISIONS-1 rocket, 2) increase wave power spectral densities substantially from observed spectrum at low rocket altitude as suggested by strong altitude dependence of wave power, and 3) strong parallel electric fields much higher than rocket altitude to drive transversely energized non-Maxwellian distributions down in altitude. Future work includes the exploration of refined parameter-space, further localization of parallel electric fields, anisotropic wave heating in the transverse plane, and modeling of energetic neutral atoms (ENAs) produced by charge-exchange between outflowing ions and background neutral populations as detected by the VISIONS-1 MILENA instruments. This project provides quantitative means to interpret VISIONS-1 data and related remote sensing approaches to study ion outflows and serves to advance our understanding of drivers and particle dynamics in auroral ionosphere and magnetosphere conditions and to improve data analysis for future sounding rocket and satellite missions.

Appendices

APPENDICES

.1 Earth's Magnetic Field

Earth's magnetic scalar potential, Φ_M, with magnetic moment, $\mathbf{M} = M_0\hat{\mathbf{e}}_\mathbf{z}$, magnetic field, $\mathbf{B}$, azimuthal symmetry without free currents ($\mathbf{J} = 0$) is given by Laplace's equation, $\nabla^2\Phi_M = 0$, which has well-known solutions in terms of Legendre polynomials of order l, $P_l[\cos(\theta)]$, [Wohlwend, 2008]:

$$\Phi_M = \sum_{l=0}^{\infty} \left[A_l r^l + B_l r^{-(l+1)}\right] P_l[\cos(\theta)], \tag{1}$$

where A_l and B_l are constants yet to be determined. Infinitely away from Earth the magnetic potential is zero (i.e., $\Phi_M \to 0$ as $r \to \infty$) and at zero distance from Earth the magnetic potential is infinite (i.e., $\Phi_M \to \infty$ as $r \to 0$). As a result $A_l \to 0$ for $r^l \to \infty$ and $B_l \to 0$ for $r^{-(l+1)} \to \infty$. Where $R_E \approx 6371$ km is the Earth's radius, for $r < R_E$, the magnetic potential is

$$\Phi_{M,\mathrm{in}} = \sum_{l=0}^{\infty} A_l r^l P_l[\cos(\theta)], \tag{2}$$

and for $r > R_E$ the magnetic potential is

$$\Phi_{M,\mathrm{out}} = \sum_{l=0}^{\infty} B_l r^{-(l+1)} P_l[\cos(\theta)]. \tag{3}$$

Magnetic potential is equal across the interface at $r = R_E$ such that $(\Phi_{M,\mathrm{in}})_{r=R_E} = (\Phi_{M,\mathrm{out}})_{r=R_E}$ [Wohlwend, 2008]:

$$\sum_{l=0}^{\infty} A_l R_E^l P_l[\cos(\theta)] = \sum_{l=0}^{\infty} B_l R_E^{-(l+1)} P_l[\cos(\theta)],$$

and

$$A_l = B_l R_E^{-(2l+1)}. \tag{4}$$

Radial divergence of the magnetic field is equal across the interface at $r = R_E$ such that $(\mathbf{B}_\mathrm{in} \cdot \hat{\mathbf{e}}_\mathbf{r})_{r=R_E} = (\mathbf{B}_\mathrm{out} \cdot \hat{\mathbf{e}}_\mathbf{r})_{r=R_E}$ and

$$(\nabla\Phi_{M,\mathrm{out}} \cdot \hat{\mathbf{e}}_\mathbf{r})_{r=R_E} = (\nabla\Phi_{M,\mathrm{in}} \cdot \hat{\mathbf{e}}_\mathbf{r})_{r=R_E} - M_0\cos(\theta), \tag{5}$$

where $\mathbf{B}_{\text{out}} = \mu_0 \mathbf{H}_{\text{out}}$, $\mathbf{B}_{\text{in}} = \mu_0(\mathbf{H}_{\text{in}}+\mathbf{M})$, $\mathbf{H}_{\text{out}} = -\nabla\Phi_{M,\text{out}}$, $\mathbf{H}_{\text{in}} = -\nabla\Phi_{M,\text{in}}$, $\mathbf{M}\cdot\hat{\mathbf{e}}_{\mathbf{r}} = M_0\cos(\theta)$, $\mu_0 = 4\pi\times 10^{-1}\ \mathrm{N}\cdot\mathrm{A}^{-2}$ is the magnetic permeability of free space, $\mathbf{H}$ is the auxiliary magnetic field, and $\mathbf{M} \neq \mathbf{M}(r)$. For interface normal components along r $(\nabla\Phi_{M,\text{out}}\cdot\hat{\mathbf{e}}_{\mathbf{r}})_{r=R_E} \rightarrow (\partial_r\Phi_{M,\text{out}})_{r=R_E}$, and $(\nabla\Phi_{M,\text{in}}\cdot\hat{\mathbf{e}}_{\mathbf{r}})_{r=R_E} \rightarrow (\partial_r\Phi_{M,\text{in}})_{r=R_E}$. Partial derivatives of Equations 2 and 3 with respect to r in Equation 5 give

$$-\sum_{l=0}^{\infty} B_l(l+1)R_E^{-(l+2)}P_l[\cos(\theta)] = \sum_{l=0}^{\infty} A_l l R_E^{l-1}P_l[\cos(\theta)] - M_0\cos(\theta). \tag{6}$$

By orthogonality of Legendre polynomials, when $l = 1$, $P_l[\cos(\theta)] = \cos(\theta)$ and Equation 6 becomes

$$-2B_1R_E^{-3}\cos(\theta) = A_1\cos(\theta) - M_0\cos(\theta),$$

such that $A_1 = M_0 - 2B_1/R_E^3$ and, by Equation 4, $A_1 = B_1/R_E^3$. As a result $A_1 = M_0/3$ and $B_1 = M_0R_E^3/3$ such that Equations 2 and 3 become

$$\Phi_{M,\text{in}} = \frac{M_0}{3}r\cos(\theta), \quad \Phi_{M,\text{out}} = \frac{M_0R_E^3}{3r^2}\cos(\theta). \tag{7}$$

Since plasma dynamics beyond Earth's surface are considered, $r > R_E$. In spherical coordinates with azimuthal symmetry the gradient becomes $\nabla = \partial_r\hat{\mathbf{e}}_{\mathbf{r}} + r^{-1}\partial_\theta\hat{\mathbf{e}}_\theta$ such that

$$\nabla\Phi_{M,\text{out}} = \left[-\frac{2M_0R_E^3\cos(\theta)}{3r^3}\right]\hat{\mathbf{e}}_{\mathbf{r}} + \left[-\frac{M_0R_E^3\sin(\theta)}{3r^3}\right]\hat{\mathbf{e}}_\theta,$$

and since $\mathbf{B}_{\text{out}} = -\mu_0\nabla\Phi_{M,\text{out}}$ the dipole magnetic field beyond $r = R_E$ is

$$\mathbf{B} = \mathbf{B}_{\text{out}} = \frac{2M_0\cos(\theta)}{r^3}\hat{\mathbf{e}}_{\mathbf{r}} + \frac{M_0\sin(\theta)}{r^3}\hat{\mathbf{e}}_\theta = \frac{M_0}{r^3}\sqrt{\ell}\hat{\mathbf{e}}_{\mathbf{q}}, \tag{8}$$

with magnitude $B = |\mathbf{B}| = \dfrac{M_0}{r^3}\sqrt{\ell}$ where $\ell = 1 + 3\cos^2(\theta)$, $M_0 = B_ER_E^3$, and $B_E = \mu_0M_0/3$ is the dipole magnetic field magnitude at the equator (i.e., $\theta = \pi/2$).

.2 Dipole Unit Basis

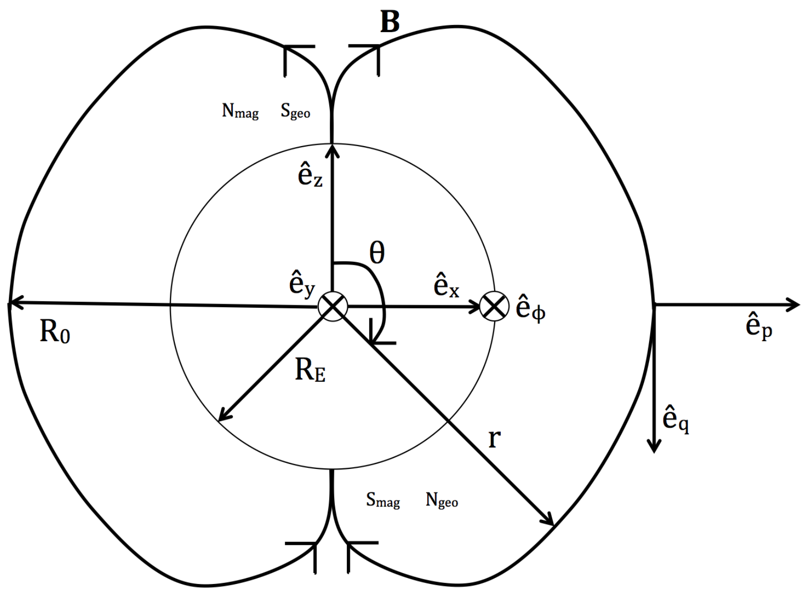

Figure 1: Configuration-space in Cartesian, $(\hat{\mathbf{e}}_\mathbf{x},\ \hat{\mathbf{e}}_\mathbf{y},\ \hat{\mathbf{e}}_\mathbf{z})$, spherical, $(\hat{\mathbf{e}}_\mathbf{r},\ \hat{\mathbf{e}}_\theta,\ \hat{\mathbf{e}}_\phi)$ and magnetic dipole, $(\hat{\mathbf{e}}_\mathbf{p},\ \hat{\mathbf{e}}_\mathbf{q},\ \hat{\mathbf{e}}_\phi)$ coordinates where R_E is the Earth radius, $r = R_0$ at the equator $(\theta = \pi/2)$, and N_{mag} (S_{mag}), and N_{geo} (S_{geo}) are the North (South) magnetic and geographic poles, respectively.

Earth's magnetic moment is considered positive along $\hat{\mathbf{e}}_\mathbf{z}$ and $\hat{\mathbf{e}}_\phi$ is positive in the geographically westward (magnetically eastward) direction as seen in Figure 1. Since q is defined as the field-aligned coordinate $\mathbf{B} = B\hat{\mathbf{e}}_\mathbf{q}$ such that $\hat{\mathbf{e}}_\mathbf{q} = \mathbf{B}/B$. Equation 8 gives

$$\hat{\mathbf{e}}_\mathbf{q} = \left[\frac{2\cos(\theta)}{\sqrt{\ell}}\right]\hat{\mathbf{e}}_\mathbf{r} + \left[\frac{\sin(\theta)}{\sqrt{\ell}}\right]\hat{\mathbf{e}}_\theta, \tag{9}$$

where $\ell = 1 + 3\cos^2(\theta)$. Contravariant dipole coordinate system is orthogonal and curvilinear such that at any position $\hat{\mathbf{e}}_\mathbf{q} \perp \hat{\mathbf{e}}_\mathbf{p}$; since $(p,\ q)$ coordinate pairs reside on the $(r,\ \theta)$ plane for unknown variables $\beta = \beta(r,\ \theta,\ \phi)$ and $\gamma = \gamma(r,\ \theta,\ \phi)$ the L-shell unit vector may be cast in the form $\hat{\mathbf{e}}_\mathbf{p} = \beta\hat{\mathbf{e}}_\mathbf{r} + \gamma\hat{\mathbf{e}}_\theta$. According to Equation 9

$$\hat{\mathbf{e}}_\mathbf{q}\cdot\hat{\mathbf{e}}_\mathbf{p} = \left[\frac{2\cos(\theta)}{\sqrt{\ell}}\right]\beta + \left[\frac{\sin(\theta)}{\sqrt{\ell}}\right]\gamma,$$

and $\hat{\mathbf{e}}_\mathbf{q}\cdot\hat{\mathbf{e}}_\mathbf{p} = 0$ such that $\beta = -\gamma\sin(\theta)/2\cos(\theta)$. Moreover, where $|\hat{\mathbf{e}}_\mathbf{p}| = 1$ such that $\beta^2+\gamma^2 = 1$, $\gamma^2\sin^2(\theta)/4\cos^2(\theta) + \gamma^2 = 1$ and, where $\sin^2(\theta) = 1 - \cos^2(\theta)$, $\gamma = \sqrt{4\cos^2(\theta)/\ell}$. Accordingly, $\gamma = \pm 2\cos(\theta)/\sqrt{\ell}$ and $\beta = \mp\sin(\theta)/\sqrt{\ell}$. For $\hat{\mathbf{e}}_\mathbf{p}$ to be positive outwards the radial component of $\hat{\mathbf{e}}_\mathbf{p}$ must be positive definite, that is $\beta > 0$. As a result, $\gamma < 0$ and the L-shell unit vector is

$$\hat{\mathbf{e}}_{\mathbf{p}} = \left[\frac{\sin(\theta)}{\sqrt{\ell}}\right]\hat{\mathbf{e}}_{\mathbf{r}} + \left[-\frac{2\cos(\theta)}{\sqrt{\ell}}\right]\hat{\mathbf{e}}_{\theta}. \tag{10}$$

The azimuthal unit vector is the cross-product of $\hat{\mathbf{e}}_{\mathbf{p}}$ and $\hat{\mathbf{e}}_{\mathbf{q}}$ according to cyclic permutation in the dipole system, $\hat{\mathbf{e}}_{\phi_d} = \hat{\mathbf{e}}_{\mathbf{p}} \times \hat{\mathbf{e}}_{\mathbf{q}}$:

$$\hat{\mathbf{e}}_{\phi_d} = \begin{vmatrix} \hat{\mathbf{e}}_{\mathbf{r}} & \hat{\mathbf{e}}_{\theta} & \hat{\mathbf{e}}_{\phi_s} \\ \sin(\theta)/\sqrt{\ell} & -2\cos(\theta)/\sqrt{\ell} & 0 \\ 2\cos(\theta)/\sqrt{\ell} & \sin(\theta)/\sqrt{\ell} & 0 \end{vmatrix},$$

where, in the spherical system, $\hat{\mathbf{e}}_{\phi_s} = \hat{\mathbf{e}}_{\mathbf{r}} \times \hat{\mathbf{e}}_{\theta}$. As a result,

$$\hat{\mathbf{e}}_{\phi} = \hat{\mathbf{e}}_{\phi_s} = \hat{\mathbf{e}}_{\phi_d}. \tag{11}$$

Solving for $\hat{\mathbf{e}}_{\mathbf{r}}$ and $\hat{\mathbf{e}}_{\theta}$ in Equations 9 and 10 gives

$$\begin{aligned} \hat{\mathbf{e}}_{\mathbf{r}} &= \left[\frac{\sqrt{\ell}}{2\cos(\theta)}\right]\hat{\mathbf{e}}_{\mathbf{q}} + \left[-\frac{\sin(\theta)}{2\cos(\theta)}\right]\hat{\mathbf{e}}_{\theta}, \\ \hat{\mathbf{e}}_{\theta} &= \left[\frac{\sin(\theta)}{2\cos(\theta)}\right]\hat{\mathbf{e}}_{\mathbf{r}} + \left[-\frac{\sqrt{\ell}}{2\cos(\theta)}\right]\hat{\mathbf{e}}_{\mathbf{p}}, \end{aligned} \tag{12}$$

which, when combining the latter into the former, renders the following relation:

$$\hat{\mathbf{e}}_{\mathbf{r}} = \left[\frac{\sqrt{\ell}}{2\cos(\theta)}\right]\hat{\mathbf{e}}_{\mathbf{q}} - \frac{\sin(\theta)}{2\cos(\theta)}\left[\frac{\sin(\theta)}{2\cos(\theta)}\hat{\mathbf{e}}_{\mathbf{r}} - \frac{\sqrt{\ell}}{2\cos(\theta)}\hat{\mathbf{e}}_{\mathbf{p}}\right].$$

The above when simplified yields the radial unit vector in dipole coordinate unit basis:

$$\hat{\mathbf{e}}_{\mathbf{r}} = \left[\frac{\sin(\theta)}{\sqrt{\ell}}\right]\hat{\mathbf{e}}_{\mathbf{p}} + \left[\frac{2\cos(\theta)}{\sqrt{\ell}}\right]\hat{\mathbf{e}}_{\mathbf{q}}, \tag{13}$$

where $\sin^2(\theta) = 1 - \cos^2(\theta)$. When combining the former relation into the latter of Equation 12

$$\hat{\mathbf{e}}_{\theta} = \frac{\sin(\theta)}{2\cos(\theta)}\left[\frac{\sqrt{\ell}}{2\cos(\theta)}\hat{\mathbf{e}}_{\mathbf{q}} - \frac{\sin\theta}{2\cos(\theta)}\hat{\mathbf{e}}_{\theta}\right] - \left[\frac{\sqrt{\ell}}{2\cos(\theta)}\right]\hat{\mathbf{e}}_{\mathbf{p}},$$

which gives the polar unit vector in dipole coordinate unit basis:

$$\hat{\mathbf{e}}_{\theta} = -\left[\frac{2\cos(\theta)}{\sqrt{\ell}}\right]\hat{\mathbf{e}}_{\mathbf{p}} + \left[\frac{\sin(\theta)}{\sqrt{\ell}}\right]\hat{\mathbf{e}}_{\mathbf{q}}. \tag{14}$$

The spherical azimuthal unit vector in dipole coordinate unit basis is $\hat{\mathbf{e}}_\phi$.

.3 Dipole Metric & Scale Factors

Components of the line segment ds^2 in dipole coordinates are the diagonals of the metric tensor, that is, the metric factors $g_{ij} = h_i^2 = h_j^2 \ \forall i = j$, where $g_{ij} = 0 \ \forall i \neq j$ for orthogonal coordinate systems:

$$ds^2 = g_{pp} dp^2 + g_{qq} dq^2 + g_{\phi\phi} d\phi^2.$$

Contravariant metric factors, g_{ii}, have associated scale factors, $h_i = |\partial_i \mathbf{r}_R| \ \forall i = p, q, \phi$. Here, $\mathbf{r}_R$ is a position vector in a reference coordinate system yet to be determined. To determine metric and scale factors of magnetic dipole coordinate systems it is noted that differential relations between spherical and dipole coordinate components are given by Jacobian matrices $\boldsymbol{J}$ and inverses $\boldsymbol{J}^{-1}$:

$$\boldsymbol{J} = \frac{\partial(p,\ q,\ \phi)}{\partial(r,\ \theta,\ \phi)} = \begin{bmatrix} \partial_r p & \partial_r q & \partial_r \phi \\ \partial_\theta p & \partial_\theta q & \partial_\theta \phi \\ \partial_\phi p & \partial_\phi q & \partial_\phi \phi \end{bmatrix}, \tag{15}$$

and

$$\boldsymbol{J}^{-1} = \frac{\partial(r,\ \theta,\ \phi)}{\partial(p,\ q,\ \phi)} = \begin{bmatrix} \partial_p r & \partial_p \theta & \partial_p \phi \\ \partial_q r & \partial_q \theta & \partial_q \phi \\ \partial_\phi r & \partial_\phi \theta & \partial_\phi \phi \end{bmatrix}. \tag{16}$$

Inverse of $\boldsymbol{J}$ is computed in terms of it's determinant, $\det(\boldsymbol{J})$, and transpose of its cofactor matrix, $[\mathrm{cof}(\boldsymbol{J})]^\intercal$:

$$\boldsymbol{J}^{-1} = \frac{1}{\det(\boldsymbol{J})} \left[\mathrm{cof}(\boldsymbol{J})\right]^\intercal.$$

Determinant and transpose of cofactor matrices of $\boldsymbol{J}$ are given by [Wohlwend, 2008]:

$$\det(\boldsymbol{J}) = \partial_r p(\partial_\theta q \partial_\phi \phi - \partial_\phi q \partial_\theta \phi) - \partial_r q(\partial_\theta p \partial_\phi \phi - \partial_\phi p \partial_\theta \phi) + \partial_r \phi(\partial_\theta p \partial_\phi q - \partial_\phi p \partial_\theta q),$$

and

$$[\mathrm{cof}(\boldsymbol{J})]^{\intercal} = \begin{bmatrix} (\partial_\theta q \partial_\phi \phi - \partial_\phi q \partial_\theta \phi) & (\partial_\theta p \partial_\phi \phi - \partial_\phi p \partial_\theta \phi) & (\partial_\theta p \partial_\phi q - \partial_\phi p \partial_\theta q) \\ (\partial_r q \partial_\phi \phi - \partial_\phi q \partial_r \phi) & (\partial_r p \partial_\phi \phi - \partial_\phi p \partial_r \phi) & (\partial_r p \partial_\phi q - \partial_\phi p \partial_r q) \\ (\partial_r q \partial_\theta \phi - \partial_\theta q \partial_r \phi) & (\partial_r p \partial_\theta \phi - \partial_\theta p \partial_r \phi) & (\partial_r p \partial_\theta q - \partial_\theta p \partial_r q) \end{bmatrix}^{\intercal},$$

respectively. According to Equations 29 and 30 the differentials are

$$\begin{array}{ccc} \partial_r p = 1/R_E \sin^2(\theta), & \partial_r q = -2R_E^2 \cos(\theta)/r^3, & \partial_r \phi = 0, \\ \partial_\theta p = -2r \cos(\theta)/R_E \sin^3(\theta), & \partial_\theta q = -R_E^2 \sin(\theta)/r^2, & \partial_\theta \phi = 0, \\ \partial_\phi p = 0, & \partial_\phi q = 0, & \partial_\phi \phi = 1, \end{array} \tag{17}$$

such that the determinant of $\boldsymbol{J}$ is

$$\det(\boldsymbol{J}) = -\frac{\ell R_E}{r^2 \sin^3(\theta)}, \tag{18}$$

and the transpose of the cofactor of $\boldsymbol{J}$ is

$$[\mathrm{cof}(\boldsymbol{J})]^{\intercal} = \begin{bmatrix} \left[-\frac{R_E^2 \sin(\theta)}{r^2}\right] & \left[-\frac{2R_E^2 \cos(\theta)}{r^3}\right] & 0 \\ \left[-\frac{2r\cos(\theta)}{R_E \sin^3(\theta)}\right] & \left[\frac{1}{R_E \sin^2(\theta)}\right] & 0 \\ 0 & 0 & \left[-\frac{\ell R_E}{r^2 \sin^3(\theta)}\right] \end{bmatrix}. \tag{19}$$

The Jacobian matrix and it's inverse is given by

$$\boldsymbol{J} = \frac{\partial(p,\ q,\ \phi)}{\partial(r,\ \theta,\ \phi)} = \begin{bmatrix} \left[\frac{1}{R_E \sin^2(\theta)}\right] & \left[-\frac{2R_E^2 \cos(\theta)}{r^3}\right] & 0 \\ \left[-\frac{2r\cos(\theta)}{R_E \sin^3(\theta)}\right] & \left[-\frac{R_E^2 \sin(\theta)}{r^2}\right] & 0 \\ 0 & 0 & 1 \end{bmatrix}, \tag{20}$$

and

$$\boldsymbol{J}^{-1} = \frac{\partial(r,\ \theta,\ \phi)}{\partial(p,\ q,\ \phi)} = \begin{bmatrix} \left[\frac{R_E \sin^4(\theta)}{\ell}\right] & \left[\frac{2R_E \sin^3(\theta)\cos(\theta)}{r\ell}\right] & 0 \\ \left[\frac{2r^3 \cos(\theta)}{\ell R_E^2}\right] & \left[-\frac{r^2 \sin(\theta)}{\ell R_E^2}\right] & 0 \\ 0 & 0 & 1 \end{bmatrix}, \tag{21}$$

Equation 21 provides differential elements required to construct metric and scale factors:

$$
\begin{aligned}
\partial_p r &= R_E \sin^4(\theta)/\ell, \quad & \partial_p \theta &= 2R_E \sin^3(\theta)\cos(\theta)/r\ell, \quad & \partial_p \phi &= 0,\\
\partial_q r &= 2r^3 \cos(\theta)/\ell R_E^2, & \partial_q \theta &= -r^2 \sin(\theta)/\ell R_E^2, & \partial_q \phi &= 0,\\
\partial_\phi r &= 0, & \partial_\phi \theta &= 0, & \partial_\phi \phi &= 1.
\end{aligned}
\tag{22}
$$

To construct the dipole coordinate metric and scale factors the reference position vector is taken to be $\mathbf{r}_R = \mathbf{r}_C$ in global Cartesian coordinates to ensure constant unit vectors in space (i.e., $\hat{\mathbf{e}}_\mathbf{i} \neq \hat{\mathbf{e}}_\mathbf{i}(r,\ \theta,\ \phi)\ \forall i = x,\ y,\ z$):

$$
\mathbf{r}_C = x(p,\ q,\ \phi)\hat{\mathbf{e}}_\mathbf{x} + y(p,\ q,\ \phi)\hat{\mathbf{e}}_\mathbf{y} + z(p,\ q,\ \phi)\hat{\mathbf{e}}_\mathbf{z}.
$$

Scale factors are given by $h_i = |\partial_i \mathbf{r}_R|\ \forall i = p,\ q,\ \phi$ and the metric factors are $g_{ii} = h_i^2$. Chain rule of differentiation is employed on $\mathbf{r}_C$. $\forall i = p,\ q,\ \phi$:

$$
\begin{aligned}
\partial_i x(p,\ q,\ \phi) &= \partial_r x(p,\ q,\ \phi)\partial_i r + \partial_\theta x(p,\ q,\ \phi)\partial_i \theta + \partial_\phi x(p,\ q,\ \phi)\partial_i \phi,\\
\partial_i y(p,\ q,\ \phi) &= \partial_r y(p,\ q,\ \phi)\partial_i r + \partial_\theta y(p,\ q,\ \phi)\partial_i \theta + \partial_\phi y(p,\ q,\ \phi)\partial_i \phi,\\
\partial_i z(p,\ q,\ \phi) &= \partial_r z(p,\ q,\ \phi)\partial_i r + \partial_\theta z(p,\ q,\ \phi)\partial_i \theta + \partial_\phi z(p,\ q,\ \phi)\partial_i \phi,
\end{aligned}
\tag{23}
$$

where $x = r\cos(\phi)\sin(\theta)$, $y = r\sin(\phi)\sin(\theta)$, and $z = r\cos(\theta)$ such that

$$
\begin{aligned}
\partial_r x &= \cos(\phi)\sin(\theta), \quad & \partial_r y &= \sin(\phi)\sin(\theta), \quad & \partial_r z &= \cos(\theta),\\
\partial_\theta x &= r\cos(\phi)\cos(\theta), & \partial_\theta y &= r\sin(\phi)\cos(\theta), & \partial_\theta z &= -r\sin(\theta),\\
\partial_\phi x &= -r\sin(\phi)\sin(\theta), & \partial_\phi y &= r\cos(\phi)\sin(\theta), & \partial_\phi z &= 0.
\end{aligned}
\tag{24}
$$

$h_p = |\partial_p \mathbf{r}_C| = \sqrt{(\partial_p x)^2 + (\partial_p y)^2 + (\partial_p z)^2}$ and $g_{pp} = h_p^2$, where

$$
\begin{aligned}
\partial_p x &= \frac{R_E \cos(\phi)\sin^3(\theta)[\sin^2(\theta) + 2\cos^2(\theta)]}{\ell}, \quad & \partial_p y &= \frac{R_E \sin(\phi)\sin^3(\theta)[\sin^2(\theta) + 2\cos^2(\theta)]}{\ell},\\
\partial_p z &= \frac{-R_E \sin^4(\theta)\cos(\theta)}{\ell}, & (\partial_p x)^2 &= \frac{R_E^2 \cos^2(\phi)\sin^6(\theta)[\sin^2(\theta) + 2\cos^2(\theta)]^2}{\ell^2},\\
(\partial_p y)^2 &= \frac{R_E^2 \sin^2(\phi)\sin^6(\theta)[\sin^2(\theta) + 2\cos^2(\theta)]^2}{\ell^2}, & (\partial_p z)^2 &= \frac{R_E^2 \sin^8(\theta)\cos^2(\theta)}{\ell^2},
\end{aligned}
$$

and p coordinate scale factors in [m] and metric factors in [m^2] are

$$
h_p = \frac{R_E \sin^3(\theta)}{\sqrt{\ell}}, \quad g_{pp} = \frac{R_E^2 \sin^6(\theta)}{\ell}.
\tag{25}
$$

$h_q = |\partial_q \mathbf{r}_C| = \sqrt{(\partial_q x)^2 + (\partial_q y)^2 + (\partial_q z)^2}$ and $g_{qq} = h_q^2$, where

$$\partial_q x = \frac{r^3 \cos(\phi)\cos(\theta)\sin(\theta)}{\ell R_E^2}, \qquad \partial_q y = \frac{r^3 \sin(\phi)\cos(\theta)\sin(\theta)}{\ell R_E^2},$$
$$\partial_q z = \frac{r^3}{\ell R_E^2}\left[2\cos^2(\theta) + \sin^2(\theta)\right], \quad (\partial_q x)^2 = \frac{r^6 \cos^2(\phi)\cos^2(\theta)\sin^2(\theta)}{\ell^2 R_E^4},$$
$$(\partial_q y)^2 = \frac{r^6 \sin^2(\phi)\cos^2(\theta)\sin^2(\theta)}{\ell^2 R_E^4}, \quad (\partial_q z)^2 = \frac{r^6}{\ell^2 R_E^4}\left[2\cos^2(\theta) + \sin^2(\theta)\right]^2,$$

and q coordinate scale factors in [m] and metric factors in [m^2] are

$$h_q = \frac{r^3}{R_E^2\sqrt{\ell}}, \quad g_{qq} = \frac{r^6}{\ell R_E^4}. \tag{26}$$

$h_\phi = |\partial_\phi \mathbf{r}_C| = \sqrt{(\partial_\phi x)^2 + (\partial_\phi y)^2 + (\partial_\phi z)^2}$ and $g_{\phi\phi} = h_\phi^2$ where

$$\partial_\phi x = -r\sin(\phi)\sin(\theta), \qquad \partial_\phi y = r\cos(\phi)\sin(\theta), \qquad \partial_\phi z = 0,$$
$$(\partial_\phi x)^2 = r^2\sin^2(\phi)\sin^2(\theta), \quad (\partial_\phi y)^2 = r^2\cos^2(\phi)\sin^2(\theta), \quad (\partial_\phi z)^2 = 0.$$

ϕ coordinate scale factors in [m] and metric factors in [m^2] are

$$h_\phi = r\sin(\theta), \quad g_{\phi\phi} = r^2\sin^2(\theta). \tag{27}$$

Volume elements dipole coordinate spatial cells are

$$d^3x = h_p h_q h_\phi \, dp \, dq \, d\phi. \tag{28}$$

.4 Magnetic Dipole Equation

Field-aligned coordinates $q \in [-1\ 1]$ are along $\mathbf{B}$ for a given L-shell:

$$q = \frac{R_E^2\cos(\theta)}{r^2} = \frac{R_E^2\cos(\theta)}{R_0^2\sin^4(\theta)}. \tag{29}$$

L-shell is denoted by the p coordinate

$$p = \frac{r}{R_E\sin^2(\theta)} = \frac{R_0}{R_E}, \tag{30}$$

where the azimuthal angle is ϕ, $r = R_0\sin^2(\theta)$, and R_0 is the radial distance to the field line at the equator [Wohlwend, 2008]. As a result, $\theta = \arcsin(\sqrt{r/R_0})$:

$$\frac{d\theta}{dr} = \frac{1}{\sqrt{1 - r/R_0}} \frac{\sqrt{R_0/r}}{2R_0},$$

and, where $\sin(\theta)/\cos(\theta) = \tan(\theta)$ and $\cos^2(\theta) = 1 - \sin^2(\theta)$,

$$r\frac{d\theta}{dr} = \frac{\tan(\theta)}{2}. \tag{31}$$

Equation 31 is known as the magnetic dipole equation [Shunk and Nagy, 2000].

.5 Magnetic Dipole Quartic Polynomial

Dipole coordinate systems are azimuthally symmetric such that magnetized particle coordinates vary in (r, θ) independently of ϕ along a given L-shell. Transformations from dipole to spherical coordinates are from $(p,\ q) \rightarrow (r,\ \theta)$ which entail finding roots of quartic polynomials [Huba et al., 2000]:

$$\gamma^4 + \frac{1}{pq^2}\gamma - \frac{1}{q^2} = 0, \tag{32}$$

where $\gamma = r/R_E$ are the roots. Equation 32 is of standard form of quartic polynomial:

$$\gamma^4 + A'\gamma^3 + B'\gamma^2 + C'\gamma + D' = 0. \tag{33}$$

Equation 33 may be recast into reduced quartic form by the substitution $\gamma = \delta - A'/4$, where

$$\begin{aligned}
\gamma^2 &= \delta^2 - 2\delta A'/4 + A'^2/16, \\
\gamma^3 &= \delta^3 - 3\delta^2 A'/4 + 3\delta A'^2/16 - A'^3/64, \\
\gamma^4 &= \delta^4 - \delta^3 A' + 3\delta^2 A'^2/8 - \delta A'^3/16 + A'^4/256,
\end{aligned}$$

such that Equation 33 becomes

$$\begin{aligned}
(\delta^4 - \delta^3 A' + 3\delta^2 A'^2/8 - \delta A'^3/16 + A'^4/256) + A'(\delta^3 - 3\delta^2 A'/4 + 3\delta A'^2/16 - A'^3/64)+ \\
B'(\delta^2 - 2\delta A'/4 + A'^2/16) + C'(\delta - A'/4) + D' = 0,
\end{aligned} \tag{34}$$

or, where

$$\begin{aligned} A &= B' - 3A'^2/8, \\ B &= A'^3/8 - A'B'/2 + C', \\ C &= D' - 3A'^4/256 + A'^2B'/16 - A'C'/4, \end{aligned} \tag{35}$$

the reduced form of the quartic polynomial is

$$\delta^4 + A\delta^2 + B\delta + C = 0. \tag{36}$$

To construct the resolvent cubic polynomial perfect squares Λ^2 and Γ^2 are formed in the factorable fashion

$$\Lambda^2 - \Gamma^2 = (\Lambda + \Gamma)(\Lambda - \Gamma).$$

To create Λ^2 and Γ^2 we add and subtract $\delta^2\eta + \eta^2/4$ from Equation 36:

$$\delta^4 + \delta^2\eta + \eta^2/4 - \delta^2\eta - \eta^2/4 + A\delta^2 + B\delta + C = 0,$$

and let $\delta^4 + \delta^2\eta + \eta^2/4 = (\delta^2 + \eta/2)^2$ such that

$$\Lambda^2 - \Gamma^2 = 0,$$

where $\Lambda^2 = (\delta^2 + \eta/2)^2$ is a perfect square, and $\Gamma^2 = \delta^2(\eta - A) - B\delta - (\eta^2/4 - C)$, or

$$\Gamma^2 = (\eta - A)\left[\delta^2 - \frac{B\delta}{(\eta - A)} + \frac{\eta^2/4 - C}{(\eta - A)}\right].$$

The bracketed term above needs to be a perfect square for Γ^2 to be a perfect square. Consider the perfect square

$$\left[\delta - \sqrt{\frac{\eta^2/4 - C}{(\eta - A)}}\right]^2 = \left[\delta^2 - 2\delta\sqrt{\frac{\eta^2/4 - C}{(\eta - A)}} + \frac{\eta^2/4 - C}{(\eta - A)}\right]$$

such that Γ^2 is a perfect square if

$$\left[\delta^2 - \frac{B\delta}{(\eta - A)} + \frac{\eta^2/4 - C}{(\eta - A)}\right] = \left[\delta^2 - 2\delta\sqrt{\frac{\eta^2/4 - C}{(\eta - A)}} + \frac{\eta^2/4 - C}{(\eta - A)}\right]$$

or $B\delta/(\eta - A) = 2\delta\sqrt{(\eta^2/4 - C)/(\eta - A)}$. As a result, $B^2 = (\eta - A)(\eta^2 - 4C)$ and the standard form for the resolvent cubic polynomial is

$$\eta^3 - 4\eta C - A\eta^2 + 4AC - B^2 = 0. \tag{37}$$

The above resolvent cubic polynomial may be recast in terms of Equation 35:

$$\begin{aligned}\eta^3 - (B' - 3A'^2/8)\eta^2 - 4(D' - 3A'^4/256 + A'^2B'/16 - A'C'/4)\eta \\ +4(B' - 3A'^2/8)(D' - 3A'^4/256 + A'^2B'/16 - A'C'/4) - (A'^3/8 - A'B'/2 + C')^2 = 0,\end{aligned} \tag{38}$$

or

$$\begin{aligned}\eta^3 + (3A'^2/8 - B')\eta^2 + (3A'^4/64 - A'^2B'/4 + A'C' - 4D')\eta \\ +(A'^6/512 - A'^4B'/64 + A'^3C'/8 - 3A'^2D'/2 + 4B'D' - C'^2) = 0.\end{aligned} \tag{39}$$

Let $\eta = \sigma - A'^2/8$ such that $\eta^2 = \sigma^2 - \sigma A'^2/4 + A'^4/64$ and $\eta^3 = \sigma^3 - 3\sigma^2 A'^2/8 + 3\sigma A'^4/64 - A'^6/512$. Equation 39 becomes

$$\begin{aligned}(\sigma^3 - 3\sigma^2A'^2/8 + 3\sigma A'^4/64 - A'^6/512) + (3A'^2/8 - B')(\sigma^2 - \sigma A'^2/4 + A'^4/64) \\ +(3A'^4/64 - A'^2B'/4 + A'C' - 4D')(\sigma - A'^2/8) \\ +(A'^6/512 - A'^4B'/64 + A'^3C'/8 - 3A'^2D'/2 + 4B'D' - C'^2) = 0,\end{aligned} \tag{40}$$

or $\sigma^3 - B'\sigma^2 + (A'C' - 4D')\sigma + (4B'D' - C'^2 - A'^2D') = 0$. As a result, the reduced resolvent cubic polynomial is

$$\sigma^3 + \bar{A}\sigma^2 + \bar{B}\sigma + \bar{C} = 0, \tag{41}$$

where

$$\bar{A} = -B', \quad \bar{B} = A'C' - 4D', \quad \bar{C} = 4B'D' - C'^2 - A'^2D'. \tag{42}$$

Let $\sigma = \lambda - \bar{A}/n$ where n is the polynomial order such that $n = 3$ for the reduced resolvent cubic polynomial and $\sigma = \lambda - \bar{A}/3$, $\sigma^2 = \lambda^2 - 2\lambda\bar{A}/3 + \bar{A}^2/9$, and $\sigma^3 = \lambda^3 - \lambda^2\bar{A} - \lambda\bar{A}^2/3 - \bar{A}^3/27$. Equation 41 becomes

$$(\lambda^3 - \lambda^2\bar{A} - \lambda\bar{A}^2/3 - \bar{A}^3/27) + \bar{A}(\lambda^2 - 2\lambda\bar{A}/3 + \bar{A}^2/9) + \bar{B}(\lambda - \bar{A}/n) + \bar{C} = 0,$$

or the standard form of the cubic polynomial

$$\lambda^3 + \bar{\bar{A}}\lambda + \bar{\bar{B}} = 0 \tag{43}$$

where

$$\bar{\bar{A}} = \bar{B} - \bar{A}^2/3, \quad \bar{\bar{B}} = 2\bar{A}^3/27 - \bar{A}\bar{B}/3 + \bar{C}. \tag{44}$$

Vieta's substitution $\lambda = \omega - \bar{\bar{A}}/3\omega$ is employed such that $\lambda^2 = \omega^2 - 2\omega\bar{\bar{A}}/3\omega + \bar{\bar{A}}^2/9\omega^2$ and $\lambda^3 = \omega^3 - \omega\bar{\bar{A}} + \bar{\bar{A}}^2/3\omega - \bar{\bar{A}}^3/27\omega^3$. As a result, Equation 43 becomes

$$(\omega^3 - \omega\bar{\bar{A}} + \bar{\bar{A}}^2/3\omega - \bar{\bar{A}}^3/27\omega^3) + \bar{\bar{A}}(\omega - \bar{\bar{A}}/3\omega) + \bar{\bar{B}} = 0$$

or

$$\omega^3 - \bar{\bar{A}}^3/27\omega^3 + \bar{\bar{B}} = 0. \tag{45}$$

Equation 45 is transformed into a quadratic polynomial by multiplying by ω^3 such that $(\omega^3)^2 + \bar{\bar{B}}\omega^3 - \bar{\bar{A}}^3/27 = 0$. Roots are given by the quadratic formula:

$$\omega^3 = \Delta \pm \sqrt{\Delta^2 + \varepsilon^3}$$

where

$$\Delta = -\bar{\bar{B}}/2, \quad \varepsilon = \bar{\bar{A}}/3 \tag{46}$$

such that $\bar{\bar{B}} = -2\Delta$, $\bar{\bar{A}} = 3\varepsilon$, and Equation 43 becomes

$$\lambda^3 + 3\varepsilon\lambda - 2\Delta = 0. \tag{47}$$

From the above cubic polynomial let $3\varepsilon\lambda - 2\Delta = \bar{G}(\lambda - \bar{H}) - \bar{H}^3$ for some constants $\bar{H}$ and $\bar{G}$ such that $3\varepsilon\lambda - 2\Delta = \bar{G}\lambda - (\bar{G}\bar{H} + \bar{H}^3)$ and $\bar{G} = 3\varepsilon$. Furthermore, $2\Delta = \bar{G}\bar{H} + \bar{H}^3$ and

$$\bar{H}^3 + \bar{G}\bar{H} - 2\Delta = 0. \tag{48}$$

Let $\bar{H} = \bar{J} + \bar{K}$ where

$$\bar{J} = \left(\Delta + \sqrt{\varepsilon^3 + \Delta^2}\right)^{1/3}, \quad \bar{K} = \left(\Delta - \sqrt{\varepsilon^3 + \Delta^2}\right)^{1/3} \tag{49}$$

such that

$$\bar{H}^2 = \left(\Delta + \sqrt{\varepsilon^3 + \Delta^2}\right)^{2/3} + \left(\Delta - \sqrt{\varepsilon^3 + \Delta^2}\right)^{2/3} - 2\varepsilon$$

and $\bar{H}^3 = 2\Delta - 3\varepsilon\bar{H}$. Equation 48 then yields $2\Delta - \bar{G}\bar{H} = 2\Delta - 3\varepsilon\bar{H}$ such that $\bar{G} = 3\varepsilon$ as expected. As a result, $\bar{H} = \bar{J} + \bar{K}$ is a solution to Equation 48. The substitution $3\varepsilon\lambda - 2\Delta = \bar{G}(\lambda - \bar{H}) - \bar{H}^3$ when combined with Equation 47 gives $\lambda^3 + \bar{G}(\lambda - \bar{H}) - \bar{H}^3 = 0$ or $(\lambda - \bar{H})(\lambda^2 + \bar{H}\lambda + \bar{H}^2 + \bar{G}) = 0$. The linear term coefficient is the quadratic polynomial, where $\bar{G} = 3\varepsilon$,

$$\lambda^2 + \bar{H}\lambda + \bar{H}^2 + 3\varepsilon = 0 \tag{50}$$

with roots given by the quadratic formula:

$$\lambda_1 = -\frac{\bar{H}}{2} + \frac{\bar{I}i\sqrt{3}}{2}, \quad \lambda_2 = -\frac{\bar{H}}{2} - \frac{\bar{I}i\sqrt{3}}{2} \tag{51}$$

where $\bar{H} = \bar{J} + \bar{K}$ and $\bar{I} = \bar{J} - \bar{K}$. The general cubic polynomial of the form $\alpha\sigma^3 + \beta\sigma^2 + \gamma\sigma + \delta = 0$ for constants α, β, γ, and δ, has a discriminant $\tilde{D}_3 = \gamma^2\beta^2 - 4\delta\beta^3 - 4\gamma^3\alpha + 18\delta\gamma\beta\alpha - 27\delta^2\alpha^2$. From Equation 41 it is apparent that $\alpha = 1$, $\beta = \bar{A}$, $\gamma = \bar{B}$, and $\delta = \bar{C}$ such that

$$\tilde{D}_3 = \bar{B}^2\bar{A}^2 - 4\bar{C}\bar{A}^3 - 4\bar{B}^3 + 18\bar{A}\bar{B}\bar{C} - 27\bar{C}^2. \tag{52}$$

The quartic discriminant, $\tilde{D}_4$, of Equation 33 is

$$\begin{aligned} \tilde{D}_4 = &\left(C'^2B'^2A'^2 - 4C'^3A'^3 - 4C'^2B'^3 + 18C'^3B'A' - 27C'^4 + 256D'^3\right) \\ &+D'\left(-4B'^3A'^2 + 18C'B'A'^3 + 16B'^4 - 80C'B'^2A' - 6C'^2A'^2 + 144C'^2B'\right) \\ &+D'^2\left(-27A'^4 + 144B'A'^2 - 128B'^2 - 192C'A'\right), \end{aligned} \tag{53}$$

where $\tilde{D}_3 = \tilde{D}_4$. Furthermore, if $\tilde{D}_3 < 0$ then there is one real root and two complex conjugate roots to the cubic polynomial. If $\tilde{D}_3 = 0$ then there are all real roots and at least two are equal. If $\tilde{D}_3 > 0$ then there are all unequal real roots. Roots of the reduced resolvent cubic polynomial of Equation 41 are given by Cardano's formula, where $\tilde{\theta} = \arccos(\Delta/\sqrt{-\varepsilon})$:

$$\begin{aligned} \sigma_1 &= 2\sqrt{-\varepsilon}\cos(\tilde{\theta}/3) - \bar{A}/3, \\ \sigma_2 &= 2\sqrt{-\varepsilon}\cos[(\tilde{\theta} + 2\pi)/3] - \bar{A}/3, \\ \sigma_3 &= 2\sqrt{-\varepsilon}\cos[(\tilde{\theta} + 4\pi)/3] - \bar{A}/3. \end{aligned} \tag{54}$$

For any sign of $\tilde{D}_3$ exists one real root $\sigma_0 \in \mathbb{R}$ of the reduced resolvent cubic polynomial of Equation 41. Four roots cast in terms of the real cubic root σ_1 of the reduced quartic polynomial of

Equation 36 are the roots of the following quadratic polynomial:

$$\delta^2 + \frac{1}{2}\left(A' \pm \sqrt{A'^2 - 4B' + 4\sigma_0}\right)\delta + \frac{1}{2}\left(\sigma_0 \pm \sqrt{\sigma_0^2 - 4D'}\right) = 0. \tag{55}$$

Roots of Equation 55 are given by the quadratic formula

$$\begin{aligned} \delta = &-\frac{1}{4}\left(A' \pm \sqrt{A'^2 - 4B' + 4\sigma_0}\right) \\ &\pm\frac{1}{2}\sqrt{\left(A' \pm \sqrt{A'^2 - 4B' + 4\sigma_0}\right)^2/4 - 2\left(\sigma_0 \pm \sqrt{\sigma_0^2 - 4D'}\right)}. \end{aligned} \tag{56}$$

Four roots of the original quartic polynomial of Equation 33 are given by

$$\begin{aligned} \gamma_1 &= -A'/4 + \bar{\mu}/2 + \bar{\nu}/2, \quad \gamma_2 = -A'/4 + \bar{\mu}/2 - \bar{\nu}/2, \\ \gamma_3 &= -A'/4 - \bar{\mu}/2 + \bar{\pi}/2, \quad \gamma_4 = -A'/4 - \bar{\mu}/2 - \bar{\pi}/2, \end{aligned} \tag{57}$$

where $\bar{\mu} = \sqrt{A'^2/4 - B' + \sigma_0}$,

$$\bar{\nu} = \begin{cases} \sqrt{3A'^2/4 - \bar{\mu}^2 - 2B' + \left(4A'B' - 8C' - A'^3\right)/4\bar{\mu}} & \text{for } \bar{\mu} \neq 0 \\ \sqrt{3A'^2/4 - 2B' + 2\sqrt{\sigma_0^2 - 4D'}} & \text{for } \bar{\mu} = 0, \end{cases}$$

and

$$\bar{\pi} = \begin{cases} \sqrt{3A'^2/4 - \bar{\mu}^2 - 2B' - \left(4A'B' - 8C' - A'^3\right)/4\bar{\mu}} & \text{for } \bar{\mu} \neq 0 \\ \sqrt{3A'^2/4 - 2B' - 2\sqrt{\sigma_0^2 - 4D'}} & \text{for } \bar{\mu} = 0. \end{cases}$$

For the dipole polynomial Equation 32, $A' = 0$, $B' = 0$, $C' = 1/pq^2$, and $D' = -1/q^2$. $\sigma_0 \in \mathbb{R}$ is the real root of the resolvent cubic polynomial and $\gamma_0 \in \mathbb{R}^+$ is the positive real root of the dipole quartic polynomial of Equation 32. For a given $(p,\ q)$ coordinate the corresponding $(r,\ \theta)$ pair is given by

$$r(p,\ q) = R_E\sqrt{\mathfrak{R}(\gamma_0) + \mathfrak{I}(\gamma_0)}, \quad \theta(p,\ q) = \begin{cases} \arcsin(\sqrt{r/pR_E}) & \text{for } q \leq 0 \\ \pi - \arcsin(\sqrt{r/pR_E}) & \text{for } q > 0. \end{cases}$$

.6 Hydrostatic Density Initialization

A thermosphere in hydrostatic equilibrium is employed to initialize ion density profiles consistent with altitude-dependent gravitational acceleration terms, $g(\tilde{q})$, along geomagnetic field lines where

$ds(\tilde{q}) = h_q(\tilde{q})dq(\tilde{q})$ and $h_q(\tilde{q})$ is the field-aligned scale factor for configuration-space grid cell index $\tilde{q}$. Hydrostatic equilibrium equates magnitudes of pressure gradients along $ds(\tilde{q})$ with magnitudes of products of mass density $\rho(\tilde{q})$ and $g(\tilde{q})$:

$$\frac{dP}{ds} = \rho(\tilde{q})g(\tilde{q}), \tag{58}$$

where pressure $P(\tilde{q})$ for isotropic ion temperature $T_\parallel$ and electron temperature T_e abides by ideal gas law equation of state $P(\tilde{q}) = n(\tilde{q})k_B T_p$ where $T_p = (T_\parallel + T_e)$ is plasma temperature in [K], $n(\tilde{q}) = \rho(\tilde{q})/m$ is plasma density in [m^{-3}], m is ion mass, k_B is Boltzmann's constant, and $T_i = T_\parallel = T_\perp$ for temperature isotropy. Equation 58 is recast into

$$\frac{1}{\rho(\tilde{q})}\, d\rho = \frac{mg(\tilde{q})}{k_B\left(T_\parallel + T_e\right)}\, ds \tag{59}$$

such that

$$\ln(\rho) + C = \frac{m}{k_B\left(T_\parallel + T_e\right)} g(\tilde{q})\, ds \tag{60}$$

where C is constant. Gravitational acceleration terms are projected onto curved magnetic field lines such that $g(\tilde{q}) = 2GM_\oplus \cos(\theta_C) r_C^{-2}/\sqrt{\ell_C}$ where G is the universal gravitational constant, $M_\oplus$ is Earth's mass, $r_C = r_C(\tilde{q})$, $\theta_C = \theta_C(\tilde{q})$, $\ell_C = \ell_C(\tilde{q})$, and $\ell_C = 1 + 3\cos^2(\theta_C)$. Moreover, $I_g(\tilde{q}) = g(\tilde{q})\, ds(\tilde{q})$ is the definite integral from 1 to $\tilde{q}$:

$$I_g(\tilde{q}) = \int_1^{\tilde{q}} \frac{2GM_\oplus \cos(\theta_C)}{r_C^2\sqrt{\ell_C}} h_q(\tilde{q})\, dq(\tilde{q}) \approx \sum_1^{\tilde{q}} \frac{2GM_\oplus \cos(\theta_C)}{r_C^2\sqrt{\ell_C}} h_q(\tilde{q})\, dq(\tilde{q}). \tag{61}$$

Equation 60 becomes

$$\ln(\rho) = \frac{mI_g(\tilde{q})}{k_B\left(T_\parallel + T_e\right)} - C. \tag{62}$$

Letting $\exp C = \breve{C}$ be another constant the general solution to Equation 58 is

$$\rho(\tilde{q}) = \breve{C} \exp\left[\frac{mI_g(\tilde{q})}{k_B\left(T_\parallel + T_e\right)}\right]. \tag{63}$$

Reference mass density at reference altitude z_0 in configuration-space grid cell $\tilde{q}_0$ is $\rho_0 = \rho(\tilde{q}_0)$ such that

$$\check{C} = \rho_0 \exp\left[\frac{-mI_g(\tilde{q}_0)}{k_B\left(T_\parallel + T_e\right)}\right] \tag{64}$$

and Equation 63 becomes

$$\rho(\tilde{q}) = \rho_0 \exp\left\{\frac{m\left[I_g(\tilde{q}) - I_g(\tilde{q}_0)\right]}{k_B\left(T_\parallel + T_e\right)}\right\}. \tag{65}$$

Dividing Equation 65 by ion mass gives ion number density profile with altitude projected onto magnetic field lines:

$$n_C(\tilde{q}) = n_0 \exp\left[\frac{m\bar{g}(\tilde{q})}{k_B\left(T_\parallel + T_e\right)}\right], \quad \bar{g} = \left[I_g(\tilde{q}) - I_g(\tilde{q}_0)\right]. \tag{66}$$

.7 Kinetic Solver

Macro-particle velocity components are computed by numerically integrating net acceleration components in time-independent global Cartesian unit bases by fourth-order Runge-Kutta (RK4). Kinetic simulation on given flux-tubes begin at time A and end at time B and split into N_t time-steps such that computational time-steps are

$$h = \frac{|(B - A)|}{N_t}. \tag{67}$$

In the modeling of wave-particle interaction by ion cyclotron resonance heating the computational time-step, h, is set to resolve the ion cyclotron interaction time, $\tau_\perp$, that is, $f_g^{-1} < h < \tau_\perp$, according to Subsection 2.2.5. Simulation time is pushed accordingly as $t \to t^N$ over a loop of all computational time-steps of index $\tilde{n} \in \begin{bmatrix} 1 & N_t \end{bmatrix}$:

$$t = \begin{cases} \tilde{n}h & \text{for } \tilde{n} = 1 \\ (\tilde{n} + 1)h & \text{for } \tilde{n} \neq 1, \end{cases} \tag{68}$$

where $t^N = (\tilde{n} + 1)h$ is the time advanced by h such that $t = B$ for $\tilde{n} = N_t$. Acceleration integrators are solved for macro-particles of index $\tilde{j} \in \begin{bmatrix} 1 & N_s \end{bmatrix}$ over all computational time-steps of index $\tilde{n} \in \begin{bmatrix} 1 & N_t \end{bmatrix}$. Fourth-order Runge-Kutta scheme of order $\mathcal{O}(h^5)$ integrate position-dependent macro-particle acceleration components in three-dimensional global Cartesian unit bases to avoid time-dependent unit vectors characteristic of curvilinear systems. Macro-particle net accelerations have the form

$$a_i(\tilde{j}) = a_i(x,\ y,\ z)_{\tilde{j}} \neq a_i(v_x,\ v_y,\ v_z)_{\tilde{j}}, \tag{69}$$

$\forall i = x,\ y,\ z$ where $(x,\ y,\ z)_{\tilde{j}}$ and $(v_x,\ v_y,\ v_z)_{\tilde{j}}$ are position and velocity coordinates of macro-particle $\tilde{j}$. Macro-particle translational velocity components are updated as

$$\begin{aligned}
v'_x(\tilde{n}+1) &= v'_x(\tilde{n}) + \frac{h}{6}\left[k^1_{v_x}(\tilde{n}) + 2k^2_{v_x}(\tilde{n}) + 2k^3_{v_x}(\tilde{n}) + k^4_{v_x}(\tilde{n})\right],\\
v'_y(\tilde{n}+1) &= v'_y(\tilde{n}) + \frac{h}{6}\left[k^1_{v_y}(\tilde{n}) + 2k^2_{v_y}(\tilde{n}) + 2k^3_{v_y}(\tilde{n}) + k^4_{v_y}(\tilde{n})\right],\\
v'_z(\tilde{n}+1) &= v'_z(\tilde{n}) + \frac{h}{6}\left[k^1_{v_z}(\tilde{n}) + 2k^2_{v_z}(\tilde{n}) + 2k^3_{v_z}(\tilde{n}) + k^4_{v_z}(\tilde{n})\right]
\end{aligned} \tag{70}$$

where

$$\begin{aligned}
k^1_{v_x}(\tilde{n}) &= a^{k^1}_x(\tilde{n}) = a_x\left[x^{k^1}(\tilde{n}),\ y^{k^1}(\tilde{n}),\ z^{k^1}(\tilde{n})\right],\\
k^2_{v_x}(\tilde{n}) &= a^{k^2}_x(\tilde{n}) = a_x\left[x^{k^2}(\tilde{n}),\ y^{k^2}(\tilde{n}),\ z^{k^2}(\tilde{n})\right],\\
k^3_{v_x}(\tilde{n}) &= k^2_{v_x}(\tilde{n}),\\
k^4_{v_x}(\tilde{n}) &= a^{k^4}_x(\tilde{n}) = a_x\left[x^{k^4}(\tilde{n}),\ y^{k^4}(\tilde{n}),\ z^{k^4}(\tilde{n})\right],\\
k^1_{v_y}(\tilde{n}) &= a^{k^1}_y(\tilde{n}) = a_y\left[x^{k^1}(\tilde{n}),\ y^{k^1}(\tilde{n}),\ z^{k^1}(\tilde{n})\right],\\
k^2_{v_y}(\tilde{n}) &= a^{k^2}_y(\tilde{n}) = a_y\left[x^{k^2}(\tilde{n}),\ y^{k^2}(\tilde{n}),\ z^{k^2}(\tilde{n})\right],\\
k^3_{v_y}(\tilde{n}) &= k^2_{v_y}(\tilde{n}),\\
k^4_{v_y}(\tilde{n}) &= a^{k^4}_y(\tilde{n}) = a_y\left[x^{k^4}(\tilde{n}),\ y^{k^4}(\tilde{n}),\ z^{k^4}(\tilde{n})\right],\\
k^1_{v_z}(\tilde{n}) &= a^{k^1}_z(\tilde{n}) = a_z\left[x^{k^1}(\tilde{n}),\ y^{k^1}(\tilde{n}),\ z^{k^1}(\tilde{n})\right],\\
k^2_{v_z}(\tilde{n}) &= a^{k^2}_z(\tilde{n}) = a_z\left[x^{k^2}(\tilde{n}),\ y^{k^2}(\tilde{n}),\ z^{k^2}(\tilde{n})\right],\\
k^3_{v_z}(\tilde{n}) &= k^2_{v_z}(\tilde{n}),\\
k^4_{v_z}(\tilde{n}) &= a^{k^4}_z(\tilde{n}) = a_z\left[x^{k^4}(\tilde{n}),\ y^{k^4}(\tilde{n}),\ z^{k^4}(\tilde{n})\right],
\end{aligned} \tag{71}$$

and

$$
\begin{aligned}
x^{k^1}(\tilde{n}) = x(\tilde{n}), \quad x^{k^2}(\tilde{n}) &= x(\tilde{n}) + hv'_x(\tilde{n})/2, \\
x^{k^4}(\tilde{n}) &= x(\tilde{n}) + hv'_x(\tilde{n}) + h^2 a_x^{k^1}(\tilde{n})/2, \\
y^{k^1}(\tilde{n}) = y(\tilde{n}), \quad y^{k^2}(\tilde{n}) &= y(\tilde{n}) + hv'_y(\tilde{n})/2, \\
y^{k^4}(\tilde{n}) &= y(\tilde{n}) + hv'_y(\tilde{n}) + h^2 a_y^{k^1}(\tilde{n})/2, \\
z^{k^1}(\tilde{n}) = z(\tilde{n}), \quad z^{k^2}(\tilde{n}) &= z(\tilde{n}) + hv'_z(\tilde{n})/2, \\
z^{k^4}(\tilde{n}) &= z(\tilde{n}) + hv'_z(\tilde{n}) + h^2 a_z^{k^1}(\tilde{n})/2.
\end{aligned}
\tag{72}
$$

Cartesian velocity components $(v'_x,\ v'_y,\ v'_z)_{\tilde{n}+1}$ of Equation 70 are transformed into dipole components $(v'_p,\ v'_{\parallel},\ v'_{\phi})_{\tilde{n}+1}$. Translational components for ions are parallel to the magnetic field such that $v'_p = v'_{\phi} = 0$ and associated Cartesian velocity components $(v_x,\ v_y,\ v_z)_{\tilde{n}+1}$ are generated. Particle positions are updated each computational time-step as

$$
\begin{aligned}
x(\tilde{n}+1) &= x(\tilde{n}) + \left(\frac{h}{6}\right)\left[k_x^1(\tilde{n}) + 2k_x^2(\tilde{n}) + 2k_x^3(\tilde{n}) + k_x^4(\tilde{n})\right], \\
y(\tilde{n}+1) &= y(\tilde{n}) + \left(\frac{h}{6}\right)\left[k_y^1(\tilde{n}) + 2k_y^2(\tilde{n}) + 2k_y^3(\tilde{n}) + k_y^4(\tilde{n})\right], \\
z(\tilde{n}+1) &= z(\tilde{n}) + \left(\frac{h}{6}\right)\left[k_z^1(\tilde{n}) + 2k_z^2(\tilde{n}) + 2k_z^3(\tilde{n}) + k_z^4(\tilde{n})\right]
\end{aligned}
\tag{73}
$$

where

$$
\begin{aligned}
k_x^1(\tilde{n}) &= v'_x(\tilde{n}), \quad k_x^2(\tilde{n}) = v'_x(\tilde{n}) + ha_x^{k^1}(\tilde{n})/2, \quad k_x^3(\tilde{n}) = k_x^2(\tilde{n}), \quad k_x^4(\tilde{n}) = v'_x(\tilde{n}) + ha_x^{k^2}(\tilde{n}), \\
k_y^1(\tilde{n}) &= v'_y(\tilde{n}), \quad k_y^2(\tilde{n}) = v'_y(\tilde{n}) + ha_y^{k^1}(\tilde{n})/2, \quad k_y^3(\tilde{n}) = k_y^2(\tilde{n}), \quad k_y^4(\tilde{n}) = v'_y(\tilde{n}) + ha_y^{k^2}(\tilde{n}), \\
k_z^1(\tilde{n}) &= v'_z(\tilde{n}), \quad k_z^2(\tilde{n}) = v'_z(\tilde{n}) + ha_z^{k^1}(\tilde{n})/2, \quad k_z^3(\tilde{n}) = k_z^2(\tilde{n}), \quad k_z^4(\tilde{n}) = v'_z(\tilde{n}) + ha_z^{k^2}(\tilde{n}).
\end{aligned}
\tag{74}
$$

Macro-particle translational velocity and position components are updated in $\forall \tilde{n} \in \begin{bmatrix} 1 & N_t \end{bmatrix}$:

$$
\left[v_x(\tilde{n}),\ v_y(\tilde{n}),\ v_z(\tilde{n})\right] = \begin{cases} \left(v_{x0},\ v_{y0},\ v_{z0}\right) & \text{for } \tilde{n} = 1 \\ \left[v_x(\tilde{n}+1),\ v_y(\tilde{n}+1),\ v_z(\tilde{n}+1)\right] & \text{for } \tilde{n} \neq 1, \end{cases}
\tag{75}
$$

$$
\left[x(\tilde{n}),\ y(\tilde{n}),\ z(\tilde{n})\right] = \begin{cases} \left(x_0,\ y_0,\ z_0\right) & \text{for } \tilde{n} = 1 \\ \left[x(\tilde{n}+1),\ y(\tilde{n}+1),\ z(\tilde{n}+1)\right] & \text{for } \tilde{n} \neq 1. \end{cases}
\tag{76}
$$

.8 Energy-Pitch Angle Distributions

Ion distribution functions of Equation 2.44, $f(\tilde{q},\ \tilde{v}_{\perp 1},\ \tilde{v}_{\perp 2},\ \tilde{v}_{\parallel})$, are transformed into distribution functions in energy, pitch-angle, and gyro-angle space $f_E(\tilde{q},\ \tilde{E},\ \tilde{\alpha},\ \tilde{\theta})$ where $\tilde{E}$, $\tilde{\alpha}$, and $\tilde{\theta}$ are indices in energy, pitch-angle, and gyro-angle grid cells and $\tilde{q}$ is the spatial cell index omitted in what follows. Three-dimensional linearly-spaced grids in $(\tilde{E},\ \tilde{\alpha},\ \tilde{\theta})$ are constructed for centered grid cell values $(E_C,\ \alpha_C,\ \theta_C)$ where $0 \leq \alpha_C \leq \pi$, $0 \leq \theta_C \leq 2\pi$, and E_C ranges energy domain in [eV] provided by $f(\tilde{v}_{\perp 1},\ \tilde{v}_{\perp 2},\ \tilde{v}_{\parallel})$. Although this study simulates the southern terrestrial magnetic hemisphere at the location of the VISIONS-1 sounding rocket, pitch-angles are measured from outward directions of the dipole field $\mathbf{B}$. Grid values $E_C = E_C(\tilde{E},\ \tilde{\alpha},\ \tilde{\theta})$, $\alpha_C = \alpha_C(\tilde{E},\ \tilde{\alpha},\ \tilde{\theta})$, and $\theta_C = \theta_C(\tilde{E},\ \tilde{\alpha},\ \tilde{\theta})$ are spherically symmetric coordinates transformed into local ion gyro-frame Cartesian coordinates $v'_{xC} = v'_{xC}(\tilde{E},\ \tilde{\alpha},\ \tilde{\theta})$, $v'_{yC} = v'_{yC}(\tilde{E},\ \tilde{\alpha},\ \tilde{\theta})$, and $v'_{zC} = v'_{zC}(\tilde{E},\ \tilde{\alpha},\ \tilde{\theta})$ from the following relations:

$$\begin{aligned}
v'_{xC}(\tilde{E},\ \tilde{\alpha},\ \tilde{\theta}) &= \sqrt{\frac{2E_C(\tilde{E},\ \tilde{\alpha},\ \tilde{\theta})}{m}} \sin\left[\alpha_C(\tilde{E},\ \tilde{\alpha},\ \tilde{\theta})\right] \cos\left[\theta_C(\tilde{E},\ \tilde{\alpha},\ \tilde{\theta})\right], \\
v'_{yC}(\tilde{E},\ \tilde{\alpha},\ \tilde{\theta}) &= \sqrt{\frac{2E_C(\tilde{E},\ \tilde{\alpha},\ \tilde{\theta})}{m}} \sin\left[\alpha_C(\tilde{E},\ \tilde{\alpha},\ \tilde{\theta})\right] \sin\left[\theta_C(\tilde{E},\ \tilde{\alpha},\ \tilde{\theta})\right], \\
v'_{zC}(\tilde{E},\ \tilde{\alpha},\ \tilde{\theta}) &= \sqrt{\frac{2E_C(\tilde{E},\ \tilde{\alpha},\ \tilde{\theta})}{m}} \cos\left[\alpha_C(\tilde{E},\ \tilde{\alpha},\ \tilde{\theta})\right]
\end{aligned} \tag{77}$$

where functional forms of energy, pitch-angle, and gyro-angle are $E = m\left(v_x^2 + v_y^2 + v_z^2\right)/2$, $\alpha = \pi/4 - \arctan\left(v_\perp/v_z\right)$, and $\theta = \arccos\left(v_x/v_\perp\right)$, respectively, for ion mass m such that $\tilde{v}_x = \tilde{v}_{\perp 2}$, $\tilde{v}_y = \tilde{v}_{\perp 1}$, and $\tilde{v}_z = \tilde{v}_{\parallel}$ are particle velocity components in local gyro-frames along $\hat{\mathbf{e}}^{\mathbf{v}}_{\mathbf{x}}$, $\hat{\mathbf{e}}^{\mathbf{v}}_{\mathbf{y}}$, and $\hat{\mathbf{e}}^{\mathbf{v}}_{\mathbf{z}}$ directions, respectively, according to Figure 2.2. Ion distribution functions $f(\tilde{v}_{\perp 1}, \tilde{v}_{\perp 2}, \tilde{v}_{\parallel})$ are interpolated onto grid values of Equation 77 to generate distributions $f[v'_{xC}(\tilde{E}, \tilde{\alpha}, \tilde{\theta}), v'_{yC}(\tilde{E}, \tilde{\alpha}, \tilde{\theta}), v'_{zC}(\tilde{E}, \tilde{\alpha}, \tilde{\theta})]$. Transformation of $f \rightarrow f_E$ requires the computation of the Jacobian determinant $|J|$ [Zettergren, 2009]

$$f_E(\tilde{E},\ \tilde{\alpha},\ \tilde{\theta}) = f[v'_{xC}(\tilde{E},\ \tilde{\alpha},\ \tilde{\theta}),\ v'_{yC}(\tilde{E},\ \tilde{\alpha},\ \tilde{\theta}),\ v'_{zC}(\tilde{E},\ \tilde{\alpha},\ \tilde{\theta})] \cdot |J| \tag{78}$$

where

$$|J| = \begin{bmatrix} \partial_{E_C} v'_{xC} & \partial_{\alpha_C} v'_{xC} & \partial_{\theta_C} v'_{xC} \\ \partial_{E_C} v'_{yC} & \partial_{\alpha_C} v'_{yC} & \partial_{\theta_C} v'_{yC} \\ \partial_{E_C} v'_{zC} & \partial_{\alpha_C} v'_{zC} & \partial_{\theta_C} v'_{zC} \end{bmatrix}, \tag{79}$$

such that, from Equation 77, the Jacobian determinant becomes [Zettergren, 2009]

$$|J| = \frac{1}{m}\sqrt{\frac{2E_C}{m}}\sin(\alpha_C). \tag{80}$$

Equation 78 gives energy-pitch angle distributions f_E in units of [$\mathrm{J}^{-1} \cdot \mathrm{m}^{-3} \cdot \mathrm{sr}^{-1}$] or [$\mathrm{eV}^{-1} \cdot \mathrm{m}^{-3} \cdot \mathrm{sr}^{-1}$].

$$f_E(\tilde{E}, \tilde{\alpha}, \tilde{\theta}) = \frac{1}{m}\sqrt{\frac{2E_C}{m}}\sin(\alpha_C) f[v'_{xC}(\tilde{E}, \tilde{\alpha}, \tilde{\theta}), v'_{yC}(\tilde{E}, \tilde{\alpha}, \tilde{\theta}), v'_{zC}(\tilde{E}, \tilde{\alpha}, \tilde{\theta})]. \tag{81}$$

f_E represents the number of ions in each three-dimensional energy-pitch-angle space grid cell divided by spatial and energy-pitch angle volumes consistent with Equation 2.44 where $d\Omega = \sin(\alpha_C)\, d\alpha_C\, d\theta_C$ is solid angle in [sr]. Integration of f_E over $dE\, d\Omega$ gives plasma density consistent with Equation 2.46:

$$f_E(\tilde{E}, \tilde{\alpha}, \tilde{\theta}) = \frac{\mathcal{N}}{dE\, d\Omega}, \quad n = \int\int\int f_E(\tilde{E}, \tilde{\alpha}, \tilde{\theta})\, dE\, d\Omega. \tag{82}$$

Differential number flux in units of [$\mathrm{eV}^{-1} \cdot \mathrm{m}^{-2} \cdot \mathrm{s}^{-1} \cdot \mathrm{sr}^{-1}$] is $\phi_N = v f_E$ and differential energy flux in units of [$\mathrm{eV} \cdot \mathrm{eV}^{-1} \cdot \mathrm{m}^{-2} \cdot \mathrm{s}^{-1} \cdot \mathrm{sr}^{-1}$] is $\phi_E = E\phi_N$ such that

$$\begin{aligned} \phi_N(\tilde{E}, \tilde{\alpha}, \tilde{\theta}) &= \frac{2E_C}{m^2} f[v'_{xC}(\tilde{E}, \tilde{\alpha}, \tilde{\theta}), v'_{yC}(\tilde{E}, \tilde{\alpha}, \tilde{\theta}), v'_{zC}(\tilde{E}, \tilde{\alpha}, \tilde{\theta})], \\ \phi_E(\tilde{E}, \tilde{\alpha}, \tilde{\theta}) &= \frac{2E_C^2}{m^2} f[v'_{xC}(\tilde{E}, \tilde{\alpha}, \tilde{\theta}), v'_{yC}(\tilde{E}, \tilde{\alpha}, \tilde{\theta}), v'_{zC}(\tilde{E}, \tilde{\alpha}, \tilde{\theta})]. \end{aligned} \tag{83}$$

Differential fluxes are sorted by pitch-angle such that, for $\alpha = 0°$ measured outwards along $\mathbf{B}$, upwards components correspond to $0° \leq \alpha \leq 30°$, transverse components at $60° \leq \alpha \leq 120°$, and upwards components from $150° \leq \alpha \leq 180°$.

.9 Spherical Unit Basis

N-dimensional contravariant position vectors $\mathbf{r} \in \mathbb{R}^N$ have the form

$$\mathbf{r} = \sum_i^N r_i \hat{\mathbf{e}}_\mathbf{i}.$$

$\mathbf{r}$ has components r_i, scale factors $h_i = |\partial_i \mathbf{r}_R|$, metric factors $g_{ii} = h_i^2$, and unit vectors $\hat{\mathbf{e}}_\mathbf{i} = h_i^{-1}\partial_i \mathbf{r}_R \; \forall i = 1, 2, 3, \ldots N$ where $\mathbf{r}_R$ is a position vector in some reference coordinate system. For expressions of spherical unit vectors in global Cartesian unit bases let $\mathbf{r} = \mathbf{r}_s$ in spherical coordinates and $\mathbf{r}_R = \mathbf{r}_C$ in global Cartesian coordinates such that $\hat{\mathbf{e}}_\mathbf{i} \neq \hat{\mathbf{e}}_\mathbf{i}(r,\ \theta,\ \phi)\ \forall i = x,\ y,\ z,$ where

$$\mathbf{r}_C = x(r,\ \theta,\ \phi)\hat{\mathbf{e}}_\mathbf{x} + y(r,\ \theta,\ \phi)\hat{\mathbf{e}}_\mathbf{y} + z(r,\ \theta,\ \phi)\hat{\mathbf{e}}_\mathbf{z},$$

$x(r,\ \theta,\ \phi) = r\cos(\phi)\sin(\theta)$, $y(r,\ \theta,\ \phi) = r\sin(\phi)\sin(\theta)$, $z(r,\ \theta,\ \phi) = r\cos(\theta)$, and $h_i = 1$ $\forall i = x,\ y,\ z$. Radial differentials of $\mathbf{r}_C$ are

$$\partial_r\mathbf{r}_C = \cos(\phi)\sin(\theta)\hat{\mathbf{e}}_\mathbf{x} + \sin(\phi)\sin(\theta)\hat{\mathbf{e}}_\mathbf{y} + \cos(\theta)\hat{\mathbf{e}}_\mathbf{z},$$

such that $|\partial_r\mathbf{r}_C| = 1$, $h_r = 1$, and $g_{rr} = 1$. Radial unit vectors in global Cartesian coordinate basis are

$$\hat{\mathbf{e}}_\mathbf{r} = [\cos(\phi)\sin(\theta)]\,\hat{\mathbf{e}}_\mathbf{x} + [\sin(\phi)\sin(\theta)]\,\hat{\mathbf{e}}_\mathbf{y} + [\cos(\theta)]\,\hat{\mathbf{e}}_\mathbf{z}. \tag{84}$$

Polar angle differentials of $\mathbf{r}_C$ are

$$\partial_\theta\mathbf{r}_C = r\cos(\phi)\cos(\theta)\hat{\mathbf{e}}_\mathbf{x} + r\sin(\phi)\cos(\theta)\hat{\mathbf{e}}_\mathbf{y} - r\sin(\theta)\hat{\mathbf{e}}_\mathbf{z},$$

such that $|\partial_\theta\mathbf{r}_C| = r$, $h_\theta = r$, $g_{\theta\theta} = r^2$, and the polar unit vector in global Cartesian coordinate basis is

$$\hat{\mathbf{e}}_\theta = [\cos(\phi)\cos(\theta)]\,\hat{\mathbf{e}}_\mathbf{x} + [\sin(\phi)\cos(\theta)]\,\hat{\mathbf{e}}_\mathbf{y} - [\sin(\theta)]\,\hat{\mathbf{e}}_\mathbf{z}. \tag{85}$$

Azimuthal angle differentials of $\mathbf{r}_C$ are

$$\partial_\phi\mathbf{r}_C = -r\sin(\phi)\sin(\theta)\hat{\mathbf{e}}_\mathbf{x} + r\cos(\phi)\sin(\theta)\hat{\mathbf{e}}_\mathbf{y}$$

such that $|\partial_\phi\mathbf{r}_C| = r\sin(\theta)$, $h_\phi = r\sin(\theta)$, $g_{\phi\phi} = r^2\sin^2(\theta)$, and the spherical azimuthal unit vector in global Cartesian coordinate basis is

$$\hat{\mathbf{e}}_\phi = [-\sin(\phi)]\,\hat{\mathbf{e}}_\mathbf{x} + [\cos(\phi)]\,\hat{\mathbf{e}}_\mathbf{y}. \tag{86}$$

Cartesian unit vectors in spherical unit bases are

$$\hat{\mathbf{e}}_\mathbf{x} = [\sin(\theta)\cos(\phi)]\,\hat{\mathbf{e}}_\mathbf{r} + [\cos(\theta)\cos(\phi)]\,\hat{\mathbf{e}}_\theta - [\sin(\phi)]\,\hat{\mathbf{e}}_\phi, \tag{87}$$

$$\hat{\mathbf{e}}_\mathbf{y} = [\sin(\theta)\sin(\phi)]\,\hat{\mathbf{e}}_\mathbf{r} + [\cos(\theta)\sin(\phi)]\,\hat{\mathbf{e}}_\theta + [\cos(\phi)]\,\hat{\mathbf{e}}_\phi, \tag{88}$$

and

$$\hat{\mathbf{e}}_{\mathbf{z}} = [\cos(\theta)]\,\hat{\mathbf{e}}_{\mathbf{r}} - [\sin(\theta)]\,\hat{\mathbf{e}}_{\theta}. \tag{89}$$

.10 Coordinate Transformations

Global Cartesian to spherical unit vector transformations, $(x,\ y,\ z) \rightarrow (r,\ \theta,\ \phi)$, are given by

$$\begin{aligned}
\hat{\mathbf{e}}_{\mathbf{x}} &= [\sin(\theta)\cos(\phi)]\,\hat{\mathbf{e}}_{\mathbf{r}} + [\cos(\theta)\cos(\phi)]\,\hat{\mathbf{e}}_{\theta} - [\sin(\phi)]\,\hat{\mathbf{e}}_{\phi},\\
\hat{\mathbf{e}}_{\mathbf{y}} &= [\sin(\theta)\sin(\phi)]\,\hat{\mathbf{e}}_{\mathbf{r}} + [\cos(\theta)\sin(\phi)]\,\hat{\mathbf{e}}_{\theta} + [\cos(\phi)]\,\hat{\mathbf{e}}_{\phi},\\
\hat{\mathbf{e}}_{\mathbf{z}} &= [\cos(\theta)]\,\hat{\mathbf{e}}_{\mathbf{r}} - [\sin(\theta)]\,\hat{\mathbf{e}}_{\theta}.
\end{aligned} \tag{90}$$

Spherical to global Cartesian unit vector transformations, $(r,\ \theta,\ \phi) \rightarrow (x,\ y,\ z)$ are

$$\begin{aligned}
\hat{\mathbf{e}}_{\mathbf{r}} &= [\sin(\theta)\cos(\phi)]\,\hat{\mathbf{e}}_{\mathbf{x}} + [\sin(\theta)\sin(\phi)]\,\hat{\mathbf{e}}_{\mathbf{y}} + [\cos(\theta)]\,\hat{\mathbf{e}}_{\mathbf{z}},\\
\hat{\mathbf{e}}_{\theta} &= [\cos(\theta)\cos(\phi)]\,\hat{\mathbf{e}}_{\mathbf{x}} + [\cos(\theta)\sin(\phi)]\,\hat{\mathbf{e}}_{\mathbf{y}} - [\sin(\theta)]\,\hat{\mathbf{e}}_{\mathbf{z}},\\
\hat{\mathbf{e}}_{\phi} &= [-\sin(\phi)]\,\hat{\mathbf{e}}_{\mathbf{x}} + [\cos(\phi)]\,\hat{\mathbf{e}}_{\mathbf{y}}.
\end{aligned} \tag{91}$$

Spherical to magnetic dipole unit vector transformations, $(r,\ \theta,\ \phi) \rightarrow (p,\ q, \phi)$, where $\ell = 1 + 3\cos^2(\theta)$, are

$$\begin{aligned}
\hat{\mathbf{e}}_{\mathbf{r}} &= \left[\frac{\sin(\theta)}{\sqrt{\ell}}\right]\hat{\mathbf{e}}_{\mathbf{p}} + \left[\frac{2\cos(\theta)}{\sqrt{\ell}}\right]\hat{\mathbf{e}}_{\mathbf{q}},\\
\hat{\mathbf{e}}_{\theta} &= -\left[\frac{2\cos(\theta)}{\sqrt{\ell}}\right]\hat{\mathbf{e}}_{\mathbf{p}} + \left[\frac{\sin(\theta)}{\sqrt{\ell}}\right]\hat{\mathbf{e}}_{\mathbf{q}},\\
\hat{\mathbf{e}}_{\phi} &= \hat{\mathbf{e}}_{\phi}.
\end{aligned} \tag{92}$$

Dipole to spherical transformations, $(p,\ q,\ \phi) \rightarrow (r,\ \theta,\ \phi)$, where $\ell = 1 + 3\cos^2(\theta)$, are given by

$$\begin{aligned}
\hat{\mathbf{e}}_{\mathbf{p}} &= \left[\frac{\sin(\theta)}{\sqrt{\ell}}\right]\hat{\mathbf{e}}_{\mathbf{r}} - \left[\frac{2\cos(\theta)}{\sqrt{\ell}}\right]\hat{\mathbf{e}}_{\theta},\\
\hat{\mathbf{e}}_{\mathbf{q}} &= \left[\frac{2\cos(\theta)}{\sqrt{\ell}}\right]\hat{\mathbf{e}}_{\mathbf{r}} + \left[\frac{\sin(\theta)}{\sqrt{\ell}}\right]\hat{\mathbf{e}}_{\theta},\\
\hat{\mathbf{e}}_{\phi} &= \hat{\mathbf{e}}_{\phi}.
\end{aligned} \tag{93}$$

Global Cartesian to dipole transformations, $(x,\ y,\ z) \rightarrow (p,\ q,\ \phi)$, where $\ell = 1 + 3\cos^2(\theta)$, give

$$\begin{aligned}
\hat{\mathbf{e}}_{\mathbf{x}} &= \left\{ \frac{\cos(\phi)\left[1 - 3\cos^2(\theta)\right]}{\sqrt{\ell}} \right\} \hat{\mathbf{e}}_{\mathbf{p}} + \left[\frac{3\cos(\theta)\sin(\theta)\cos(\phi)}{\sqrt{\ell}} \right] \hat{\mathbf{e}}_{\mathbf{q}} - [\sin(\phi)]\, \hat{\mathbf{e}}_{\phi}, \\
\hat{\mathbf{e}}_{\mathbf{y}} &= \left\{ \frac{\sin(\phi)\left[1 - 3\cos^2(\theta)\right]}{\sqrt{\ell}} \right\} \hat{\mathbf{e}}_{\mathbf{p}} + \left[\frac{3\cos(\theta)\sin(\theta)\sin(\phi)}{\sqrt{\ell}} \right] \hat{\mathbf{e}}_{\mathbf{q}} + [\cos(\phi)]\, \hat{\mathbf{e}}_{\phi}, \\
\hat{\mathbf{e}}_{\mathbf{z}} &= \left[\frac{3\cos(\theta)\sin(\theta)}{\sqrt{\ell}} \right] \hat{\mathbf{e}}_{\mathbf{p}} + \left[\frac{3\cos^2(\theta) - 1}{\sqrt{\ell}} \right] \hat{\mathbf{e}}_{\mathbf{q}}.
\end{aligned} \tag{94}$$

Dipole to global Cartesian unit vector transformations, $(p,\ q,\ \phi) \to (x,\ y,\ z)$, where $\ell = 1 + 3\cos^2(\theta)$, are

$$\begin{aligned}
\hat{\mathbf{e}}_{\mathbf{p}} &= \left\{ \frac{\cos(\phi)\left[1 - 3\cos^2(\theta)\right]}{\sqrt{\ell}} \right\} \hat{\mathbf{e}}_{\mathbf{x}} + \left\{ \frac{\sin(\phi)\left[1 - 3\cos^2(\theta)\right]}{\sqrt{\ell}} \right\} \hat{\mathbf{e}}_{\mathbf{y}} + \left[\frac{3\cos(\theta)\sin(\theta)}{\sqrt{\ell}} \right] \hat{\mathbf{e}}_{\mathbf{z}}, \\
\hat{\mathbf{e}}_{\mathbf{q}} &= \left[\frac{3\cos(\theta)\sin(\theta)\cos(\phi)}{\sqrt{\ell}} \right] \hat{\mathbf{e}}_{\mathbf{x}} + \left[\frac{3\cos(\theta)\sin(\theta)\sin(\phi)}{\sqrt{\ell}} \right] \hat{\mathbf{e}}_{\mathbf{y}} + \left[\frac{3\cos^2(\theta) - 1}{\sqrt{\ell}} \right] \hat{\mathbf{e}}_{\mathbf{z}}, \\
\hat{\mathbf{e}}_{\phi} &= -\sin(\phi)\hat{\mathbf{e}}_{\mathbf{x}} + \cos(\phi)\hat{\mathbf{e}}_{\mathbf{y}}.
\end{aligned} \tag{95}$$

Global Cartesian to spherical basis transformation for a vector $\mathbf{v} \in \mathbb{R}^3$ of the form

$$\mathbf{v} = v_x\hat{\mathbf{e}}_{\mathbf{x}} + v_y\hat{\mathbf{e}}_{\mathbf{y}} + v_z\hat{\mathbf{e}}_{\mathbf{z}}, \tag{96}$$

by Equations 90 is given by

$$\begin{aligned}
\mathbf{v} = &\left[v_x \sin(\theta)\cos(\phi) + v_y \sin(\theta)\sin(\phi) + v_z \cos(\theta)\right] \hat{\mathbf{e}}_{\mathbf{r}} \\
&+ \left[v_x \cos(\theta)\cos(\phi) + v_y \cos(\theta)\sin(\phi) - v_z \sin(\theta)\right] \hat{\mathbf{e}}_{\theta} \\
&+ \left[-v_x \sin(\phi) + v_y \cos(\phi)\right] \hat{\mathbf{e}}_{\phi}.
\end{aligned} \tag{97}$$

Spherical to global Cartesian basis transformation for a vector $\mathbf{v} \in \mathbb{R}^3$ of the form

$$\mathbf{v} = v_r\hat{\mathbf{e}}_{\mathbf{r}} + v_\theta\hat{\mathbf{e}}_{\theta} + v_\phi\hat{\mathbf{e}}_{\phi}, \tag{98}$$

by Equations 91 is given by

$$\begin{aligned}\mathbf{v} = &\left[v_r \sin(\theta)\cos(\phi) + v_\theta \cos(\theta)\cos(\phi) - v_{\phi_s}\sin(\phi)\right]\hat{\mathbf{e}}_\mathbf{x} \\ &+ \left[v_r \sin(\theta)\sin(\phi) + v_\theta \cos(\theta)\sin(\phi) + v_\phi \cos(\phi)\right]\hat{\mathbf{e}}_\mathbf{y} \\ &+ \left[v_r \cos(\theta) - v_\theta \sin(\theta)\right]\hat{\mathbf{e}}_\mathbf{z}.\end{aligned} \tag{99}$$

Spherical to dipole basis transformation for a vector $\mathbf{v} \in \mathbb{R}^3$ of the form of Equation 98, by Equations 92 is given by

$$\mathbf{v} = \left[\frac{v_r \sin(\theta)}{\sqrt{\ell}} - \frac{2v_\theta \cos(\theta)}{\sqrt{\ell}}\right]\hat{\mathbf{e}}_\mathbf{p} + \left[\frac{2v_r \cos(\theta)}{\sqrt{\ell}} + \frac{v_\theta \sin(\theta)}{\sqrt{\ell}}\right]\hat{\mathbf{e}}_\mathbf{q} + v_\phi \hat{\mathbf{e}}_\phi, \tag{100}$$

where $\ell = 1 + 3\cos^2(\theta)$. Dipole to spherical basis transformation for a vector $\mathbf{v} \in \mathbb{R}^3$ of the form

$$\mathbf{v} = v_p \hat{\mathbf{e}}_\mathbf{p} + v_q \hat{\mathbf{e}}_\mathbf{q} + v_\phi \hat{\mathbf{e}}_\phi, \tag{101}$$

by Equations 93 is then

$$\mathbf{v} = \left[\frac{2v_q \cos(\theta)}{\sqrt{\ell}} + \frac{v_p \sin(\theta)}{\sqrt{\ell}}\right]\hat{\mathbf{e}}_\mathbf{r} + \left[\frac{v_q \sin(\theta)}{\sqrt{\ell}} - \frac{2v_p \cos(\theta)}{\sqrt{\ell}}\right]\hat{\mathbf{e}}_\theta + v_\phi \hat{\mathbf{e}}_\phi. \tag{102}$$

Dipole to global Cartesian basis transformation for $\mathbf{v} \in \mathbb{R}^3$ of the form of Equation 101, by Equations 95 is given by

$$\begin{aligned}\mathbf{v} = &\left(\frac{\cos(\phi)}{\sqrt{\ell}}\left\{3v_q \cos(\theta)\sin(\theta) + v_p\left[1 - 3\cos^2(\theta)\right]\right\} - v_\phi \sin(\phi)\right)\hat{\mathbf{e}}_\mathbf{x} \\ &+ \left(\frac{\sin(\phi)}{\sqrt{\ell}}\left\{3v_q \cos(\theta)\sin(\theta) + v_p\left[1 - 3\cos^2(\theta)\right]\right\} + v_\phi \cos(\phi)\right)\hat{\mathbf{e}}_\mathbf{y} \\ &+ \left\{\frac{v_q\left[3\cos^2(\theta) - 1\right]}{\sqrt{\ell}} + \frac{3v_p \cos(\theta)\sin(\theta)}{\sqrt{\ell}}\right\}\hat{\mathbf{e}}_\mathbf{z}.\end{aligned} \tag{103}$$

Lastly, global Cartesian to dipole basis transformations for $\mathbf{v} \in \mathbb{R}^3$ of the form of Equation 96, by Equations 94 are given by

$$\begin{aligned}\mathbf{v} = &\left\{ \frac{\left[1 - 3\cos^2(\theta)\right]}{\sqrt{\ell}}[v_x \cos(\phi) + v_y \sin(\phi)] + \frac{3v_z \cos(\theta)\sin(\theta)}{\sqrt{\ell}} \right\} \hat{\mathbf{e}}_{\mathbf{p}} \\ &+ \left\{ \frac{3\cos(\theta)\sin(\theta)}{\sqrt{\ell}}[v_x \cos(\phi) + v_y \sin(\phi)] + \frac{v_z \left[3\cos^2(\theta) - 1\right]}{\sqrt{\ell}} \right\} \hat{\mathbf{e}}_{\mathbf{q}} \\ &+ \left[-v_x \sin(\phi) + v_y \cos(\phi)\right] \hat{\mathbf{e}}_{\phi}.\end{aligned} \tag{104}$$

Bibliography

T. Abe, T. Okuzawa, K. Oyama, H. Fukunishi, and R. Fujii. Variation of thermal electron energy distribution associated with field-aligned currents. *Geophysical Research Letters*, 18:349–352, 1991.

H. Alfvén and C. G. Falthammar. *Cosmical electrodynamics: fundamental principles.* Claredon, Oxford, Englad, 1963.

R. R. Anderson and K. Maeda. VLF emissions associated with enhanced magnetospheric electrons. *Journal of Geophysical Research*, 82(1):135–146, 1977.

M. André and A. W. Yau. Theories and observations of ion energization and outflows in the high latitude magnetosphere. *Space Science Reviews*, 80:27–48, 1997.

M. André, P. Norqvist, L. Andersson, L. Eliasson, A. I. Eriksson, L. Blomberg, R. E. Erlandson, and J. Waldemark. Ion energization mechanisms at 1700 km in the auroral region. *Journal of Geophysical Research*, 103(4199-4222), 1998.

R. L. Arnoldy. Transverse ion acceleration by active experiments. *Auroral Plasma Dynamics, Geophysical Monograph Series*, 80:195, 1993.

W. I. Axford. The polar wind and the terrestrial helium budget. *Journal of Geophysical Research*, 73:6855–6859, 1968.

P. M. Banks and T. E. Holzer. The polar wind. *Journal of Geophysical Research*, 73:6846–6854, 1968.

A. R. Barakat and I. A. Barghouthi. The effect of wave-particle interactions on the polar wind O^+. *Geophysical Research Letters*, 21:2279–2282, 1994.

A. R. Barakat and R. W. Shunk. O^+ ions in the polar wind. *Journal of Geophysical Research*, 88: 7887–7894, 1983.

A. R. Barakat, I. A. Barghouthi, and R. W. Shunk. Double-hump H^+ velocity distribution in the polar wind. *Geophysical Research Letters*, 22:1857–1860, 1995.

A. R. Barakat, J. V. Eccles, and R. W. Shunk. Oscillating ionospheric outflow. *Geophysical Research Letters*, 2015.

I. A. Barghouthi. A Monte Carlo study for ion outflows at high altitude and high latitude: Barghouthi model. *Journal of Geophysical Research*, 113, 2008.

I. A. Barghouthi and M. A. Atout. Monte Carlo modeling of toroidal ion distributions and ion temperatures at high altitudes equatorward of the cusp: Effect of finite gyroradius. *Journal of Geophysical Research*, 111, 2006.

I. A. Barghouthi, A. R. Barakat, and R. W. Shunk. Monte Carlo study of the transition region in the polar wind: An improved collision model. *Journal of Geophysical Research*, 98(17):583–17591, 1993.

I. A. Barghouthi, A. R. Barakat, and A. M. Persoon. The effects of altitude-dependent wave particle interactions on the polar wind plasma. *Astrophysics and Space Science*, 259:117–140, 1998.

P. L. Blelly and D. Alcaydé. Electron heat flow in the auroral ionosphere inferred from EISCAT-VHF observations. *Journal of Geophysical Research*, 99(13):181–188, 1994.

P. L. Blelly, A. Robineau, and D. Alcaydé. Numerical modelling of intermittent ion outflow events above EISCAT. *Journal of Atmospheric and Terrestrial Physics*, 58(1-4):273–285, 1996.

M. Bouhram, N. Dubouloz, M. Malingre, J. R. Jasperse, R. Pottelette, C. Senior, D. Delcourt, C. W. Carlson, I. Roth, M. Berthomier, and J. A. Sauvaud. Ion outflow and associated perpendicular heating in the cusp observed by Interball Auroral Probe and Fast Auroral Snapshot. *Journal of Geophysical Research*, 107(A2), 2002.

M. Bouhram, M. Malingre, J. R. Jasperse, and N. Dubouloz. Modeling transverse heating and outflow of ionospheric ions from the dayside cusp/cleft. 1 A parametric study. *Annales Geophysicae*, 21:1753–1771, 2003a.

M. Bouhram, M. Malingre, J. R. Jasperse, N. Dubouloz, and J. A. Sauvaud. Modeling transverse heating and outflow of ionospheric ions from the dayside cusp/cleft. 2 Applications. *Annales Geophysicae*, 21:1773–1791, 2003b.

H. C. Brinton, J. M. Grebowsky, and H. G. Mayr. Altitude variation of ion composition in the midlatitude trough region: Evidence for upward plasma flow. *Journal of Geophysical Research*, 76:3738–3745, 1971.

D. G. Brown, G. R. Wilson, and J. L. Horwitz. 'Self-consistent' production of ion conics on return current region auroral field lines: a time-dependent, semi-kinetic model. *Geophysical Research Letters*, 18(10):1841–1844, 1991.

D. G. Brown, J. L. Horwitz, and G. R. Wilson. Synergistic effects of hot plasma-driven potentials and wave-driven ion heating on auroral ionospheric plasma transport. *Journal of Geophysical Research*, 100:17499–17514, 1995.

R. W. Cannata and T. I. Gombosi. Modeling of the solar cycle dependence of quiet-time ion upwelling at high geomagnetic latitudes. *Geophysical Research Letters*, 16:1141, 1989.

T. Chang and G. B. Crew. Transverse acceleration of oxygen ions by electromagnetic ion cyclotron resonance with broad band left-hand polarized waves. *Geophysical Research Letters*, 13(7): 636–639, 1986.

C. R. Chappell, T. E. Moore, and J. H. Waite. The ionosphere as a fully adequate source of plasma for the Earth's magnetosphere. *Journal of Geophysical Research*, 92:5896–5910, 1987.

C. R. Chappell, B. L. Giles, T. E. Moore, D. C. Delcourt, P. D. Craven, and M. O. Chandler. The adequacy of the ionospheric source in supplying magnetospheric plasma. *Journal of Atmospheric and Solar-Terrestrial Physics*, 62(421), 2000.

C. C. Chaston, J. W. Bonnell, C. W. Carlson, J. P. McFadden, R. E. Ergun, and R. J. Strangeway. Kinetic effects in the acceleration of electrons by small scale Alfvén wave: A FAST case study. *Geophysical Research Letters*, 30(6):1289, 2003.

C. C. Chaston, J. W. Bonnell, C. W. Carlson, J. P. McFadden, R. E. Ergun, R. J. Strangeway, and E. J. Lund. Auroral ion acceleration in dispersive Alfvén waves. *Journal of Geophysical Research*, 109(A04205), 2004.

J. B. Cladis. Transport of ionospheric ions in the magnetosphere: Theory and observations. *Advances in Space Research*, 8(165), 1988.

H. E. Coffey. Geomagnetic and solar data. *Journal of Geophysical Research*, 87(926), 1982a.

H. E. Coffey. Geomagnetic and solar data. *Journal of Geophysical Research*, 87(1733), 1982b.

H. E. Coffey. Geomagnetic and solar data. *Journal of Geophysical Research*, 87(5310), 1982c.

M. R. Collier, D. Chornay, J. Clemmons, J. W. Keller, J. Klenzing, J. Kujawksi, J. McLain, R. Pfaff, R. Rowland, and M. Zettergren. VISIONS remote observations of a spatially-structured filamentary source of energetic neutral atoms near the polar cap boundary during an auroral substorm. *Advances in Space Research*, 56(10):2097–2105, 2015.

H. L. Collin, W. K. Peterson, O. W. Lennartsson, and J. F. Drake. The seasonal variation of auroral ion beams. *Geophysical Research Letters*, 25:4071, 1998.

G. B. Crew, T. Chang, and J. M. Retterer. Ion cyclotron resonance heated conics: Theory and observations. *Journal of Geophysical Research*, 95(A4):3959–3985, 1990.

S. A. Curtis. Equatorial trapped plasmasphere ion distributions and transverse stochastic accelerations. *Journal of Geophysical Research*, 90(1765), 1985.

D. Delcourt. *Circulation des ions ionospheriques suprathermiques dans la magnetosphere terrestre*. PhD thesis, Toulouse University, 1985.

D. C. Delcourt, B. L. Giles, C. R. Chappell, and T. E. Moore. Low-energy bounding ions in the magnetosphere: A three-dimensional numerical study of Dynamics Explorer 1 data. *Journal of Geophysical Research*, 93:1859, 1988.

D. C. Delcourt, C. R. Chappell, T. E. Moore, and J. H. Waite. A three-dimensional numerical model of ionospheric plasma in the magnetosphere. *Journal of Geophysical Research*, 94(11): 893, 1989.

D. C. Delcourt, J. A. Sauvaud, and T. E. Moore. Polar wind ion dynamics in the magnetotail. *Journal of Geophysical Research*, 98:9155, 1993.

H. G. Demars, R. W. Shunk, and A. R. Barakat. Comparing fluid and particle-in-cell solutions for the polar wind. *Journal of Geophysical Research*, 104:28535–28545, 1999.

A. J. Dessler and F. C. Michel. Plasma in the geomagnetic tail. *Journal of Geophysical Research*, 71(1421), 1966.

N. Dubouloz, D. Delcourt, M. Malingre, J. J. Berthelier, and D. Chugunin. Remote analyis of cleft ion acceleration using thermal plasma measurements from Interball Auroral Probe. *Geophysical Research Letters*, 25:2925, 1998.

T. E. Eastman, L. A. Frank, and C. Y. Huang. The boundary layers as the primary transport regions of the Earth's magnetotail. *Journal of Geophysical Research*, 90:9541, 1985.

O. Eldridge. Electron cyclotron heating as resonant diffusion. *Physics of Fluids*, 676(15), 1972.

G. M. Estep. *A coupled fluid-generalized semi-kinetic model for treating time-dependent ionospheric outflows.* PhD thesis, University of Alabama, 1998.

G. M. Estep, Y. J. Su, J. L. Horwitz, P. G. Richards, G. R. Wilson, and D. G. Brown. A dynamic coupled fluid-semikinetic model for ionosphere-magnetosphere plasma transport: Effects of ionization by soft electron precipitation. *Eos Transactions AGU*, 79(17):S317, 1998.

S. Figueiredo, G. Marklund, T. Karlsson, T. Johansson, Y. Ebihara, N. Ejiri, M. Ivchenko, P. A. Lindqvist, H. Nilsson, and A. Fazakerley. Temporal and spatial evolution of discrete auroral arcs as seen by cluster. *Annals of Geophysics*, 23:2531–2557, 2005.

F. R. E. Forme. A new interpretation of the origin of enhanced ion acoustic fluctuations in the upper ionosphere. *Geophysical Research Letters*, 20:2347–2350, 1993.

F. R. E. Forme, J. E. Wahlund, H. J. Opgenoorth, M. A. L. Persson, and E. Mishin. Effects of current driven instabilities on the ion and electron temperatures in the topside ionosphere. *Journal of Atmospheric and Terrestrial Physics*, 55:647–666, 1993.

C. Foster and M. Lester. Observations of nightside auroral plasma upflows in the F-region and topside ionosphere. *Annals of Geophysics*, 14:1274–1283, 1996.

G. Ganguli, M. J. Keskinen, H. Romero, R. Heelis, T. Moore, and C. Pollock. Coupling of microproceses and macroproceses due to velocity shear: An application to the low-altitude ionosphere. *Journal of Geophysical Research*, 99(8873), 1994.

S. B. Ganguli. The polar wind. *Reviews of Geophysics*, 34:311, 1996.

B. L. Giles. *Inner magnetosphere circulation of thermal ions inferred from observed pitch angle distributions.* PhD thesis, University of Alabama, 1993.

A. Glocer, G. Toth, and M. C. Fok. Including kinetic ion effects in the coupled global ionospheric outflow solution. *Journal of Geophysical Research- Space Physics*, 123:1851–2871, 2018.

S. N. Golovato, R. A. Breun, J. R. Ferron, R. H. Goulding, N. Hershkowitz, S. F. Horne, and L. Yujiri. Fueling and heating of tandem mirror end cells using rf at the ion cyclotron frequency. *Physics of Fluids*, 28(2), 1985.

D. J. Gorney, Y. T. Chiu, and D. R. Croley. Trapping of ion conics by downward electric fields. *Journal of Geophysical Research*, 90:4205, 1985.

M. Hirahara. Relationship of topside ionospheric ion outflows to auroral forms and precipitation, plasma waves, and convection observed by Polar. *Journal of Geophysical Research*, 103(17): 391, 1998.

C. W. Ho, J. L. Horwitz, and G. R. Wilson. Dynamics of the H^+ and O^+ polar wind in the transition region as influenced by ionospheric convection and electron heating. *Journal of Geophysical Research*, 102:395, 1997.

W. M. Hooke and M. A. Rothman. A survey of experiments of ion cyclotron resonance in plasmas. *Nuclear Fusion*, 4(33), 1964.

J. L. Horwitz. Velocity filter mechanism for ion bowl distributions (Bimodal conics). *Journal of Geophysical Research*, 91:4513, 1986.

J. L. Horwitz. Parabolic heavy ion flow in the polar magnetosphere. *Journal of Geophysical Research*, 92(175), 1987.

J. D. Huba, G. Joyce, and J. A. Fedder. Sami2 is Another Model of the Ionospere (SAMI2): A new low-latitude ionosphere model. *Journal of Geophysical Research*, 105(A10):23035–23053, 2000.

M. M. Huddleston, C. J. Pollock, M. P. Wuest, J. S. Pichett, T. E. Moore, and W. K. Peterson. Toroidal ion distributions observed at high altitudes equatorward of the cusp. *Geophysical Research Letters*, 27:469–472, 2000.

M. M. Huddleston, C. R. Chappell, D. C. Delcourt, T. E. Moore, B. L. Giles, and M. O. Chandler. An examination of the process and magnitude of ionospheric plasma supply to the magnetosphere. *Journal of Geophysical Research*, 110(A12202), 2005.

S. Ichimaru. *Basic principles of plasma physics: A statistical approach.* W. A. Benjamin, Reading, Massachusetts, 1973.

U. Inan, Y. Chiu, and G. Davidson. Whistler-mode chorus and morning-side aurorae. *Geophysical Research Letters*, 19:653–656, 1992.

J. R. Jasperse. Ion heating, electron acceleration, and the self-consistent parallel E-field in downward auroral current regions. *Geophysical Research Letters*, 25:3485, 1998.

T. Johansson, S. Figueiredo, T. Karlsson, G. Marklund, A. Fazakerley, S. Buchert, P. A. Lindqvist, and H. Nilsson. Intense high-altitude auroral electric fields- temporal and spatial characteristics. *Annals of Geophysics*, 22:2485–2495, 2004.

T. Johansson, G. Marklund, T. Karlsson, S. Lileo, P. A. Lindqvist, A. Marchaudon, H. Nilsson, and A. Fazakerley. On the profile of intense high-alititude auroral electric fields at magnetospheric boundaries. *Annals of Geophysics*, 24:1713–1723, 2006.

T. Johansson, G. Marklund, T. Karlsson, S. Lileo, P. A. Lindqvist, H. Nilsson, and S. Buchert. Scale sizes of intense auroral electric fields observed by cluster. *Annals of Geophysics*, 25:2413–2425, 2007.

G. O. L. Jones, P. J. S. Williams, K. J. Winser, M. Lockwood, and K. Suvanto. Large plasma velocities along the magnetic field line in the auroral zone. *Nature*, 336:231–232, 1988.

G. V. Khazanov, M. W. Liemohn, and T. E. Moore. Photoelectron effects on the self-consistent potential in the collisionless polar wind. *Journal of Geophysical Research*, 102:7509–7522, 1997.

P. M. Kintner, J. Bonnell, R. Arnoldy, K. Lynch, C. Pollock, and T. Moore. SCIFER- transverse ion acceleration and plasma waves. *Geophysical Research Letters*, 23:1873–1876, 1996.

M. G. Kivelson and H. E. Spence. On the possibility of quasi-static convection in the quiet magnetotail. *Geophysical Research Letters*, 15:1541, 1988.

D. M. Klumpar, W. K. Peterson, and E. G. Shelley. Direct evidence for two-stage (bimodal) acceleration of ionospheric ions. *Journal of Geophysical Research*, 89(10):779, 1984.

D. J. Knudsen, B. A. Whalen, T. Abe, and A. Yau. Temporal evolution and spatial dispersion of ion conics: evidence of a polar cusp heating wall. *Solar System Plasmas in Space and Time, Geophysical Monograph Series*, 84:163–169, 1994.

J. Lemaire. O^+, H^+, and He^+ ion distributions in a new polar wind model. *Journal of Atmospheric and Terrestrial Physics*, 34:1647–1658, 1972.

J. Lemaire and M. Scherer. Kinetic models of the solar and polar winds. *Reviews of Geophysics and Space Physics*, 11(427), 1973.

O. W. Lennartsson. Ion composition aspects of magnetotail plasma flows. *Journal of Geophysical Research*, 106(15):621, 2001.

P. Li, G. R. Wilson, J. L. Horwitz, and T. E. Moore. Effect of mid-altitude ion heating on ion outflow at polar latitudes. *Journal of Geophysical Research*, 93(9753), 1988.

X. Li and T. Temerin. Ponderomotive effects on ion acceleration in the auroral zone. *Geophysical Research Letters*, 20:13–16, 1993.

Ø. Lie-Svendsen and M. H. Rees. An improved kinetic model for the polar outflow of a minor ion. *Journal of Geophysical Research*, 101:2415–2433, 1996.

M. Lockwood, M. O. Chandler, J. L. Horwitz, J. H. Waite, T. E. Moore, and C. R. Chappell. The cleft ion fountain. *Journal of Geophysical Research*, 90:9736, 1985a.

M. Lockwood, J. H. Waite, T. E. Moore, J. F. E. Johnson, and C. R. Chappell. A new source of suprathermal O^+ ions near the dayside polar cap boundary. *Journal of Geophysical Research*, 90:4099, 1985b.

M. Loranc, W. B. Hanson, R. A. Heelis, and J. P. St-Maurice. A morphological study of vertical ionospheric flows in the high-latitude F region. *Journal of Geophysical Research*, 96:3627–3646, 1991.

A. T. Y. Lui, D. Venkatesan, C. D. Anger, S. I. Akasofu, W. J. Heikkila, J. D. Winningham, and J. R. Burrows. Simultaneous observations of particle precipitations and auroral emissions by the isis 2 satellite in the 19-24 MLT sector. *Journal of Geophysical Research*, 82(16):2210–2226, 1977.

E. J. Lund, E. Moebius, C. W. Carlson, R. E. Ergun, L. M. Kistler, B. Klecker, D. M. Klumpar, J. P. McFadden, M. A. Popecki, R. J. Strangeway, and Y. K. Tung. Transverse ion acceleration mechanism in the aurora at solar minimum: occurrence distributions. *Journal of Atmospheric and Terrestrial Physics*, 62:467–475, 2000.

K. A. Lynch, R. L. Arnoldy, P. M. Kintner, and J. Bonnell. The AMICIST auroral sounding rocket: a comparison of transverse ion acceleration mechanisms. *Geophysical Research Letters*, 23: 3293–3296, 1996.

K. A. Lynch, R. L. Arnoldy, P. M. Kintner, P. Schuck, J. W. Bonnell, and V. Coffey. Auroral ion acceleration from lower hybrid solitary structure: a summary of sounding rocket observations. *Journal of Geophysical Research*, 104(A12):28151–28534, 1999.

G. Marklund, T. Karlsson, and J. Clemmons. On low-altitude particle acceleration and intense electric fields and their relation to black aurora. *Journal of Geophysical Research*, 102:17509–17522, 1997.

G. Marklund, M. Ivchenko, T. Karlsson, A. Fazakerley, M. Dunlop, P. A. Lindqvist, S. Buchert, C. Owen, M. Taylor, A. Vaivads, P. Carter, M. Andre, and A. Balogh. Temporal evolution of the electric field accelerating electrons away from the auroral ionosphere. *Nature*, 414:724–727, 2001.

G. Marklund, T. Johansson, S. Lileo, and T. Karlsson. Cluster observations of an auroral potential and associated field-aligned current reconfiguration during thinning of the plasma sheet boundary layer. *Journal of Geophysical Research*, 112(A01208), 2007.

G. T. Marklund. Electric Fields and Plasma Processes in the Auroral Downward Current Region, Below, Within, and Above the Acceleration Region. *Space Science Reviews*, 142:1–21, 2009.

G. T. Marklund, I. Sandahl, and H. Opgenoorth. A study of the dynamics of a discrete auroral arc. *Planetary and Space Science*, 30(2):179–197, 1982.

G. T. Marklund, L. G. Blomberg, C. G. Falthammar, and P. A. Lindqvist. On intense diverging electric fields associated with black aurora. *Geophysical Research Letters*, 21:1859–1862, 1994.

G. T. Marklund, S. Sadeghi, T. Karlsson, P. Lindqvist, H. Nilsson, C. Forsyth, A. Fazakerley, E. A. Lucek, and J. Pickett. Altitude distribution of the auroral acceleration potential determined from Cluster satellite data at different heights. *Physical Review Letters*, 106:055002, 2011.

J. P. McFadden, C. W. Carlson, and M. H. Boehm. Structure of an energetic narrow discrete arc. *Journal of Geophysical Research*, 95:6533–6547, 1990.

J. P. McFadden, C. W. Carlson, R. E. Ergun, F. S. Mozer, M. Temerin, W. Peria, D. M. Klumpar, E. G. Shelley, W. K. Peterson, E. Moebius, L. Kistler, R. Elphic, R. Strangeway, C. Cattell, and R. Pfaff. Spatial structure and gradients of ion beams observed by FAST. *Geophysical Research Letters*, 25(12):2012–2024, 1998.

C. I. Meng, B. Mauk, and C. E. McIlwain. Electron precipitation of evening diffuse aurora and its conjugate electron fluxes near the magnetospheric equator. *Journal of Geophysical Research*, 84 (A6):2545–2558, 1979.

H. G. Mitchell and P. J. Palmadesso. A dynamic model for the auroral field line plasma in the presence of field-alinged current. *Journal of Geophysical Research*, 88:2123, 1983.

T. E. Moore. Superthermal ionospheric outflows. *Reviews of Geophysics*, 22:2164–2174, 1984.

T. E. Moore and J. L. Horwitz. Stellar ablation of planetary atmospheres. *Reviews of Geophysics*, 45(RG3002), 2007.

T. E. Moore, J. H. Waite, M. Lockwood, and C. R. Chappell. Observations of coherent transverse ion acceleration. *Ion Acceleration in the Magnetosphere and Ionosphere, Geophysical Monograph Series*, 38:50, 1986.

T. E. Moore, R. Lundin, D. Alcaydé, M. André, S. B. Ganguli, M. Temerin, and A. Yau. Source processes in the high-altitude ionosphere. *Space Science Reviews*, 88:7–84, 1999.

T. Nagai, J. H. Waite, J. L. Green, C. R. Chappell, R. C. Olsen, and R. H. Comfort. First measurements of supersonic polar wind in the polar magnetosphere. *Geophysical Research Letters*, 11: 669–672, 1984.

B. Ni, R. M. Thorne, X. Zhang, J. Bortnik, Z. Pu, L. Xie, Z. Hu, D. Han, R. Shi, C. Zhou, and X. Gu. Origins of the Earth's Diffuse Auroral Precipitation. *Space Science Reviews*, 200(205-259), 2016.

A. Nishida. Formation of a plasmapause or magnetospheric plasma knee by combined action of magnetospheric convection and plasma escape from the tail. *Journal of Geophysical Research*, 71(5669), 1966.

P. Norqvist, M. André, and M. Tyrland. A statistical study of ion energization mechanisms in the auroral region. *Journal of Geophysical Research*, 103(23):459, 1998.

K. Nykyri, A. Otto, E. Adamson, E. Dougal, and J. Mumme. Cluster observations of a cusp diamagnetic cavity: Structure, size, and dynamics. *Journal of Geophysical Research*, 116(A03228), 2011.

K. Nykyri, C. Chu, X. Ma, S. A. Fuselier, and R. Rice. First mms observation and energetic particles trapped in high-latitude magnetic field depressions. *Journal of Geophysical Research-Space Physics*, 124:197–210, 2019.

Y. Ogawa, R. Fujii, S. C. Buchert, S. Nozawa, and S. Ohtani. Simultaneous EISCAT Svalbard radar and DMSP observations of ion upflow in the dayside polar ionosphere. *Journal of Geophysical Research- Space Physics*, 108:1101, 2003.

W. K. Peterson. On the sources of energization of molecular ions at ionospheric altitudes. *Journal of Geophysical Research*, 99:23257–23274, 1994.

S. M. Petrinec, D. L. Chenette, J. Mobilia, M. A. Rinaldi, and W. L. Imhof. Statistical X ray auroral emissions- PIXIE observations. *Geophysical Research Letters*, 26(11):1565–1568, 1999.

J. M. Retterer, T. Chang, and J. R. Jasperse. Ion acceleration in the suprathermal region: a Monte Carlo model. *Geophysical Research Letters*, 10:583–586, 1983.

J. M. Retterer, T. Chang, and J. R. Jasperse. *Particle acceleration by intense auroral VLF turbulence.*, volume 119. Physics of Space Plasmas, Sci. Publishers, Cambridge, Angleterre, 1989.

P. G. Richards and D. G. Torr. Auroral modeling of the 3371 Angstrom emission rate: Dependence on characteristic electron energy. *Journal of Geophysical Research*, 95:10337–10344, 1990.

H. Rishbeth and O. K. Garriott. *Introduction to Ionospheric Physics.*, volume 14 of *International geophysics series*. New York: Academic Press, 1969.

J. A. Sauvaud and D. Delcourt. A numerical study of suprathermal ionospheric ion trajectories in three-dimensional electric and magnetic field models. *Journal of Geophysical Research*, 92: 5873, 1987.

D. Schriver. Particle simulation of the auroral zone showing parallel electric fields, waves, and plasma acceleration. *Journal of Geophysical Research*, 104(14):655, 1999.

M. Schulz. Particle drift and loss rates under strong pitch angle diffusion in Dungey's model magnetosphere. *Journal of Geophysical Research*, 103(A1):61–67, 1998.

M. Schulz and L. J. Lanzerotti. *Particle Diffusion in the Radiation Belts.* Springer-Verlag, New York, 1974.

P. W. Schunk and J. J. Sojka. A three-dimensional time-dependent model of the polar wind. *Journal of Geophysical Research*, 94:8973–8991, 1989.

Y. Seo, R. Canton, and J. L. Horwitz. Statistical relationships between high-latitude ionospheric F region/topside upflows and their drivers: DE-2 observations. *Journal of Geophysical Research*, 102:7493, 1997.

R. D. Sharp, R. G. Johnson, and E. G. Shelley. Observations of an ionospheric acceleration mechanism producing energetic (keV) ions primarily normal to the geomagnetic field direction. *Journal of Geophysical Research*, 82:3324, 1977.

E. G. Shelley, R. G. Johnson, and R. D. Sharp. Satellite observations of energetic heavy ions during a geomagnetic storm. *Journal of Geophysical Research*, 77:6104, 1972.

E. G. Shelley, R. D. Sharp, and R. G. Johnson. Satellite observations of an ionospheric acceleration mechanism. *Geophysical Research Letters*, 3:654, 1976.

R. W. Shunk and A. F. Nagy. *Ionospheres- Physics, Plasma Physics, and Chemistry.* Cambridge Atmospheric and Space Science Series. Cambridge University Press, 2000.

N. Singh and C. B. Chan. Numerical simulation of plasma processes driven by transverse ion heating. *Journal of Geophysical Research*, 98(A7):11677–11687, 1993.

J. P. St-Maurice and R. W. Shunk. Ion velocity distributions in the high-latitude ionosphere. *Reviews of Geophysics*, 17:99–134, 1979.

R. J. Strangeway, R. E. Ergun, Y. J. Su, C. W. Carlson, and R. C. Elphic. Factors controlling ionospheric outflows as observed at intermediate altitudes. *Journal of Geophysical Research*, 110, 2005.

Y. J. Su, J. L. Horwitz, G. R. Wilson, P. G. Richards, D. G. Brown, and C. W. Ho. Self-consistent simulation of the photoelectron driven polar wind from 120 km to 9 R_e altitude. *Journal of Geophysical Research*, 103:2279–2296, 1998.

Y. J. Su, R. G. Canton, J. L. Horwitz, and P. G. Richards. Systematic modeling of soft-electron precipitation effects on high-latitude F region and topside ionospheric upflows. *Journal of Geophysical Research*, 104:153–163, 1999.

B. Thelin, B. Aparicio, and R. Lundin. Observations of upflowing ionospheric ions in the mid-altitude cusp/cleft region with the Viking satellite. *Journal of Geophysical Research*, 95:5931–5939, 1990.

B. J. Thompson and R. L. Lysak. Electron acceleration by inertial Alfvén waves. *Journal of Geophysical Research*, 101:5359, 1996.

A. Vaivads, M. André, S. Buchert, A. Eriksson, A. Olsson, J. E. Wahlund, P. Janhunen, G. Marklund, L. Kistler, C. Mouikis, D. Winningham, A. Fazakerley, and P. Newell. What high altitude observations tell us about the auroral acceleration: A Cluster/DMSP conjunction. *Geophysical Research Letters*, 30(1106), 2003.

J. E. Wahlund and H. J. Opgenoorth. EISCAT observations of strong ion outflows from the F-region during auroral activity: preliminary results. *Geophysical Research Letters*, 16, 1989.

J. E. Wahlund, H. J. Opgenoorth, I. Haggstrom, K. J. Winser, and G. O. L. Jones. EISCAT observations of topside ionospheric ion outflows during auroral activity: revisited. *Journal of Geophysical Research*, 97:3019–3037, 1992.

J. E. Wahlund, H. J. Opgenoorth, F. R. E. Forme, M. A. L. Persson, I. Haggstrom, and J. Lillensten. Electron energization in the topside auroral ionosphere: on the importance of ion-acoustic turbulence. *Journal of Atmospheric and Terrestrial Physics*, 55:623–645, 1993.

J. H. Waite. Escape of suprathermal O^+ ions in the polar cap. *Journal of Geophysical Research*, 90:1619–1630, 1985.

G. R. Wilson. Semikinetic modeling of the outflow of ionospheric plasma through the topside collisional to collisionless transition region. *Journal of Geophysical Research*, 97:10551–10565, 1992.

G. R. Wilson. Kinetic modeling of O^+ upflows resulting from E×B convection heating in the high-latitude F region ionosphere. *Journal of Geophysical Research*, 99(A9):17453–17466, 1994.

G. R. Wilson. Development of non-Maxwellian velocity distributions as a consequence of nonlocal Coulomb collisions. *Cross-Scale Coupling in Space Plasma, Geophysical Monograph Series*, 93:47–60, 1995.

G. R. Wilson, C. W. Ho, J. L. Horwitz, and N. Singh. A new kinetic model for time-dependent polar plasma outflow: Initial results. *Geophysical Research Letters*, 17(3):263–266, 1990.

J. D. Winningham and J. Burch. Observation of large scale ion conic generation with DE-1. In J. Belcher, H. Bridge, T. Chang, B. Coppi, and J. R. Jasperse, editors, *Physics of Space Plasmas*, number 5 in SPI Conference Proceedings and Reprint Series, Cambridge, Mass., 1984a. Scientific Publishers, Inc.

J. D. Winningham and J. Burch. Observations of large-scale ion conic generation with DE-1. *Physics of Space Plasmas*, 5:137–158, 1984b.

K. J. Winser, G. O. L. Jones, and P. J. S. Williams. Large field-aligned velocities observed by EISCAT. *Journal of Atmospheric and Terrestrial Physics*, 50:379–382, 1988.

D. Winske and N. Omidi. A nonspecialists guide to kinetic simulations of space plasmas. *Journal of Geophysical Research*, 101:17287–17304, 1996.

C. S. Wohlwend. *Modeling the electrodynamics of the low-latitude ionosphere.* PhD thesis, Utah State University, 2008.

J. Wu, M. Blanc, D. Alcaydé, A. R. Barakat, J. Fontanari, P. L. Blelly, and W. Kofman. Observations of the structure and vertical transport of the polar upper ionosphere with the EISCAT-VHE radar. 2- first investigations of the topside O^+ and H^+ vertical ion flows. *Annals of Geophysics*, 10:375–393, 1992.

X. Y. Wu, J. L. Horwitz, G. M. Estep, Y. J. Su, D. G. Brown, and P. G. Richards. Dynamics fluid-kinetic (DyFK) modeling of auroral plasma outflow driven by soft electron precipitation and transverse ion heating. *Journal of Geophysical Research*, 104(A8):17263–17275, 1999.

X. Y. Wu, J. L. Horwitz, and Y. Seo. Statistical analysis of F region and topside ionospheric ion field-aligned flow at high latitudes. *Journal of Geophysical Research*, 105:2477, 2000.

X. Y. Wu, J. L. Horwitz, and J. N. Tu. Dynamic fluid kinetic (DyFK) simulation of auroral ion transport: Synergistic effects of parallel potentials, transverse ion heating, and soft electron precipitation. *Journal of Geophysical Research*, 107(A10):1283, 2002.

A. W. Yau and M. Andre. Sources of ion outflow in the high latitude ionosphere. *Space Science Reviews*, 80(1), 1997.

A. W. Yau, E. G. Shelley, W. K. Peterson, and L. Lenchyshyn. Energetic auroral and polar ion outflow at DE-1 altitudes: Magnitude, composition, magnetic activity dependence and long-term variations. *Journal of Geophysical Research*, 90:8417, 1985.

W. Zeng, J. L. Horwitz, and J. N. Tu. Characteristic ion distributions in the dynamic auroral transition region. *Journal of Geophysical Research*, 111, 2006.

M. Zettergren. *Model-based optical and radar remote sensing of transport and composition in the auroral ionosphere.* PhD thesis, Boston University, 2009.

M. Zettergren and J. Semeter. Ionospheric plasma transport and loss in auroral downward current regions. *Journal of Geophysical Research- Space Physics*, 117(A6):6306, 2012.

Y. Zheng, T. E. Moore, F. S. Mozer, C. T. Russell, and R. J. Strangeway. Polar study of ionospheric ion outflow versus energy input. *Journal of Geophysical Research*, 110, 2005.